DEVELOPING DESIGN CRITERIA AND SCALE-UP METHODS FOR WATER-STABLE METAL-ORGANIC FRAMEWORKS FOR ADSORPTION APPLICATIONS

A Dissertation
Presented to
The Academic Faculty

by

Himanshu Jasuja

In Partial Fulfillment
of the Requirements for the Degree
Doctor of Philosophy in the
School of Chemical and Biomolecular Engineering

Georgia Institute of Technology
August 2014

DEVELOPING DESIGN CRITERIA AND SCALE-UP METHODS FOR WATER-STABLE METAL-ORGANIC FRAMEWORKS FOR ADSORPTION APPLICATIONS

Approved by:

Dr. Krista S. Walton, Advisor
School of Chemical and Biomolecular Engineering
Georgia Institute of Technology

Dr. David S. Sholl
School of Chemical and Biomolecular Engineering
Georgia Institute of Technology

Dr. William J. Koros
School of Chemical and Biomolecular Engineering
Georgia Institute of Technology

Dr. Angus P. Wilkinson
School of Chemistry and Biochemistry
Georgia Institute of Technology

Dr. J. Carson Meredith
School of Chemical and Biomolecular Engineering
Georgia Institute of Technology

Date Approved: [June 02, 2014]

To my mother, Veena Jasuja and my father, Charan Das Jasuja

ACKNOWLEDGEMENTS

Firstly, I would like to acknowledge my young, dynamic advisor Dr. Krista S. Walton for accepting me into her research group, fulfilling my PhD research requirements by purchasing various chemicals and equipment, allowing me to attend technical conferences, providing constructive feedback on my writing and presentation skills, and writing recommendation letters for me whenever requested. I think joining her group was the best thing happened to me back in 2010 and I feel tremendously lucky to have her as my PhD advisor. I really appreciate her approach of not spoon feeding her students and let them learn from their mistakes. I am quite sure that my learnings in Walton research group will fetch me success in my future endeavors too.

I also wish to thank my committee members, Dr. David S. Sholl, Dr. J. Carson Meredith, Dr. William J. Koros, and Dr. Angus P. Wilkinson for their time and valuable inputs. I would like to express my deepest appreciation for Dr. Sholl for writing recommendation letters whenever an industry recruiter asked and letting me collaborate with his group members for the computational validation of my experimental findings.

Most importantly, I am also thankful to all the former and current Walton group members (Dr. Huang, Dr. Schoenecker, Dr. Karra, Dr. Cai, Dr. Stults, Christine, Deonte, Dr. Grabicka, Nick, Greg, Karen, Will, Yang, Ken, Mike M., Michael D., Erica, Jun, Dr. Duerinck, and Lalit) for their help and friendship, which certainly made my stay in Walton group enjoyable. Especial thanks to my go to man Nick aka ‘Boss’ for the amazing collaborative work on the MOF water stability, undergraduate researcher Deonte for his help with the batch scale-up experiments, and Dr. Huang for his help with the

reitveld refinement of powder XRD data and solving the single crystal x-ray diffraction data for my new MOF crystals. I would also like to acknowledge Dr. Schoenecker, Greg, and Dr. Stults for training me on lab equipment such as IGA-1,-3, BET machine, and TGA. I also owe a big thanks to Dr. Grabicka for the polish candies/ ice-creams☺ and being an awesome lab manger ensuring smooth operation of the Walton group labs.

Outside of the Walton research Group, I thank Greg, Matt, and Dr. Decoste at ECBC for the help with ammonia breakthrough experiments, Dr. Leisen at Georgia Tech NMR center for his help in collecting the NMR spectra, Dr. Bacsa at Emory University for collecting the single crystal X-ray data, and Dr. Nair's research group (especially Dr. Kassaee) for training me to use their powder X-ray diffraction equipment. I would also like to acknowledge former and current Sholl group members (Dr. Haldoupis, Dr. Zang, Amberish, Dalar, and Jason) for various technical discussions that helped my research immensely. I also thank our neighbors, i.e., members of Dr. Kohl's research group (John, Dr. Stark, and Brennen) for letting me use their equipment for my experiments and of Dr. Koros's research group (Dr. Bhuwania, Steven, and Stephanie) for lending me liquid nitrogen whenever needed. I am also very grateful to the administrative staff (Leslie, Rod, Brad, Janice, Todd, Claudia, Juanita, Kevin, and Michelle) of ChBE for their help and support throughout my graduate studies.

My mother always wanted me to become a surgeon (real doctor!!) and even when I decided to get a PhD and become a not so real doctor☺, my family has always been a constant source of love, concern, and support. Thanks a ton guys! I would also like to whole-heartedly thank the all-mighty, and my friends for keeping me afloat during tough

times. Last but not the least; I would like to thank the Army Research Office and Air Products & Chemicals Inc. Graduate Fellowship Program for the financial support.

TABLE OF CONTENTS

LIST OF TABLES

LIST OF FIGURES

Page

LIST OF SYMBOLS AND ABBREVIATIONS

Symbols

P	Pressure
P_o	Saturation Vapor Pressure
λ	Wavelength
θ	Scattering Angle
ΔG°	Change in Free Energy
E_a	Activation Energy
K_H	Henry's Constant
CO_2	Carbon Dioxide
CH_4	Methane
N_2	Nitrogen
H_2O	Water
pK_a	Basicity of Ligand
Zr	Zirconium
Zn	Zinc
Co	Cobalt
Ni	Nickel
Cu	Copper
Mo	Molybdenum
$M(NO_3)_2$	Metal (II) Nitrate
$ZrCl_4$	Zirconium (IV) Chloride
MeOH	Methanol
EtOH	Ethanol
$CHCl_3$	Chloroform

Abbreviations

Å	Angstrom
K	Kelvin
^{o}C	Degree Celsius
eV	Electron Volt
hr(s)	Hour(s)
M	Molarity
g	Gram
mg	Milligram
kg	Kilogram
L	Liters
mL	Milliliters
cm^3/g	Cubic Centimeter per Gram
cm^3/min	Cubic Centimeter per Minute
mg/m^3	Milligram per Cubic Meter
m^2/g	Square Meter per Gram
nm	Nanometer
ppm	Parts per Million
BDC	1,4-Benzene Dicarboxylic Acid
NDC	Naphthalene Dicarboxylic Acid
ADC	9,10-Anthracene Dicarboxylic Acid
BTC	1,3,5-Benzene Tricarboxylic Acid
DABCO	1,4-Diazabicyclo[2.2.2]octane
BPY	4,4’-Bipyridyl
BTTB	4,4’,4’’,4’’’-Benzene-1,2,4,5-Tetrayltetrabenzoic Acid

SBU	Secondary Building Unit
PXRD	Powder X-ray Diffraction
FTIR	Fourier Transform Infrared
BET	Brunauer, Emmett, and Teller
DA	Dubinin-Astakov
TGA	Thermal Gravimetric Analysis
NMR	Nuclear Magnetic Resonance
CPMAS	Cross Polarization Magic-Angle Spinning
IGA	Intelligent Gravimetric Analyzer
MOF	Metal-Organic Framework
STY	Space Time Yield
RH	Relative Humidity
CIF	Crystallographic Information File
PSM	Post-Synthetic Modification
TIC	Toxic Industrial Chemical
CWA	Chemical Warfare Agent
CBRN	Chemical, Biological, Radiological, and Nuclear
HT	High-Throughput
UiO	University of Oslo
MIL	Materials from Institut Lavoisier
ZIF	Zeolitic Imidazolate Framework
DMF	N,N′-Dimethylformamide
DEF	N,N′-Diethylformamide
DMA	N,N′-Dimethylacetamide
ECBC	Edgewood Chemical Biological Center

SUMMARY

Metal-organic frameworks (MOFs) are a relatively new class of porous materials, assembled from inorganic metal nodes and organic ligands. MOFs have garnered significant attention in the porous materials and adsorption field in recent years due to their various attractive features such as high surface areas and pore volumes, uniform pore sizes which are easily tunable, chemically functionalized adsorption sites, and potential for post-synthetic modification (PSM). These features give MOFs enormous potential for use in applications such as air purification, gas storage, adsorption separations, catalysis, gas sensing, and drug delivery. Therefore, synthesis and adsorption studies of porous MOFs have increased tremendously in recent years. Among the aforementioned applications, air purification and air quality control are important topics because existing porous media are ineffective at the adsorptive removal of toxic industrial chemicals (TICs) and chemical warfare agents (CWAs). Thus, there is a critical need for radical improvements in these purification systems. MOFs have shown great potential to become next-generation filter media as they outperform the traditional porous materials such as activated carbons and zeolites in the air purification of TICs such as ammonia and sulfur dioxide.

In spite of the numerous desirable attributes of MOFs, the practical use of these new materials in applications ranging from adsorption separations to controlled storage and release hinges on their stability in humid or aqueous environments. The sensitivity of certain MOFs under humid conditions is well known, but systematic studies of water adsorption properties of MOFs are scarce. This information is critical for identifying

structural factors that are important for the development of next-generation, water stable metal-organic frameworks. In addition to the water stability issue, difficulty in the scale-up of MOF synthesis has also plagued MOFs. Hence, the goal of this Ph.D. dissertation research has been to design ammonia-selective, water stable MOF(s) that can be synthesized on a large scale. This work will have a direct impact on moving the MOF field forward to the commercial level. To achieve the aforementioned goal, this Ph.D. dissertation research has been divided into the following three objectives:

(1) Advance our understanding of water stability of MOFs and develop design criteria for the construction of water-stable MOFs.

(2) Design water stable, ammonia-selective MOF(s) for next-generation CBRN (chemical, biological, radiological, and nuclear) filter media.

(3) Investigate the scale-up of the UiO-66 MOF scaffold.

Through the research efforts over the past four years, it is discovered that it is possible to adjust the water stability of a pillared MOF both in the positive and negative directions by proper shielding since shielding controls the accessibility of the metal centers for water molecules. This study is the first of its kind and is of high value for the MOF community. This shielding concept is further extended by synthesizing four novel isostructural MOFs with methyl functional groups at different positions on the BDC (benzene dicarboxylate) linker. For the first time, light is shed on the important distinction between kinetic and thermodynamic water stability and experimental evidence for a kinetically governed water stability mechanism in these MOFs is provided. It is also demonstrated that, using catenation in combination with a pillaring strategy, it is possible to obtain water stable MOFs even when the pillar ligand has lower basicity (pK_a value).

Ammonia breakthrough measurements have shown that a functionalized Zr-based UiO-66 material (e.g., UiO-66-OH) is promising, as it could offer a method for targeting the removal of specific chemical threats in an environmentally-stable framework that does not degrade in the presence of water, a well-known issue with MOFs. Large scale synthesis of a water stable MOF, UiO-66, is studied using glass vials and Teflon lined autoclaves. UiO-66 synthesis methods have been refined such that it is now possible to produce more than 70 times the yield obtained from the original synthesis report using the same reaction volume. Hence, space time yield (STY) has now increased to 196 kg/m^3day^{-1}, higher than that of most of the zeolites (STY ~ 50-150 kg/m^3day^{-1}) and BASF MOFs such as Basolite F300 (STY ~ 20 kg/m^3day^{-1}), Basolite Z1200 (STY ~ 100 kg/m^3day^{-1}), and Basolite A100 (STY ~ 160 kg/m^3day^{-1}). This would result in a significant reduction of the MOF production cost at the industrial scale.

More broadly, this Ph.D. dissertation work will lead to commercial applications of MOFs, which can revolutionize a variety of gas separation and storage problems such as CO_2 capture, natural gas upgrading, and methane and hydrogen storage for clean fuel technologies. This would greatly reduce the environmental concerns faced by our society today.

CHAPTER 1

INTRODUCTION

1.1 Classification of Porous Materials

The synthesis and characterization of porous materials for use as adsorbents and catalysts have been an active area of research for decades due to numerous uses in applications ranging from petrochemicals and catalysis to adsorption-based selective separations.[1] Porous materials can be classified into three categories based on their pore size, set out by IUPAC:[2] (1) microporous materials with pore size less than 2 nm, (2) mesoporous materials with pore size between 2 nm and 50 nm, and (3) macroporous materials with pore size greater than 50 nm. Porous materials can also be classified (Figure 1.1) based on the constituents (organic or inorganic or organic-inorganic hybrid) of their frameworks.[3] Traditional porous materials such as zeolites (inorganic) and activated carbons (organic) have been a focal point until mid-1990s.[4] However, limited new developments in synthetic zeolites and difficulties in controlling pore size distributions in activated carbons has led to the emergence of organic-inorganic hybrid structures known as metal-organic frameworks (MOFs) or porous coordination polymers (PCPs) as new contenders in the last 15 years.[5,6]

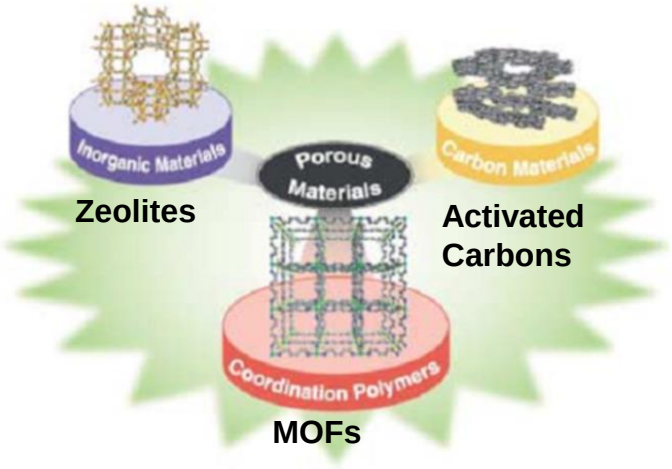

Figure 1.1 Various types of porous materials. This figure has been adapted from literature.[3]

1.1.1 Activated Carbon

Micro- or mesoporous carbonaceous materials are advantageous over other porous materials due to their low cost and have been used for applications such as air and water purification.[7,8] Activated carbons can be produced from a wide variety of cheap carbon sources such as wood, coal, coke pitch, coconut shells, and scraps of polymeric materials, which leads to variations in their pore size distributions and surface structures.[9] Activated carbons are synthesized from their carbon precursors usually in two-steps: (1) carbonization and (2) activation.[10] In the first step, pyrolysis of carbon precursors is performed to produce char followed by chemical treatment with acid or base or partial gasification with steam or air to generate active sites. Activated carbons produced in this manner are highly porous (high specific surface areas and pore volumes), but have a disordered (amorphous) structure unlike zeolites and MOFs. Due to their carbonaceous nature, activated carbons adsorb by van der Waals force or London dispersion force and

have higher affinity for nonpolar and weakly polar organic molecules compared to other adsorbents.[7]

1.1.2 Zeolites

Zeolites are porous crystalline aluminosilicates with the general formula $M^{n+}_{x/n}[(AlO_2)_x(SiO_2)_y]^{x-}\cdot wH_2O$ and consist of a periodic arrangement of tetrahedral $Si(Al)O_4$ units such that each apical oxygen atom is shared between two adjacent tetrahedra.[3,11] Aluminum atoms in zeolites introduce negative charge on the framework, which is balanced by exchangeable alkali or alkaline earth metal (M) cations in the pore space and this gives zeolites high affinity (hydrophilic) for polar molecules. However, pure silicates (SiO_2) do not contain charge on the framework since silicon is tetravalent and are hydrophobic. Zeolites have been a focal point of research in the field of porous materials since 1960[4] and their worldwide consumption is 5 million metric tons per year approximately due to their usage as fluid catalytic cracking (FCC) catalysts in petrochemical refineries, ion-exchangers for water softening, and adsorbents in gas separation.[12,13] However, new developments in synthetic zeolites have been limited due to the relatively small size of the pores, difficulty in the tuning of these pores, and difficulty in chemical modification of the surface. Moreover, there are only 213 (natural + artificial) zeolites structures[14] available even when these materials have been used commercially as adsorbents, ion exchangers, and catalysts since 1960.[4]

1.1.3 Metal Organic Frameworks (MOFs)

Remarkable progress in coordination chemistry and supramolecular assemblies has led to the development of a new class of structures known as metal-organic frameworks (MOFs) or porous coordination polymers (PCPs).[3,4] MOFs are fascinating

crystalline, porous materials synthesized by self-assembly of organic ligands and metal oxide clusters.[5] Figure 1.2a shows a cartoon representation[15]of a construction of a three-dimensional porous MOF (e.g., IRMOF-1 or MOF-5) via solvothermal method. These hybrid-materials provide us several advantages over pure inorganic or pure organic porous materials such as ultralow densities, extremely high surface areas and pore volumes, uniform pore sizes and chemically functionalized sorption sites.[5] Moreover, their pore sizes and chemical functionalities can be tuned by modifying the metal group (e.g., MOF-74 or CPO-27 system with open Mg,[16] Zn,[17] Co,[18] and Ni[19] sites) or pre-synthesis ligand functionalization (Figure 1.2b)[20] or post-synthetic modification (PSM, Figure 1.2c).[21] Hence, more than 10,000 MOF structures[22] have already been synthesized experimentally since their discovery in 1990-2000 and more than 120,000 hypothetical MOF structures have been envisaged by Wilmer et al.[23] This is considered to be a major advantage of MOFs over traditional porous materials. However, their stability especially under humid or aqueous environments is poor compared to the traditional porous materials.[24]

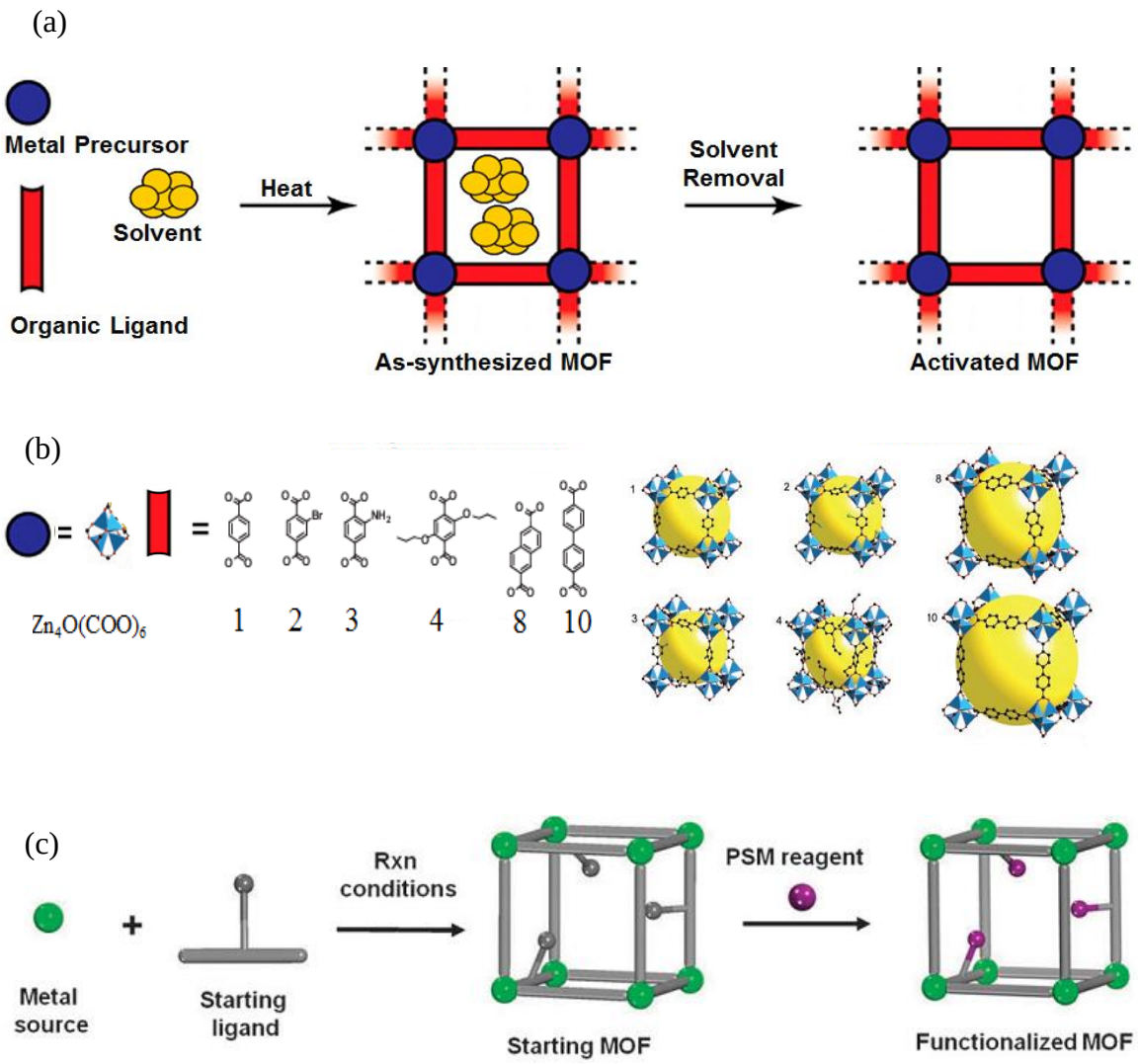

Figure 1.2 (a) Schematic displaying construction of an as-synthesized and activated MOF (e.g., IRMOF-1). (b) Tunability of IRMOF-n, with n = 1,2,3,4,8,10 (Metal cluster = $Zn_4O(COO)_6$ unit with zinc (blue), oxygen (red), and carbon (black). The large yellow spheres represent the largest van der Waals spheres that would fit in the cavities without touching the frameworks. All hydrogen atoms have been omitted for clarity. (c) A general scheme illustrating the concept of post-synthetic modification of MOFs. These figures have been adapted from literature.[15,20,21]

1.2 Synthesis of MOFs

MOFs are typically synthesized using batch solvothermal reactions similar to zeolites. However, there have been some publications reporting continuous-flow solvothermal MOF synthesis processes.[25-27] In the batch solvothermal MOF synthesis,[28] metal precursors (inorganic component) and ligands (organic component) are mixed in a pure solvent or appropriate mixture of solvents, and the resulting mixture is heated (Figure 1.2a) at low temperature (< 250 ^{0}C) in sealed vessels ("one-pot" synthesis) such as Teflon-lined stainless steel reactors[29] and glass vials. Apart from water, the main solvents used are alcohols (methanol and ethanol) and amides (dimethylformamide, diethylformamide, and dimethylacetamide). In order to optimize MOF synthesis conditions or synthesize a new MOF, high-throughput (HT) methods could be used since HT-methods provide an array of MOF synthesis trials with various different reactants and solvents (Figure 1.3).[30,31] MOFs have also been synthesized using non-conventional synthesis techniques such as microwave,[32] electrochemical,[33] organic solvent free synthesis[34,35,36] (e.g., mechanochemical synthesis[36]), and ultrasonic synthesis.[37] However, syntheses using these non-conventional techniques are still in their formative stages and cannot be applied to a wide range of MOFs unlike solvothermal method. Hence, these methods will require more time to become fully established.[36]

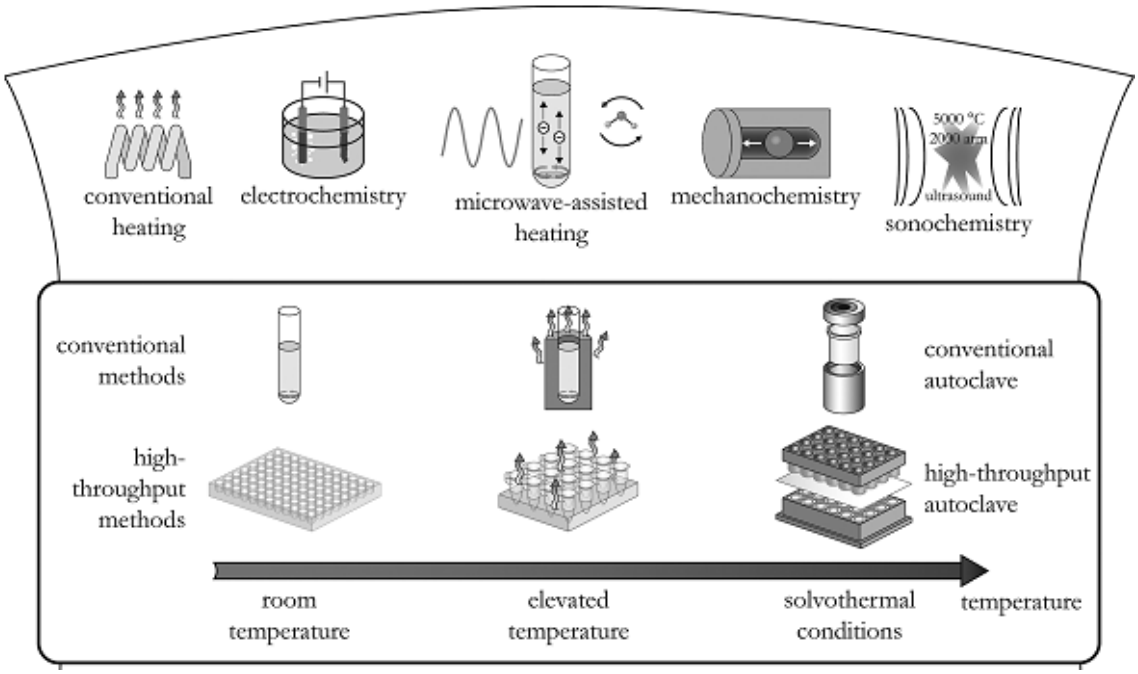

Figure 1.3 Schematic displaying MOF syntheses using conventional and non-conventional techniques. This figure has been adapted from literature.[38]

1.3 Potential Applications of MOFs

As discussed in section 1.1.3, MOFs possess tremendously high porosities and tunability compared to traditional porous materials such as zeolites, mesoporous silicas, and activated carbons.[3] Hence, MOFs have attracted significant amount of interest (Figure 1.4) in the last decade from various disciplines and physicists, chemists, material scientists, and chemical engineers are trying to utilize their potential in specialized applications such as nonlinear optics, magnetism, photoluminescence, catalysis, chiral separation applications, and drug delivery[39-46] and environmental applications such as air purification, methane or hydrogen storage in fuel tanks, gas separation (CO_2 capture), and gas sensing.[8,9,28,47-58]

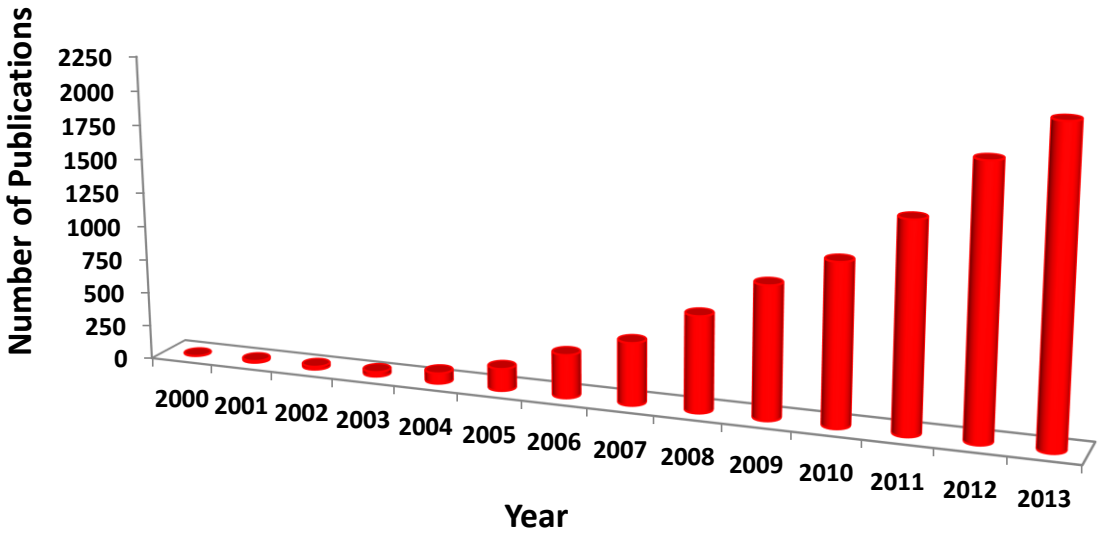

Figure 1.4 Number of publications containing the term "metal-organic frameworks" (Source: ISI Web of Science, retrieved April, 14th, 2014).

1.4 Motivation and Objectives of This Dissertation

Among the various potential applications (section 1.3) of MOFs, air purification is an important topic, because existing chemical, biological, radiological, and nuclear (CBRN) filters do a poor job of filtering toxic industrial chemicals (TICs) and chemical warfare agents (CWAs) such as ammonia, carbon disulfide, ethylene oxide, and formaldehyde.[59] Current CBRN filters use ASZM-TEDA (activated carbon impregnated with copper (A), silver (S), zinc (Z), molybdenum (M), and triethylenediamine (TEDA), marketed by Calgon Carbon Corporation[60]), which was designed to be a chrome-free replacement of ASC carbon (impregnated with copper (A), silver (S), and chromium (C)). Ammonia is among the high-hazard gases[59] and is also one of the most highly-produced inorganic chemicals because of its various usages in commercial (pharmaceuticals, cleaning products, and fertilizers) and military applications

(explosives).[58] There are numerous large-scale ammonia production plants worldwide with China, India, Russia, and the United States as the main contributors.[61] Hence, there is an urgent need for the search of proper adsorbents for radical improvements in the performance of the current CBRN filters towards TICs such as ammonia. There are a few publications in the literature reporting TIC adsorption in MOFs due to the defense-based nature of this application. Work done by Yaghi et al.[62] on TICs such as sulfur dioxide and ammonia shows that MOFs have a great potential to become next-generation filter media as they outperform the traditional porous materials such as BPL carbon, and zeolite 13X. Cu-BTC (HKUST-1) and Mg-MOF-74 have displayed high ammonia capacities (greater than ~ 5 mmol/g) due to the unsaturated metal centers; however, their structures collapse upon exposure to humid environments.[58,63,64] Stability of MOFs under humid environments is a fundamental requirement for their use in CBRN filters.[58]

Sensitivity to water vapor is widely considered to be a major weakness of MOFs compared to conventional adsorbents from an applications perspective, and the degradation of certain MOFs (e.g., IRMOF-1 or MOF-5) after exposure to humid conditions has been well documented.[24,65-79] Most of the previous studies done to address water stability of MOFs have focused on the hydrophobicity(philicity) of MOFs. It has been demonstrated that the introduction of water repellent functional groups within the frameworks can largely enhance the hydrophobic properties of MOFs. The stability of the MOFs in humid air can also be improved to some extent because less water could be adsorbed within the more hydrophobic pores.[74-77,80-88] However, it is extremely difficult to fully exclude water from adsorbing on the frameworks during long exposure times, even with highly hydrophobic pores. If the stability is simply due to decreased uptake of water,

then the quantity of water adsorbed on the MOFs over a long exposure time could eventually disrupt the structures significantly. Moreover, water adsorption isotherms have not been reported in the previous studies[70-72,74-76,84-87] and it is unclear whether the MOF is inherently stable due to the functional groups protecting the coordination sites or if it only appears stable because so little water adsorbs. So, there is a need to perform systematic water stability studies so that we can develop design criteria for the construction of water-stable MOFs. This type of work is of high value not only for the MOF community, but also for the fields of adsorption and porous materials.

In addition to the water stability issue, commercial and industrial applications of MOFs have also been hindered by difficulties in the scale-up of MOF synthesis methods. There are a few publications on MOF scale-up in the literature with varying level of details.[52,89,90,91,92] BASF is the only major company known to be working towards the industrial-scale synthesis of MOFs.[32-35,93] Six BASF MOFs (Basolite A100 or MIL-53(Al), Basolite C300 or HKUST-1, Basolite F300 or Fe-BTC, Basolite M050 or Mg-Formate, Basolite A520 or Al-Fumarate, and Basolite Z1200 or ZIF-8)[12,28,33,93] can be obtained commercially through Sigma Aldrich with prices up to ~ 30 $/g MOF.[94] With such a high price, MOFs cannot compete in the 3 billion dollar adsorbent market[95] and their synthesis cost must be reduced. Moreover, only Al-based Basolite MOFs (A100, A520) and Basolite Z1200 are stable under humid conditions.[12] Hence, currently only three water stable MOFs are commercially available and there is significant opportunity for the scale-up of other water stable MOF systems such as UiO-66,[64,68,72] MIL-100(Al),[96] and MIL-101(Al).[97]

Thus, the overall goal of this Ph.D. dissertation research is to design ammonia-selective, water stable MOFs, which can be synthesized on a large scale. This work will have a direct impact on moving the MOF field forward to the commercial level. The specific objectives of this Ph.D. dissertation are as follows:

(1) Advance our understanding of water stability of MOFs and develop design criteria for the construction of water-stable MOFs.

(2) Design water stable, ammonia-selective MOF(s) for next-generation CBRN (chemical, biological, radiological, and nuclear) filter media.

(3) Investigate the scale-up of the UiO-66 MOF scaffold.

The main contributions of this dissertation are two-fold. First, the systematic water vapor adsorption studies performed in this work (Chapters 3-6, Appendix F) on isostructural series of MOFs have advanced the fundamental understanding of water stability of MOFs. Hence, it is now possible to identify set of structural factors (though incomplete) governing structural stability of MOFs and direct the future synthesis efforts towards the construction of new water stable MOFs. Second, the effect of solvent reduction on the solvothermal synthesis of the UiO-66 MOF shown in this work (Chapter 9) will provide a platform for the future scale-up efforts for various functionalized variations of UiO-66 (Chapters 7,8), which have shown good performance for ammonia removal (Chapter 7) from air.

1.5 References

(1) Davis, M. E. Ordered Porous Materials for Emerging Applications. *Nature* **2002**, *417*, 813-821.

(2) Rouquerol, J.; Avnir D.; Fairbridge C. W.; Everett D. H.; Haynes J. M.; Pernicone N.; Ramsay J. D. F.; Sing K. S. W.; Unger K. K. Recommendations for the characterization of porous solids (Technical Report). *Pure Appl. Chem.* **1994**, 66, 1739-1758.

(3) Kitagawa, S.; Kitaura, R.; Noro, S. Functional Porous Coordination Polymers. *Angew. Chem.-Int. Edit.* **2004**, *43*, 2334-2375.

(4) Ferey, G. Hybrid Porous Solids: Past, Present, Future. *Chem. Soc. Rev.* **2008**, *37*, 191-214.

(5) Garibay, S. J.; Cohen, S. M. Isoreticular Synthesis and Modification of Frameworks with the UiO-66 Topology. *Chem. Commun.* **2010**, *46*, 7700-7702.

(6) Ferey, G.; Mellot-Draznieks, C.; Serre, C.; Millange, F. Crystallized Frameworks with Giant Pores: Are There Limits to the Possible? *Acc. Chem. Res.* **2005**, *38*, 217-225.

(7) Yang, R. T. Adsorbents. Fundamentals and Applications; *John Wiley & Sons, Inc:* Hoboken, New Jersey, **2003**.

(8) D'Alessandro, D. M.; Smit, B.; Long, J. R., Carbon dioxide capture: prospects for new materials. *Angewandte Chemie* **2010,** *49* (35), 6058-82.

(9) Choi, S.; Drese, J. H.; Jones, C. W., Adsorbent Materials for Carbon Dioxide Capture from Large Anthropogenic Point Sources. *ChemSusChem* **2009,** *2* (9), 796-854.

(10) Davini, P. Flue gas treatment by activated carbon obtained from oil-fired fly ash. *Carbon* **2002,** *40* (11), 1973-1979.

(11) Walton, K. S.; Abney, M. B.; LeVan, M. D., CO_2 adsorption in Y and X zeolites modified by alkali metal cation exchange. *Microporous Mesoporous Mater.* **2006**, 91, 78-84.

(12) Yilmaz, B.; Trukhan, N.; Muller, U., Industrial Outlook on Zeolites and Metal Organic Frameworks. *Chinese Journal of Catalysis* **2012,** *33* (1), 3-10.

(13) Park, K. S.; Ni, Z.; Côté, A. P.; Choi, J. Y.; Huang, R.; Uribe-Romo, F. J.; Chae, H. K.; O'Keeffe, M.; Yaghi, O. M., Exceptional chemical and thermal stability of zeolitic imidazolate frameworks. *Proceedings of the National Academy of Sciences* **2006,** *103* (27), 10186-10191.

(14) Database of Zeolite Structures. http://www.iza-structure.org/databases/.

(15) Cook, T. R.; Zheng, Y. R.; Stang, P. J., Metal-organic frameworks and self-assembled supramolecular coordination complexes: comparing and contrasting the design, synthesis, and functionality of metal-organic materials. *Chem Rev* **2013,** *113* (1), 734-77.

(16) Dietzel, P. D. C.; Blom R.; Fjellvag H. Base-induced formation of two magnesium metal-organic framework compounds with a bifunctional tetratopic ligand. European *Journal of Inorganic Chemistry* **2008**, 23, 3624-3632.

(17) Rosi N. L.; Kim J.; Eddaoudi M.; Chen B. L.; O'Keeffe M.; Yaghi O. M. Rod packings and metal-organic frameworks constructed from rod-shaped secondary building units. *Journal of the American Chemical Society* **2005**, 127(5), 1504-1518.

(18) Dietzel P. D. C.; Johnsen R. E.; Blom R.; Fjellvag H. Structural changes and coordinatively unsaturated metal atoms on dehydration of honeycomb analogous microporous metal-organic frameworks. *Chem.-Eur. J.* **2008**, 14(8), 2389-2397.

(19) Bonino F.; Chavan S.; Vitillo J. G. Local structure of CPO-27-Ni metallorganic framework upon dehydration and coordination of NO. *Chem. Mat.* **2008**, 20(15), 4957-4968.

(20) Eddaoudi, M.; Kim, J.; Rosi, N.; Vodak, D.; Wachter, J.; O'Keeffe, M.; Yaghi, O. M. Systematic Design of Pore Size and Functionality in Isoreticular MOFs and Their Application in Methane Storage. *Science* **2002**, *295*, 469-472.

(21) Tanabe, K. K.; Cohen, S. M., Postsynthetic modification of metal-organic frameworks--a progress report. *Chem Soc Rev* **2011,** *40* (2), 498-519.

(22) Cambridge Crystallographic Data Center. http://www.ccdc.cam.ac.uk/.

(23) Christopher, E. W.; Michael, L.; Chang Yeon, L.; Omar, K. F.; Brad, G. H.; Joseph, T. H.; Randall, Q. S., Large-scale screening of hypothetical metal–organic frameworks. *Nature Chemistry* **2011,** *4* (2), 83-89.

(24) Burtch, N. C.; Jasuja, H.; Walton, K. S. Water Stability and Adsorption in Metal-Organic Frameworks. *Chem Rev* **2014,** *Submitted*.

(25) Schoenecker, P. M.: High-throughput synthesis and application development of water-stable MOFs, Ph.D. Thesis, Georgia Institute of Technology, Atlanta, GA, 2012.

(26) Gimeno-Fabra, M.; Munn, A. S.; Stevens, L. A.; Drage, T. C.; Grant, D. M.; Kashtiban, R. J.; Sloan, J.; Lester, E.; Walton, R. I. Instant MOFs: continuous synthesis of metal-organic frameworks by rapid solvent mixing. *Chemical Communications* **2012,** *48* (86), 10642-10644.

(27) Arnau, C.-S.; Inhar, I.; Mary, C.-S.; Daniel, M. A spray-drying strategy for synthesis of nanoscale metal–organic frameworks and their assembly into hollow superstructures. *Nature Chemistry* **2013,** *5* (3), 203-211.

(28) Czaja, A. U.; Trukhan, N.; Muller, U. Industrial applications of metal-organic frameworks. *Chemical Society Reviews* **2009,** *38* (5), 1284-1293.

(29) Parr Acid Digestion. http://www.parrinst.com/products/sample-preparation/acid-digestion/.

(30) Banerjee R.; Phan A.; Wang B. High-throughput synthesis of zeolitic imidazolate frameworks and application to CO_2 capture. *Science* **2008**, 319(5865), 939-943.

(31) Reinsch, H.; Stock, N., High-throughput studies of highly porous Al-based MOFs. *Microporous and Mesoporous Materials* **2013,** *171* (0), 156-165.

(32) Ni, Z.; Masel, R. I. *United States Patent Application Publication* **2009**, *11/785,102*.

(33) Mueller, U.; Puetter, H.; Hesse, M.; Wessel, H. WO 2005/049892.

(34) Leung E, Müller U, Cox G. WO 2010/106121 A1. 2010.

(35) Leung E, Müller U, Cox G, Mattenheimer H, Blei S. EP Patentanmeldung 10183283.0, 2010.

(36) Meek, S. T.; Greathouse, J. A.; Allendorf, M. D., Metal-organic frameworks: a rapidly growing class of versatile nanoporous materials. *Advanced materials* **2011**, *23* (2), 141.

(37) Khan, N. A.; Jhung, S. H., Facile syntheses of metal–organic framework Cu3 (BTC)2(H2O)3 under ultrasound. *Korean Chem Soc* **2009**, 30, 2921-26.

(38) Stock, N.; Biswas, S., Synthesis of Metal-Organic Frameworks (MOFs): Routes to Various MOF Topologies, Morphologies, and Composites. *Chemical Reviews* **2011,** *112* (2), 933-969.

(39) An, J.; Geib, S. J.; Rosi, N. L., Cation-Triggered Drug Release from a Porous Zinc-Adeninate Metal-Organic Framework. *Journal of the American Chemical Society* 2009, 131, 8376.

(40) Horcajada, P.; Serre, C.; Maurin, G.; Ramsahye, N. A.; Balas, F.; Vallet-Regi, M.; Sebban, M.; Taulelle, F.; Ferey, G., Flexible porous metal-organic frameworks for a controlled drug delivery. *Journal of the American Chemical Society* 2008, 130, 6774-6780.

(41) Horcajada, P.; Chalati, T.; Serre, C.; Gillet, B.; Sebrie, C.; Baati, T.; Eubank, J. F.; Heurtaux, D.; Clayette, P.; Kreuz, C.; Chang, J.-S.; Hwang, Y. K.; Marsaud, V.; Bories, P.-N.; Cynober, L.; Gil, S.; Ferey, G.; Couvreur, P.; Gref, R., Porous metal-organic-framework nanoscale carriers as a potential platform for drug delivery and imaging. *Nature Materials* 2010, 9, 172-178.

(42) Taylor-Pashow, K. M. L.; Della Rocca, J.; Xie, Z.; Tran, S.; Lin, W., Postsynthetic Modifications of Iron-Carboxylate Nanoscale Metal-Organic Frameworks for Imaging and Drug Delivery. *Journal of the American Chemical Society* 2009, 131, 14261.

(43) Janiak, C., Engineering coordination polymers towards applications. *Dalton Transactions* 2003, 2781-2804.

(44) Lee, J.; Farha, O. K.; Roberts, J.; Scheidt, K. A.; Nguyen, S. T.; Hupp, J. T., Metal-organic framework materials as catalysts. *Chemical Society Reviews* 2009, 38, 1450-1459.

(45) Morris, R. E.; Bu, X., Induction of chiral porous solids containing only achiral building blocks. *Nature Chemistry* 2010, 2, 353-361.

(46) Allendorf, M. D.; Bauer, C. A.; Bhakta, R. K.; Houk, R. J. T., Luminescent metal-organic frameworks. *Chemical Society Reviews* 2009, 38, 1330-1352.

(47) Thomas, K. M., Adsorption and desorption of hydrogen on metal-organic framework materials for storage applications: comparison with other nanoporous materials. *Dalton Transactions* 2009.

(48) Achmann, S.; Hagen, G.; Kita, J.; Malkowsky, I. M.; Kiener, C.; Moos, R., Metal-Organic Frameworks for Sensing Applications in the Gas Phase. *Sensors* 2009, 9, 1574-1589.

(49) Khoshaman, A. H.; Bahreyni, B., Application of metal organic framework crystals for sensing of volatile organic gases. *Sensors and Actuators B-Chemical* 2012, 162, 114-119.

(50) Zou, R.; Abdel-Fattah, A. I.; Xu, H.; Zhao, Y.; Hickmott, D. D., Storage and separation applications of nanoporous metal-organic frameworks. *Crystengcomm* 2010, 12.

(51) Ma, S.; Meng, L., Energy-related applications of functional porous metal-organic frameworks. *Pure and Applied Chemistry* 2011, 83.

(52) Mueller, U.; Schubert, M.; Teich, F.; Puetter, H.; Schierle-Arndt, K.; Pastre, J., Metal-organic frameworks - prospective industrial applications. *Journal of Materials Chemistry* 2006, 16, 626-636.

(53) Kuppler, R. J.; Timmons, D. J.; Fang, Q.-R.; Li, J.-R.; Makal, T. A.; Young, M. D.; Yuan, D.; Zhao, D.; Zhuang, W.; Zhou, H.-C., Potential applications of metal-organic frameworks. *Coordination Chemistry Reviews* 2009, 253.

(54) Yang, H.; Xu, Z.; Fan, M.; Gupta, R.; Slimane, R. B.; Bland, A. E.; Wright, I., Progress in carbon dioxide separation and capture: A review. *Journal of Environmental Sciences-China* 2008, 20, 14-27.

(55) Keskin, S.; Van Heest, T. M.; Sholl, D. S. Can Metal-Organic Framework Materials Play a Useful Role in Large-Scale Carbon Dioxide Separations? *ChemSusChem* **2010**, *3*, 879-891.

(56) Keskin, S.; Kizilel, S. Biomedical Applications of Metal Organic Frameworks. *Ind. Eng. Chem. Res.* **2011**, *50*, 1799-1812.

(57) Sumida, K.; Rogow, D. L.; Mason, J. A.; McDonald, T. M.; Bloch, E. D.; Herm, Z. R.; Bae, T. H.; Long, J. R., Carbon dioxide capture in metal-organic frameworks. Chem Rev **2012**, *112 (2)*, 724-81.

(58) DeCoste, J. B.; Peterson, G. W. Metal-Organic Frameworks for Air Purification of Toxic Chemicals. Chem. Rev. **2014**, (DOI: 10.1021/cr4006473).

(59) Karwacki, C. J., Jones P. Toxic Industrial Chemicals Assessment of NBC Filter Performance, Edgewood Chemical Biological Center, 2000.

(60)http://www.calgoncarbon.com/media/images/site_library/46_RespiratorsHP_10223w.pdf , last accessed on 02/12/2014.

(61) http://minerals.usgs.gov/minerals/pubs/commodity/nitrogen/nitromcs05.pdf. last accessed on 02/12/2014.

(62) (a) Britt, D.; Tranchemontagne, D.; Yaghi, O. M., Metal-organic frameworks with high capacity and selectivity for harmful gases. *Proc. Natl. Acad. Sci. U.S.A.* **2008,** *105* (33), 11623-11627; (b) Glover, T. G.; Peterson, G. W.; Schindler, B. J.; Britt, D.; Yaghi, O., MOF-74 building unit has a direct impact on toxic gas adsorption. *Chem. Eng. Sc.* **2011,** *66* (2), 163-170.

(63) Peterson, G. W.; Wagner, G. W.; Balboa, A.; Mahle, J.; Sewell, T.; Karwacki, C. J., Ammonia Vapor Removal by Cu3(BTC)2 and Its Characterization by MAS NMR. *J. Phys. Chem. C* **2009,** *113* (31), 13906-13917.

(64) DeCoste, J. B.; Peterson, G. W.; Schindler, B. J.; Killops, K. L.; Browe, M. A.; Mahle, J. J., The effect of water adsorption on the structure of the carboxylate containing metal-organic frameworks Cu-BTC, Mg-MOF-74, and UiO-66. *J. Mater. Chem. A* **2013,** *1* (38), 11922-11932.

(65) Greathouse, J. A.; Allendorf, M. D., The interaction of water with MOF-5 simulated by molecular dynamics. *J Am Chem Soc* **2006,** *128* (33), 10678-9.

(66) Li, Y.; Yang, R. T., Gas adsorption and storage in metal-organic framework MOF-177. *Langmuir* **2007,** *23* (26), 12937-44.

(67) Low, J. J.; Benin, A. I.; Jakubczak, P.; Abrahamian, J. F.; Faheem, S. A.; Willis, R. R., Virtual high throughput screening confirmed experimentally: porous coordination polymer hydration. *J Am Chem Soc* **2009,** *131* (43), 15834-42.

(68) Schoenecker, P. M.; Carson, C. G.; Jasuja, H.; Flemming, C. J. J.; Walton, K. S., Effect of Water Adsorption on Retention of Structure and Surface Area of Metal–Organic Frameworks. *Industrial & Engineering Chemistry Research* **2012,** *51* (18), 6513-6519.

(69) Kusgens, P.; Rose, M.; Senkovska, I.; Frode, H.; Henschel, A.; Siegle, S.; Kaskel, S., Characterization of metal-organic frameworks by water adsorption. *Microporous and Mesoporous Materials* **2009,** *120* (3), 325-330.

(70) Cychosz, K. A.; Matzger, A. J., Water stability of microporous coordination polymers and the adsorption of pharmaceuticals from water. *Langmuir* **2010,** *26* (22), 17198-202.

(71) Choi, H. J.; Dinca, M.; Dailly, A.; Long, J. R., Hydrogen storage in water-stable metal-organic frameworks incorporating 1,3-and 1,4-benzenedipyrazolate. *Energy & Environmental Science* **2010,** *3* (1), 117-123.

(72) Cavka, J. H.; Jakobsen, S.; Olsbye, U.; Guillou, N.; Lamberti, C.; Bordiga, S.; Lillerud, K. P., A new zirconium inorganic building brick forming metal organic frameworks with exceptional stability. *J Am Chem Soc* **2008,** *130* (42), 13850-1.

(73) Dietzel, P. D.; Morita, Y.; Blom, R.; Fjellvag, H., An in situ high-temperature single-crystal investigation of a dehydrated metal-organic framework compound and field-induced magnetization of one-dimensional metal-oxygen chains. *Angewandte Chemie* **2005,** *44* (39), 6354-8.

(74) Ma, D.; Li, Y.; Li, Z., Tuning the moisture stability of metal-organic frameworks by incorporating hydrophobic functional groups at different positions of ligands. *Chem Commun (Camb)* **2011,** *47* (26), 7377-9.

(75) Yang, J.; Grzech, A.; Mulder, F. M.; Dingemans, T. J., Methyl modified MOF-5: a water stable hydrogen storage material. *Chem Commun (Camb)* **2011,** *47* (18), 5244-6.

(76) Nguyen, J. G.; Cohen, S. M., Moisture-resistant and superhydrophobic metal-organic frameworks obtained via postsynthetic modification. *J Am Chem Soc* **2010,** *132* (13), 4560-1.

(77) Serre, C., Superhydrophobicity in highly fluorinated porous metal-organic frameworks. *Angewandte Chemie* **2012,** *51* (25), 6048-50.

(78) Liang, Z. J.; Marshall, M.; Chaffee, A. L., CO_2 adsorption, selectivity and water tolerance of pillared-layer metal organic frameworks. *Microporous and Mesoporous Materials* **2010,** *132* (3), 305-310.

(79) Kondo, A.; Daimaru, T.; Noguchi, H.; Ohba, T.; Kaneko, K.; Kanoh, H., Adsorption of water on three-dimensional pillared-layer metal organic frameworks. *J Colloid Interface Sci* **2007,** *314* (2), 422-6.

(80) Decoste, J. B.; Peterson, G. W.; Smith, M. W.; Stone, C. A.; Willis, C. R., Enhanced Stability of Cu-BTC MOF via Perfluorohexane Plasma-Enhanced Chemical Vapor Deposition. *Journal of the American Chemical Society* **2012,** *134* (3), 1486-1489.

(81) Wu, T.; Shen, L.; Luebbers, M.; Hu, C.; Chen, Q.; Ni, Z.; Masel, R. I., Enhancing the stability of metal-organic frameworks in humid air by incorporating water repellent functional groups. *Chem Commun (Camb)* **2010,** *46* (33), 6120-2.

(82) Cai, Y.; Zhang, Y. D.; Huang, Y. G.; Marder, S. R.; Walton, K. S., Impact of Alkyl-Functionalized BTC on Properties of Copper-Based Metal-Organic Frameworks. *Crystal Growth & Design* **2012,** *12* (7), 3709-3713.

(83) Taylor, J. M.; Vaidhyanathan, R.; Iremonger, S. S.; Shimizu, G. K., Enhancing water stability of metal-organic frameworks via phosphonate monoester linkers. *J Am Chem Soc* **2012,** *134* (35), 14338-40.

(84) Yang, C.; Kaipa, U.; Mather, Q. Z.; Wang, X.; Nesterov, V.; Venero, A. F.; Omary, M. A., Fluorous metal-organic frameworks with superior adsorption and hydrophobic properties toward oil spill cleanup and hydrocarbon storage. *J Am Chem Soc* **2011,** *133* (45), 18094-7.

(85) Li, T.; Chen, D.-L.; Sullivan, J. E.; Kozlowski, M. T.; Johnson, J. K.; Rosi, N. L., Systematic modulation and enhancement of CO_2 : N2 selectivity and water stability in an isoreticular series of bio-MOF-11 analogues. *Chemical Science* **2013,** *4* (4), 1746-1755.

(86) Makal, T. A.; Wang, X.; Zhou, H.-C., Tuning the Moisture and Thermal Stability of Metal–Organic Frameworks through Incorporation of Pendant Hydrophobic Groups. *Crystal Growth & Design* **2013,** *13* (11), 4760-4768.

(87) Liu, H.; Zhao, Y.; Zhang, Z.; Nijem, N.; Chabal, Y. J.; Peng, X.; Zeng, H.; Li, J., Ligand Functionalization and Its Effect on CO_2 Adsorption in Microporous Metal–Organic Frameworks. *Chemistry – An Asian Journal* **2013,** *8* (4), 778-785.

(88) Chen, T.-H.; Popov, I.; Zenasni, O.; Daugulis, O.; Miljanic, O. S., Superhydrophobic perfluorinated metal-organic frameworks. *Chem. Commun.* **2013,** *49* (61), 6846-6848.

(89) Min Wang, Q.; Shen, D.; Bülow, M.; Ling Lau, M.; Deng, S.; Fitch, F. R.; Lemcoff, N. O.; Semanscin, J., Metallo-organic molecular sieve for gas separation and purification. *Microporous and Mesoporous Materials* **2002,** *55* (2), 217-230.

(90) Seo, Y.-K.; Yoon, J. W.; Lee, J. S.; Lee, U. H.; Hwang, Y. K.; Jun, C.-H.; Horcajada, P.; Serre, C.; Chang, J.-S., Large scale fluorine-free synthesis of hierarchically porous iron(III) trimesate MIL-100(Fe) with a zeolite MTN topology. *Microporous and Mesoporous Materials* **2012,** *157* (0), 137-145.

(91) Majano, G.; Pérez-Ramírez, J., Scalable Room-Temperature Conversion of Copper(II) Hydroxide into HKUST-1 (Cu3(btc)2). *Advanced Materials* **2013,** *25* (7), 1052-1057.

(92) Huo, J.; Brightwell, M.; El Hankari, S.; Garai, A.; Bradshaw, D., A versatile, industrially relevant, aqueous room temperature synthesis of HKUST-1 with high space-time yield. *Journal of Materials Chemistry A* **2013,** *1* (48), 15220-15223.

(93) Gaab, M.; Trukhan, N.; Maurer, S.; Gummaraju, R.; Müller, U., The progression of Al-based metal-organic frameworks – From academic research to industrial production and applications. *Microporous and Mesoporous Materials* **2012,** *157* (0), 131-136.

(94) http://www.sigmaaldrich.com/catalog/product/aldrich/688614?lang=en&region=US, LA on 24th Feb. 2014.

(95) Cychosz K. A., Ahmad R., Matzger A. J. Liquid phase separations by crystalline microporous coordination polymers. Chem. Sci. Sep **2010**;1(3):293-302.

(96) Jeremias, F.; Khutia, A.; Henninger, S. K.; Janiak, C., MIL-100(Al, Fe) as water adsorbents for heat transformation purposes-a promising application. *J. Mater. Chem.* **2012,** *22* (20), 10148-10151.

(97) Hartmann, M.; Fischer, M., Amino-functionalized basic catalysts with MIL-101 structure. *Microporous and Mesoporous Mater.* **2012,** *164* (0), 38-43.

CHAPTER 2

MATERIALS AND EXPERIMENTAL METHODS

2.1 Materials

Throughout my PhD research, all the MOFs were synthesized using the solvothermal method based on published procedures or with some slight modifications. MOFs used in my PhD research can be classified into following two categories according to their topology.

2.1.1 Pillared MOF Topology

Pillared MOFs are synthesized by mixing two types of organic ligands, usually aromatic dicarboxylates (e.g., BDC, Figure 2.1) or tetracarboxylates (e.g., BTTB, Figure 2.1) and diamines (e.g., BPY, DABCO, Figure 2.1) with the metal salt. Metal ions and carboxylate ligands form the 2-D sheets while diamines act as pillars connecting the sheets in the third dimension.[1] MOFs synthesized in this fashion have produced several examples of non-catenated (e.g., Zn-BDC-DABCO or DMOF[2], Zn-TMBDC-BPY[3]) as well as catenated structures (e.g., Zn-BDC-BPY or MOF-508[4], Zn-BTTB-BPY[6]). Catenation is the interpenetration or interweaving of two or more identical and independent frameworks.[5] Figure 2.2 shows a cartoon representation of non-catenated pillared MOFs (e.g., Zn-BDC-DABCO[2], Zn-TMBDC-BPY[3]) and two-fold catenation in pillared layer frameworks (e.g., MOF-508[4], Zn-BTTB-BPY[6]). In my PhD work, I have synthesized various catenated and non-catenated pillared MOFs.

DMOF-**X**/Zn-BDC-**X**-DABCO: A zinc-based non-catenated pillared MOF consisting of paddlewheel Zn clusters (Figure 2.3-Left) connected by benzenedicarboxylate linkers (BDC-**X**) to form 2-dimensional layers, which are connected to each other via pillar linker DABCO (1,4-diazabicyclo[2.2.2]octane) and this give rise to a 3-dimensional structure. In total, 14 different isostructural MOFs (4 are new MOFs) belonging to this family were synthesized by placing various functional groups (**X**) on the benzene dicarboxylate (BDC) linker. The structure of DMOF is shown in Figure 2.3- right. Refer to Chapters 3 and 4 for details.

MOF-508-**X**/Zn-BDC-**X**-BPY: A zinc-based pillared MOF with same topology as DMOF but now pillar linker is BPY (4,4'-bipyridyl). MOF-508[4] (*2-fold catenated*) & MOF-508-TM[3] were synthesized with BDC and TMBDC (tetramethyl BDC) linkers respectively. Refer to Chapters 5 for details.

Co-TMBDC-DABCO, Ni-TMBDC-DABCO, and Cu-TMBDC-DABCO: Non-catenated pillared new MOFs with same topology as DMOF-TM[3] or Zn-TMBDC-DABCO[3] but with varying metal clusters. Refer to Chapter 6 for details.

Zn-BTTB-DMBPY and Co-BTTB-DMBPY: *2-fold catenated* new pillared MOFs with same topology as MOF-508[4] or Zn-BTTB-BPY[6] but now BTTB (4,4',4'',4'''-benzene-1,2,4,5-tetrayltetrabenzoic acid) instead of BDC form the 2-dimensional layers with metal clusters, which are connected to each other via pillar linker DMBPY (2,2'-dimethyl-4,4'-bipyridyl) instead of BPY. The structure of M-BTTB-DMBPY (where M = Co and Zn) is shown in Figure 2.4. Refer to Chapters 6 for details.

2.1.2 UiO-66 MOF Topology

Cavka et al. was the first to synthesize a zirconium (IV)-based MOF (UiO-66) with exceptional thermal, chemical, and mechanical stability.[7] This stability has been attributed to the highly oxophilic nature of zirconium (IV), leading to the formation of a highly stable inorganic brick [$Zr_6O_4(OH)_4$]. These Zr_6-octahedra are bound to twelve 1,4-benzenedicarboxylic acid (BDC) ligands (each Zr atom is 8-coordinated) leading to a 3D arrangement of micro pores (6 Å). The structure of UiO-66 is shown in Figure 2.5. In total, 10 different isostructural MOFs (2 are new MOFs) belonging to UiO-66 family were synthesized by placing various functional groups (**X**) on the benzene dicarboxylate (BDC) linker. Refer to Chapters 7, 8 and Appendix F for details.

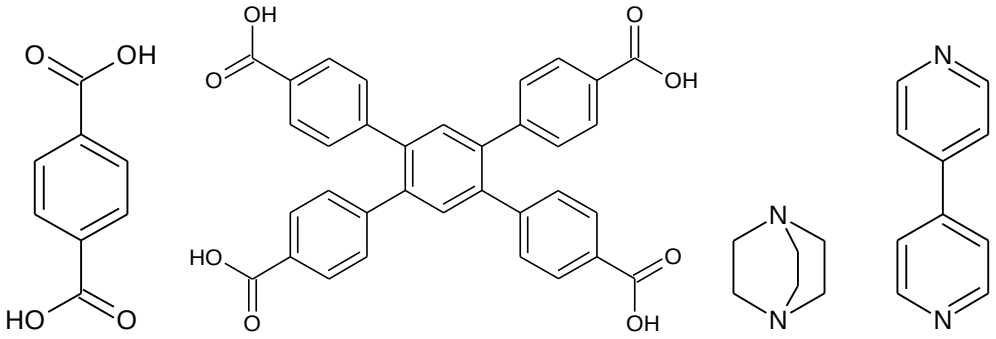

BDC **BTTB** **DABCO** **BPY**

Figure 2.1 Structures of dicarboxylate or tetracarboxylate ligands (BDC, BTTB) and diamine pillar ligands (DABCO, BPY).

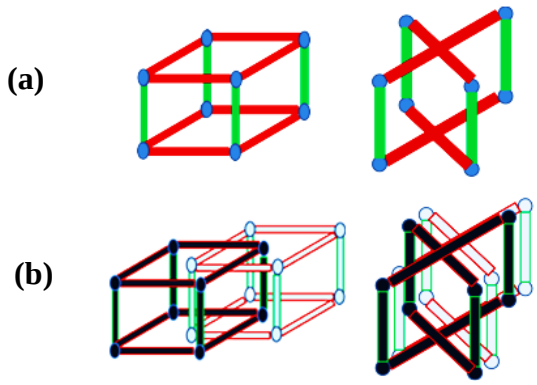

Figure 2.2 Illustration of pillared layer frameworks synthesized from dicarboxylate ligand (a, left) and tetracarboxylate ligand (a, right) and pillar ligand. In (a) red and green lines depict carboxylate ligand and pillar ligand respectively and the blue corners are the metal nodes. b) two-fold catenation in pillared layer frameworks synthesized from dicarboxylate ligand (b, left) and tetracarboxylate ligand (b, right). Black and white represents different frameworks.

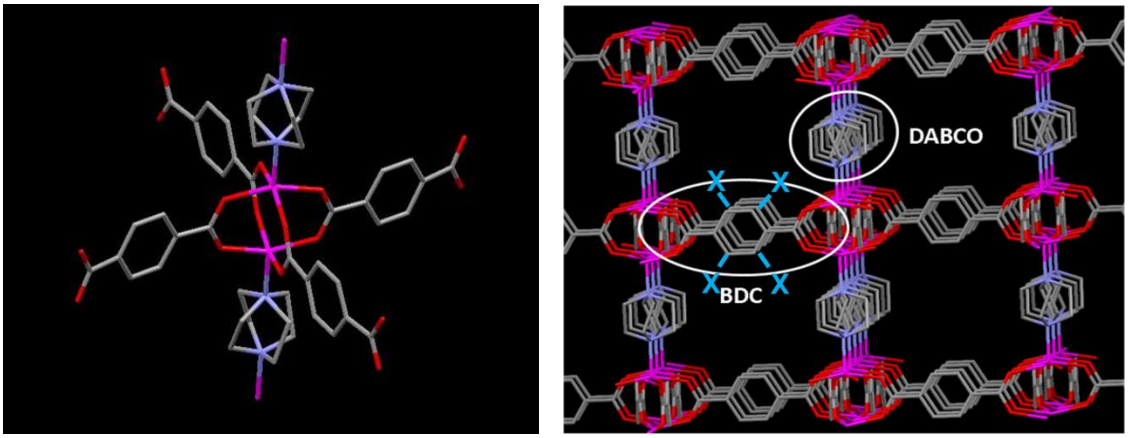

Figure 2.3 Left: Coordination environment around the metal (M) in the paddle wheel secondary building unit (SBU) of [M(BDC)(DABCO)$_{0.5}$], where M = Zn, Cu, Co, and Ni. Right: Illustration of [M(BDC)(DABCO)$_{0.5}$] structure (C- grey, M- pink, O- red, N- purple, and H- omitted for clarity). BDC ligand was functionalized with various groups (X) to synthesize the DMOF-X family.

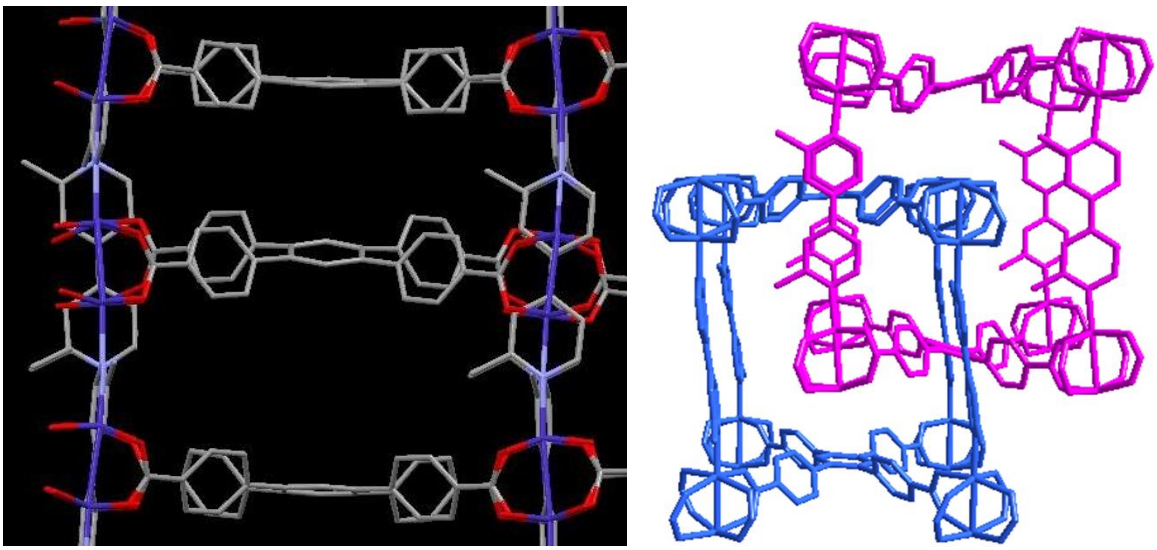

Figure 2.4 Left: Structure of pillared MOFs M-BTTB-DMBPY (where M = Co and Zn). (C- grey, M- blue, O- red, N- purple, and H- omitted for clarity). Right: 2-fold catenation in M-BTTB-DMBPY (where M = Co and Zn). Pink and blue represents different frameworks.

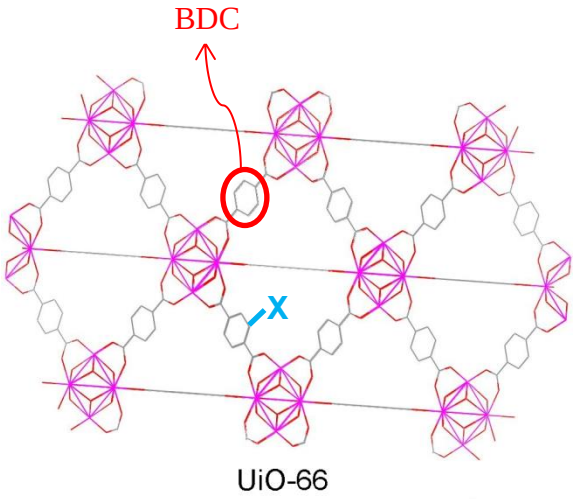

Figure 2.5 Illustration of UiO-66 framework structure (C- grey, Zr- pink, O- red, and H- omitted for clarity). BDC ligand was functionalized with various groups (X) to synthesize the UiO-66-X family.

2.2 Material Characterization Techniques

After the synthesis of porous materials, the next step is to characterize them using various techniques so that we can confirm their successful synthesis or identify any defects or impurities present in their structure. MOFs are fascinating crystalline materials; hence, X-Ray diffraction (XRD) is extensively used for their characterization. XRD is a non-destructive analytical technique based on the constructive interference (Bragg's law) of diffracted X-rays.[8]

2.2.1 Single Crystal X-Ray Diffraction (XRD)

Crystal structures of new MOFs are usually analyzed using single-crystal X-Ray diffraction since it provides detailed structural information, i.e., definitive data on the location of the atoms and the connectivity of the atoms in the structure (unit cell dimensions, bond-lengths, and bond-angles). However, single crystal XRD often requires high quality single crystals to obtain a structural solution without any disorder(s). Single crystal X-Ray data for this work were collected at the Emory Chemistry Department facility on a Bruker APEX II CCD sealed tube diffractometer by using Mo-*K*α (λ = 0.71073 Å) radiation with a graphite monochromator. Crystals of the MOFs were mounted on nylon CryoLoops with Paratone-N. To solve the structures, direct methods and further refinement by full-matrix least-squared techniques were used in the SHELXTL-97 software suite.

2.2.2 Powder X-Ray Diffraction (PXRD)

In principle (Bragg's law), PXRD is same as single crystal XRD with only difference that now diffraction pattern is obtained from a powder sample, rather than from a high quality single crystal. This makes PXRD a simple and convenient

experimental technique to implement than single crystal XRD and hence, now phase purity of the bulk sample can be determined easily. PXRD patterns of as-synthesized and activated or water exposed samples of MOFs can be compared to determine the changes occurred during activation or water exposure. However, PXRD provides only information about the long-range crystallinity of the structure and it is not capable of detecting surface collapse (defects) or early stages of collapse. PXRD patterns for this work were obtained using a X'Pert X-Ray PANalytical diffractometer[9] with a X'celerator module using Cu Kα (λ = 1.5418 Å) radiation at room temperature, with a step size of 0.02˚ in two theta (2θ).

2.2.3 Fourier Transform Infrared (FTIR) Spectroscopy

Vibrational spectroscopy techniques such as Fourier-transform infrared (FTIR), and Raman could be used to provide key information on the framework structure, framework dynamics, host–guest interactions with adsorbed species such as water and CO_2, and identify possible changes in chemical species or groups present in the framework upon adsorption. FTIR spectrum in my PhD work was recorded with a PerkinElmer Spectrum One[10] in the range 400 – 4000 cm^{-1}. To record the IR spectrum, an IR beam is passed through the sample (in pelletized form) and sample absorbs IR light with frequency same as the vibrational frequency of a bond. Hence, we can examine the transmitted light to quantify how much energy was absorbed at each frequency corresponding to various bonds present in the structure.

2.2.4 Thermal Gravimetric Analysis (TGA)

Thermogravimetric analyses (TGA) in this work were carried out under helium in the temperature range of 30-800 ˚C on a NETZSCH STA 449 F1 Jupiter® device[11] with

a heating rate of 5 ˚C /min, flow rate of 20 mL/min, and approximately 10 mg of sample size was used. The main goal here was to obtain information about dehydration (removal of physisorbed water), desolvation (removal of synthesis solvents), and decomposition of various MOFs.

2.2.5 Nuclear Magnetic Resonance (NMR) Spectroscopy

NMR probes short-range ordering and local structure around the target nucleus and hence, it can be considered complementary to XRD.[12] NMR spectra were collected at the Georgia Tech NMR center facility. Small amounts of the activated MOF samples were digested with NaOH in D_2O and subsequently subjected to ^{1}H liquid state NMR measurements using Varian Mercury Vx300. A Bruker DSX300 solid-state NMR spectrometer was used to record the ^{13}C CP-MAS NMR spectrum. A Bruker AV3-400 spectrometer was used in conjunction with magic-angle spinning (MAS) and proton decoupling to measure variable contact-time solid state NMR data.

2.3 Adsorption Isotherm Measurements

After the preliminary confirmation of successful synthesis through techniques such as XRD, FTIR, TGA, and NMR another important step is to evaluate the performance of porous materials as adsorbents for various gas separation/storage applications. In order to remove guest solvent molecules from the pores of MOFs and access the porosity, they are carefully heated under vacuum. This process is known as activation, which is necessary for most applications.[5] The ideal adsorbent should possess characteristics such as high porosity, reversible adsorption, and structural stability. Hence, we have carried out N_2 adsorption at -196 ^{o}C, room temperature CO_2/CH_4 adsorption, and water adsorption studies.

2.3.1 Nitrogen Adsorption Isotherm Measurements

Nitrogen adsorption measurements at -196 ^{o}C were performed on activated MOF samples using a Quadrasorb system from Quantachrome Instruments.[13] A sample size of approximately 20-30 mg was used to collect these isotherms. Specific surface areas and micropore volumes were calculated by fitting the Brunauer, Emmett, and Teller (BET) model[14] and Dubinin-Astakov (DA) model[14] respectively, to the nitrogen adsorption isotherms. BET theory was applied over the pressure range $P/P_o < 0.05$ to ensure that consistent, physically meaningful parameters were obtained.[15]

2.3.2 Single Component Gas Adsorption Isotherm Measurements

An Intelligent Gravimetric Analyzer (IGA-1 series, Hiden Isochema[16]) was used to collect pure gas (CO_2 and CH_4) adsorption isotherms at room temperature and pressures up to 20 bar. Samples were activated *in situ* under vacuum at MOF specific activation temperature until no further weight loss was observed. After activation, the system was maintained under vacuum, and the temperature was adjusted to the room temperature. A sample size of approximately 30 mg was used for the measurements, and a maximum equilibration time of 30 minutes was used for each point in the isotherm.

2.3.3 Water Vapor Adsorption Isotherm Measurements

Water vapor isotherm measurements were carried out at 25 ^{o}C and 1 bar using a gravimetric adsorption apparatus, i.e., IGA-3 series device from Hiden Isochema.[17] Prior to the run, approximately 25-45 mg sample sizes were loaded into the IGA-3 device followed by *in situ* activation until no further weight loss was observed. To mimic real humid environment conditions, dry air was chosen as the carrier gas. A portion of the carrier gas was bubbled through a canister filled with deionized water. Two mass flow

controllers were used to vary the ratio of saturated air to dry air so that desired relative humidity (RH) can be achieved. Water adsorption experiments were conducted up to 90 % RH with total gas flow rate of 200 cm^3/min and typical equilibrium times ranging from 15 min to 24 h for each point in the adsorption isotherm. Water exposed samples were reactivated to calculate the loss in BET surface area.

2.4 Adsorber Dynamics: Bed Profiles and Breakthrough Curves

For a given separation, choosing a proper adsorbent is a difficult task. The main factors that are important for the design of the separation process are: (1) capacity of the adsorbent in the operating conditions, and (2) the length of the unused bed (LUB).[18] In order to calculate adsorbent capacity and LUB, breakthrough curves should be obtained. The breakthrough curve is a plot of the concentration measured usually at or near to the outlet of an adsorption column, versus time. Breakthrough curves can be simulated by solving the mass and heat balance equations for both the bed and adsorbent particles, along with the adsorption equilibrium isotherms. In order to design adsorbers, the shape or the width of the breakthrough curve is extremely significant because the steepness of the breakthrough curve determines the extent to which the capacity of an adsorbent bed can be utilized, i.e., steep curve implies low value of LUB.[19] Thus, the shape of the curve is important in determining the length of the adsorption bed. In actual practice, the steepness of the breakthrough curves can increase or decrease, depending on the type of adsorption isotherm involved. For the favorable isotherm of the Langmuir or Freundlich type, the high concentration regions move faster than the low concentration regions, and the wave front steepens with time (self-sharpening wave-front[20], Figure 2.6a). Thus, now the breakthrough curve becomes steeper than the regular S-shape (Figure 2.6b) curve. In

this study, we will focus on enhancing the interaction of ammonia with MOF by integrating functional groups such as –OH and –COOH into the framework so that capacity of an adsorbent bed can be utilized effectively. MOF samples were shipped to our collaborators' facility in Maryland for ammonia breakthrough measurements under dry and wet (80% RH) conditions using a micro-breakthrough system, which has been detailed elsewhere.[21]

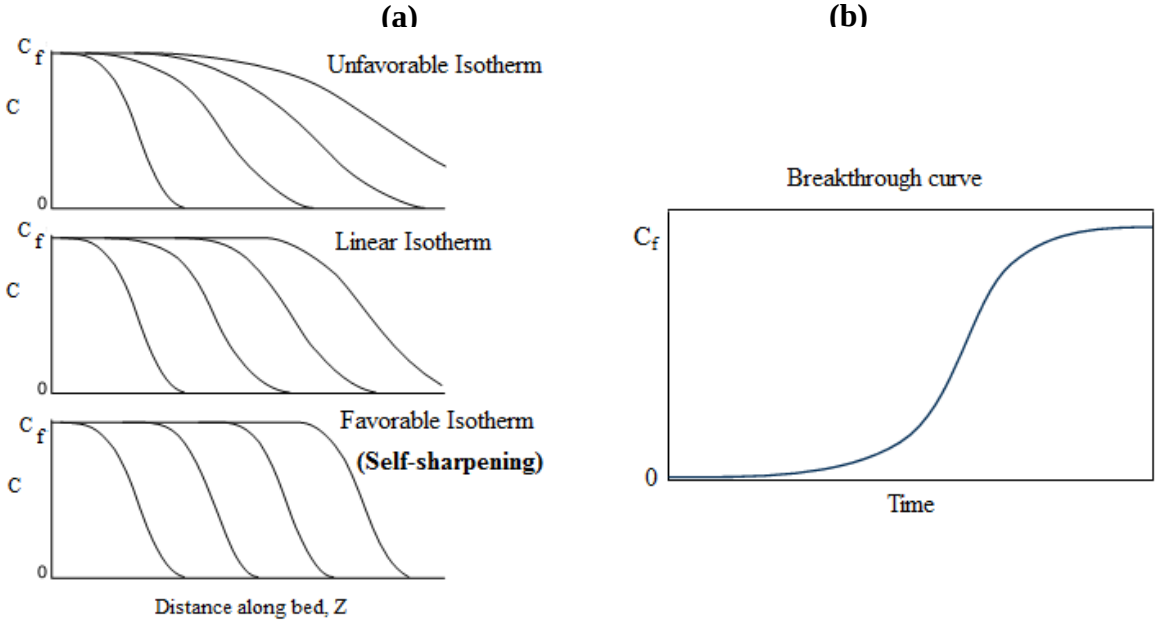

Figure 2.6 (a) Self-sharpening wavefront caused by favorable isotherm. (b) Regular S-shaped breakthrough curve. This figure has been adapted from literature.[20]

2.5 References

(1) Liang, Z. J.; Marshall, M.; Chaffee, A. L., CO_2 adsorption, selectivity and water tolerance of pillared-layer metal organic frameworks. *Microporous and Mesoporous Materials* **2010,** *132* (3), 305-310.

(2) Dybtsev, D. N.; Chun, H.; Kim, K., Rigid and flexible: a highly porous metal-organic framework with unusual guest-dependent dynamic behavior. *Angewandte Chemie* **2004,** *43* (38), 5033-6.

(3) Chun, H.; Dybtsev, D. N.; Kim, H.; Kim, K., Synthesis, X-ray crystal structures, and gas sorption properties of pillared square grid nets based on paddle-wheel motifs: implications for hydrogen storage in porous materials. *Chemistry* **2005,** *11* (12), 3521-9.

(4) Chen, B.; Liang, C.; Yang, J.; Contreras, D. S.; Clancy, Y. L.; Lobkovsky, E. B.; Yaghi, O. M.; Dai, S., A microporous metal-organic framework for gas-chromatographic separation of alkanes. *Angewandte Chemie* **2006,** *45* (9), 1390-3.

(5) Farha, O. K.; Hupp, J. T., Rational design, synthesis, purification, and activation of metal-organic framework materials. *Acc Chem Res* **2010,** *43* (8), 1166-75.

(6) Karra, R. J.: Development of porous metal-organic frameworks for gas adsorption applications, Ph.D. Thesis, Georgia Institute of Technology, Atlanta, GA, 2011.

(7) Cavka, J. H.; Jakobsen, S.; Olsbye, U.; Guillou, N.; Lamberti, C.; Bordiga, S.; Lillerud, K. P., A new zirconium inorganic building brick forming metal organic frameworks with exceptional stability. *J Am Chem Soc* **2008,** *130* (42), 13850-1.

(8) http://serc.carleton.edu/research_education/geochemsheets/techniques/SXD.html, last accessed on 02/14/2014.

(9) http://www.panalytical.com/XPert3-Powder.htm, last accessed on 02/14/2014.

(10) http://www.perkinelmer.com/catalog/category/id/ftir%20ftnir%20spectrometers, last accessed on 02/14/2014.

(11) http://www.netzsch-thermal-analysis.com/us/products-solutions/simultaneous-thermogravimetry-differential-scanning-calorimetry/sta-449-f1-jupiter.html, last accessed on 02/14/2014.

(12) Sutrisno, A.; Huang, Y., Solid-state NMR: A powerful tool for characterization of metal–organic frameworks. *Solid State Nuclear Magnetic Resonance* **2013,** *49–50* (0), 1-11.

(13) http://www.quantachrome.com/product_listing/surface_area_analyzers.html, last accessed on 02/14/2014.

(14) Duong, D. D. In Adsorption Analysis: Equilibria and Kinetics; Imperial College Press: London, UK, 1998.

(15) Walton, K. S.; Snurr, R. Q., Applicability of the BET method for determining surface areas of microporous metal-organic frameworks. *J Am Chem Soc* **2007,** *129* (27), 8552-6.

(16) http://www.hidenisochema.com/our_products/instruments/?id=6&title=iga_001, last accessed on 02/14/2014.

(17) http://www.hidenisochema.com/our_products/instruments/?id=8&title=iga_003, last accessed on 02/14/2014.

(18) Yang, R. T. Adsorbents. Fundamentals and Applications; *John Wiley & Sons, Inc:* Hoboken, New Jersey, **2003**.

(19) Yang, R. T. Gas Separation by Adsorption Processes; *Imperial College Press:* London, UK, **1997**.

(20) Perry, R. H.; Green, D. W. Perry's Chemical Engineers' Handbook (7th Edition). McGraw-Hill, **1997**.

(21) Glover, T. G.; Peterson, G. W.; Schindler, B. J.; Britt, D.; Yaghi, O., MOF-74 building unit has a direct impact on toxic gas adsorption. *Chemical Engineering Science* **2011,***66* (2), 163-170.

CHAPTER 3

ADJUSTING THE STABILITY OF METAL–ORGANIC FRAMEWORKS UNDER HUMID CONDITIONS BY LIGAND FUNCTIONALIZATION

3.1 Introduction

Remarkable progress in coordination chemistry and supramolecular assemblies has led to the development of a class of structures known as metal-organic frameworks (MOFs). MOFs are fascinating crystalline, porous materials synthesized by self-assembly of organic ligands and metal oxide clusters. These materials have recently attracted intense research interest due to their potential applications in separations, gas storage, chemical sensing, and catalysis.[1-6] MOFs exhibit high surface areas and pore volumes, and regular porous structures with various chemical functionalities.[7-12] MOF synthesis has focused largely on carboxylate-based bridging ligands.[1-12] However, a number of reports have shown that these carboxylate-based MOFs often lose their structures quickly under humid conditions.[13-27] Water molecules adsorb and disorder the framework by hydrolyzing the carboxylate groups coordinated to the metal centers. This hydrothermal stability is a critical issue for MOFs if they are to be used as adsorbents because humidity is present in many typical adsorption systems. The adsorbent may be exposed to moisture

during handling, under process conditions, or during regeneration, which will limit the usage of the material.

In spite of the importance of this issue, water adsorption in MOFs and the subsequent impact on structural stability have been addressed in a limited number of studies relative to other adsorbates. In general, it is known that 4-coordinated zinc-oxygen MOFs (MOF-5, UMCM-1) are unstable in water.[13-16] However, nitrogen-coordinated MOFs are known to have good water stability due to the higher basicity of these ligands compared to carboxylic acid. Imidazolate-based ZIF-8 is stable after exposure to high humidity levels,[17] however, structure of ZIF-8 changes upon soaking in liquid water for 3 months.[18] Pyrazolate-based MOFs show remarkable structural integrity after exposure to boiling water and other solvents.[19] Among the carboxylate MOFs, hydrophilic MIL-100 and MIL-101, 8-coordinated zirconium MOF UiO-66, and MOF-74/CPO-27 have all been described as water stable under certain conditions.[17, 20-21]

While acid-base effects are known to be important in determining the impact of water adsorption on MOF structures, steric factors have also shown promise. Ma et al.[22] examined the change in water stability of three pillared MOFs constructed from zinc, BDC, and 4,4'-bipyridine (BPY) functionalized with methyl groups at various positions. It was shown that adding methyl groups at the 2,2' position on BPY results in a stable structure (SCUTC-18) after exposure to humid air. The stable material was reported to adsorb only 4 wt% of water vapor, but the relative humidity at equilibrium was not given. The results suggest the potential of using hydrophobic functional groups to protect the coordination bond from hydrolysis. However, it is unclear whether the SCUTC-18 MOF is inherently stable due to the methyl groups protecting the coordination sites or if it only

appears stable because so little water adsorbs. It has been proposed previously that MOF stability in humid environments can be enhanced by increasing the hydrophobicity through the presence of alkyl or fluorinated groups (CF_3).[23-25] Nevertheless, still it is extremely difficult to fully exclude water from adsorbing on these hydrophobic frameworks during long exposure times, even with highly hydrophobic pores. If the stability is simply due to decreased uptake of water, then the quantity of water adsorbed on the MOFs over a long exposure time could eventually disrupt the structures significantly. Thus, there is a critical need in this field to develop hypotheses for the construction of water-stable MOFs.

The effects of topology, porosity, metal-ligand coordination, and ligand character must be decoupled to allow elucidation of the degradation mechanisms of MOFs in humid environments. However, the systematic approach that is necessary for such a study is difficult to adopt because the variety of isostructural families of MOFs with a wide range of functional groups is quite small. In this work, we have identified the $[Zn(BDC)(DABCO)_{0.5}]$ (DMOF) structure (Figure 3.1) as a convenient system for evaluating the influence of ligand functionalization on water stability while holding topology and porosity constant. A broad range of functional groups on the ligand offers different extent of shielding to the metal-ligand bond from the water molecules. DMOF is a non-catenated pillared MOF in which coordination between zinc ions and benzenedicarboxylates form the 2D layers, and DABCO (1,4-diazabicyclo[2.2.2]octane) ligands act as pillars connecting the 2D layers to each other.[26] The guest-free (activated) frameworks have 3D interconnected pores running along the a, b, and c directions. DMOF was first synthesized in 2004 by Dybstev et al.[28] In 2010, Liang et al. reported

that this MOF begins decomposing around 40% RH and collapses after 60% RH.[26] Here, we have modified the BDC ligand rather than the pillar ligand (as in the work of Ma et al.[22]) to synthesize a family of 8 isostructural DMOF materials[29-35] (DMOF-X, Figure 3.2). Since the parent structure has known water tolerance up to 60% RH, the functional groups were chosen such that they offer different extent of shielding to the Zn-O bond. In fact, we expect that polar functional groups will have a negative effect, i.e., they will facilitate hydrolysis of Zn-O bond, while non-polar groups will shield the Zn-O bond. Hence, we hope to adjust the behavior such that non-polar versions (DMOF-A, -N, -TM) are stable at higher humidities and polar versions (DMOF-Br, -Cl_2, -NO_2, -OH) degrade at lower humidities compared to the parent DMOF. Water adsorption isotherms at 298 K were measured up to 90 % RH. Powder X-ray diffraction (PXRD) and BET modelling[36] of N_2 isotherms were used to determine the structure loss after exposure to humid conditions. Our study demonstrates that the incorporation of non-polar functional groups on the BDC linker effectively shields the Zn-O bond from water molecules and improves the water stability of the MOF significantly, even while adsorbing more than 25 wt% of water.

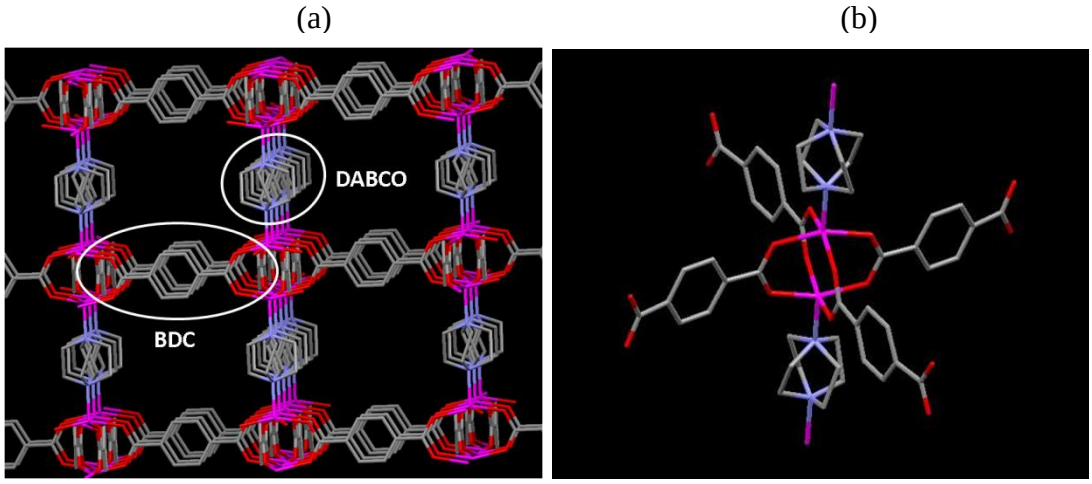

Figure 3.1 (a) Wireframe view of the 3D framework of [Zn(BDC)(DABCO)$_{0.5}$] (DMOF). The BDC ligand was functionalized as shown in Figure 3.2. (b) Coordination environment around the zinc metal in the paddle wheel secondary building unit (SBU) of DMOF.

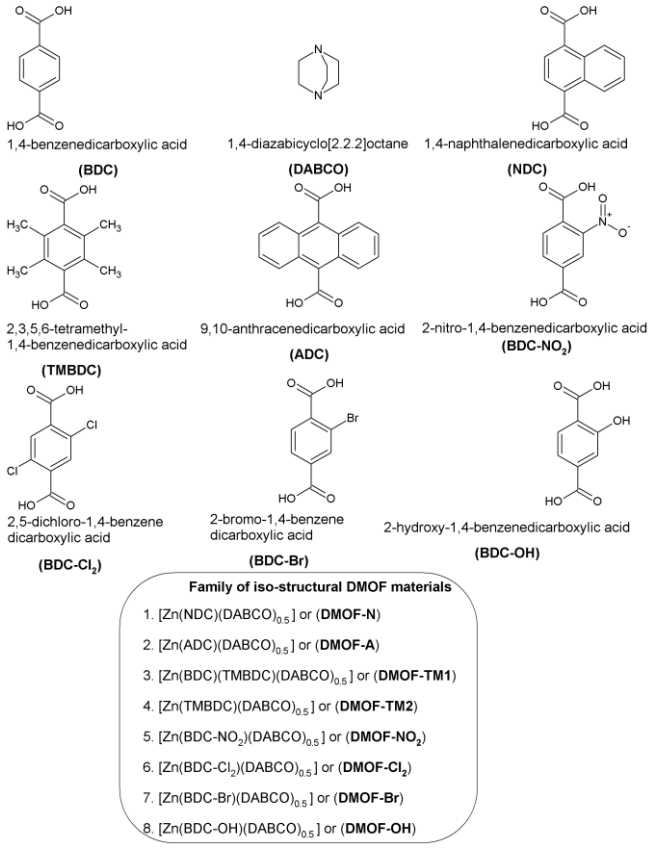

Figure 3.2 Organic ligands employed in this work and family of iso-structural DMOF materials (DMOF-X).

3.2 Experimental Section

3.2.1 Materials

All the employed chemicals were commercially available and used as received without further purification from the following sources: Sigma-Aldrich, N,N′-dimethylformamide (DMF), 9,10-anthracenedicarboxylic acid (ADC); Chem Service Inc., tetramethyl-1,4-benzenedicarboxylic acid (TMBDC); TCI America, 1,4-naphthalenedicarboxylic acid (NDC), 2-nitro-1,4-benzenedicarboxylic acid (BDC-NO_2), 2-bromo-1,4-benzenedicarboxylic acid (BDC-Br), 2,5 dichloro-1,4-benzenedicarboxylic acid (BDC-Cl_2); International Laboratory, 2-hydroxy-1,4-benzenedicarboxylic acid (BDC-OH); Acros, 1,4-diazabicyclo[2.2.2]octane (DABCO), 1,4-benzenedicarboxylic acid (BDC), methanol (MeOH).

After modulation of the BDC ligand we have synthesized a family of 8 isostructural DMOF materials[29-35] (DMOF-X, Figure 3.2): [Zn(NDC)$(DABCO)_{0.5}$] (DMOF-N), [Zn(ADC)$(DABCO)_{0.5}$] (DMOF-A), [Zn$(BDC)_{0.5}(TMBDC)_{0.5}(DABCO)_{0.5}$] (DMOF-TM1), [Zn(TMBDC)$(DABCO)_{0.5}$] (DMOF-TM2), [Zn(BDC-$NO_2$)$(DABCO)_{0.5}$] (DMOF-$NO_2$), [Zn(BDC-Br)$(DABCO)_{0.5}$] (DMOF-Br), [Zn(BDC-$Cl_2$)$(DABCO)_{0.5}$] (DMOF-$Cl_2$), and [Zn(BDC-OH)$(DABCO)_{0.5}$] (DMOF-OH). The ligands are shown in Figure 3.2 and include 2-nitro 1,4-benzenedicarboxylic acid (BDC-NO_2), 2-bromo 1,4-benzenedicarboxylic acid (BDC-Br), 2,5-dichloro-1,4-benzenedicarboxylic acid (BDC-Cl_2), 2-hydroxy 1,4-benzenedicarboxylic acid (BDC-OH), 1,4-naphthalenedicarboxylic acid (NDC), 9,10-anthracenedicarboxylic acid (ADC), 1,4-benzenedicarboxylic acid (BDC), and tetra methyl 1,4-benzenedicarboxylic acid (TMBDC). DMOF-TM1 was synthesized using equal amounts of BDC and TMBDC to obtain a material where only

half of the BDC ligands are functionalized with methyl groups. DMOF-TM2 was synthesized with only TMBDC. Detailed synthesis procedures are provided in the Appendix A.

3.2.2 Characterization

3.2.2.1 PXRD (Powder X-Ray Diffraction)

Powder X-ray diffraction patterns (PXRD) were collected using an X'Pert X-ray PANalytical diffractometer with an X'celerator module using Cu Kα (λ = 1.5418 Å) radiation at room temperature, with a step size of 0.02˚ in two theta (2θ). From these patterns, the phase purity of as-synthesized samples can be confirmed by comparison with the simulated patterns from single crystal X-ray diffraction (Appendix A, Figures. A.1-A.8). PXRD patterns of as-synthesized samples were also compared with patterns of water-exposed samples and with samples obtained after activating/ regenerating the water-exposed samples to determine the stability of MOFs under humid conditions.

3.2.2.2 Surface Area Analysis

Specific surface areas were determined by applying the BET model to nitrogen adsorption isotherms measured at 77 K for each activated MOF before and after water exposure using a Quadrasorb system from Quantachrome Instruments. It should be noted that surface area values for the same MOF may differ in various publications due to lack of consistency on the pressure range used to fit the BET model. Here, the BET theory was applied over the pressure range determined using the method of Walton et al.[36], which typically leads to analysis in the low pressure range ($P/P_o < 0.05$).

Table 3.1 Activation Conditions for Isostructural Pillared MOFs (DMOF-X)

Material	Activation process (under vacuum)	Thermal Stability‡ (^oC)
DMOF	110 ^oC (12 h)	300
DMOF-N	25 ^oC (12h)#	320
DMOF-A	120 ^oC (12 h)	350
DMOF-TM1	110 ^oC (12 h)	320
DMOF-TM2	110 ^oC (12 h)	320
DMOF-NO_2	110 ^oC (12 h)	300
DMOF-Br	110 ^oC (12 h)	300
DMOF-Cl_2	110 ^oC (12 h)	300
DMOF-OH	110 ^oC (12 h)	300

‡Obtained from literature[29-35]
#Solvent exchange with chloroform

3.2.2.3 Water Vapor Adsorption Isotherm Measurements

Water vapor adsorption isotherms were obtained using an Intelligent Gravimetric Analyzer (IGA-3 series, Hiden Isochema). Dry air was used as the carrier gas, with a portion being effervesced through a canister filled with deionized water. The ratio of saturated air and dry air was changed using two mass flow controllers to control the relative humidity (RH). Due to water condensation in the equipment at higher humidities, experiments were conducted only up to 90% RH. The total gas flow rate was set at 200 cc/min for all the experiments, and each adsorption/desorption step was given sufficient time to approach equilibrium for all RH points. Typical equilibrium times ranged from 15

minutes to 20 h. Before starting the adsorption measurement, the sample was heated under vacuum at the activation temperatures of the samples given in Table 3.1 until no further weight loss was observed.

3.3 Results and Discussion

The purity of the obtained samples was confirmed by comparison of PXRD patterns for as-synthesized MOFs and PXRD patterns simulated from the single-crystal structures (Appendix A, Figures. A.1-A.8). The porosity of all the synthesized MOFs after solvent removal was confirmed by N_2 adsorption isotherms measured at 77 K. These isotherms showed typical Type I behavior according to the IUPAC classification[3] (Appendix A, Figures. A.10-A.17). The BET surface areas and micro pore volumes of synthesized MOFs are presented in Table 3.2 and are comparable to those reported in literature.[29-35] The values of BET surface areas before and after water exposure (90% RH) show that DMOF-NO_2, DMOF-Br, DMOF-Cl_2, and DMOF-OH are not stable after water adsorption experiments. The non-polar versions DMOF-N and DMOF-TM1 are partially stable, while DMOF-A and DMOF-TM2 are fully stable.

Table 3.2 Comparison of Properties of Isostructural Pillared MOFs

Material	Pore Volume† (cm^3/g)	Pore Diameter (c, a, b)‡ (Å)	Surface Area* (m^2/g)		
			Before exposure to 90% RH	After exposure to 90% RH	% Loss
[16]DMOF	0.75	7.5x7.5,4.8x3.2,4.8x3.2	1980	7	100
DMOF-N	0.57	5.7, -, -	1420	1050	26
DMOF-A	0.33	-,4.8x3.2,4.8x3.2	760	726	4
DMOF-TM1	0.53	3.5-7.5, -, -	1210	822	32
DMOF-TM2	0.51	3.5, -, -	1050	1050	0
DMOF-NO_2	0.53	6.2x4.3, -, -	1310	38	97
DMOF-Br	0.53	5.0x2.0, -, -	1315	1	100
DMOF-Cl_2	0.45	3.8x3.8, -, -	1175	1	100
DMOF-OH	0.54	7.5x7.5,4.7x3.2, 4.7x3.2	1130	2	100

†Obtained from the Dubinin-Astakov model of N_2 adsorption at 77K
‡Obtained from literature[29-35]
*BET Analysis[36]

Figure 3.3 shows the water vapor adsorption isotherms at 25 ˚C for DMOF-NO_2, DMOF-Br, DMOF-Cl_2, and DMOF-OH. The order of polarity[37] of the functional groups follows: -OH > -NO_2 > -Cl > -Br. In the lower humidity region it is expected that the MOF with the most polar functional group will have the highest adsorption interaction. The functionalized MOFs do adsorb more water than the parent material at low RH, but the order does not strictly follow the polarity. The structures are decomposing along the isotherm, so it is difficult to decouple the effects of pore size, local functionalization or heterogeneity, and wetting on this type of adsorption behavior. The water vapor capacities at 90% relative humidity are 5.78 mmol/g (10.42 wt %) for DMOF-OH, 7.39

mmol/g (13.30 wt %) for DMOF-NO_2, 4.30 mmol/g (7.74 wt %) for DMOF-Cl_2, and 3.36 mmol/g (6.06 wt %) for DMOF-Br. The isotherms are also shown on a per pore volume basis (Appendix A, Figure A.20). For stable materials, the adsorption loadings at saturation should follow the trend of pore volume. However, since these MOFs begin degrading upon early water exposure, the actual remaining pore volume of each MOF at this stage is unknown. The desorption branch of the isotherms for each MOF in Figure 3.3 shows significant hysteresis, and a substantial amount of water is retained even when the stream is switched to dry air (0% RH point in desorption curve). This suggests that most of the adsorbed water molecules are strongly bound to the functional groups on the BDC ligand. Liang et al.[26] also reported a substantial amount of water being retained at 0% RH as a result of the structural change that occurs upon exposure to 60% RH.

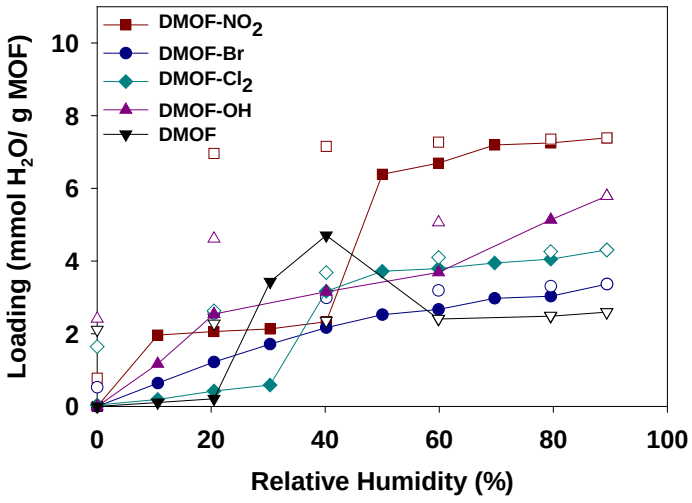

Figure 3.3 Water vapor sorption/desorption isotherms for desolvated compounds of DMOF-NO_2, DMOF-Br, DMOF-Cl_2, and DMOF-OH (closed symbols – adsorption, open symbols – desorption). Lines connecting the adsorption points are to guide the eye.

Figure 3.4 shows that PXRD pattern of DMOF-Br changes significantly after water adsorption compared to its as-synthesized pattern. The PXRD pattern of the regenerated (activation after water exposure) sample closely matches that of the water-exposed sample, which implies that the decomposition of the MOF is taking place during water adsorption itself and not during the regeneration. The N_2 adsorption isotherms were measured again after regenerating the water-exposed samples (conditions shown in Table 3.1). As reported in Table 3.2, the samples are essentially nonporous. These results are consistent with the PXRD analysis. Similar results were also obtained for DMOF-OH, DMOF-NO_2, and DMOF-Cl_2. The PXRD patterns are shown in Figure 3.4.

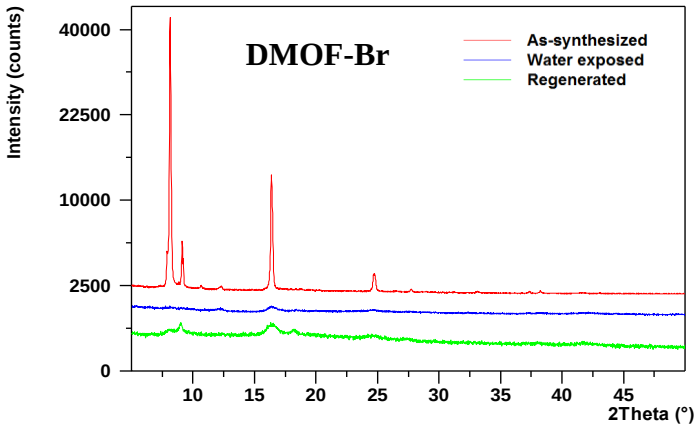

Figure 3.4 PXRD patterns for as-synthesized, water-exposed (after 90% RH), and regenerated DMOF-Br, DMOF-NO_2, DMOF-Cl_2, and DMOF-OH (top to bottom).

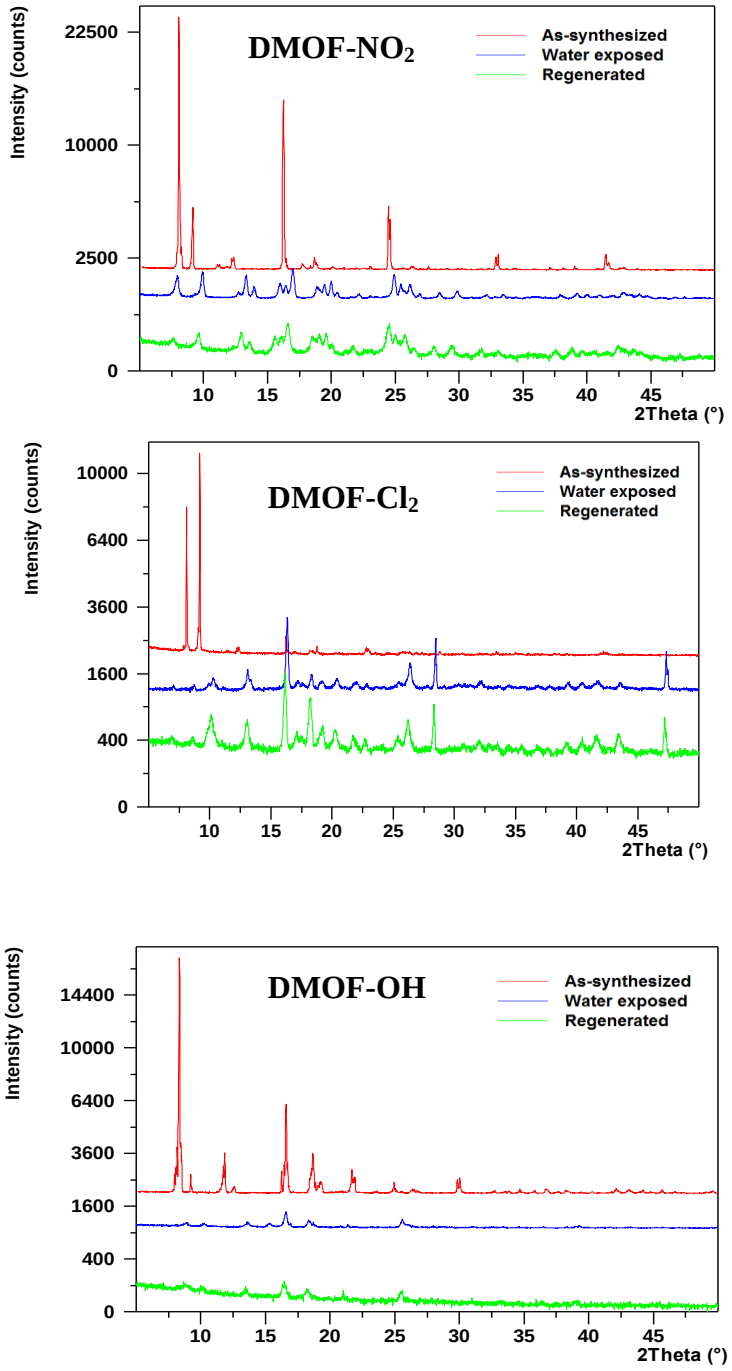

Figure 3.4 Continued.

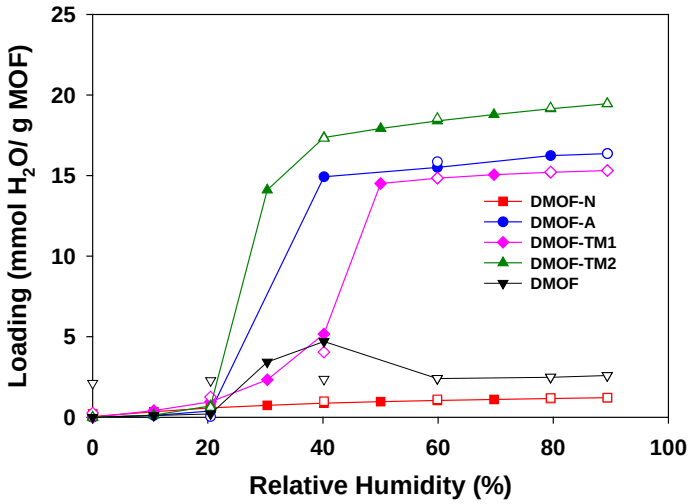

Figure 3.5 Water vapor sorption/desorption isotherms for desolvated compounds of DMOF-N, DMOF-A, DMOF-TM1, and DMOF-TM2 (closed symbols – adsorption, open symbols – desorption). Lines connecting the adsorption points are to guide the eye.

Figure 3.5 shows the water vapor adsorption isotherms at 25 ˚C for DMOF-N, DMOF-A, DMOF-TM1, and DMOF-TM2. DMOF-TM1 is synthesized using half BDC and half TMBDC, while DMOF-TM2 is synthesized only from TMBDC. The isotherms are essentially reversible, and water is not retained in the MOFs when the stream is switched to dry air. This suggests that adsorbed molecules are not strongly bound in these MOFs, as opposed to our observation for the polar functional group versions. PXRD patterns for these MOFs remain unchanged after water exposure up to 90% RH and regeneration, with the exception of DMOF-TM1 (Figure 3.6). The surface area of DMOF-TM1 decreased by 30% after regeneration. Somewhat surprisingly, the surface area of DMOF-N decreased by ~25% after regeneration, in spite of the unchanged PXRD. However, the stability is still greater than DMOF, which undergoes 100% loss of surface area. Surface areas remain unchanged for the other two MOFs (DMOF-A,

DMOF-TM2). Thus, BET results of DMOF-N, and DMOF-TM1 illustrate that PXRD or isotherm character alone (i.e., reversibility) is not sufficient to determine the water stability of MOFs.

The very low water adsorption isotherm of DMOF-N (Figure 3.5) is puzzling compared to the trends of the other MOFs, and measurements were repeated to confirm the low loadings (Appendix A, Figure A.19). It might be expected that this MOF should exhibit similar behavior to DMOF-A, but the adsorption loadings are below even the parent DMOF. The presence of the naphthalene group should result in a more hydrophobic material than DMOF, but this cannot also explain the large adsorption difference compared to DMOF-A, DMOF-TM1, and DMOF-TM2. Both of these structures undergo pore-filling below 40% RH, with final loadings above 15 mmol/g. For DMOF-A, all pore openings are restricted by the aromatics on both sides of the BDC linker. However, DMOF-N will experience 50% less pore restriction from the naphthalene group in alternating pores. As a result, pore-filling should occur at lower RH for DMOF-A relative to DMOF-N. The parent DMOF undergoes 100% degradation above 40-60 % RH, so a direct comparison with DMOF-N is not possible from a structural standpoint. Pore-filling may eventually occur in DMOF-N near 100% RH, but this could not be tested due to equipment constraints. The water vapor capacities at 90% RH are 1.21 mmol/g (2.19 wt %) for DMOF-N, 16.36 mmol/g (29.46 wt %) for DMOF-A, 15.31 mmol/g (27.56 wt %) for DMOF-TM1 and 19.45 mmol/g (35.02 wt %) for DMOF-TM2. Water vapor capacities follow the trend of the pore volumes only for water stable MOFs. This explains why the capacity follows the order DMOF-TM2 > DMOF-A > DMOF-TM1> DMOF-N; DMOF-TM1 and DMOF-N partially lose their structures

after water exposure (Table 3.2). Hence, water vapor capacities at saturation will not correspond to crystallographic pore volume for partially or fully decomposed MOFs. To control for differences in MOF weight, Figure 3.5 isotherms were normalized according to the pore volume (Appendix A, Figure A.21). DMOF-A adsorbs ~ 50 mmol/cm^3 at saturation while DMOF-TM2 adsorbs ~ 40 mmol/cm^3. This trend is due to DMOF-A possessing the smallest pore volume on a per mass basis (Table 3.2).

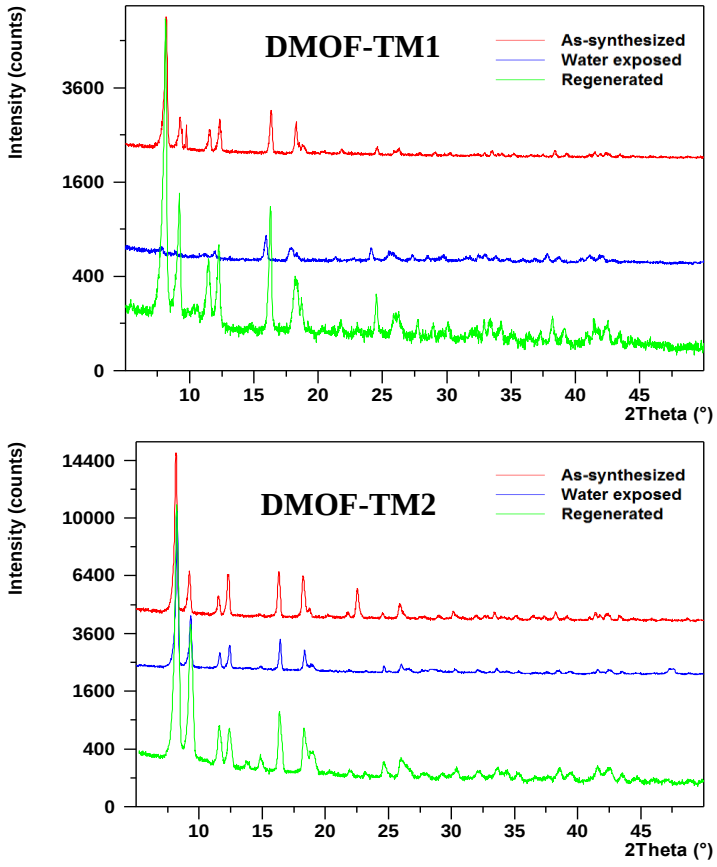

Figure 3.6 PXRD patterns for as-synthesized, water-exposed (after 90% RH), and regenerated DMOF-TM1, DMOF-TM2, DMOF-A, and DMOF-N (top to bottom).

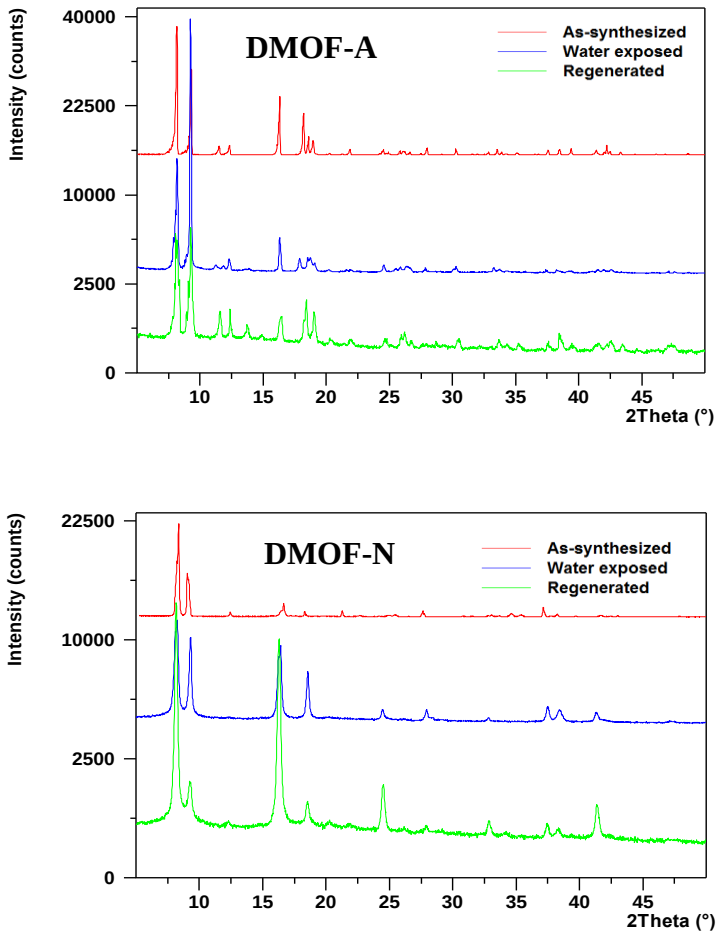

Figure 3.6 Continued.

It is noteworthy that DMOF-A and DMOF-TM2 retain their porous properties despite adsorbing large amounts of water vapor (30 wt% and 35 wt%, respectively). Thus, these MOFs are actually water stable, and this stability is not simply due to the presence of water repellent functional groups that prevent or reduce water adsorption. The reduction of water adsorption has been proposed previously as a method to enhance MOF stability in humid environments.[24] However, DMOF-A and DMOF-TM2 are stable even after adsorbing large amounts of water vapor because of the introduction of non-

polar groups (e.g., 4 methyls in DMOF-TM2) at the most adjacent sites of each coordinating oxygen atom of the dicarboxylate linker (BDC). These non-polar groups shield the metal ions from attack by water molecules, and thus enhance the water resistance of the MOF significantly compared to the parent DMOF.

This conclusion is supported by the recent work of Kaskel et al. wherein they reported that the BET surface area of $Zn_2(ADB)_2(DABCO)$ MOF or DUT-30(Zn) (ADB = 9,10-anthracene dibenzoate) decreases from 960 m^2/g to 40 m^2/g upon water exposure.[38] Counter to this we observed negligible loss in surface area for DMOF-A, which is isostructural to DUT-30(Zn). Figure 3.7 shows that for DMOF-A, the two fused benzene rings on the ligand are in a position to shield the metal ions from attack by water molecules while in DUT-30(Zn), these fused benzene rings are too far away from the coordinating oxygens to effectively shield the metal-oxygen coordination. In a similar fashion, we can explain the partial stability of DMOF-N and DMOF-TM1. DMOF-N undergoes partial decomposition due to insufficient shielding provided by the one fused benzene ring (see Figure 3.2 for structure of ligand NDC). DMOF-TM1 is also prone to attack from water molecules on the unshielded coordinating oxygen atom of the BDC linker. This also explains why the parent DMOF decomposes between 40-60% RH, while DMOF-NO_2, -Br, -Cl_2, and –OH decompose sooner. For example, DMOF-OH has already begun to decompose upon exposure to 20% RH (Appendix A, Figure A.9). These polar functional groups facilitate water adsorption and bring the molecules into close contact with the unshielded coordinating oxygen atom of the BDC linker. This in turn leads to breakage of the coordination bond between metal and ligand and collapse of the MOF structure. More studies on a larger set of MOFs are required to fully understand the

water stability of MOFs, but we can include DMOF-A and DMOF-TM2 among porous materials that are robust even in high humid conditions.

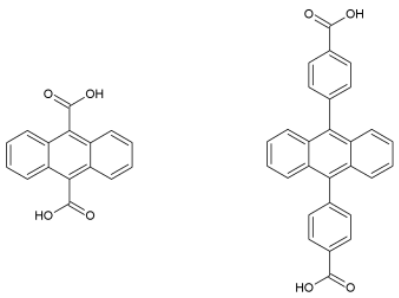

Figure 3.7 Structures of dicarboxylate ligands used in the synthesis of DMOF-A (ADC) and DUT-30(Zn).[38]

3.4 Conclusions

In summary, we have shown that it is possible to adjust the water stability of a pillared MOF both in the positive and negative directions by proper functionalization of the BDC ligand. Our study shows that placing non-polar shielding groups (e.g., methyl) on the BDC linker enhances the stability of the MOF compared to the parent DMOF, while placing polar groups (e.g., -OH) on the BDC linker destabilizes the structure at lower humidity compared to the parent MOF. DMOF-A and DMOF-TM2 do not lose any surface area or crystallinity after water exposure (up to 90 % RH) even though they adsorb large amounts of water at ~ 20 % RH. For DMOF-N and DMOF-TM1 there is a slight decrease in surface areas due to insufficient shielding, but the stability is still much higher than the parent MOF. The results of this work offer one method for controlling the structural collapse of MOFs during water exposure and, more generally, provide an important step towards understanding the water adsorption behavior of MOFs.

3.5 References

(1) Ferey, G. Some Suggested Perspectives for Multifunctional Hybrid Porous Solids. *Dalton Trans.* **2009**, 4400.

(2) Kuppler, R. J.; Timmons, D. J.; Fang, Q. R.; Li, J. R.; Makal, T. A.; Young, M. D.; Yuan, D. Q.; Zhao, D.; Zhuang, W. J.; Zhou, H. C. Potential Applications of Metal-Organic Frameworks. *Coord. Chem. Rev.* **2009**, *253*, 3042.

(3) Kitagawa, S.; Kitaura, R.; Noro, S., Functional porous coordination polymers. *Angew. Chem.-Int. Edit.* **2004,** *43* (18), 2334-2375.

(4) Keskin, S.; van Heest, T. M.; Sholl, D. S., Can Metal-Organic Framework Materials Play a Useful Role in Large-Scale Carbon Dioxide Separations? *ChemSusChem* **2010,** *3* (8), 879-891.

(5) Li, J.-R.; Kuppler, R. J.; Zhou, H.-C., Selective gas adsorption and separation in metal-organic frameworks. *Chem. Soc. Rev.* **2009,** *38* (5), 1477-1504.

(6) Karra, J. R.; Walton, K. S., Effect of open metal sites on adsorption of polar and nonpolar molecules in metal-organic framework Cu-BTC. *Langmuir* **2008,** *24* (16), 8620-8626.

(7) Caskey, S. R.; Wong-Foy, A. G.; Matzger, A. J., Dramatic tuning of carbon dioxide uptake via metal substitution in a coordination polymer with cylindrical pores. *J. Am. Chem. Soc.* **2008,** *130* (33), 10870.

(8) Rowsell, J. L. C.; Yaghi, O. M. Effects of Functionalization, Catenation, and Variation of the Metal Oxide and Organic Linking Units on the Low-Pressure Hydrogen Adsorption Properties of Metal-Organic Frameworks. *J. Am. Chem. Soc.* **2006**, *128*, 1304.

(9) Wang, Z. Q.; Tanabe, K. K.; Cohen, S. M. Tuning Hydrogen Sorption Properties of Metal-Organic Frameworks by Postsynthetic Covalent Modification. *Chem.-Eur. J.* **2010**, *16*, 212.

(10) Farha, O. K.; Hupp, J. T. Rational Design, Synthesis, Purification, and Activation of Metal-Organic Framework Materials. *Accounts Chem. Res.* **2010**, *43*, 1166.

(11) Tanabe, K. K.; Cohen, S. M. Postsynthetic Modification of Metal-Organic Frameworks-a Progress Report. *Chem. Soc. Rev.* **2011**, *40*, 498.

(12) Eddaoudi, M.; Kim, J.; Rosi, N.; Vodak, D.; Wachter, J.; O'Keeffe, M.; Yaghi, O. M., Systematic design of pore size and functionality in isoreticular MOFs and their application in methane storage. *Science* **2002,** *295* (5554), 469-472.

(13) Greathouse, J. A.; Allendorf, M. D., The interaction of water with MOF-5 simulated by molecular dynamics. *J. Am. Chem. Soc.* **2006,** *128* (33), 10678-10679.

(14) Li, Y.; Yang, R. T., Gas adsorption and storage in metal-organic framework MOF-177. *Langmuir* **2007,** *23* (26), 12937-12944.

(15) Low, J. J.; Benin, A. I.; Jakubczak, P.; Abrahamian, J. F.; Faheem, S. A.; Willis, R. R., Virtual High Throughput Screening Confirmed Experimentally: Porous Coordination Polymer Hydration. *J. Am. Chem. Soc.* **2009,** *131* (43), 15834-15842.

(16) Schoenecker, P. M.; Carson, C. G.; Jasuja, H.; Flemming, C. J. J.; Walton, K. S., Effect of Water Adsorption on Retention of Structure and Surface Area of Metal–Organic Frameworks. *Ind. Eng. Chem. Res.* **2012,** *51* (18), 6513-6519.

(17) Kuesgens, P.; Rose, M.; Senkovska, I.; Froede, H.; Henschel, A.; Siegle, S.; Kaskel, S., Characterization of metal-organic frameworks by water adsorption. *Microporous Mesoporous Mat.* **2009,** *120* (3), 325-330.

(18) Cychosz, K. A.; Matzger, A. J., Water Stability of Microporous Coordination Polymers and the Adsorption of Pharmaceuticals from Water. *Langmuir* **2010,** *26* (22), 17198-17202.

(19) Choi, H. J.; Dinca, M.; Dailly, A.; Long, J. R., Hydrogen storage in water-stable metal-organic frameworks incorporating 1,3-and 1,4-benzenedipyrazolate. *Energy & Environmental Science* **2010,** *3* (1), 117-123.

(20) Cavka, J. H.; Jakobsen, S.; Olsbye, U.; Guillou, N.; Lamberti, C.; Bordiga, S.; Lillerud, K. P., A new zirconium inorganic building brick forming metal organic frameworks with exceptional stability. *J. Am. Chem. Soc.* **2008,** *130* (42), 13850-13851.

(21) Dietzel, P. D. C.; Morita, Y.; Blom, R.; Fjellvag, H., An in situ high-temperature single-crystal investigation of a dehydrated metal-organic framework compound and field-induced magnetization of one-dimensional metaloxygen chains. *Angew. Chem.-Int. Edit.* **2005,** *44* (39), 6354-6358.

(22) Ma, D.; Li, Y.; Li, Z., Tuning the moisture stability of metal-organic frameworks by incorporating hydrophobic functional groups at different positions of ligands. *Chem. Commun.* **2011,** *47* (26), 7377-7379.

(23) Yang, J.; Grzech, A.; Mulder, F. M.; Dingemans, T. J., Methyl modified MOF-5: a water stable hydrogen storage material. *Chem. Commun.* **2011,** *47* (18), 5244-5246.

(24) Nguyen, J. G.; Cohen, S. M., Moisture-Resistant and Superhydrophobic Metal-Organic Frameworks Obtained via Postsynthetic Modification. *J. Am. Chem. Soc.* **2010,** *132* (13), 4560-4561.

(25) Serre, C., Superhydrophobicity in Highly Fluorinated Porous Metal-Organic Frameworks. *Angew. Chem.-Int. Edit.* **2012,** *51* (25), 6048-6050.

(26) Liang, Z.; Marshall, M.; Chaffee, A. L., CO_2 adsorption, selectivity and water tolerance of pillared-layer metal organic frameworks. *Microporous Mesoporous Mat.* **2010,** *132* (3), 305-310.

(27) Kondo, A.; Daimaru, T.; Noguchi, H.; Ohba, T.; Kaneko, K.; Kanob, H., Adsorption of water on three-dimensional pillared-layer metal organic frameworks. *J. Colloid and Interface Sci.* **2007,** *314* (2), 422-426.

(28) Dybtsev, D. N.; Chun, H.; Kim, K., Rigid and flexible: A highly porous metal-organic framework with unusual guest-dependent dynamic behavior. *Angew. Chem.-Int. Edit.* **2004,** *43* (38), 5033-5036.

(29) Tanaka, D.; Horike, S.; Kitagawa, S.; Ohba, M.; Hasegawa, M.; Ozawa, Y.; Toriumi, K., Anthracene array-type porous coordination polymer with host-guest charge transfer interactions in excited states. *Chem. Commun.* **2007,** (30), 3142-3144.

(30) Zhao, Y. G.; Wu, H. H.; Emge, T. J.; Gong, Q. H.; Nijem, N.; Chabal, Y. J.; Kong, L. Z.; Langreth, D. C.; Liu, H.; Zeng, H. P.; Li, J., Enhancing Gas Adsorption and Separation Capacity through Ligand Functionalization of Microporous Metal-Organic Framework Structures. *Chem.- Eur. J.* **2011,** *17* (18), 5100-5108.

(31) Chen, Z.; Xiang, S.; Arman, H. D.; Li, P.; Zhao, D.; Chen, B., Significantly Enhanced CO_2/CH_4 Separation Selectivity within a 3D Prototype Metal–Organic Framework Functionalized with OH Groups on Pore Surfaces at Room Temperature. *Eur. J. Inorg. Chem.* **2011,** (14), 2227-2231.

(32) Tanaka, D.; Higuchi, M.; Horike, S.; Matsuda, R.; Kinoshita, Y.; Yanai, N.; Kitagawa, S., Storage and sorption properties of acetylene in jungle-gym-like open frameworks. *Chem.-Asian J.* **2008,** *3* (8-9), 1343-1349.

(33) Uemura, K.; Onishi, F.; Yamasaki, Y.; Kita, H., Syntheses, crystal structures, and water adsorption behaviors of jungle-gym-type porous coordination polymers containing nitro moieties. *J. Solid State Chem.* **2009,** *182* (10), 2852-2857.

(34) Chun, H.; Dybtsev, D. N.; Kim, H.; Kim, K., Synthesis, X-ray Crystal Structures, and Gas Sorption Properties of Pillared Square Grid Nets Based on Paddle-Wheel Motifs: Implications for Hydrogen Storage in Porous Materials. *Chem. –Eur. J.* **2005,** *11* (12), 3521-3529.

(35) Uemura, K.; Yamasaki, Y.; Onishi, F.; Kita, H.; Ebihara, M., Two-Step Adsorption on Jungle-Gym-Type Porous Coordination Polymers: Dependence on Hydrogen-Bonding Capability of Adsorbates, Ligand-Substituent Effect, and Temperature. *Inorganic Chemistry* **2010,** *49* (21), 10133-10143.

(36) Walton, K. S.; Snurr, R. Q., Applicability of the BET method for determining surface areas of microporous metal-organic frameworks. *J. Am. Chem. Soc.* **2007,** *129* (27), 8552-8556.

(37) Stahl, E., Thin-layer chromatography: A laboratory handbook. Springer, Ed. 1969.

(38) Hauptvogel, I. M.; Biedermann, R.; Klein, N.; Senkovska, I.; Cadiau, A.; Wallacher, D.; Feyerherm, R.; Kaskel, S., Flexible and Hydrophobic Zn-Based Metal-Organic Framework. *Inorganic Chemistry* **2011,** *50* (17), 8367-8374.

CHAPTER 4

KINETIC WATER STABILITY OF AN ISOSTRUCTURAL FAMILY OF ZINC-BASED PILLARED METAL–ORGANIC FRAMEWORKS

4.1 Introduction

Metal-organic frameworks (MOFs) are a relatively new class of nanoporous materials that have received significant attention due to their exceptionally high porosities and chemically tunable structures.[1-6] As a result, MOFs have become ideal candidates for applications such as air purification, chemical sensing, hydrogen storage, catalysis, and CO_2 capture.[7-13] MOFs are characterized by their metal-ion clusters and organic ligands. An increasing number of MOFs with highly desirable properties such as open-metal sites and amine-functionalized groups have been synthesized in the literature, giving them enormous potential for revolutionizing the adsorption field.[9] Industrial adsorbents, e.g., those used in CO_2 capture applications, come in direct contact with moisture via the operating conditions and regeneration steps involved in the process. One key challenge in the commercialization of MOFs is a lack of fundamental understanding regarding the factors that influence their stability under humid conditions.

Despite the poor hydrothermal stability of many MOFs, reports on water adsorption and its subsequent impact on structural stability are scarce relative to other studies performed with gases such as CO_2, CH_4, N_2, and H_2. Carboxylate-based MOFs are especially prone to breakdown in the presence of humid conditions,[14-18] a

characteristic that has been attributed to the relatively weak metal-ligand bond formed between oxygen and the metal.[19] However, notable exceptions to these trends are also present; for example, the chromium-based MIL-53 and MIL-101 structures are stable due to the inertness of the Cr metal[20-21] while UiO-66 and MIL-125 are stable due to the high nuclearity and coordination number of their secondary building units.[21-23] Our group recently reported an experimental investigation into the loss of crystallinity and surface area caused by exposure to humid conditions in various prototypical MOF systems containing open-metal sites, amine-functional groups, carboxylate coordination and nitrogen coordination.[24] Past studies have attempted to understand the poor hydrothermal stability of the well-studied IRMOF-1 experimentally[25] and computationally[26-28] through the use of reactive force fields and first principles molecular dynamics simulations.

Long and co-workers were the first to showcase that, from a thermodynamic standpoint, MOF stability can be related to the basicity (pK_a) of the ligand.[17,29] Because MOFs are derived from Lewis acid-base coordination complexes between metal ions and ligands, the pK_a of the isolated ligand can be used to predict the thermodynamic strength of the resulting metal-ligand bond. This work was further supported by Low et al.[19] who also found that the strength of the bond between metal oxide cluster and the bridging linker is important in defining the hydrothermal stability of various MOFs. Other studies have since been carried out under humid conditions to characterize the stability and water adsorption properties of MOFs such as MOF-177, Cu-BTC, ZIF-8, MIL-101(Cr), MIL-100(Fe), MIL-53 (Al, Cr, V), and UiO-66.[14,19,20,30-35] From these studies it was concluded that, while 4-coordinated zinc-oxygen MOFs tend to be unstable in water,[14,19,24] nitrogen-coordinated MOFs have better water stability due to the higher basicity (pK_a) of nitrogen-

based ligands.[24,31] By this same logic, MOFs with the highly basic pyrazolate ligand (pK_a ~19.8)[29] show outstanding thermodynamic stability upon exposure to humid conditions and boiling water[17] whereas the slightly lower basicity of imidazole-based MOFs (pK_a ~18.6)[29] such as ZIF-8 make their structures stable after exposure to humid conditions[30] but not after prolonged exposure to liquid water.[25] In this case, the former series of pyrazolate-based MOFs have thermodynamic stability in the presence of liquid water whereas the latter's stability is purely kinetic.[25] Recently, thermodynamic stability of two new MOFs MOOFOUR-1-Ni and CROFOUR-1-Ni was also confirmed since their as-synthesized samples retain crystallinity even when immersed in water for months, boiling water for one day, or 0.1 N NaOH for a week.[36]

While acid-base effects are critical to determining the thermodynamic stability of MOFs in the presence of water, ligand functionalization can be seen as a promising approach for tuning the kinetic stability. Ma et al.[15] compared the water stability of three isostructural, pillared MOFs built from zinc, 1,4-benzenedicarboxylic acid (BDC), and methyl-functionalized variations of the 4,4'-bipyradine (BPY) ligand. It was found that, while the addition of methyl groups to BPY enhanced the structural stability of the parent structure under humid conditions, the degree of improvement was sensitive to the specific placement of the methyl groups. In particular, the addition of methyl groups at the 2,2' position on BPY resulted in a more water stable structure (SCUTC-18) than the one containing methyl groups at the 3,3' position (SCUTC-19). It is interesting to note that, while this point was not made in the original study, the pK_a values of the two functionalized ligands used in these isostructural MOFs are nearly the same (pK_a = 5.58 for SCUTC-18 vs. pKa = 5.29 for SCUTC-19).[37] As a result, one would not predict the

thermodynamic stability of the two structures to largely differ; instead, differences in the kinetic stability of these structures are likely responsible for the observed differences in water stability. However, because no water vapor adsorption isotherms were reported, it is difficult to determine whether SCUTC-18 is more stable due to an inherent change in structural stability or simply from the exclusion of water from entering its pores due to the non-polar methyl groups. Along these same lines, the incorporation of hydrophobic alkyl and trifluoromethyl functional groups have been shown to improve the apparent water stability of other MOF variations as well.[16,38-42] However, similar to the study by Ma et al.[15], broader insight into the inherent stability of the MOF structures cannot be extracted.

To date, there are a few MOFs (e.g., UiO-66, MIL-100(Fe), MIL-101 (Cr)) that remain stable after the adsorption of large amounts of water vapor.[24,30,32-33] MOFs with open metal sites such as Cu-BTC or HKUST-1, and MOF-74 or CPO-27 are also quite hydrophilic however they degrade in humid air.[24] From a practical standpoint, preventing water from entering a porous material may be an acceptable short-term approach to improving its performance under humid conditions. However, during long exposure times, some amount of water will likely still adsorb into the pores of the framework, regardless of how hydrophobic the pores may be. Furthermore, from a fundamental standpoint, it is of much greater interest to understand how the inherent stability of a structure can be tuned so that it remains stable even after water has entered the pores. Such knowledge is critical to the development of design criteria for a broad range of next-generation, water stable MOFs that are not necessarily hydrophobic in character.

Because there are so many interdependent factors, which govern MOF stability under humid conditions (metal type and coordination state, framework dimensionality, interpenetration, etc.) it is desirable to keep as many of these variables constant as possible. As such, water adsorption and characterization studies on isostructural MOF series are critical to isolating the specific factors that govern structural stability. DMOF (Figure 4.1) is a mixed-ligand MOF that contains zinc clusters connected in the 2D plane by 1,4-benzenedicarboxylic acid (BDC) and the pillar linker 1,4-diazabicyclo[2.2.2]octane (DABCO) connecting the third dimension.[43] Due to the partial stability of the parent structure under humid conditions (until ~30% relative humidity),[31] it provides the ideal system to systematically tune properties and study their resulting impact on water stability. In our previous work[44] (Chapter 3) we performed a water adsorption study on a series of structures in the DMOF family that have been already reported in literature. The goal was to showcase that it is possible to adjust the water stability of a pillared MOF both in the positive and negative directions by proper functionalization of the BDC ligand. In this work, we have extended this concept by synthesizing four novel isostructural MOFs with methyl functional groups at different positions on the BDC linker. We have also performed water adsorption studies on these newly synthesized DMOF variations, as well as a number of already reported functionalized analogues containing polar (fluorine) and non-polar (methyl) functional groups on the BDC ligand (Table 4.1). Furthermore, we also calculated the pK_a values for the functionalized ligands to investigate whether the difference in structural stability among members of this isostructural, pillared family under humid conditions is thermodynamic or kinetic in nature. Through an analysis of molecular simulations,

experimental water adsorption isotherms, PXRD patterns, and N_2 adsorption at 77K before and after water exposure we are able to obtain important insight into the impact of water adsorption on the observed trends in kinetic water stability of these structures.

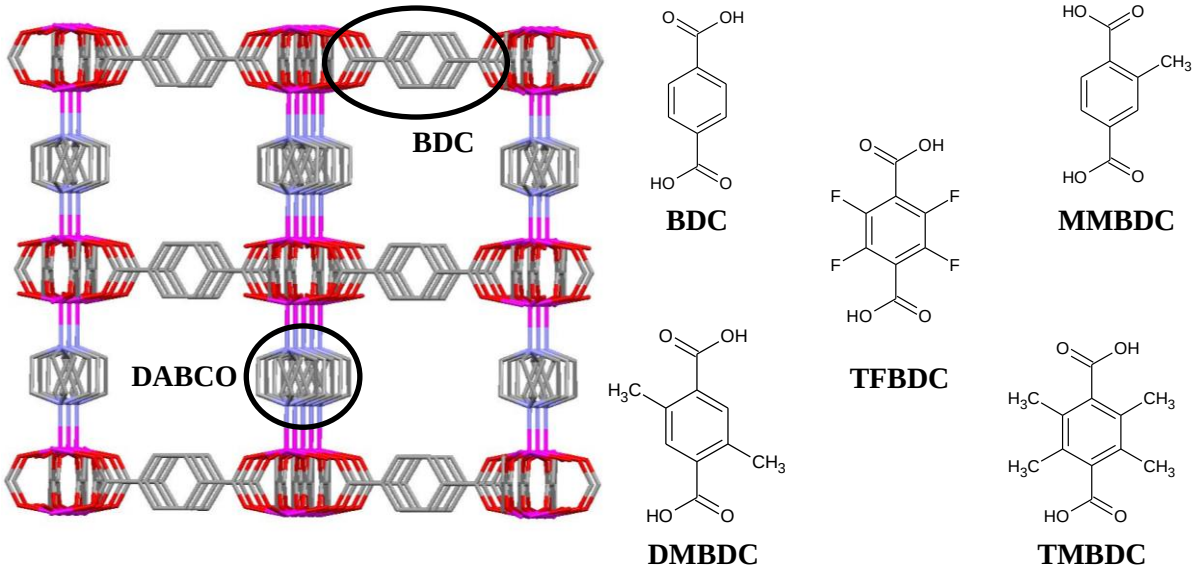

Figure 4.1 Left, the 3D structure of DMOF or [Zn(BDC)(DABCO)$_{0.5}$]. Hydrogen atoms are omitted for clarity. Color code: Zn: pink; O: red; C: grey; N: purple. Right, the functionalized BDC ligands used to synthesize the DMOF-X family.

Table 4.1 Family of Isostructural Pillared MOFs in This Work.

MOF		Carboxylate Ligand
Formula	**Tag**	
$[Zn(BDC)(DABCO)_{0.5}]$	[24,43]DMOF	100% BDC
$[Zn(BDC)_{0.5}(MMBDC)_{0.5}(DABCO)_{0.5}]$	†DMOF-MM1	50% BDC: 50% MMBDC
$[Zn(MMBDC)(DABCO)_{0.5}]$	†DMOF-MM2	100% MMBDC
$[Zn(BDC)_{0.5}(DMBDC)_{0.5}(DABCO)_{0.5}]$	†DMOF-DM1	50% BDC: 50% DMBDC
$[Zn(DMBDC)(DABCO)_{0.5}]$	†DMOF-DM2	100% DMBDC
$[Zn(BDC)_{0.5}(TMBDC)_{0.5}(DABCO)_{0.5}]$	[43]DMOF-TM1	50% BDC: 50% TMBDC
$[Zn(TMBDC)(DABCO)_{0.5}]$	[43]DMOF-TM2	100% TMBDC
$[Zn(TFBDC)(DABCO)_{0.5}]$	[43]DMOF-TF	100% TFBDC

†New MOFs synthesized in this work

4.2 Experimental and Simulation Details

4.2.1 Synthesis

All the required chemicals were used as procured (without any purification) from commercial suppliers: Sigma-Aldrich, N,N′-dimethylformamide (DMF), 2,3,5,6-tetrafluoro-1,4-benzenedicarboxylic acid (TFBDC); Combi-Blocks, 2-monomethyl 1,4-benzene-dicarboxylic acid (MMBDC); TCI America, 2,5-dimethyl-1,4-benzenedicarboxylic acid (DMBDC); Chem Service Inc., 2,3,5,6-tetramethyl-1,4-

benzenedicarboxylic acid (TMBDC); Acros, 1,4-diazabicyclo[2.2.2]octane (DABCO), 1,4-benzenedicarboxylic acid (BDC), methanol (MeOH).

By varying the functional group(s) added on the BDC linkers (Figure 4.1) we obtained an isostructural pillared MOF family, DMOF-X, as summarized in Table 4.1. DMOF-MM1, MM2, DM1, and DM2 are novel MOFs whereas as DMOF-TM1, TM2, and TF are synthesized as reported in literature.[45] DMOF-MM1, DM1, and TM1 were synthesized using equal amounts of BDC and the respective mono, di, and tetramethyl functionalized BDC to obtain a material where only half of the BDC ligands are functionalized with methyl groups. However, DMOF-MM2, DM2, TM2, and TF were synthesized using only the indicated functionalized ligand. Detailed synthesis procedures are provided in the Appendix B.

4.2.2 Characterization

4.2.2.1 Single Crystal XRD (X-Ray Diffraction)

Single crystal X-ray data of DMOF-DM1 and DMOF-DM2 were collected on a Bruker APEX II CCD sealed tube diffractometer by using Mo-*K*α (λ = 0.71073 Å) radiation with a graphite monochromator. Crystals of the MOFs were mounted on nylon CryoLoops with Paratone-N. The structure was solved by direct methods and refined by full-matrix least-squared techniques using the SHELXTL-97 software suite. Crystallographic details are listed below (Figure 4.2, Table 4.2).

Table 4.2 Crystallographic Data for DMOF-DM1 and DMOF-DM2.

Compound	DMOF-DM1	DMOF-DM2
Formula	$C_{12}H_{12}ZnNO_4$	$C_{19}H_{28}N_3O_6Zn$
Fw	299.61	459.81
Crystal size(mm)	0.182 x 0.252 x 0.328	0.156 x 0.312 x 0.407
Space group	*P4/mmm*	*I41/acd*
a = (Å)	15.3916(15)	21.624(9)
b =(Å)	15.3916(15)	21.624(9)
c(Å)	9.588(2)	38.385(9)
V(Å^3)	2271.3(6)	17949(11)
Z	4	32
λ(*Mo K*α)(Å)	0.71073	0.71073
D_c(g/cm^3)	0.8760	1.361
μ(mm^{-1})	7.303	1.132
T(K)	173(2)	110(2)
*R*int	0.1061	0.0732
parameters	72	268
R_1, *w*R(I > 2σ(I))[a]	0.1470, 0.5084	0.0515, 0.1400
R_1, *w*R(all data)[b]	0.2166, 0.5507	0.0625, 0.1503
$w=1/〔\sigma^2(F_0^2)+(aP)^2+bP〕$	a= 0.2, b=0.0	a= 0.0857, b= 43.2120
Goodness-of-fit-on F^2	1.981	1.028
$\Delta\rho_{min}$ and $\Delta\rho_{max}$(e Å^{-3})	-1.286 , 3.283	-0.456, 1.086

[a] $R = \sum||F_0|-|F_c||)/\sum|F_0|$
[b] $wR = |\sum w(F_0-F_c)^2/\sum w(F_0^2)^2|^{1/2}$

Figure 4.2 Photographs of single crystal of DMOF-1 (left, size (mm) – 0.182 x 0.252 x 0.328), and DMOF-DM2 (right, size (mm) – 0.156 x 0.312 x 0.407)

4.2.2.2 PXRD (Powder X-Ray Diffraction)

Powder X-ray diffraction patterns were obtained using an X'Pert X-ray PANalytical diffractometer with an X'celerator module using Cu Kα (λ = 1.5418 Å) radiation at room temperature, with a step size of 0.02˚ in two theta (2θ). PXRD patterns of the as-synthesized MOFs confirm that these materials are isostructural to the parent DMOF structure (Figure 4.3). Moreover, by comparison of as-synthesized samples with the simulated patterns from single crystal X-ray diffraction (Appendix B, Figures B.1-B.7), phase purity was confirmed. Comparison of PXRD patterns of as-synthesized samples with samples obtained after water exposure and samples obtained after regenerating the water-exposed samples was used to characterize the impact of water adsorption on the crystallinity of the functionalized, isostructural DMOF variations.

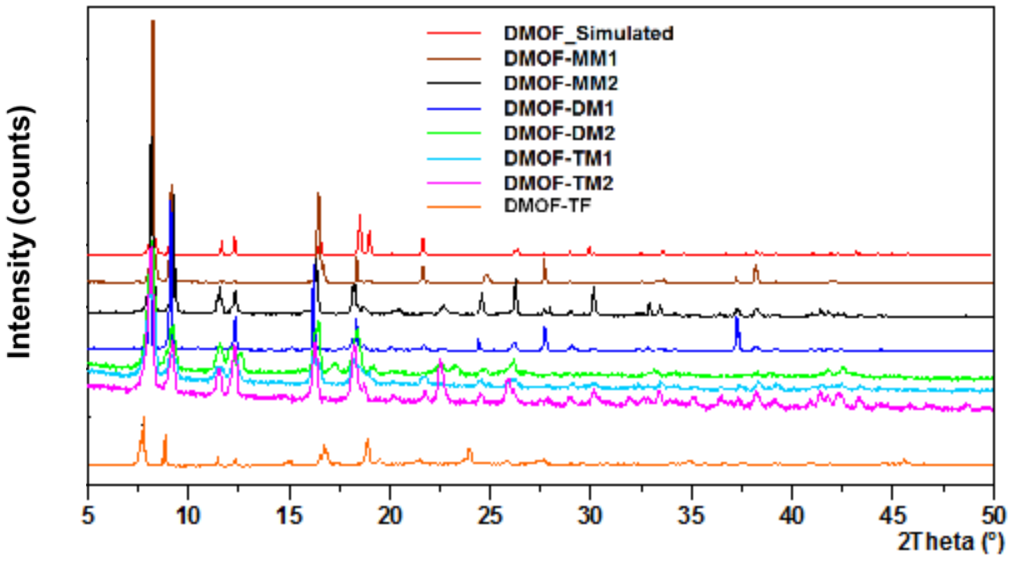

Figure 4.3 Comparison of PXRD patterns for as-synthesized DMOF-X (where X = MM1, MM2, DM1, DM2, TM1, TM2, & TF) and theoretical pattern of DMOF from single crystal data.

4.2.2.3 N_2 Adsorption Measurements

Nitrogen adsorption measurements (Appendix B, Figures B.8-B.14) at 77 K were performed for each activated (refer Table 4.3 for details on the activation process) MOF before and after water exposure using a Quadrasorb system from Quantachrome Instruments. A sample size of approximately 20-30 mg was used to collect these isotherms. Specific surface areas (m^2/g) were determined by applying the BET model to the obtained adsorption isotherms. BET theory was applied over the pressure range $P/P_o < 0.05$ to ensure that consistent, physically meaningful parameters were obtained.[46]

Table 4.3 Activation Conditions for Isostructural Pillared MOFs (DMOF-X)

Material	Activation process (under vacuum)	Thermal Stability (^{o}C)
DMOF-MM1	110 ^{o}C (12 h)	250-300
DMOF-MM2	110 ^{o}C (12 h)	250-300
DMOF-DM1	110 ^{o}C (12 h)	250-300
DMOF-DM2	110 ^{o}C (12 h)	250-300
DMOF-TM1	110 ^{o}C (12 h)	320‡
DMOF-TM2	110 ^{o}C (12 h)	320‡
DMOF-TF	95 ^{o}C (12 h)	300‡

‡ Obtained from literature[45]

4.2.2.4 Thermogravimetric−Mass Spectroscopic (TG-MS) Analysis

Thermogravimetric analyses (TGA) of as-synthesized samples (Figure 4.5a) of newly synthesized MOFs (DMOF-X, X = MM1, MM2, DM1, and DM2) were carried out under helium in the temperature range of 30-600 ˚C on a NETZSCH STA 449 F1 Jupiter® device with a heating rate of 5 ˚C /min and flow rate of 20 mL/min. To ensure that only half of the BDC ligands are functionalized by dimethyl functionality in DMOF-DM1, we performed the TG analysis with parallel online mass spectrometric (MS) analysis on the activated DMOF-DM1 sample (Figure 4.5b).

4.2.2.5 ^{1}H Nuclear Magnetic Resonance (H NMR)

To confirm the successful synthesis of DMOF-MM1, MM2, and DM1, Varian Mercury Vx 300 was used to record the ^{1}H NMR spectrum of activated samples of

DMOF-MM1, MM2, and DM1 (Figures 4.6-4.8). Small amounts of the activated MOF samples (activated under vacuum at 110 ^{o}C for 12 hr) were digested with NaOH in D_2O and subsequently subjected to ^{1}H NMR measurements.

4.2.2.6 Water Vapor Adsorption Isotherm Measurements

Water vapor adsorption isotherms were measured at 298 K and 1 bar using an IGA-3 (Intelligent Gravimetric Analyzer) series device from Hiden Isochema. Samples loaded in the IGA-3 device were activated (see Table 4.3 for details) *in situ* to remove any guest molecules from the structure. A sample size of approximately 30-40 mg was used to collect water adsorption isotherms. Using two mass flow controllers, the ratio of saturated and dry air was varied to control the relative humidity (RH) of the sample environment. Saturated air is generated by bubbling a percentage of dry air through a canister filled with deionized water. For all the experiments, the total gas flow rate was set at 200 cm^3/min. Variable timeouts were used, with a maximum limit of 20 h for each adsorption/desorption point so that sufficient time was available to approach equilibrium for all isotherm points. Due to the possibility of water condensation in the equipment at higher humidities, experiments were conducted only up to 90% RH. After water exposure, samples were regenerated at the activation conditions given in Table 4.3.

4.2.3 Computational Details

All structures used in classical simulations were optimized via periodic quantum mechanics calculations using the VASP package. Ionic relaxations were first performed on the unit cells obtained from experimental CIFs with 400 eV plane wave cut-offs, PAW pseudo potentials[47] and the PBE-GGA[48] until forces on all atoms were less than 30 meV/Å. Tip4p-Ew[49], a four point model optimized for the Ewald charge summation

method used in periodic systems, was used to describe water molecules, and framework partial charges were assigned from the quantum mechanical electrostatic potential via the REPEAT charge-fitting method.[50] The DREIDING force field[51] was used to obtain Lennard-Jones parameters for all framework atoms and Lorentz-Berthelot mixing rules were applied to calculate intermolecular van der Waals interactions between water and framework atoms. All transition state calculations were performed using the QST/LST method on Accelrys DMOL3 program at high precision with the DNP basis set, GGA-PBE functional, and all electron treatment of core electrons. Further simulation details can be found in the Appendix B.

4.3 Results and Discussion

4.3.1 Structure Characterization and Physical Properties

As mentioned before, DMOF-MM1, MM2, DM1, and DM2 are new MOFs. However, we were only able to obtain single crystals for the DMOF-DM1 and DM2 structures. Single crystal X-ray diffraction (XRD) analysis of DMOF-DM1, and DM2 shows that these frameworks are isostructural to the parent DMOF, containing the same $Zn_2(COO)_4$ paddle-wheel secondary building units (SBUs) bridged by their respective carboxylate BDC ligand to form the 2D layers. DABCO ligands act as pillars by occupying axial sites of the Zn_2 paddle wheels and extending the 2D layers into a 3D structure (Figure 4.4). Single crystal XRD analysis shows that DMOF-DM1 crystallizes in the P4/mmm space group and, similar to the DMOF-TM1 and TM2 structures reported by Chun et al.,[45] contains structural disorder in the CIFs. However, DMOF-DM2 crystallizes in I41/acd space group and does not have any disorder. Crystallographic details are listed in Table 4.2.

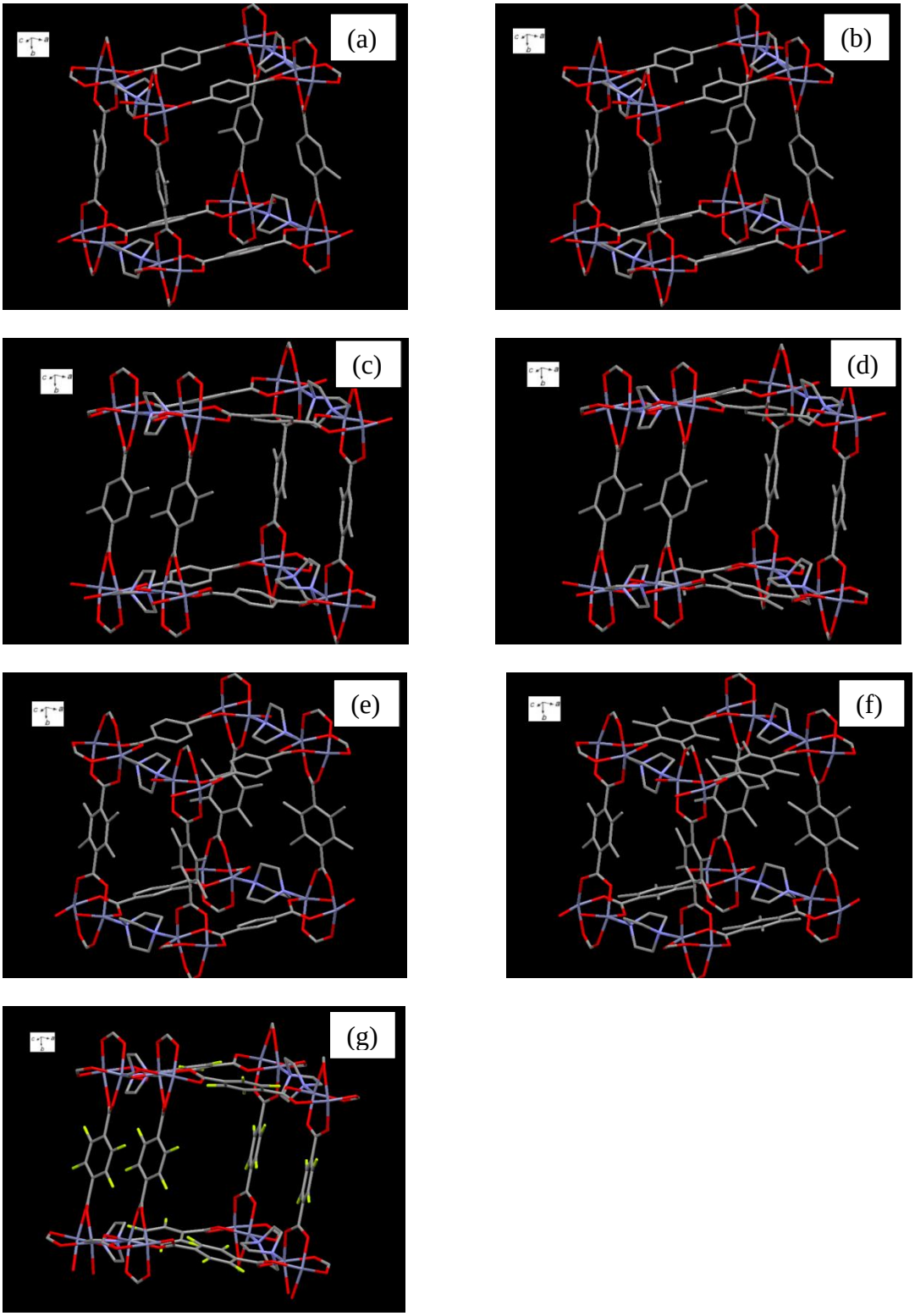

Figure 4.4 Structures of (a) DMOF-MM1, (b) DMOF-MM2, (c) DMOF-DM1, (d) DMOF-DM2, (e) DMOF-TM1, (f) DMOF-TM2, and (g) DMOF-TF. Hydrogen atoms are omitted for clarity.

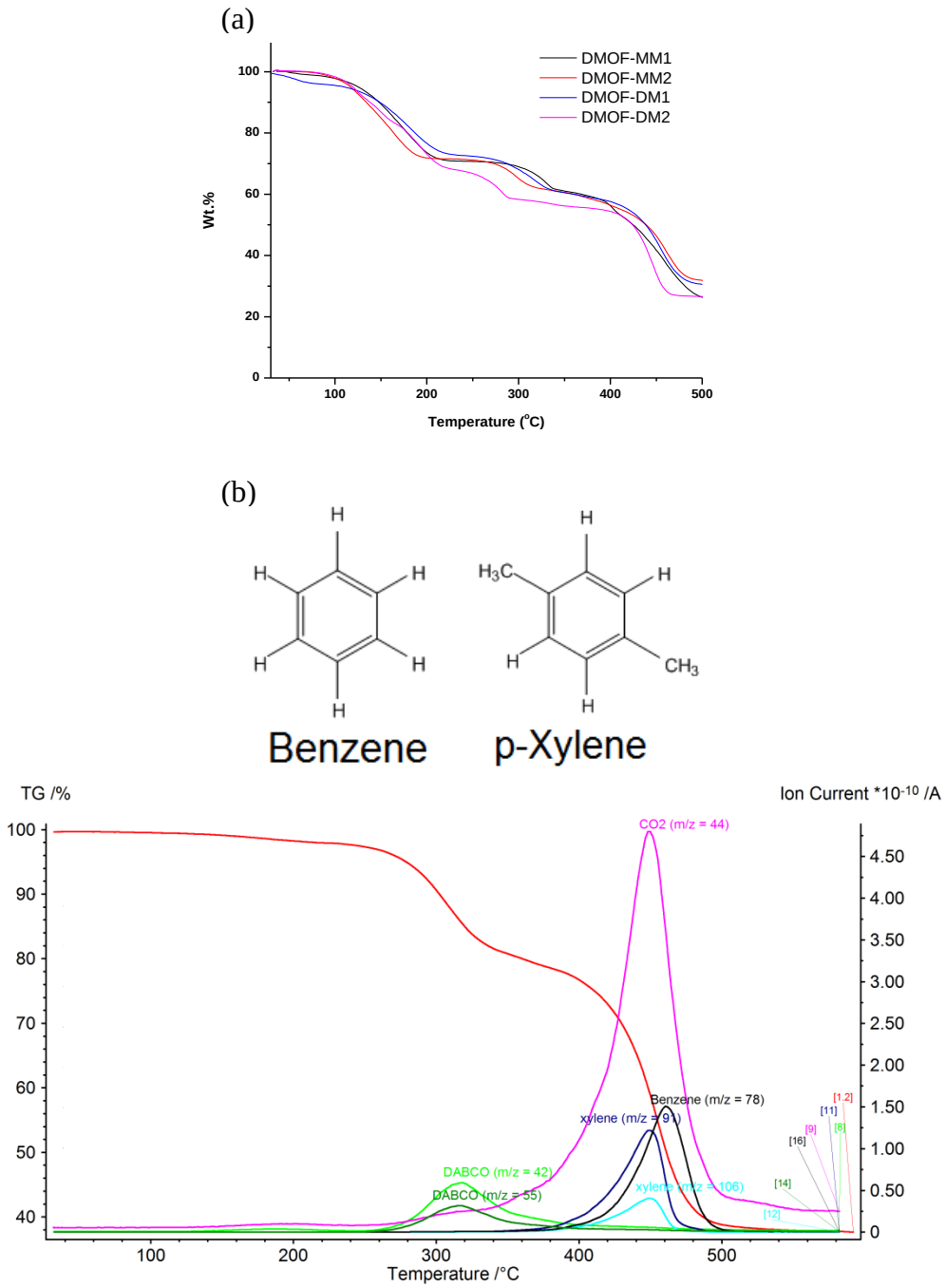

Figure 4.5 (a) TGA curve of newly synthesized DMOF-X (X = MM1, MM2, DM1, DM2) in helium flux (top) and (b) MS signal of carbon dioxide (at m/z value of 44), DABCO (m/z value of 42, 55), benzene (at m/z value of 78), and p-xylene (at m/z value of 91, 106) along the TGA experiment on the *activated* DMOF-DM1.

To confirm that DMOF-DM1 consists of both BDC and DMBDC, we performed TGA experiments on the activated sample of DMOF-DM1 followed by mass spectrometric (MS) analysis (Figure 4.5b). Around the decomposition temperature of DMOF-DM1, we first see the MS signal appear at m/z values of 42 and 55 due to DABCO, followed by CO_2 (at m/z value of 44), benzene (at m/z value of 78), and p-xylene (at m/z value of 91, 106). This suggests bond cleavage between the DABCO ligand and the SBU as well as cleavage of the bond of terminal carboxyl groups with both benzene and p-xylene rings. Quantitative confirmation that only half of the BDC ligands in DMOF-DM1 contain dimethyl functionality was obtained using ^{1}H NMR measurements on the activated DMOF-DM1 sample (Figure 4.8). Similar logic was given by Chun et al.[45] to confirm the successful synthesis of DMOF-TM1.

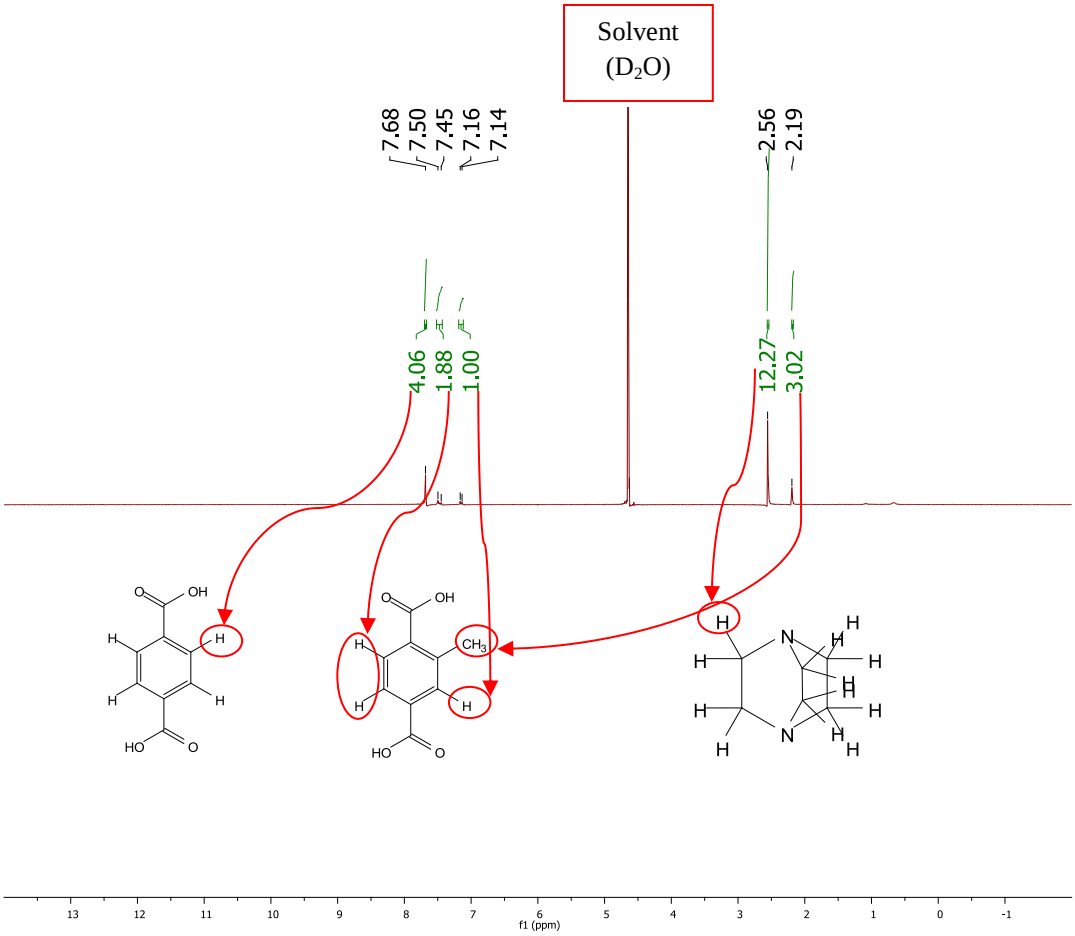

Figure 4.6 NMR spectrum of activated DMOF-MM1 (values labeled in green color are the areas under the peaks (positions labeled in black) corresponding to different types of ^{1}H present).

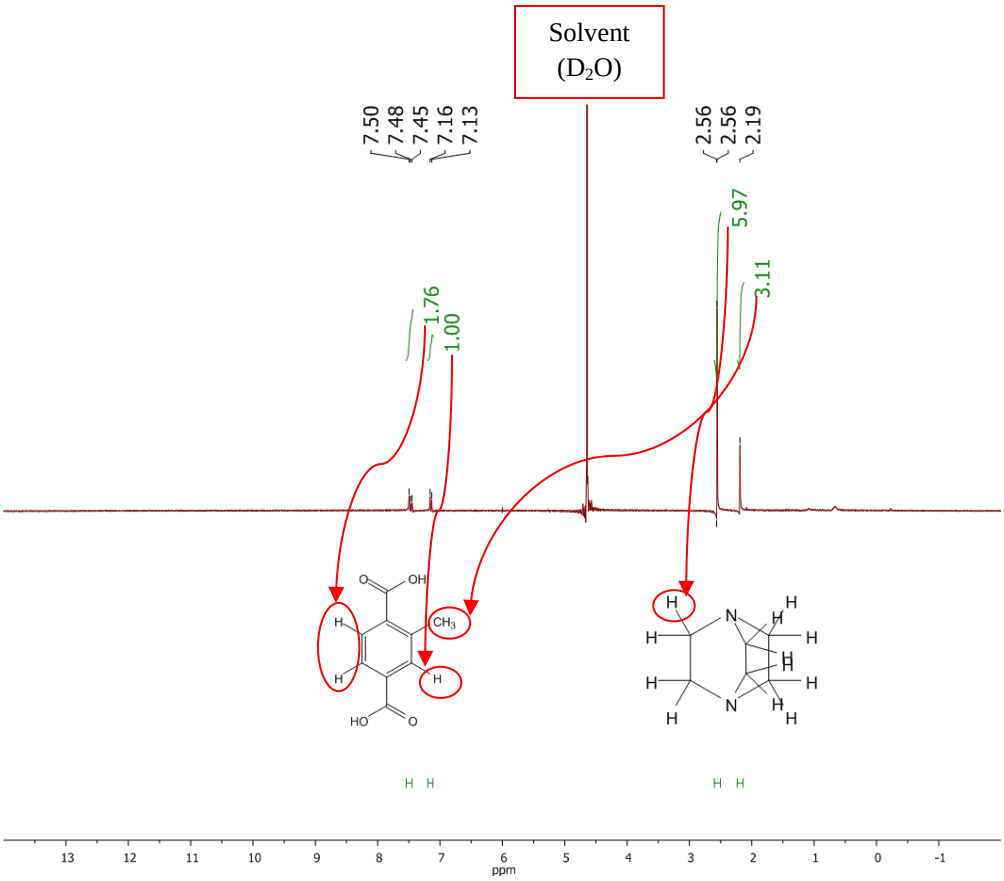

Figure 4.7 NMR spectrum of activated DMOF-MM2 (values labeled in green color are the areas under the peaks (positions labeled in black) corresponding to different types of ^{1}H present).

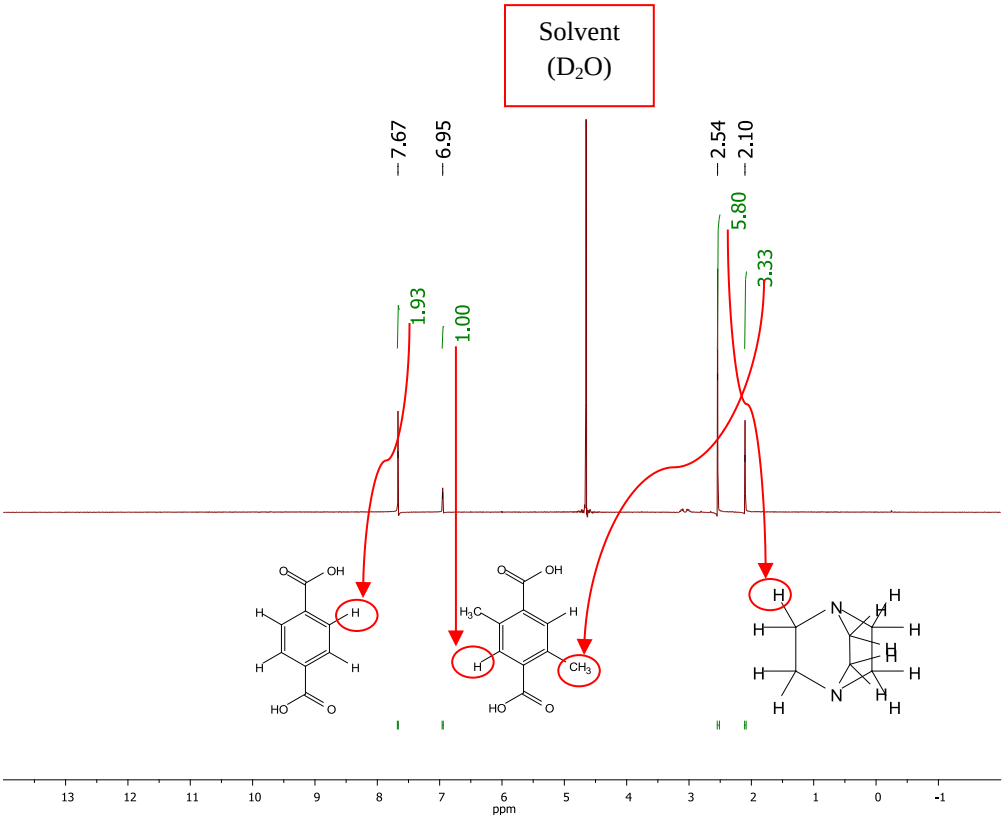

Figure 4.8 NMR spectrum of activated DMOF-DM1 (values labeled in green color are the areas under the peaks (positions labeled in black) corresponding to different types of ^{1}H present).

We could not obtain good quality single crystals for DMOF-MM1 and DMOF-MM2, so we again used ^{1}H NMR to confirm their successful synthesis (Figures 4.6-4.7). TGA analyses of the as-synthesized samples of DMOFs-MM1, -MM2, -DM1, and -DM2 show that they all decompose in the 250-300 ^{o}C range (Figure 4.5a, Table 4.3), similar to the parent material.[52] Comparison of PXRD patterns (Figure 4.3) of these newly synthesized MOFs with simulated pattern of DMOF also confirm that these MOFs belong to the same isostructural family as DMOF-TM1, DMOF-TM2, and DMOF-TF, which were reported by Chun et al.[45]

The purity of all the synthesized samples can be confirmed by comparing PXRD patterns of as-synthesized MOF samples with patterns simulated from their single-crystal

structures (Appendix B, Figures B.1-B.7). Since we could not obtain single-crystal structures for DMOF-MM1, and MM2, we used simulated patterns of isostructural MOFs: DMOF-TM1, and TM2. As expected, N_2 adsorption measurements (Appendix B, Figures B.8-B.14) at 77 K on the activated MOF samples show that a higher degree of functionalization leads to a reduction in porosity (Table 4.4) compared to the parent MOF. These nitrogen isotherms showed typical Type I behavior according to the IUPAC classification.[9]

Table 4.4 Comparison of Properties of Isostructural Pillared MOFs

Material	Pore Volume[†] (cm^3/g)	Pore Diameter (c, a, b) (Å)	Surface Area[a] (m^2/g) Before	After[b]	% Loss
[24]DMOF	0.75	[‡]7.5x7.5,4.8x3.2,4.8x3.2	1980	7	100
DMOF-MM1	0.76	< 7.5x7.5,4.8x3.2,4.8x3.2	1856	14	99
DMOF-MM2	0.72	< 7.5x7.5,4.8x3.2,4.8x3.2	1686	7	100
DMOF-DM1	0.61	5.84-7.5, -, -	1494	40	97
DMOF-DM2	0.51	5.84, -, -	1115	14	99
DMOF-TM1	0.53	[‡]3.5-7.5, -, -	1210	822	32
DMOF-TM2	0.51	[‡]3.5, -, -	1050	1050	0
DMOF-TF	0.45	[‡]6, -, -	1205	1	100

[†]Obtained from the Dubinin-Astakov model of N_2 adsorption at 77K
[‡]Obtained from literature[24,45]
[a]BET Analysis[46]
[b]After 90% RH exposure

4.3.2 Structural Stability under Humid Conditions

4.3.2.1 Water Isotherms, PXRD Patterns, and Surface Areas

Water vapor adsorption isotherm behavior, along with PXRD patterns and BET surface areas before and after water exposure (up to 90% RH), were used to investigate the stability of this isostructural series under humid conditions. The observed trends in water stability indicate that the stability of structures in this series is directly related to the number and placement of methyl groups on the BDC ligand. The water stability characteristics of these MOFs can be put into three different classifications: fully stable (DMOF-TM2), partially stable (DMOF-TM1), and unstable (all remaining structures). Table 4.4 shows key structural properties, along with BET surface areas before and after water exposure, for all the different structures. Water isotherms are shown in Figure 4.9, and PXRD patterns before and after water exposure for the fully stable DMOF-TM2, the partially stable DMOF-TM1, and the unstable DMOF-DM2 structure (representative of all unstable MOFs in this study) are shown in Figure 4.10. PXRD patterns and adsorption isotherms for rest of the structures in the series can be found in the Figures 4.11-4.14. In general, adsorption capacities at saturation are dictated by the accessible pore volume. However, this trend breaks down for materials that degrade under the adsorption conditions. Thus, the fully stable DMOF-TM2 undergoes complete pore-filling, while the partially stable DMOF-TM1 adsorbs appreciable amounts of water but does not reach the high loadings expected from the pore volume due to the collapse of the structure at high RH. On the other hand, the completely unstable DMOF-DM2 displays adsorption behavior that is similar to the also unstable parent DMOF.

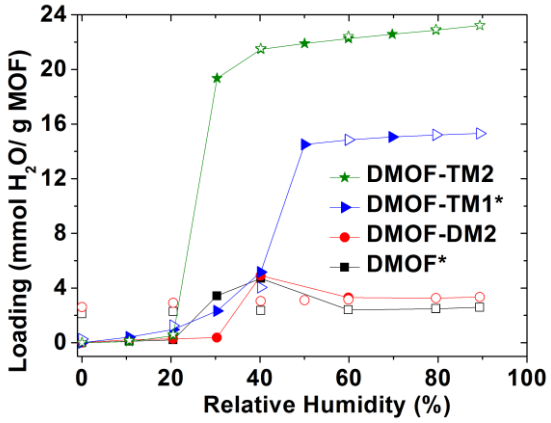

Figure 4.9 Water vapor adsorption isotherms at 298K and 1 bar for fully stable (DMOF-TM2), partially stable (DMOF-TM1), and a representative unstable (DMOF-DM2) structure (closed symbols – adsorption, open symbols – desorption). Lines connecting the adsorption points are to guide the eye. *Reported from our previous work.[24,44]

In our previous study[44] DMOF-TM2 showed no loss of surface area or change in crystallinity after prolonged exposure to humid conditions. In the current work, the cyclic stability of this MOF was examined by performing three cycles of water vapor adsorption/desorption measurements on the sample. As shown in Figure 4.15a, no hysteresis or change in adsorption properties is observed throughout the cyclic adsorption measurements. PXRD patterns (Figure 4.15b) and BET surface area show no change in the crystal structure even after three adsorption/desorption cycles. Moreover, DMOF-TM2 is stable (Figure 4.15c) even after ageing for approximately one year. Given the complete loss of crystallinity and surface area for the parent DMOF structure,[24] the stability of this functionalized variation after high water uptake is remarkable; only a few structures, such as UiO-66 and members of the MIL series of materials, are reported to exhibit such stability after adsorbing large amounts of water.[24,30,32-33] MOF-74 materials were also shown to be completely stable during cyclic dehydration/rehydration

experiments by Dietzel and co-workers. However, it was possible only under inert environment (Ar/ N_2).[53-54] For example, Ni-MOF-74 was reported to decompose in the presence of air during identical testing.[55] Similarly, Schoenecker et al.[24] also found that Mg-MOF-74 decomposes upon exposure to air with 90% RH in the first adsorption/desorption cycle.

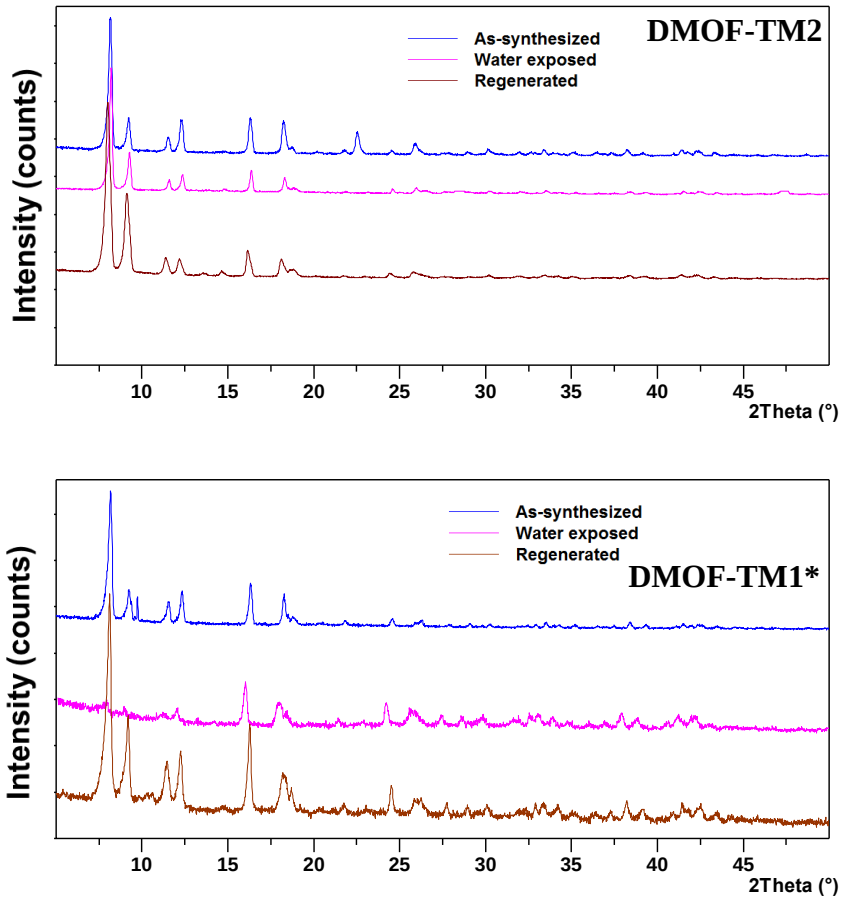

Figure 4.10 Change in PXRD patterns before and after water exposure (up to 90% RH) for fully stable (DMOF-TM2, top), partially stable (DMOF-TM1, middle), and a representative unstable (DMOF-DM2, bottom) structure. *Reported from our previous work.[44]

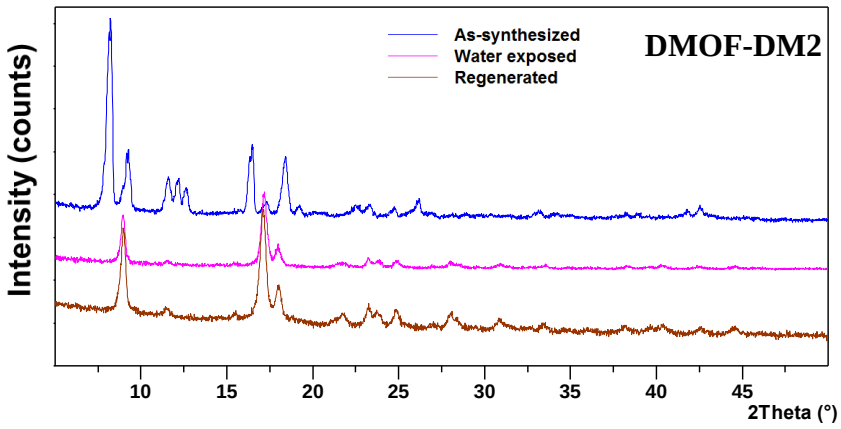

Figure 4.10 Continued.

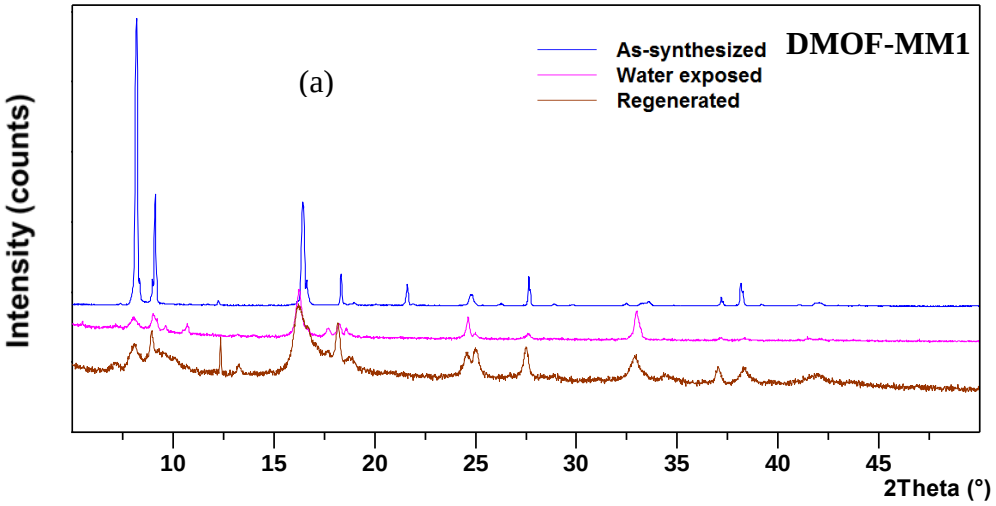

Figure 4.11 PXRD patterns for as-synthesized, water-exposed (up to 90% RH), and regenerated a) DMOF-MM1 (top) and b) DMOF-MM2 (bottom).

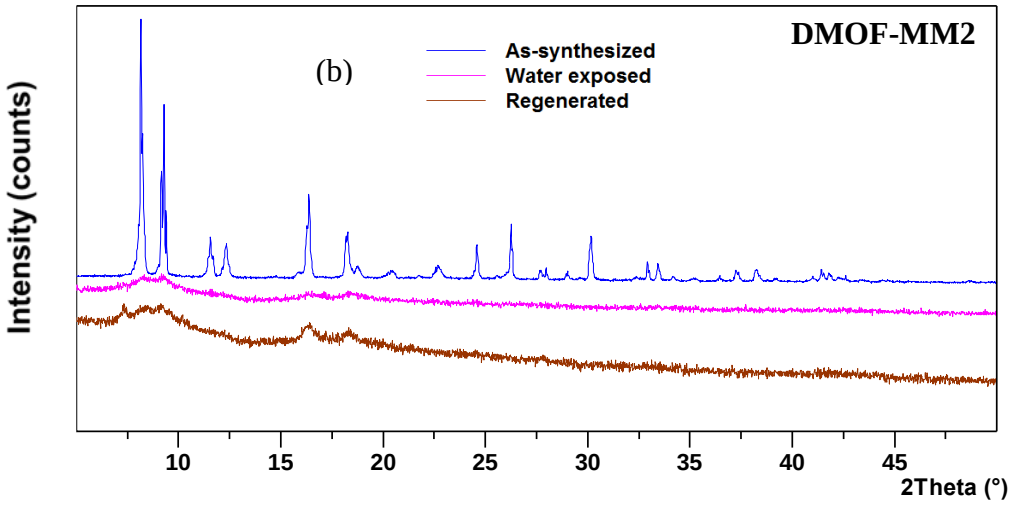

Figure 4.11 Continued.

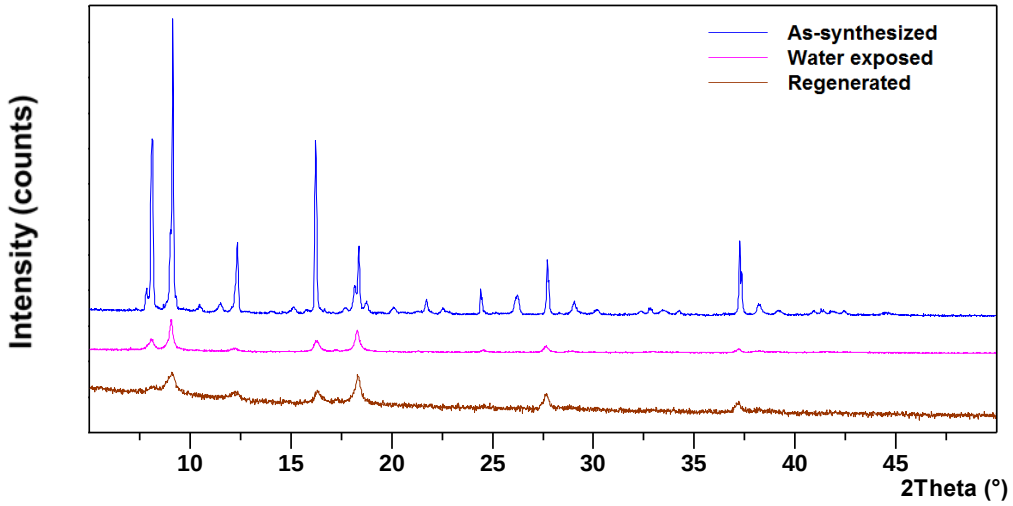

Figure 4.12 PXRD patterns for as-synthesized, water-exposed (up to 90% RH), and regenerated DMOF-DM1.

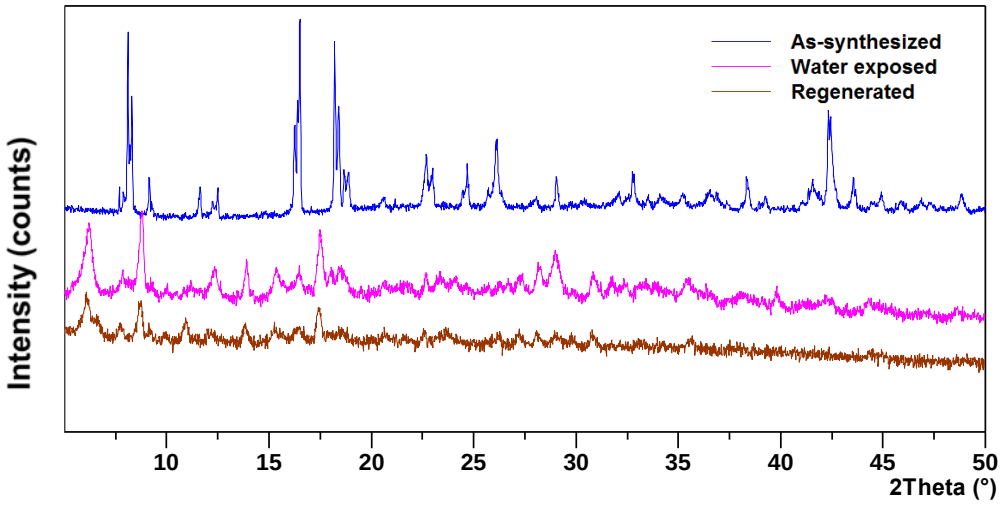

Figure 4.13 PXRD patterns for as-synthesized, water-exposed (up to 90% RH), and regenerated DMOF-TF.

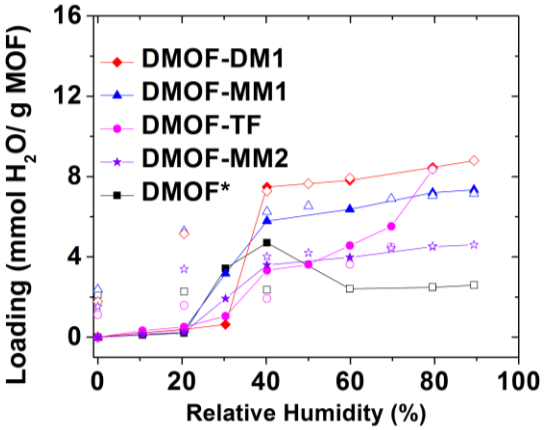

Figure 4.14 Water vapor adsorption isotherms at 298K and 1 bar for unstable MOFs: DMOF-DM1, DMOF-MM1, DMOF-TF, DMOF-MM2, and DMOF. *Reported from our previous work[24]

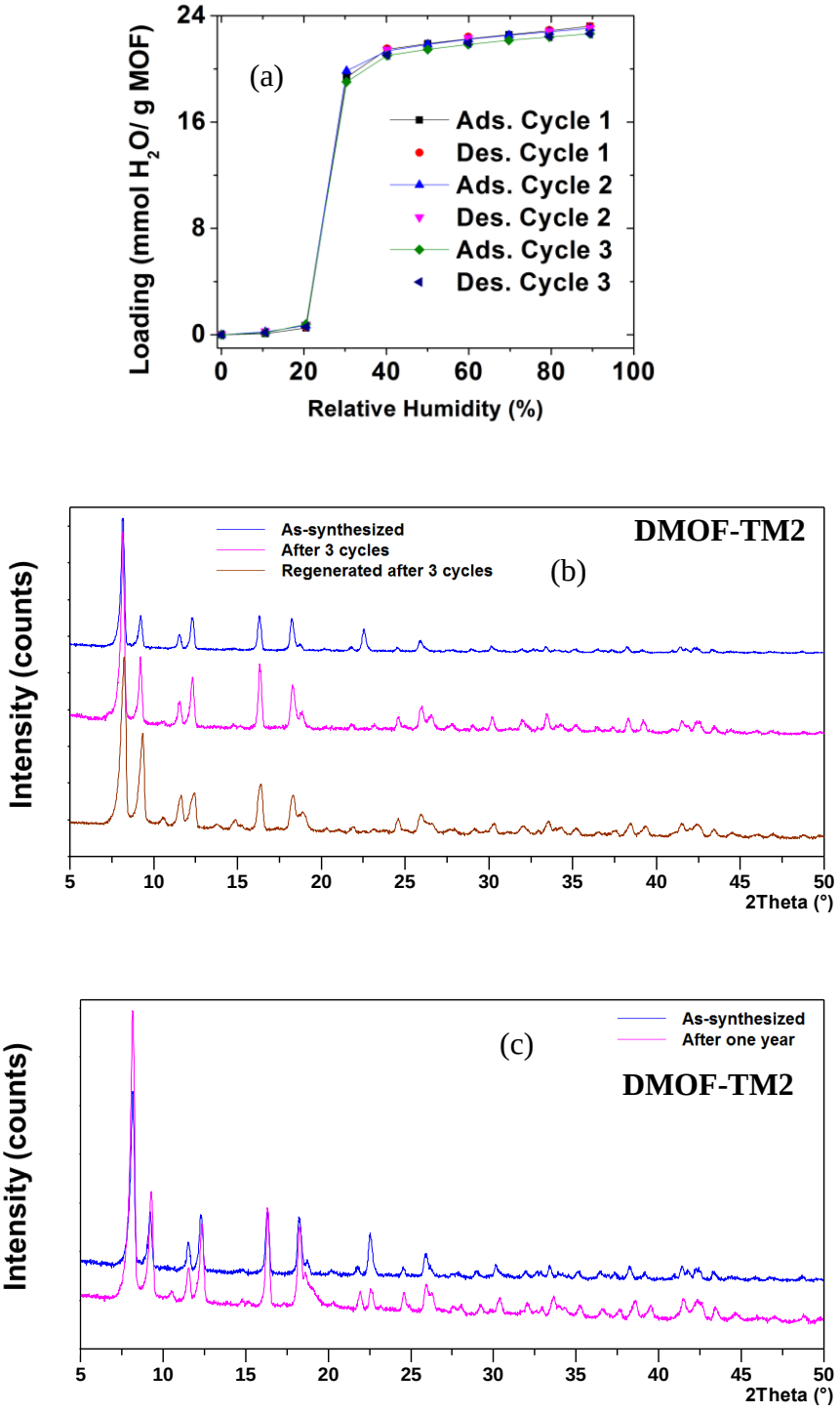

Figure 4.15 (a) Cyclic water vapor adsorption isotherms at 298K and 1 bar for DMOF-TM2. Lines connecting the adsorption points are to guide the eye, (b) change in PXRD pattern before and after cyclic water vapor adsorption measurements (up to 90% RH) for this MOF, (c) change in PXRD pattern after ageing of DMOF-TM2 for one year, and (d) change in PXRD pattern upon soaking DMOF-TM2 in liquid water.

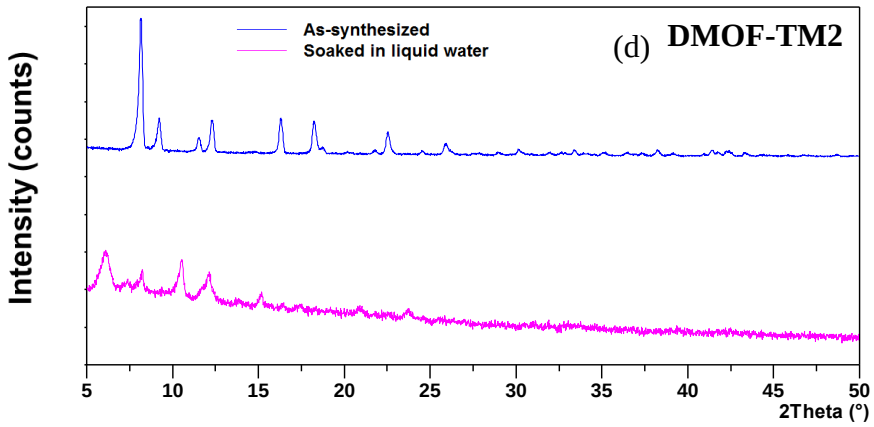

Figure 4.15 Continued.

Interestingly, the DMOF-TM1 structure, containing equal amounts of the tetramethyl and unfunctionalized variations of BDC, was the only partially stable MOF identified in this series. For this structure, the same type V adsorption behavior found in DMOF-TM2 was observed during the vapor adsorption isotherm; however, the loss of BET surface area (~30%) and crystallinity (Figure 4.10) after water adsorption measurements indicate that the structure does not have the same structural stability as the DMOF-TM2 variation under humid conditions. Furthermore, despite the greater pore volume of the DMOF-TM1 structure, it has a lower saturation uptake than the DMOF-TM2 structure as well. These findings highlight the importance of the tetramethyl BDC ligand in providing stability in these structures. While a 50:50 ratio of the tetramethyl BDC and BDC ligands is enough to create a partially stable MOF, only through full ligand incorporation of the tetramethyl can complete stability be achieved. In contrast, the DMOF-DM2 structure contains the same relative number of methyl groups per unit cell as DMOF-TM1 yet, as discussed in the following section, is found to be completely

unstable in the presence of water (Figures 4.9 and 4.10). This further suggests that the number of non-polar groups alone is not enough to dictate water stability; instead, the precise placement of methyl groups on the BDC ligand is critically important to the water stability. Ma et al.[15] also observed a similar trend, however, in their publication the pillar ligand (BPY) was modified rather than the carboxylate ligand (BDC).

All of the remaining structures were found to be fully unstable after 90% RH exposure. These structures, containing varying amounts of non-polar (MM1, MM2, DM1, DM2) and polar (fluorine) functional groups on the BDC ligand, exhibited significant structural decay in the presence of humid conditions. This is indicated by both the shape of their adsorption isotherms (leveling off well below their expected saturation uptakes values) and the complete loss of crystallinity and surface area observed during their subsequent characterization after water adsorption. Furthermore, the residual water content present in these structures after complete desorption to 0% RH conditions suggests that all the water adsorbed in the structures is not physisorbed and, instead, some fraction participates in irreversible hydrolysis reactions with the zinc metal in the structure. Notably, it was found that DMOF-TF, a functionalized structure with full incorporation of polar, fluorine groups through the tetrafluoro-BDC ligand, also did not result in the same improvement in water stability as the DMOF-TM2 variation. This suggests that greater shielding due to the larger van der Waals radii of fluorine and methyl groups (1.5Å and 2.0Å) versus that of hydrogen (1.3 Å) is not the only factor contributing to water stability and, factors such as the polarity of the functional groups must also be considered. In previous work,[44] we showed the same water instability is present for other members of the isostructural DMOF family containing larger, polar

functional groups such as $–NO_2$ and –OH, but these groups were present on a single aromatic carbon while the fluoro groups functionalize all four sites in this work. Molecular insight into why this is the case is further explored in the computational results section.

4.3.2.2 Kinetic versus Thermodynamic Stability

In order to understand the water stability trends in this series of MOFs it is important first to discern whether thermodynamic or kinetic stability trends are what govern the behavior of these structures. While a MOF that is thermodynamically stable in the presence of water is such because the change in free energy ($\Delta G°$) of a hydrolysis reaction is not favored, in kinetically stable MOFs, the stability instead relies on there being a sufficiently high activation energy barrier (E_a) for the hydrolysis reaction. As mentioned earlier, the strength of Lewis acid-base interactions can be used to rationalize thermodynamic stability trends whereas other, more complex structural considerations are needed to understand the activation energy barrier for kinetically governed ligand displacement reactions to occur.

To ensure we are investigating the correct phenomena in our series of MOFs, experiments were performed on these structures to confirm the observed breakdown mechanisms were purely kinetic in nature. The first evidence of the purely kinetic stability in these MOFs came from immersing the DMOF-TM2 structure in liquid water at room temperature. Subsequent structural analysis after liquid water exposure indicated a complete loss of crystallinity (Figure 4.15d). Secondly, the trends in water stability observed in the different MOF structures were compared to the predicted thermodynamic stability based on the pK_a of the different BDC ligands (Table 4.5). If the trends were

thermodynamic in nature, one would expect the stability trends to correlate directly with ligand pK_a; on the contrary, the cyclically stable DMOF-TM2 (TMBDC, pK_a = 3.80) and partially stable DMOF-TM1 (TMBDC, pK_a = 3.80 and BDC, pK_a = 3.73) structures contain ligands with pK_a values that are similar to the remaining unstable MOFs grafted with non-polar groups (pK_a = 3.73-3.77), indicating that there is no correlation between expected thermodynamic stability trends and our observed trends in water stability.

Table 4.5 Comparison of pKa Values[37] of Functionalized BDC Ligands in Isostructural Pillared MOFs (DMOF-X)

MOF	**Carboxylate Ligand**	**pK_a**
DMOF	BDC	3.73
DMOF-MM2	MMBDC	*3.76
DMOF-DM2	DMBDC	3.77
DMOF-TM2	TMBDC	3.80
DMOF-MM1	BDC, MMBDC	3.73, *3.76
DMOF-DM1	BDC, DMBDC	3.73, 3.77
DMOF-TM1	BDC, TMBDC	3.73, 3.80
DMOF-TF	TFBDC	1.42

*average of two pKa values arising due to asymmetry of mono functionalization

4.3.2.3 Computational Results

In order for a ligand displacement hydrolysis reaction to occur between the nucleophilic oxygen on a water molecule (denoted O_w) and an electrophilic zinc (Zn), two molecular events must occur. Firstly, the adsorbed water molecules must come close enough to the Zn metal to allow significant interaction to occur between the Zn and O_w electron orbitals and, secondly, the energetics of this interaction must be such that the kinetic barrier to a ligand substitution reaction can be overcome. The first event, dealing with the proximity of O_w and Zn within a structure, can be addressed through classical molecular dynamics simulations whereas the second question, dealing with the kinetic barriers to reaction, can only be addressed through a more detailed quantum mechanical description of the system.

To investigate the first question, classical Monte Carlo simulations with the Tip4p-Ew water model were run in the DMOF, DMOF-TF and DMOF-TM2 structures. These structures were chosen for the simulations as they represent both stable (DMOF-TM2) and unstable (DMOF, DMOF-TF) structures with no shielding (DMOF), shielding via polar groups (DMOF-TF), and shielding via non-polar groups (DMOF-TM2). Simulations were run under the approximate loadings present in the DMOF at the onset of structural breakdown, as indicated by the change in shape of the DMOF adsorption isotherm (occurring at ~4.6 mol/kg water loading). The accurate prediction of bond breakage and formation using classical simulations is especially difficult, given the generic nature of classical force fields. Thus, the goal of these simulations was not to capture ligand substitution events occurring in the system, but instead to provide insight into any differences in water behavior present in the DMOF-TM2 vs. DMOF and DMOF-

TF structures that make the former structure stable and the latter structures unstable. An investigation into the partial stability of the DMOF-TM1 structure would also be of interest but, given the large disorder present in the experimental CIF for this structure, it is impossible to assign locations to the 50% TMBDC and 50% BDC ligands present in the structure.

(a)

(b)

(c)

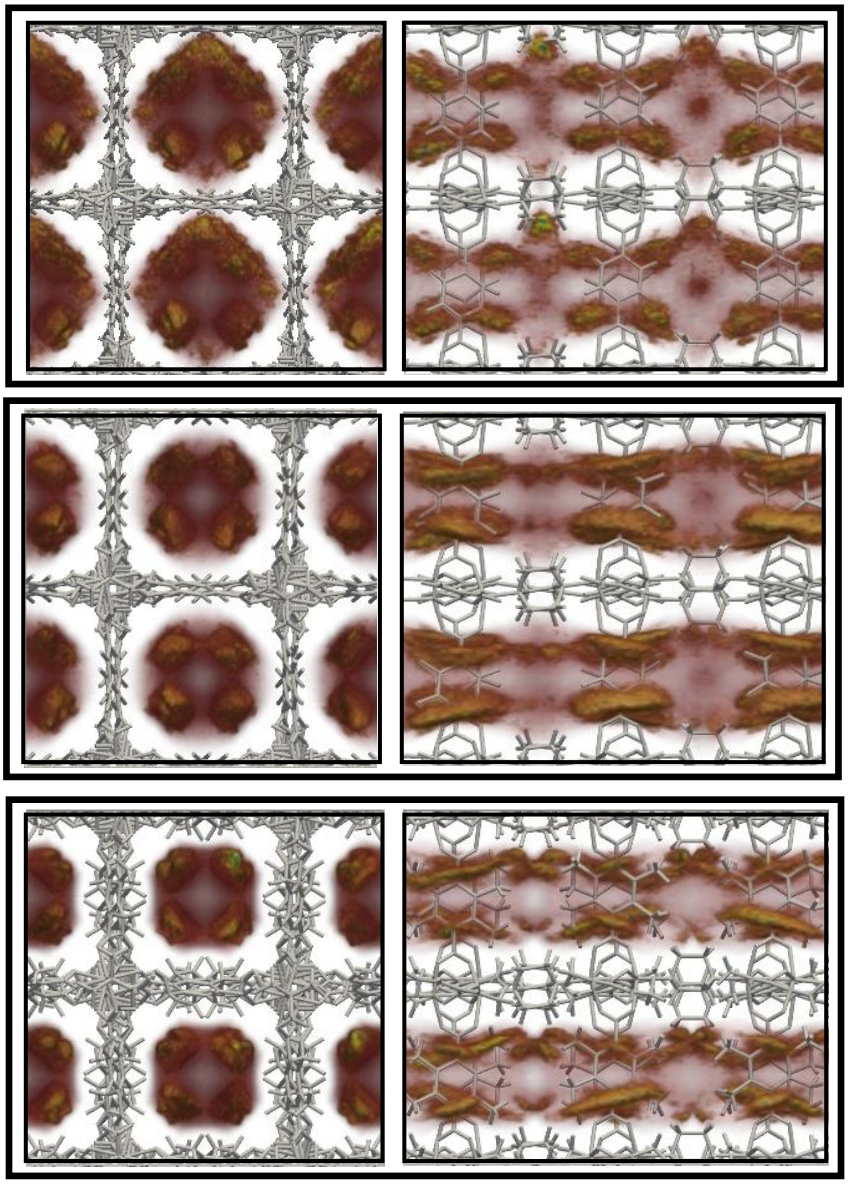

Figure 4.16 Water density distributions for DMOF (a), DMOF-TF (b), and DMOF-TM2 (c) structures shown in the c-direction (left) and a-direction (right).

Figure 4.16 shows the water density distributions obtained from these simulations. The pronounced difference in water confinement within the pores, evident from the density distributions shown in the c-direction, provides important insight into the observed differences in kinetic water stability within these systems. While the frameworks were treated as rigid in these simulations, the parent DMOF-1 is known to be weakly flexible and, in the presence of adsorbates such as benzene and isopropyl alcohol,[43,56] reported to exhibit breathing behavior. In the case of isopropyl alcohol, hydrogen bonding interactions between the OH group on the adsorbate and the oxygen atoms on the BDC ligand were shown to induce a structural transformation from the native wide pore conformation to a narrow pore conformation in the framework.[57] As a result, it is expected that the water molecules near the BDC ligand present in the DMOF and, to a lesser degree, DMOF-TF structures would cause the same structural transformation to occur. The result of this breathing behavior, depicted in Figure 4.17, is the likely explanation for the poor structural stability in DMOF and DMOF-TF (along with the other unstable MOFs observed in this study). After this structural change occurs, water is able to come much closer to the zinc hydrolysis sites located at the pore corners with greater than 90° angles. It is important to note that, while this same breathing behavior was observed in the parent DMOF structure during isopropyl adsorption, no alcoholysis reaction was observed because of the weaker nucleophilicity of this adsorbate relative to water (due to steric effects). In the case of DMOF-TM2, the structure is fully stable because no water molecules are able to come close enough to the BDC ligand to participate in hydrogen bonding interactions (due to shielding effects from the non-polar methyl groups).

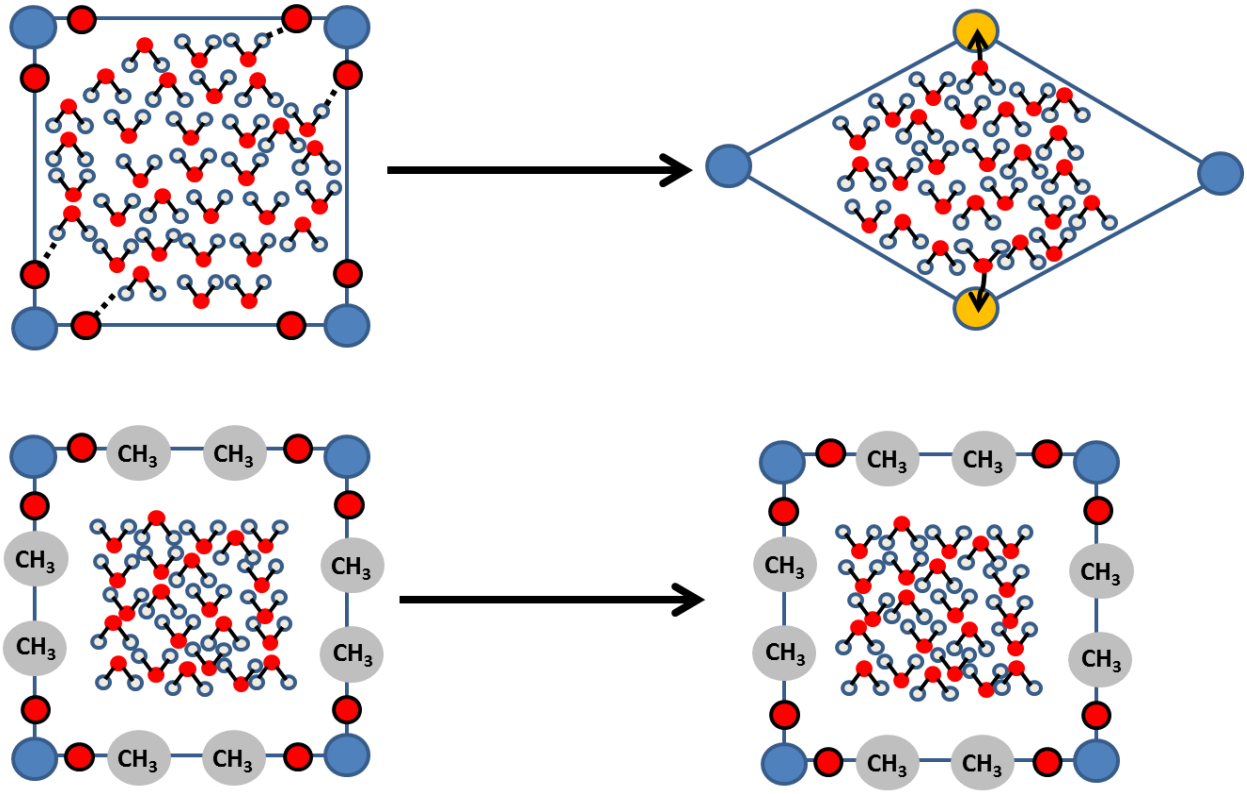

Figure 4.17 Schematic of likely structural transformations, shown in the c-direction, for DMOF and DMOF-TM2 structures in the presence of water. The large red circles depict carboxylate oxygens, small red and white circles portray oxygen and hydrogen atoms in water, respectively, and large blue circles represent stable Zn clusters. The large yellow circles denote Zn clusters that will be prone to hydrolysis.

In order to investigate the second prerequisite to a ligand displacement reaction, dealing with the activation energy barrier to reaction once water is sufficiently close to a zinc atom, quantum mechanical calculations were performed on chemical clusters that are representative of the DMOF and DMOF-TM2 structures. This technique, similar to the approach used by Low et al.,[19] assumes that the behavior of a truncated MOF cluster is representative of the behavior observed in the true periodic system. Figure 4.18 shows the reactants and products of two possible ligand displacement mechanisms involving the

interaction of a single water molecule with zinc to displace either the BDC or DABCO ligand. Interestingly, these calculations failed to qualitatively capture the experimentally observed trends in kinetic water stability in the system. While the barrier to a displacement reaction involving DABCO was found to be much higher (~2-3x) than the barrier associated with BDC, the trends in activation energy for the BDC ligand in DMOF (15.8 kcal/mol) versus DMOF-TM2 (9.1 kcal/mol) followed trends that were opposite of what was expected from experiment. The deficiencies of a clustering approach in finding appropriate activation energies in MOF systems is noteworthy, and suggests that more detailed, periodic treatments of such systems are necessary in order determine accurate kinetics information in MOFs. The likely reason for these discrepancies arise from the unphysical dynamics that are introduced when treating crystalline structures as non-periodic clusters; without the structural constraints arising from the interconnected metal clusters in truly periodic systems, clusters are able to achieve bending and torsion angles during hydrolysis reactions that would be highly unphysical in the real system. Furthermore, the sterics of the adjacent methyl groups present in the periodic DMOF-TM2 system would also create large energetic penalties to a ligand displacement reaction that are not captured in the consideration of only one isolated cluster.

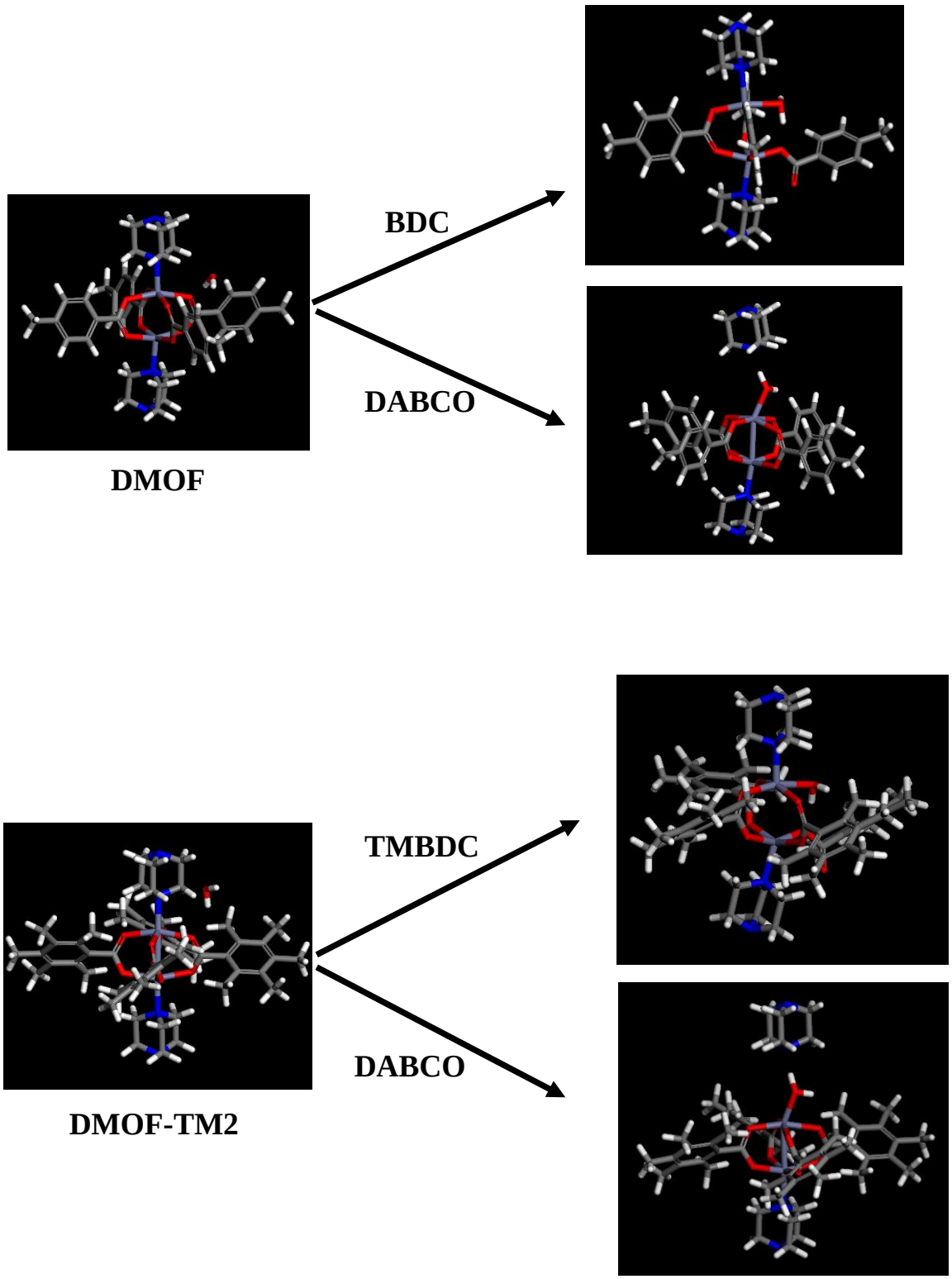

Figure 4.18 Product and reactant clusters used in quantum mechanical calculations for determining barriers to the ligand displacement reactions involving BDC and DABCO in the DMOF and DMOF-TM2 structures.

4.4. Conclusions

In this work, we have carried out a systematic study into the effects of ligand functionalization on the water stability of a series of isostructural MOFs of the family $Zn(BDC\text{-}X)(DABCO)_{0.5}$. We shed light on the important distinction between kinetic and thermodynamic water stability and provide experimental evidence for a kinetically governed water stability mechanism in these MOFs. In this case, the full incorporation of non-polar methyl groups is critical to promoting the cyclic stability in this series. As such, we show that the kinetically unstable parent structure can be made cyclically stable in the presence of humid conditions through the incorporation tetramethyl-BDC ligand. Given the large water uptake in this methyl functionalized structure, we show that the water stability improvement in this MOF is not due to the exclusion of water from entering the pores of the MOF. Through molecular simulations we show that the reason for the improvement in kinetic stability is due to shielding of the carboxylate oxygen in the DMOF-TM2 structure, which prevents hydrogen bonding interactions and subsequent structural transformations from occurring. As a result, the electrophilic zinc atoms in this structure are inaccessible to the nucleophilic oxygen atoms in water, thus preventing any ligand displacement hydrolysis reactions from occurring. This systematic study provides initial insight into important structural factors that are important for the development of next-generation, water stable metal-organic frameworks.

4.5 References

(1) Zhou, H. C.; Long, J. R.; Yaghi, O. M., Introduction to Metal–Organic Frameworks. *Chem. Rev.* **2012,** 112 (2), 673-674.

(2) Rowsell, J. L. C.; Yaghi, O. M., Effects of functionalization, catenation, and variation of the metal oxide and organic linking units on the low-pressure hydrogen adsorption properties of metal-organic frameworks. *J. Am. Chem. Soc.* **2006,** *128* (4), 1304-1315.

(3) Cook, T. R.; Zheng, Y.-R.; Stang, P. J., Metal–Organic Frameworks and Self-Assembled Supramolecular Coordination Complexes: Comparing and Contrasting the Design, Synthesis, and Functionality of Metal–Organic Materials. *Chem. Rev.* **2012,** (DOI: 10.1021/cr3002824).

(4) Farha, O. K.; Hupp, J. T., Rational Design, Synthesis, Purification, and Activation of Metal-Organic Framework Materials. *Acc. Chem. Res.* **2010,** *43* (8), 1166-1175.

(5) Tanabe, K. K.; Cohen, S. M., Postsynthetic modification of metal-organic frameworks-a progress report. *Chem. Soc. Rev.* **2011,** *40* (2), 498-519.

(6) Eddaoudi, M.; Kim, J.; Rosi, N.; Vodak, D.; Wachter, J.; O'Keeffe, M.; Yaghi, O. M., Systematic design of pore size and functionality in isoreticular MOFs and their application in methane storage. *Science* **2002,** *295* (5554), 469-472.

(7) Ferey, G., Some suggested perspectives for multifunctional hybrid porous solids. *Dalton Trans.* **2009,** (23), 4400-4415.

(8) Kuppler, R. J.; Timmons, D. J.; Fang, Q. R.; Li, J. R.; Makal, T. A.; Young, M. D.; Yuan, D. Q.; Zhao, D.; Zhuang, W. J.; Zhou, H. C., Potential applications of metal-organic frameworks. *Coord. Chem. Rev.* **2009,** *253* (23-24), 3042-3066.

(9) Kitagawa, S.; Kitaura, R.; Noro, S., Functional porous coordination polymers. *Angew. Chem.-Int. Edit.* **2004,** *43* (18), 2334-2375.

(10) Sumida, K.; Rogow, D. L.; Mason, J. A.; McDonald, T. M.; Bloch, E. D.; Herm, Z. R.; Bae, T.-H.; Long, J. R., Carbon Dioxide Capture in Metal–Organic Frameworks. Chem. Rev. **2011,** 112 (2), 724-781..

(11) Li, J.-R.; Kuppler, R. J.; Zhou, H.-C., Selective gas adsorption and separation in metal-organic frameworks. *Chem. Soc. Rev.* **2009,** *38* (5), 1477-1504.

(12) Karra, J. R.; Walton, K. S., Effect of open metal sites on adsorption of polar and nonpolar molecules in metal-organic framework Cu-BTC. *Langmuir* **2008,** *24* (16), 8620-8626.

(13) Mueller, U.; Schubert, M.; Teich, F.; Puetter, H.; Schierle-Arndt, K.; Pastre, J., Metal-organic frameworks - prospective industrial applications. *J. Mater. Chem.* **2006,** *16* (7), 626-636.

(14) Li, Y.; Yang, R. T., Gas adsorption and storage in metal-organic framework MOF-177. *Langmuir* **2007,** *23* (26), 12937-12944.

(15) Ma, D.; Li, Y.; Li, Z., Tuning the moisture stability of metal-organic frameworks by incorporating hydrophobic functional groups at different positions of ligands. *Chem. Commun.* **2011,** *47* (26), 7377-7379.

(16) Yang, J.; Grzech, A.; Mulder, F. M.; Dingemans, T. J., Methyl modified MOF-5: a water stable hydrogen storage material. *Chem. Commun.* **2011,** *47* (18), 5244-5246.

(17) Choi, H. J.; Dinca, M.; Dailly, A.; Long, J. R., Hydrogen storage in water-stable metal-organic frameworks incorporating 1,3-and 1,4-benzenedipyrazolate. *Energy Environ. Sc.* **2010,** *3* (1), 117-123.

(18) Kaye, S. S.; Dailly, A.; Yaghi, O. M.; Long, J. R., Impact of preparation and handling on the hydrogen storage properties of Zn_4O(1,4-benzenedicarboxylate)$_3$ (MOF-5). *J. Am. Chem. Soc.* **2007,** *129* (46), 14176-+.

(19) Low, J. J.; Benin, A. I.; Jakubczak, P.; Abrahamian, J. F.; Faheem, S. A.; Willis, R. R., Virtual High Throughput Screening Confirmed Experimentally: Porous Coordination Polymer Hydration. *J. Am. Chem. Soc.* **2009,** *131* (43), 15834-15842.

(20) Kang, I. J.; Khan, N. A.; Haque, E.; Jhung, S. H., Chemical and Thermal Stability of Isotypic Metal-Organic Frameworks: Effect of Metal Ions. *Chem. Eur. J.* **2011,** *17* (23), 6437-6442.

(21) Kim, M.; Cohen, S. M., Discovery, development, and functionalization of Zr(IV)-based metal-organic frameworks. *Crystengcomm* **2012,** *14* (12), 4096-4104.

(22) Cavka, J. H.; Jakobsen, S.; Olsbye, U.; Guillou, N.; Lamberti, C.; Bordiga, S.; Lillerud, K. P., A new zirconium inorganic building brick forming metal organic

frameworks with exceptional stability. *J. Am. Chem. Soc.* **2008,** *130* (42), 13850-13851.

(23) Garibay, S. J.; Cohen, S. M., Isoreticular synthesis and modification of frameworks with the UiO-66 topology. *Chem. Commun.* **2010,** *46* (41), 7700-7702.

(24) Schoenecker, P. M.; Carson, C. G.; Jasuja, H.; Flemming, C. J. J.; Walton, K. S., Effect of Water Adsorption on Retention of Structure and Surface Area of Metal–Organic Frameworks. *Ind. Eng. Chem. Res.* **2012,** *51* (18), 6513-6519.

(25) Cychosz, K. A.; Matzger, A. J., Water Stability of Microporous Coordination Polymers and the Adsorption of Pharmaceuticals from Water. *Langmuir* **2010,** *26* (22), 17198-17202.

(26) Greathouse, J. A.; Allendorf, M. D., The interaction of water with MOF-5 simulated by molecular dynamics. *J. Am. Chem. Soc.* **2006,** *128* (33), 10678-10679.

(27) Bellarosa, L.; Calero, S.; Lopez, N., Early stages in the degradation of metal-organic frameworks in liquid water from first-principles molecular dynamics. *Phys. Chem. Chem. Phys.* **2012,** *14* (20), 7240-7245.

(28) Han, S. S.; Choi, S. H.; van Duin, A. C. T., Molecular dynamics simulations of stability of metal-organic frameworks against H_2O using the ReaxFF reactive force field. *Chem. Commun.* **2010,** *46* (31), 5713-5715.

(29) Colombo, V.; Galli, S.; Choi, H. J.; Han, G. D.; Maspero, A.; Palmisano, G.; Masciocchi, N.; Long, J. R., High thermal and chemical stability in pyrazolate-bridged metal-organic frameworks with exposed metal sites. *Chem. Sc.* **2011,** *2* (7), 1311-1319.

(30) Kuesgens, P.; Rose, M.; Senkovska, I.; Froede, H.; Henschel, A.; Siegle, S.; Kaskel, S., Characterization of metal-organic frameworks by water adsorption. *Microporous and Mesoporous Mater.* **2009,** *120* (3), 325-330.

(31) Liang, Z.; Marshall, M.; Chaffee, A. L., CO_2 adsorption, selectivity and water tolerance of pillared-layer metal organic frameworks. *Microporous and Mesoporous Mater.* **2010,** *132* (3), 305-310.

(32) Soubeyrand-Lenoir, E.; Vagner, C.; Yoon, J. W.; Bazin, P.; Ragon, F.; Hwang, Y. K.; Serre, C.; Chang, J.-S.; Llewellyn, P. L., How Water Fosters a Remarkable 5-Fold Increase in Low-Pressure CO_2 Uptake within Mesoporous MIL-100(Fe). *J. Am. Chem. Soc.* **2012,** *134* (24), 10174-10181.

(33) Wiersum, A. D.; Soubeyrand-Lenoir, E.; Yang, Q. Y.; Moulin, B.; Guillerm, V.; Ben Yahia, M.; Bourrelly, S.; Vimont, A.; Miller, S.; Vagner, C.; Daturi, M.; Clet, G.; Serre, C.; Maurin, G.; Llewellyn, P. L., An Evaluation of UiO-66 for Gas-Based Applications. *Chem.- Asian J.* **2011,** *6* (12), 3270-3280.

(34) Valenzano, L.; Civalleri, B.; Chavan, S.; Bordiga, S.; Nilsen, M. H.; Jakobsen, S.; Lillerud, K. P.; Lamberti, C., Disclosing the Complex Structure of UiO-66 Metal Organic Framework: A Synergic Combination of Experiment and Theory. *Chem. Mater.* **2011,** *23* (7), 1700-1718.

(35) Liang, Z.; Marshall, M.; Chaffee, A. L., CO_2 Adsorption-Based Separation by Metal Organic Framework (Cu-BTC) versus Zeolite (13X). *Energy Fuels* **2009,** *23*, 2785-2789.

(36) Mohamed, M. H.; Elsaidi, S. K.; Wojtas, L.; Pham, T.; Forrest, K. A.; Tudor, B.; Space, B.; Zaworotko, M. J., Highly Selective CO_2 Uptake in Uninodal 6-Connected "mmo" Nets Based upon MO_4^{2-} (M = Cr, Mo) Pillars. *J. Am. Chem. Soc.* **2012,** (DOI: 10.1021/ja309452y).

(37) Hilal, S., Karickhoff, S. W., Carreira, L. A. , A Rigorous Test for SPARC's Chemical Reactivity Models: Estimation of More Than 4300 Ionization pKa's. *Quant. Struc. Act. Rel.* **1995,** *14*, 348.

(38) Wu, T.; Shen, L.; Luebbers, M.; Hu, C.; Chen, Q.; Ni, Z.; Masel, R. I., Enhancing the stability of metal-organic frameworks in humid air by incorporating water repellent functional groups. *Chem. Commun.* **2010,** *46* (33).

(39) Nguyen, J. G.; Cohen, S. M., Moisture-Resistant and Superhydrophobic Metal-Organic Frameworks Obtained via Postsynthetic Modification. *J. Am. Chem. Soc.* **2010,** *132* (13), 4560-+.

(40) Cai, Y.; Zhang, Y. D.; Huang, Y. G.; Marder, S. R.; Walton, K. S., Impact of Alkyl-Functionalized BTC on Properties of Copper-Based Metal-Organic Frameworks. *Crys. Growth Des.* **2012,** *12* (7), 3709-3713.

(41) Serre, C., Superhydrophobicity in Highly Fluorinated Porous Metal-Organic Frameworks. *Angew. Chem.-Int. Edit.* **2012,** *51* (25), 6048-6050.

(42) Taylor, J. M.; Vaidhyanathan, R.; Iremonger, S. S.; Shimizu, G. K. H., Enhancing Water Stability of Metal–Organic Frameworks via Phosphonate Monoester Linkers. *J. Am. Chem. So*c. **2012,** 134 (35), 14338-14340.

(43) Dybtsev, D. N.; Chun, H.; Kim, K., Rigid and flexible: A highly porous metal-organic framework with unusual guest-dependent dynamic behavior. *Angew. Chem.-Int. Edit.* **2004,** *43* (38), 5033-5036.

(44) Jasuja, H.; Huang, Y.; Walton, K. S., Adjusting the Stability of Metal-Organic Frameworks under Humid Conditions by Ligand Functionalization. *Langmuir* **2012,** (In press, DOI: 10.1021/la304151r).

(45) Chun, H.; Dybtsev, D. N.; Kim, H.; Kim, K., Synthesis, X-ray Crystal Structures, and Gas Sorption Properties of Pillared Square Grid Nets Based on Paddle-Wheel Motifs: Implications for Hydrogen Storage in Porous Materials. *Chem.–Eur. J.* **2005,** *11* (12), 3521-3529.

(46) Walton, K. S.; Snurr, R. Q., Applicability of the BET method for determining surface areas of microporous metal-organic frameworks. *J. Am. Chem. Soc.* **2007,** *129* (27), 8552-8556.

(47) Blochl, P. E., Projector Augmented-Wave Method. *Phys. Rev. B* **1994,** *50* (24), 17953-17979.

(48) Perdew, J. P.; Burke, K.; Ernzerhof, M., Generalized gradient approximation made simple. *Phys. Rev. Lett.* **1996,** *77* (18), 3865-3868.

(49) Horn, H. W.; Swope, W. C.; Pitera, J. W.; Madura, J. D.; Dick, T. J.; Hura, G. L.; Head-Gordon, T., Development of an improved four-site water model for biomolecular simulations: TIP4P-Ew. *J. Chem. Phys.* **2004,** *120* (20), 9665-9678.

(50) Campana, C.; Mussard, B.; Woo, T. K., Electrostatic Potential Derived Atomic Charges for Periodic Systems Using a Modified Error Functional. *J. Chem. Theory Comput.* **2009,** *5* (10), 2866-2878.

(51) Mayo, S. L.; Olafson, B. D.; Goddard, W. A., DREIDING - A Generic Force-Field For Molecular Simulations. *J. Phys. Chem.* **1990,** *94* (26), 8897-8909.

(52) Lee, J. Y.; Olson, D. H.; Pan, L.; Emge, T. J.; Li, J., Microporous Metal–Organic Frameworks with High Gas Sorption and Separation Capacity. *Adv. Funct. Mater.* **2007,** *17* (8), 1255-1262.

(53) Dietzel, P. D. C.; Morita, Y.; Blom, R.; Fjellvag, H., An in situ high-temperature single-crystal investigation of a dehydrated metal-organic framework compound and field-induced magnetization of one-dimensional metaloxygen chains. *Angew. Chem.-Int. Edit.* **2005,** *44* (39), 6354-6358.

(54) Dietzel, P. D. C.; Blom, R.; Fjellvag, H., Base-induced formation of two magnesium metal-organic framework compounds with a bifunctional tetratopic ligand. *Eur. J. Inorg. Chem.* **2008,** (23), 3624-3632.

(55) Dietzel, P. D. C.; Panella, B.; Hirscher, M.; Blom, R.; Fjellvag, H., Hydrogen adsorption in a nickel based coordination polymer with open metal sites in the cylindrical cavities of the desolvated framework. *Chem. Commun.* **2006,** (9), 959-961.

(56) Uemura, K.; Yamasaki, Y.; Komagawa, Y.; Tanaka, K.; Kita, H., Two-Step Adsorption/Desorption on a Jungle-Gym-Type Porous Coordination Polymer. *Angew. Chem.-Int. Edit.* **2007,** *46* (35), 6662-6665.

(57) Grosch, J. S.; Paesani, F., Molecular-Level Characterization of the Breathing Behavior of the Jungle-Gym-type DMOF-1 Metal-Organic Framework. *J. Am. Chem. Soc.* **2012,** *134* (9), 4207-4215.

CHAPTER 5

EFFECT OF CATENATION AND BASICITY OF PILLARED LIGANDS ON THE WATER STABILITY OF MOFS

5.1 Introduction

Pressure swing adsorption is acknowledged to be one of the most proficient and economic separation processes for CO_2 capture from power plant flue gas and natural gas streams.[1] Traditional porous materials such as zeolites and impregnated carbons are capable of performing these separations with good CO_2 selectivity but are often difficult and costly to regenerate, especially when exposed to humid conditions.[1] Advancements in coordination chemistry have led to the development of a new class of porous structures known as metal-organic frameworks (MOFs). MOFs are constructed by self-assembly of organic ligands and metal oxide clusters. MOFs have garnered significant attention as possible adsorbents for hydrogen or methane storage[2] and have been extensively examined for CO_2 capture from power plant flue gas and natural gas streams.[2f,3] MOFs are promising for these applications due to various features such as high crystallinity, ultralow densities, high surface areas and pore volumes, uniform pore sizes, and chemical functionalities.[3f] The pore sizes and chemical functionalities can be tuned by modifying the metal group or organic linker.[2g,4]

Commercial application of MOFs in air purification, gas separation, storage, and catalysis hinges on their stability in water. The MOF literature has shown that many zinc-

carboxylate MOFs are prone to breakdown in the presence of humid conditions.[5] However, a variety of carboxylate based MOFs such as the MIL materials and UiO-66 family show good structural integrity after water exposure.[6] Nitrogen-coordinated pillared MOFs have also shown better water stability than carboxylate ligand based MOFs,[5b,7] e.g., MOF-5 vs. DMOF.[3g,8] The greater stability of pillared MOFs has been attributed to the higher basicity, i.e., higher pK_a value (Table 5.1) of the pillar ligand (e.g., DABCO, BPY, Figure 5.1) relative to the dicarboxylate ligand (e.g., BDC, TMBDC, Figure 5.1). By this same logic, MOFs based on highly basic pyrazole (pK_a ~19.8)[9] and imidazole (pK_a ~18.6)[9] ligands are found to be stable upon exposure to humid conditions.[5d,5f] This reasoning is further strengthened by the work of Low et al.[7] who found that the strength of the bond between the metal oxide cluster and the bridging linker is important in defining the hydrothermal stability of the MOFs. The metal, being a Lewis acid, will form a stronger bond with the more basic (higher pK_a) ligand.

Table 5.1 Comparison of pKa Values[19] of Ligands Used in Isostructural Pillared MOFs

MOF	Ligand	pKa
DMOF	BDC, DABCO	3.73, 8.86
MOF-508	BDC, BPY	3.73, 4.60
DMOF-TM	TMBDC, DABCO	3.80, 8.86
MOF-508-TM	TMBDC, BPY	3.80, 4.60

Pillared MOFs are solvothermally synthesized by mixing two types of organic ligands, usually aromatic dicarboxylates (e.g., BDC, TMBDC, Figure 5.1) and diamines (e.g., BPY, DABCO, Figure 5.1) with the metal salt. Metal ions and dicarboxylates form

the 2-D sheets while diamines act as pillars connecting the sheets in the third dimension.[3g] MOFs synthesized in this fashion have produced several examples of non-catenated (e.g., DMOF[10]) as well as catenated structures (e.g., MOF-508[11]). Catenation is the interpenetration or interweaving of two or more identical and independent frameworks.[12] Figure 5.2 shows a cartoon representation of non-catenated pillared MOFs (e.g., Zn-TMBDC-BPY[13] synthesized using TMBDC and BPY) and two-fold catenation in pillared layer frameworks (e.g., MOF-508[11] synthesized using BDC and BPY).

An isostructural family of MOFs provides a good test system for evaluating the effect of metal type and coordination state, framework dimensionality, interpenetration, and ligand character on the water stability by enabling the variation of one factor at a time. In previous work (Chapters 3 and 4),[14] we evaluated the effect of water adsorption on the stability of several DMOF variants. We found that functionalizing benzenedicarboxylic acid with four methyl groups results in a MOF that is highly stable under humid conditions up to 90% relative humidity (RH). Notably, this material also maintains its stability after multiple water adsorption/desorption cycles.[14b] This high stability is attributed to effective shielding of the zinc cluster by the methyl groups. In this paper, using four isostructural pillared MOFs from this same family, we evaluate the effect of basicity (pK_a value) of the pillar ligand and catenation in the framework on the water stability of MOFs. We consider two sets of materials for the comparisons. *Set a.* includes the parent DMOF structure[10] [$Zn(BDC)(DABCO)_{0.5}$] and MOF-508[11] [$Zn(BDC)(BPY)_{0.5}$], which has similar topology to DMOF, but the longer diamine linker (BPY) leads to two-fold catenation. *Set b.* includes the tetramethyl versions of the *set a.* materials: DMOF-TM[13] [$Zn(TMBDC)(DABCO)_{0.5}$] and [$Zn(TMBDC)(BPY)_{0.5}$] or

MOF-508-TM,[13] where MOF-508-TM is no longer catenated due to the steric effects introduced by the methyl groups. Each set has two MOFs made up of the same dicarboxylate ligand (Set a. BDC, and Set b. TMBDC) but with pillared ligands (DABCO and BPY) of different basicity. Only MOF-508 has two-fold interpenetration, and it is synthesized with the less basic ligand BPY. Therefore in *set a*. we can evaluate the effect of catenation on water stability, and from *set b.* we can examine the effect of basicity (pK_a value) of the pillar ligand.

5.2 Experimental

5.2.1 Materials

All chemicals were used as received from the following sources: Sigma-Aldrich: N,N′-dimethylformamide (DMF), 4-4' bipyridyl (BPY); Chem Service Inc.: tetra methyl 1,4-benzenedicarboxylic acid (TMBDC); and Acros: 1,4-benzenedicarboxylic acid (BDC), 1,4-diazabicyclo[2.2.2]octane (DABCO), ethanol (EtOH). Ligands used in constructing the MOFs are shown in Figure 5.1 and include 1,4-benzenedicarboxylate (BDC), tetra methyl 1,4-benzenedicarboxylate (TMBDC), 4,4'-bipyridine (BPY), and 1,4-diazabicyclo[2.2.2]octane (DABCO). All the MOFs were synthesized solvothermally.

DMOF. Synthesis of Zn-BDC-DABCO or DMOF was performed as suggested by Wang et. al.[15] for Zn-BDC-NH_2-DABCO. $Zn(NO_3)_2.6H_2O$ (6 mmol) and BDC (6 mmol) were dissolved in DMF (150 mL) and then DABCO (9.63 mmol) was added at room temperature in a glass beaker. The resulting slurry was stirred for 3 hrs. After filtering the white precipitate, the resulting solution was divided equally into 10 glass vials that were then placed in a sand bath and heated in a programmable oven at a rate of 2.5 °C/min from 35–120°C. The temperature was held constant at 120°C for 12 h, and the

oven was then cooled at a rate of 2.5 °C/min to a final temperature of 35°C. The resulting solid was filtered and repeatedly washed with DMF. The resulting brick-shaped colorless crystals obtained after drying were transferred to a vial. The as-synthesized compound was activated at 110^{o}C overnight under vacuum to remove solvent molecules.

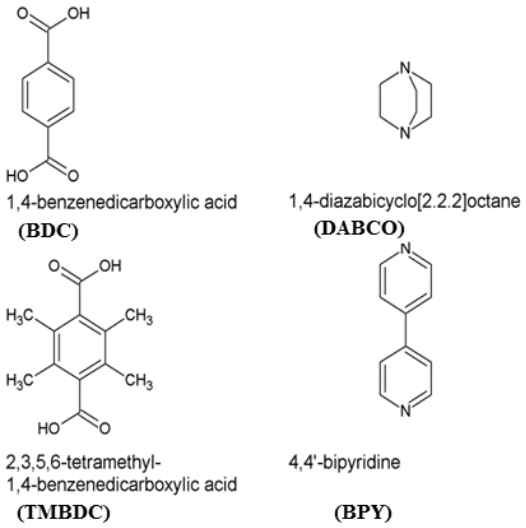

Figure 5.1 Organic ligands employed in this work.

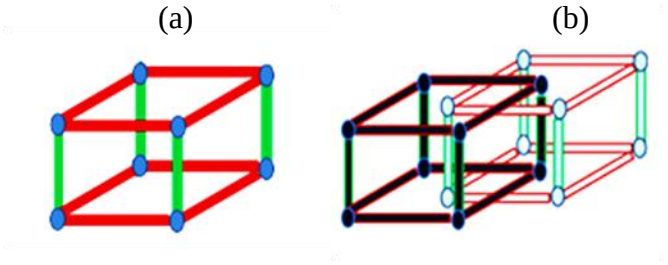

Figure 5.2 Illustration of (a) non-catenated pillared layer frameworks (*DMOF*, *DMOF-TM*, *MOF-508-TM*) synthesized from dicarboxylate (red) and pillar ligand (green). The blue corners are the metal nodes. b) two-fold catenation in pillared layer frameworks (*MOF-508*). Black and white represents two different frameworks.

MOF-508. Zn-BDC-BPY or MOF-508 was synthesized according to literature procedure:[11] $Zn(NO_3)_2.6H_2O$ (1.18 mmol), BDC (1.18 mmol), and BPY (0.59 mmol) were dissolved in DMF and ethanol (1:1, 100 mL) at room temperature in a glass beaker. The resulting solution was transferred into a glass jar, which was kept in a preheated oven at 90^{o}C for 24 hrs. The solution was then cooled to room temperature in air, and the resulting solid was filtered and repeatedly washed with DMF. The white block-shaped crystals obtained after drying were transferred to a vial. Activated samples of MOF-508 were prepared by heating the as-synthesized compound at 110^{o}C overnight under vacuum.

DMOF-TM. Zn-TMBDC-DABCO or DMOF-TM was prepared according to the literature procedure.[13] $Zn(NO_3)_2.6H_2O$ (0.63 mmol), TMBDC (0.63 mmol) and DABCO (0.31 mmol) were dissolved in 15mL DMF by stirring for 2-3 hrs at room temperature. The resulting solution was transferred to a Teflon-lined stainless steel reactor and placed in a preheated oven at 120 ^{o}C for 48 hrs. The solution was then cooled to room temperature in air, and the resulting white solid was filtered and repeatedly washed with DMF. Activated samples of DMOF-TM were prepared by heating the as-synthesized samples at 110^{o}C overnight under vacuum.

MOF-508-TM. Zn-TMBDC-BPY or MOF-508-TM was synthesized following the literature procedure[13] in which $Zn(NO_3)_2.6H_2O$ (0.6 mmol), TMBDC (0.6 mmol) and BPY (0.3 mmol) were mixed in DMF (9 mL) at room temperature in a glass beaker and homogenized by stirring for 3 hrs. After filtering the white precipitate, the resulting solution was poured into a glass vial, which was placed in a sand bath in a preheated oven at 120 ^{o}C for 48 hrs. After the solution was cooled to room temperature in air, the

resulting white solid was filtered and repeatedly washed with DMF. Activated samples were prepared by performing solvent exchange with chloroform and then evacuating overnight under vacuum at room temperature.

Figures C.1-C.4 in Appendix C show that PXRD patterns of all the synthesized MOFs match well with their corresponding pattern simulated from single crystal XRD data, confirming the purity of our samples.

5.2.2 Methods

5.2.2.1 Powder X-Ray Diffraction

Powder X-ray diffraction (PXRD) patterns were measured using a X'Pert X-ray PANalytical diffractometer with an X'celerator module using Cu Kα (λ = 1.5418 Å) radiation at room temperature, with a step size of 0.02˚ over the two theta (2θ) range of 5-50˚.

5.2.2.2 Nitrogen Adsorption

Adsorption isotherms (Appendix C, Figures C.10-C.13) for nitrogen gas were measured at 77 K using a Quadrasorb system from Quantachrome Instruments for each activated MOF sample before and after water exposure. The activation process for each MOF is given in Table 5.2. BET surface areas and micropore volumes were calculated by fitting the BET model and Dubinin-Astakov (DA) model, respectively, to their nitrogen adsorption isotherms. Surface area values for the same MOF may differ in various publications due to lack of consistency in activation procedures and in the pressure range used to fit the BET model. Here, the BET model was applied over the pressure range ($P/P_o < 0.05$), which gives model parameters that satisfy the consistency criteria.[16]

5.2.2.3 Water Vapor Adsorption

Adsorption isotherms for water vapor were measured at 298 K and 1 bar using an Intelligent Gravimetric Analyzer (IGA-3 series) device from Hiden Isochema. Prior to the run, samples were activated (heated under vacuum, Table 5.2) *in situ* to remove the solvent/guest molecules. The relative humidity (RH) was monitored using two mass flow controllers. These controllers vary the ratio of saturated air and dry air to obtain the desired RH. Saturated air is generated by effervescing a percentage of dry air through a vessel filled with deionized water. To avoid water condensation in the IGA-3, experiments were conducted only up to 90% RH. Total gas flow rate was set at 200 cm^3/min and typical equilibrium times ranged from 15 minutes to 20 hr for each adsorption/desorption point in the isotherm.

Table 5.2 Comparison of Properties of Pillared MOFs

Material	Pore Volume[†] (cm^3/g)	Pore Diameter (c, a, b) [‡] (Å)	Activation process (under vacuum)	Surface Area[*] (m^2/g) Before	After[a]
[17]DMOF	0.75	7.5x7.5,4.8x3.2,4.8x3.2	110 ^oC (12 h)	1980	7
MOF-508[$]	0.42	4x4, -, -	110 ^oC (12 h)	800	800
[14a]DMOF-TM	0.51	3.5, -, -	110 ^oC (12 h)	1050	1050
MOF-508-TM	0.56	3.5,8x10,8x10	25 ^oC (12h)[#]	1330	4

[a]After 90% RH.

[#]Solvent exchange with chloroform.

[‡]Obtained from literature.[11,13,20]

[$]Only this MOF is doubly interpenetrated 3-D pillared MOF.

[†]Obtained from the Dubinin-Astakov model of N_2 adsorption77K.

[*]BET Analysis.[16]

5.3 Results and Discussion

Figure 5.3a shows the water vapor adsorption isotherms at 298 K for DMOF and MOF-508. For DMOF, the amount of water vapor adsorbed increases until the initiation of structural collapse at 40 %RH. Water vapor adsorption decreases at 60 %RH and remains almost constant thereafter. Similar peculiar behavior was also observed by Schoenecker et al.[17] for Zn based DMOF and Liang et al.[3g] for both Zn and Ni versions of DMOF. However, for MOF-508, we observe that water vapor is almost negligible.

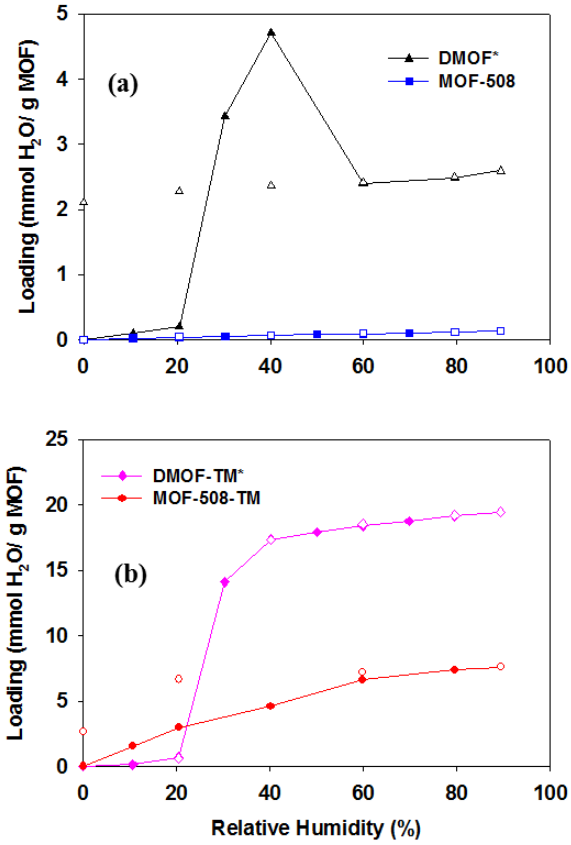

Figure 5.3 Water vapor sorption/desorption isotherms for desolvated compounds of (a) DMOF, and MOF-508; (b) DMOF-TM, and MOF-508-TM (closed symbols – adsorption, open symbols – desorption). Lines connecting the adsorption points are to faciliate viewing. *Reported from our previous works.[14a,17]

Low water vapor uptake in the doubly interpenetrated MOF-508 is not surprising as similar behavior was observed by Xie et al.[18] for another interpenetrated MOF (SNU-80) with BET surface area of 1035 m^2/g and DA pore volume of 0.43 cm^3/g. At room temperature, SNU-80 excludes water molecules even under saturated water vapor pressure, although its pores (3.8-6.5 Å) are larger than the size of most common gases. The water vapor capacities at 90% RH are 2.59 mmol/g for DMOF, and 0.13 mmol/g for MOF-508. Counter to MOF-508, a substantial amount of water (2.11 mmol/ g) is retained in DMOF when the stream is switched to dry air. Hence, only DMOF shows a large hysteresis, which indicates a change in structure upon water exposure.[3g]

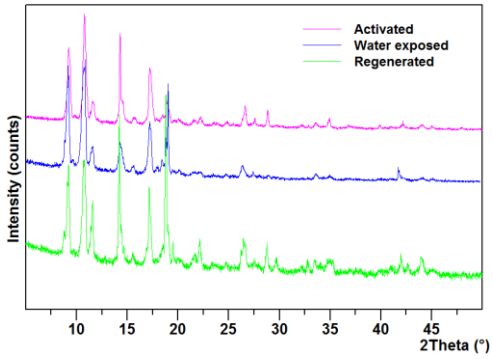

Figure 5.4 PXRD patterns for activated, water-exposed, and regenerated MOF-508.

In contrast to the known instability (Appendix C, Figure C.5) of DMOF,[17] the PXRD patterns of activated, water exposed, and regenerated (activated after water exposure) samples of MOF-508 (Figure 5.4) remain unchanged. In Figure 5.4 we have chosen to present the PXRD pattern of *activated*, and not as-synthesized, MOF-508 because it was previously reported by Chen et al.[11] and also observed by us that PXRD

patterns for as-synthesized and activated MOF-508 are significantly different from each other (Appendix C, Figure C.6). Due to this interesting behavior of MOF-508 upon activation, Chen et al. named as-synthesized sample as MOF-508a and activated sample as MOF-508b. However, PXRD patterns for as-synthesized and activated DMOF are very similar (Appendix C, Figure C.7).[20] As reported in Table 5.2, upon exposure to 90% RH DMOF completely loses its surface area while MOF-508 does not. Thus, surface area results are in agreement with the PXRD analyses.

Counter to our observation, Liu et al.[21] reported that noticeable changes are observed in the PXRD patterns for MOF-508 upon exposure to water vapor (at 318 K) for 1 day. However, unlike Figure 5.4, they compared the PXRD pattern of water-exposed MOF-508 with as-synthesized MOF-508 (MOF-508a). This misled the authors to conclude that MOF-508 is unstable upon exposure to water and highlights the need for surface area analysis in addition to PXRD. As mentioned before, we have instead compared PXRD pattern of water exposed MOF-508 sample with activated MOF-508 sample (MOF-508b). Moreover, the PXRD pattern of the water-exposed sample obtained in their work matches perfectly with ours (Appendix C, Figure C.8). Similarly, Ma et al.[5b] reported that MOF-508 loses ca. 87% of its surface area after one week of exposure to ambient air. This contradiction is due to significant differences in purity of the samples. The purity of MOF-508 used in our work appears to be higher compared to Ma et al.,[5b] which is clearly visible from Figure S7(a) of their publication. Simulated patterns of MOF-508 in Figure S7(a) do not match with the pattern obtained from the CIFs (crystallographic information files) of MOF-508a and MOF-508b provided by Chen et al.[11] Moreover, their experimental PXRD patterns for as-synthesized and activated MOF-

508 are exactly same, which again contradicts Chen et al.[11] It is possible that variations in the synthesis procedures of Ma et al.[5b] compared to the original report led to impure product. Impurity in MOF-508 sample synthesized by Ma et al.[5b] is also indicated by the low BET surface area (398 m^2/g) obtained for MOF-508, while we report BET surface area of 800 m^2/g in good agreement with Chen et al (Langmuir surface area of 946 m^2/g).[11] Thus, both of the previous water stability studies (Liu et al.[21] and Ma et al.[5b]) performed on MOF-508 so far are incomplete/ incorrect and hence, are misleading.

In this work, we observe that MOF-508 is stable (after 90% RH exposure) in spite of being synthesized with a pillar ligand (BPY) of lesser basicity (pK_a= 4.60)[19] compared to DABCO (pK_a= 8.86).[19] Intuitively, we would expect that the Lewis acid metal sites should form stronger bonds with more basic (higher pK_a) ligands, and DMOF should have been more water stable than MOF-508. However, MOF-508 appears to be stable because it possesses two-fold catenation. Catenated crystal structures are more thermodynamically stable[22] and also lead to lower water adsorption loadings.[18] Due to similar reasons, SNU-80 synthesized by Xie et al.[18] was also found to be water-stable.

Figure 5.3b shows the water vapor adsorption isotherms at 298 K for non-catenated 3D pillared MOFs: DMOF-TM, and MOF-508-TM. Unlike MOF-508, MOF-508-TM is not interpenetrated due to the steric effects of the four methyl groups on the BDC linker. For both MOFs, the amount of water vapor adsorbed increases with % RH. For MOF-508-TM, the water vapor capacity at 90% RH is less (~7.60 mmol/g) than DMOF-TM (~19.45 mmol/g) even though the former has a higher pore volume. Pore-filling occurs in DMOF-TM at ~ 20 % RH due to the presence of smaller pores than

MOF-508-TM. Pore-filling does not occur in MOF-508-TM because decomposition of the structure occurs along the isotherm (Appendix C, Figure C.9).

As shown in our previous studies,[14a,b] the isotherm for DMOF-TM does not exhibit hysteresis, and water is not retained in the pores when the stream was switched to dry air. For MOF-508-TM, a substantial amount (~2.69 mmol/g) of water is retained, and it shows significant hysteresis, which often indicate structure decomposition.[3g] Figures 5.5a and 5.5b show that DMOF-TM does not lose its crystallinity after exposure to such high levels of humidity, but MOF-508-TM decomposes under these conditions. The collapse of MOF-508-TM appears to proceed by cleavage of the Zn-N (or Zn-BPY) bond as other studies on DMOF have shown that indeed the DABCO ligand leaves the structure first upon exposure to water, while the Zn–BDC sheets remain intact.[14c,d] The pK_a value of DABCO (pillar ligand in DMOF-TM) is almost double the pK_a (4.60) of BPY (pillar ligand in MOF-508-TM). As a result, the Zn-DABCO bond will be stronger than the Zn-BPY bond. DeCoste et al.,[23] showed that rotational effects of double ring structures can lead to decomposition of MOFs after exposure to water and other solvents. This result for UiO-67 was in stark contrast to the highly stable UiO-66, which is synthesized with BDC. BPY could experience similar rotational effects, which would also contribute to the instability observed here. In agreement with PXRD results, Table 5.2 shows that MOF-508-TM completely loses its surface area after water exposure and regeneration, while DMOF-TM does not.

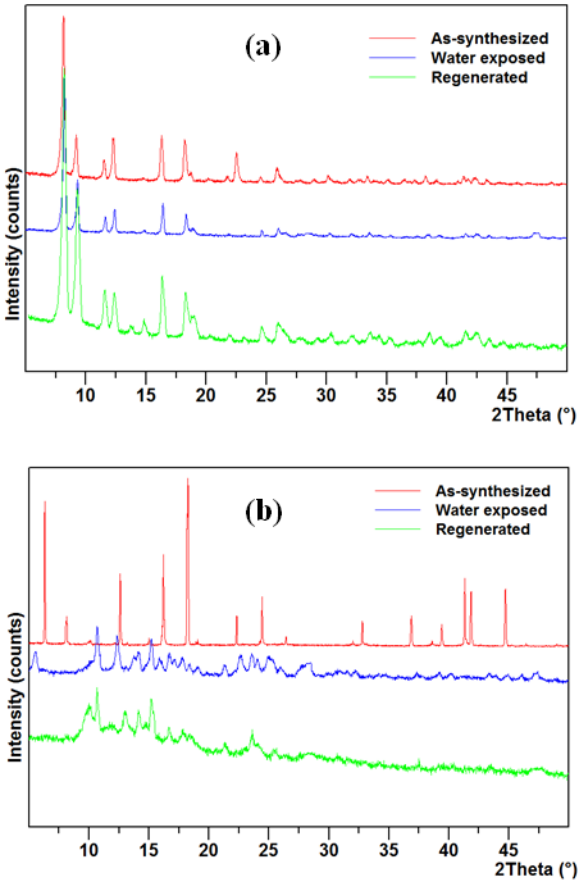

DMOF-TM

MOF-508-TM

Figure 5.5 PXRD patterns for as-synthesized, water-exposed, and regenerated (a) DMOF-TM[14a] and (b) MOF-508-TM.

We expected MOF-508-TM to possess higher water stability than MOF-508 because the zinc clusters are shielded by four methyl groups and that is why our previous work,[14a,b] shows DMOF-TM to be extremely stable compared to parent DMOF. However, MOF-508-TM collapses upon water exposure and MOF-508 does not, even when both contain Zn-BPY bonds. MOF-508 is stable as it is two-fold catenated, which makes its water uptake very small compared to MOF-508-TM. Moreover, when we exposed MOF-508-TM to low level of relative humidity (only up to 10% RH), we observed lesser loss in crystallinity (Appendix C, Figure C.9) and now BET surface area of the regenerated

sample increased to 51 m^2/g (10% RH exposure) from 4 m^2/g (90% RH exposure). Hence, we notice that breakage of the weak Zn-BPY bond depends on the amount of water vapor adsorbed. Water uptake for MOF-508-TM (~1.4 mmol/ g) even at 10% RH exposure is ten times higher than the uptake for MOF-508 (~0.13 mmol/ g) at 90% RH exposure. Therefore, MOF-508 is stable even after 90% RH exposure while MOF-508-TM decomposes even before 10% RH. In contrast, DMOF-TM is highly stable, even when adsorbing large amounts of water vapor due to a combination of shielded zinc clusters and higher basicity DABCO ligand.

5.4 Conclusions

In this work we have carried out the systematic water adsorption studies required to evaluate the effect of basicity (pK_a value) of the pillar ligand and catenation in the framework on the water stability of MOFs. We have illustrated that in non-interpenetrated MOFs, one constructed from a pillar ligand of higher pK_a value is more stable under humid conditions. However, when the framework is interpenetrated, the MOF (MOF-508) pillared by ligand of lower pK_a value is actually more stable than the non-interpenetrated MOF (DMOF) pillared by ligand of higher pK_a value. Water stability of these interpenetrated MOFs is due to inherently higher thermodynamic stability of catenated structures and also significantly reduced water adsorption loadings. Thus, using interpenetration in combination with ligands of relatively high basicity can lead to MOFs with good water stability.

5.5 References

(1) Q. Y. Yang, A. D. Wiersum, H. Jobic, V. Guillerm, C. Serre, P. L. Llewellyn and G. Maurin, *J. Phys. Chem. C*, 2011, **115**, 13768-13774.

(2) (a) T. Duren, L. Sarkisov, O. M. Yaghi and R. Q. Snurr, *Langmuir*, 2004, **20**, 2683-2689. (b) S. Kitagawa, R. Kitaura and S. Noro, *Angew. Chem., Int. Ed.*, 2004, **43**, 2334-2375. (c) Y. H. Hu and L. Zhang, *Adv. Mater.*, 2010, **22,** E117-E130. (d) L. J. Murray, M. Dinca and J. R. Long, *Chem. Soc. Rev.*, 2009, **38**, 1294-1314. (e) N. Nijem, J.-F. Veyan, L. Kong, K. Li, S. Pramanik, Y. Zhao, J. Li, D. Langreth and Y. J. Chabal, *J. Am. Chem. Soc.*, 2010, **132**, 1654-1664. (f) R. Zou, A. I. Abdel-Fattah, H. Xu, Y. Zhao and D. D. Hickmott, *CrystEngComm*, 2010, **12**, 1337-1353. (g) M. Eddaoudi, J. Kim, N. Rosi, D. Vodak, J. Wachter, M. O'Keeffe and O. M. Yaghi, *Science*, 2002, **295**, 469-472.

(3) (a) B. Arstad, H. Fjellvåg, K. Kongshaug, O. Swang and R. Blom, *Adsorption*, 2008, **14**, 755-762. (b) D. Britt, H. Furukawa, B. Wang, T. G. Glover and O. M. Yaghi, *Proc. Nat. Acad. Sci.* USA 2009, **106**, 20637-20640. (c) S. R. Caskey, A. G. Wong-Foy and A. J. Matzger, *J. Am. Chem. Soc.*, 2008, **130**, 10870. (d) Z. Chen, S. Xiang, H. D. Arman, J. U. Mondal, P. Li, D. Zhao and B. Chen, *Inorg. Chem.*, 2011, **50**, 3442-3446. (e) S. Keskin, T. M. van Heest and D. S. Sholl, *ChemSusChem*, 2010, **3**, 879-891. (f) J. R. Li, R. J. Kuppler and H. C. Zhou, *Chem. Soc. Rev.*, 2009, **38**, 1477-1504. (g) Z. Liang, M. Marshall and A. L. Chaffee, *Microporous Mesoporous Mater.*, 2010, **132**, 305-310. (h) A. R. Millward and O. M. Yaghi, *J. Am. Chem. Soc.*, 2005, **127**, 17998-17999. (i) Y. G. Zhao, H. H. Wu, T. J. Emge, Q. H. Gong, N. Nijem, Y. J. Chabal, L. Z. Kong, D. C. Langreth, H. Liu, H. P. Zeng and J. Li, *Chem.- Eur. J.*, 2011, **17**, 5100-5108.

(4) J. R. Karra and K. S. Walton, *Langmuir*, 2008, **24**, 8620-8626.

(5) (a) Y. Li and R. T. Yang, *Langmuir*, 2007, **23**, 12937-12944. (b) D. Ma, Y. Li and Z. Li, *Chem. Commun.*, 2011, **47**, 7377-7379. (c) J. Yang, A. Grzech, F. M. Mulder and T. J. Dingemans, *Chem. Commun.*, 2011, **47**, 5244-5246. (d) H. J. Choi, M. Dinca, A. Dailly and J. R. Long, *Energy Environ. Sci.*, 2010, **3**, 117-123. (e) S. S. Kaye, A. Dailly, O. M. Yaghi and J. R. Long, *J. Am. Chem. Soc.*, 2007, **129**, 14176. (f) C. R. Wade, T. Corrales-Sanchez, T. C. Narayan and M. Dinca,. *Energy Environ. Sci.* 2013***, 6*** **(7)**, 2172-2177.

(6) (a) P. Kuesgens, M. Rose, I. Senkovska, H. Froede, A. Henschel, S. Siegle and S. Kaskel, *Microporous Mesoporous Mater.*, 2009, **120**, 325-330. (b) G. Akiyama, R. Matsuda and S. Kitagawa, *Chem. Lett.*, 2010, **39**, 360-361. (c) M. Kim and S. M. Cohen, *CrystEngComm*, 2012, **14,** 4096-4104. (d) J. Ehrenmann, S. K. Henninger and C. Janiak, *Eur. J. Inorg. Chem.*, 2011, **4**, 471-474. (e) J. H. Cavka, S. Jakobsen, U. Olsbye, N. Guillou, C. Lamberti, S. Bordiga and K. P. Lillerud, *J. Am. Chem. Soc.*, 2008, **130**, 13850-13851. (f) S. J. Garibay and S. M. Cohen, *Chem. Commun.*, 2010, **46**, 7700-7702. (g) F. Jeremias, V. Lozan, S. K. Henninger and C. Janiak, *Dalton Trans.*, 2013 (DOI: 10.1039/C3DT51471D). (h) C. Janiak, and S. K. Henninger Chimia, *Int. J.Chem.*, 2013, **67 (6)**, 419-424. (i) A. Khutia, H. U. Rammelberg, T. Schmidt, S. Henninger and C. Janiak, *Chem. Mater.* 2013, **25 (5)**,

790-798. (j) F. Jeremias, A. Khutia, S. K. Henninger and C. Janiak, *J. Mater. Chem.* 2012, **22 (20),** 10148-10151. (k) S. K. Henninger, F. Jeremias, H. Kummer and C. Janiak, *Eur. J. Inorg. Chem.*, 2012, **16,** 2625-2634.(l) S. K. Henninger, H. A. Habib and C. Janiak, *J. Am. Chem. Soc.*2009, **131 (8)**, 2776-2777.

(7) J. J. Low, A. I. Benin, P. Jakubczak, J. F. Abrahamian, S. A. Faheem and R. R. Willis, *J. Am. Chem. Soc.*, 2009, **131**, 15834-15842.

(8) J. A. Greathouse and M. D. Allendorf, *J. Am. Chem. Soc.*, 2006, **128**, 10678-10679.

(9) V. Colombo, S. Galli, H. J. Choi, G. D. Han, A. Maspero, G. Palmisano, N. Masciocchi and J. R. Long, *Chem. Sci.*, 2011, **2**, 1311-1319.

(10) D. N. Dybtsev, H. Chun and K. Kim, *Angew. Chem., Int. Ed.*, 2004, **43**, 5033-5036.

(11) B. L. Chen, C. D. Liang, J. Yang, D. S. Contreras, Y. L. Clancy, E. B. Lobkovsky, O. M. Yaghi and S. Dai, *Angew. Chem., Int. Ed.*, 2006, **45**, 1390-1393.

(12) O. K. Farha and J. T. Hupp, *Acc. Chem. Res.* 2010, **43**, 1166-1175.

(13) H. Chun, D. N. Dybtsev, H. Kim, and K. Kim, *Chem. Eur. J.*, 2005, **11**, 3521-3529.

(14) (a) H. Jasuja and K. S. Walton, *Langmuir* 2012, **28** (49), 16874-16880. (b) H. Jasuja, N. C. Burtch, Y. Huang, Y. Cai and K. S. Walton, *Langmuir* 2012, **29** (2), 633-642. (c) K. Tan, N. Nijem, P. Canepa, Q. Gong, J. Li, T. Thonhauser and Y. J. Chabal,*Chem. Mater.*, 2012, 24, 3153–3157; (d) Z. Chen, S. C. Xiang, D. Y. Zhao and B. L. Chen,*Cryst. Growth Des.*, 2009,9, 5293–5296.

(15) Z. Wang, K. K. Tanabe and S. M. Cohen, *Inorg. Chem.*, 2009, **48**, 296-306.

(16) K. S. Walton and R. Q. Snurr, *J. Am. Chem. Soc.*, 2007, **129**, 8552-8556.

(17) P. M. Schoenecker, C. G. Carson, H. Jasuja, C. J. J. Flemming and K. S. Walton, *Ind. Eng. Chem. Res.*, 2012, **51**, 6513-6519.

(18) L.-H. Xie and M. P. Suh, *Chem. Eur. J.*, 2011, **17**, 13653-13656.

(19) S. Hilal, S. W. Karickhoff and L. A. Carreira, *Quant. Struc. Act. Rel.* 1995, **14**, 348.

(20) J. Y. Lee, D. H. Olson, L. Pan, T. J. Emge and J. Li, *Adv. Funct. Mater.*, 2007, **17**, 1255-1262.

(21) H. Liu, Y. G. Zhao, Z. J. Zhang, N. Nijem, Y. J. Chabal, H. P. Zeng and J. Li, *Adv. Funct. Mater.* 2011, **21** (24), 4754-4762.

(22) J. Zhang, L. Wojtas, R. W. Larsen, M. Eddaoudi and M. J. Zaworotko, *J. Am. Chem. Soc.*, 2009, **131**, 17040.

(23) J. B. DeCoste, G. W. Peterson, H. Jasuja, T. G. Glover, Y. Huang and K. S. Walton, *J. Mater. Chem. A.* 2013, **1**, 5642.

CHAPTER 6

SYNTHESIS OF NOVEL COBALT, NICKEL, COPPER, AND ZINC-BASED WATER STABLE PILLARED METAL-ORGANIC FRAMEWORKS

This work was conducted in collaboration with the Walton group members- Yang Jiao, Nicholas C. Burtch, and You-gui Huang.

6.1 Introduction

Metal-organic frameworks (MOFs) are constructed by the self-assembly of organic ligands and metal-containing nodes.[1] MOFs have garnered much attention in a variety of fields related to porous materials such as adsorption-based gas storage and gas separation, catalysis, sensing, and drug delivery.[2-18] This is due to their record breaking values of surface area and pore volume, facile pore tunability, and almost infinite set of structure possibilities with diverse topologies. However, their poor stability under humid or aqueous environments is one of the major constraints to them being used in industrial applications such as air purification, CO_2 capture, catalysis, and methane or hydrogen storage in fuel tanks.[19-51] Thermodynamically, water being a more basic ligand (pK_a value ~ 15.7), it can easily displace the less basic organic ligands (typically carboxylates) coordinated to the metal centers and hence, can breakdown the framework.

Despite the significance of this issue, the literature consists of a few systematic water stability studies for MOFs.[19-21,24-25,37-40,44-46,48,51-55] Moreover, the prevailing literature is rather scattered in the type of water exposure conditions, and particular characterization techniques used to quantify water stability of MOFs experimentally vary

significantly among publications. In most of the studies reported,[27-29,31-33,56-58] MOFs are exposed to ambient air in the lab or soaked in liquid water, but water adsorption isotherms are rarely reported and post-exposure powder X-ray diffraction (PXRD) alone is widely used to characterize MOFs.[26,35,43,47,49,50,59-63] PXRD is a simple technique, which provides only information about the long-range crystallinity of the structure, and it is not capable of detecting surface collapse. Hence, it is a qualitative technique and not a comprehensive way to characterize MOFs post water exposure. This has led to misleading conclusions about the water stability of MOFs. For example, Jasuja et al.[39] and Liu et al.[59] reported contrasting observations about the stability of MOF-508 with the former highlighting the need for surface area analysis in addition to PXRD to reach a conclusion with a higher confidence level.

Overall, it has been seen that the strength of the bond between the metal centers and the ligand is a strong indicator of the MOF hydrothermal stability.[24] Carboxylate ligand-based MOFs such as MOF-5 and UMCM-1 are highly unstable under humid conditions due to the low basicity (pK_a) of carboxylate ligands and low coordination number of metal centers (only four-coordinated).[22-25] However, some carboxylate ligand-based MOFs such as UiO-66(Zr),[29] MIL-125(Ti),[53] PCN-56-59(Zr),[60] DUT-51,67-69,[54,61] and MIL-140(Zr)[62] have been reported to be water stable due to high oxophilicity and high coordination number of metal centers (eight-coordinated). Similarly, other carboxylate-based MOFs such as MIL-53(Cr)[44] and MIL-101(Cr)[26] are water stable as metal centers are inert towards water and hence, now MOF hydrolysis is unfavorable. Imidazolate[26-27] (pK_a value ~ 18.6) and pyrazolate[28,47] (pK_a value ~ 19.8) based MOFs are highly stable under humid or aqueous environments as the pK_a values of these nitrogen

coordinating ligands are higher than that of water (pK_a value ~ 15.7). Hence, water stability of nitrogen-coordinated pillared MOFs[37-39] (Zn and Ni-based DMOF is stable up to 30% relative humidity[35]) is greater than highly unstable MOFs such as MOF-5 and UMCM-1[22,25] due to the higher basicity (pK_a) of pillar ligands compared to carboxylate ligands.[24-25,31,37-39]

Although, the impact of water adsorption and its subsequent effect on the thermodynamic stability of MOF structures could be defined by the acid-base effects of metal centers and ligands, hydrophobicity and ligand sterics could also be important in defining the kinetic stability of MOFs as they can increase the activation energy barrier for the hydrolysis reaction. Ligand functionalization is a promising approach to empower aforementioned kinetic factors, which play a significant role in the stability of the framework. It has been reported earlier that MOF stability in humid environments can be improved by incorporating hydrophobic functional groups[31-34,40,49-51,55-58,63] such as alkyl or fluorinated groups, but there is a need to decouple hydrophobicity from steric effects by measuring water adsorption isotherms. Taylor et al.[51] showed that CALF-25 adsorbs appreciable amount of water unlike highly hydrophobic fluorous metal–organic frameworks (FMOFs) such as FMOF-1[55] and is still water resistant as now the non-polar alkyl functional groups provide steric protection to the metal centers. However, in majority of the reports[27-29,31-33,56-58] water adsorption isotherms have not been measured. For example, Ma et al.[31] showed that adding methyl groups at the 2,2’ position on BPY results in a more stable structure (SCUTC-18) than adding methyl groups at the 3,3’ position (SCUTC-19) but did not report water adsorption isotherms. Hence, it is difficult to conclude whether the MOF is now inherently more stable due to change in ligand

sterics or is stable simply due to increase in hydrophobicity as a result of functionalization with nonpolar groups. Thus, there is a critical requirement in the MOF field to perform systematic water stability studies and water-exposed MOFs should be characterized comprehensively so that we can isolate the specific factors governing structural stability of MOFs and direct the future synthesis efforts towards the construction of new water stable MOFs.

The explanation of the MOF degradation mechanisms under humid environments is a complex problem because there are various independent factors, which play a critical role in the stability of MOFs. To decouple the effects of metal-ligand coordination environment, topology, porosity, metal-type, and ligand-type on the structural stability of MOFs, studies on isostructural series of MOFs are needed since now we can systematically study the impact of each specific factor on the MOF water stability by only varying that specific factor. The effect of the metal-type incorporated in MOF systems such as MOF-74 and DMOF on the water stability was examined by Liu et al.[52] and Tan et al.[21] respectively. It was reported that for both MOF systems, the Ni-based variation (Ni-DMOF and Ni-MOF-74) was less vulnerable to hydrolysis. Ni^{2+} has the lowest standard reduction potential among the metals considered in these studies, which makes it less likely for the metal centers to react with water.[52] Along the same lines, water stability of MOF-5 is shown to increase upon doping with Ni^{2+}.[64] Decoste et al.[19] reported that UiO-67 MOF-based on double ring ligand BPDC (biphenyl dicarboxylate) is less stable than single ring ligand BDC (benzene dicarboxylate)-based MOF UiO-66, due to steric and rotational effects of phenyl rings and hence, stressed the need of probing the ligand ring motions. We have recently shown (Chapters 3,4) that the water-unstable

Zn-DMOF structure can be made kinetically stable by functionalizing benzenedicarboxylic acid with non-polar groups, as these groups provide effective shielding to the metal centers.[37,38] In another report (Chapter 5),[39] we also reported that catenation in pillared MOFs can improve water resistance of MOFs even when the basicity of the pillar ligand is reduced. Catenation is the interpenetration of two or more identical and independent frameworks (Figure 6.1b).[11] This catenation can make the ligand displacement difficult by locking it in place within the framework. It should be noted that most of these aforementioned studies are systematic and MOFs were characterized comprehensively after water exposure using techniques such as porosity analysis via N_2 or CO_2 adsorption and FTIR spectroscopy in addition to PXRD.

In this work, we have extended our previous work (Chapters 3-5)[37-39,65] by synthesizing cobalt, nickel, copper, and zinc-based new water stable pillared MOFs of similar topology (Figure 6.1b, Appendix D, Figure D.1) using 2,3,5,6-tetramethyl-1,4-benzenedicarboxylic acid (TMBDC), 4,4',4'',4''-benzene-1,2,4,5-tetrayl tetrabenzoic acid (BTTB) as carboxylate ligands and 1,4-diazabicyclo[2.2.2]octane (DABCO), 2,2'-dimethyl 4,4'-bipyridine (DMBPY) as pillar ligands (Figure 6.1a). Longer diamine ligand (DMBPY) leads to two-fold catenation (Figure 6.1b, Appendix D, Figure D.1c) in the framework. Experiments were performed to measure water adsorption isotherms at 25 ^{o}C and 1 bar. PXRD patterns and results from BET modeling[66] of N_2 adsorption isotherms at -196 ^{o}C were compared before and after water exposure to determine the impact of water adsorption and its subsequent effect on the stability of MOF structures.

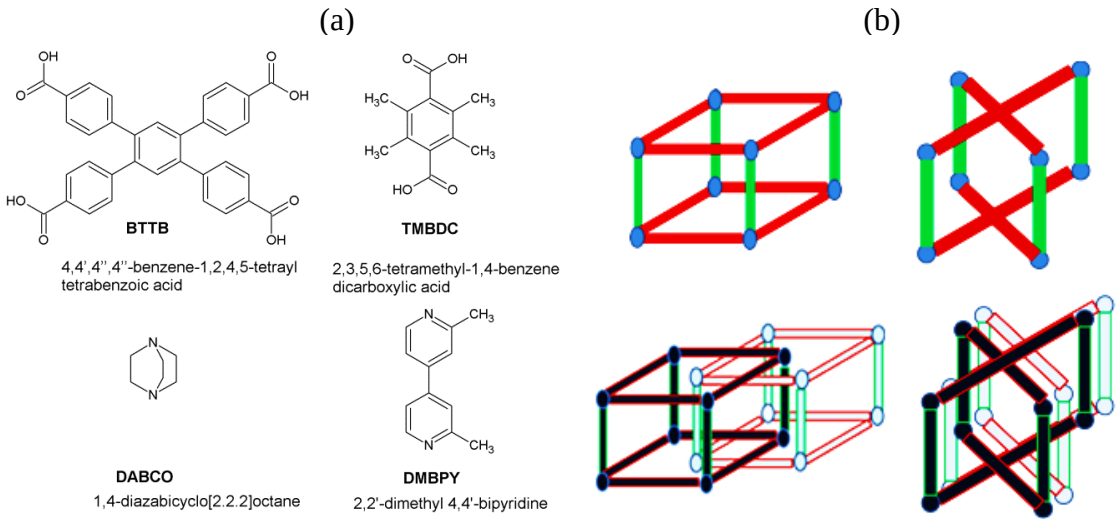

Figure 6.1 (a) Carboxylate (top) and diamine pillar (bottom) ligands used in this work. (b) Illustration of non-catenated (top) and 2-fold catenated (bottom) pillared layer metal-organic frameworks synthesized from dicarboxylate (left) and tetracarboxylate ligands (right). The blue corners are the metal nodes, red represents linkage via carboxylate ligands, and green represents linkage via pillar ligands. Black and white represents two different frameworks.

6.2 Experimental Section

6.2.1 Materials

All the chemicals employed in this work were commercially available and used as-received without further purification from the following sources: Sigma-Aldrich, N,N-diethylformamide (DEF), N,N-dimethylformamide (DMF), 4,4',4'',4'''-benzene-1,2,4,5-tetrayl tetrabenzoic acid (BTTB); Chem Service Inc., 2,3,5,6-tetramethyl-1,4-benzenedicarboxylic acid (TMBDC); Acros, 1,4-diazabicyclo[2.2.2]octane (DABCO), ethanol (EtOH); Angene Internationals Limited, 2,2'-dimethyl 4,4'-bipyridine (DMBPY).

All the new pillared MOFs reported in this work are summarized in Figure 6.2 and were synthesized solvothermally. Metal ions and carboxylate ligands form the 2-D

sheets while diamine ligands act as pillars connecting these 2-D sheets in the third dimension (Figure 6.1b, Appendix D, Figure D.1). Detailed synthesis procedures are as follows:

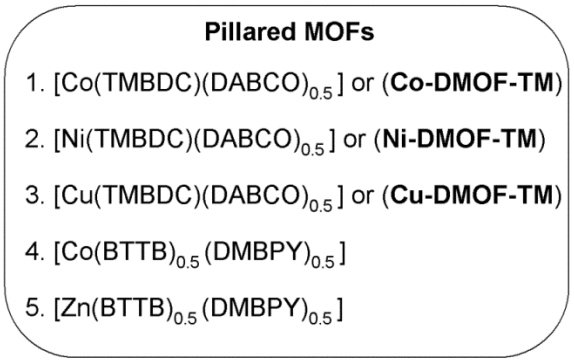

Figure 6.2 New water stable pillared MOFs synthesized in this work.

M-DMOF-TM (where M = Co, Ni, Cu). $M(TMBDC)(DABCO)_{0.5}$ or M-DMOF-TM were prepared with slight modification from the report of Chun et al.[67] for Zn-DMOF-TM, i.e., 0.63 mmol of metal salt ($Co(NO_3)_2.6H_2O$, $Ni(NO_3)_2.6H_2O$, $Cu(NO_3)_2.3H_2O$), 0.63 mmol of TMBDC ligand, and 0.31 mmol of DABCO ligand were dissolved in 15mL DMF and left for stirring for 3 hrs at room temperature. The resulting solution was filtered and filtrate was transferred to a Teflon-lined stainless steel reactor and placed in a preheated oven at 120 ^oC for 48 hrs. The solution was then cooled to room temperature in air, and the resulting solid was filtered and repeatedly washed with DMF. Activated samples of M-DMOF-TM were prepared by heating the as-synthesized samples at 110 ^oC overnight under vacuum.

M-BTTB-DMBPY (where M = Co, Zn). $M(BTTB)_{0.5}(DMBPY)_{0.5}$ or M-BTTB-DMBPY were prepared as suggested by Karra et al.[65] for M-BTTB-BPY, i.e., 0.2 mmol of metal salt ($Co(NO_3)_2.6H_2O$, $Zn(NO_3)_2.6H_2O$), 0.1 mmol of BTTB ligand, and 0.1 mmol of DMBPY ligand were dissolved in 5 mL of DEF/ethanol/water (2:2:1, v/v). Two drops of 1N HCl was added to the mixture and the final mixture was placed in a Teflon-lined stainless steel reactor and placed in a preheated oven at 100 ^oC for 96 hrs. The solution was then cooled to room temperature in air, and the resulting solid was filtered and repeatedly washed with DEF. Activated samples were prepared by performing solvent exchange with chloroform and then evacuating overnight under vacuum at 120 ^oC.

6.2.2 Characterization

6.2.2.1 Single Crystal XRD (X-Ray Diffraction)

A Bruker APEX II CCD sealed tube diffractometer with Mo-*K*α (λ = 0.71073 Å) radiation and a graphite monochromator was used to collect single crystal X-ray data for Co-BTTB-DMBPY. MOF Crystals were mounted on nylon CryoLoops with Paratone-N. The structure was solved by direct methods and refined by full-matrix least-squared techniques using the SHELXTL-97 software suite. Crystallographic details are provided in the Supporting Information (Appendix D, Figure D.20, Table D.1, CCDC 992483 contains the crystallographic information file-CIF).

6.2.2.2 PXRD (Powder X-Ray Diffraction)

A X'Pert X-ray PANalytical diffractometer with an X'celerator module and Cu Kα (λ = 1.5418 Å) radiation was used to collect PXRD patterns at room temperature,

with a step size of 0.02˚ in two theta (2θ). The phase purity of the as-synthesized MOF samples can be confirmed by comparing PXRD patterns with the simulated patterns from single crystal X-ray diffraction (Appendix D, Figures D.3-D.7). To determine the impact of water adsorption and its subsequent effect on the stability of MOF structures, PXRD patterns of as-synthesized samples were compared with patterns of water-exposed samples and regenerated samples (obtained after activating the water exposed samples).

6.2.2.3 BET Analysis

A Quadrasorb system from Quantachrome Instruments was used to measure nitrogen adsorption isotherms (Appendix D, Figures D.15-D.19) at -196 ^{o}C and the BET model was fitted to these isotherms so that the BET surface areas could be determined for each activated MOF before and after water exposure. Here, the method of Walton et al.[66] was used to correctly fit the BET model over the low pressure range ($P/P_o < 0.05$).

6.2.2.4 Thermogravimetric Analysis

A NETZSCH STA 449 F1 Jupiter® device was used to perform thermogravimetric analyses (TGA) of the as-synthesized and activated MOF samples (Appendix D, Figures D.8-D.9) under helium in the temperature range of 30-600 ˚C with a heating rate of 5 ˚C /min and flow rate of 20 mL/min.

6.2.2.5 Fourier Transform Infrared Spectroscopy

Fourier transform Infrared (FTIR) spectra of the as-synthesized and activated MOF samples (Appendix D, Figures D.10-D.14) were recorded with a PerkinElmer Spectrum One as KBr pellets in the range 400 – 4000 cm^{-1}. Figures D.10-D.14 (Appendix D), confirm the presence of methyl moieties in the frameworks.

6.2.2.6 Water Vapor Adsorption Isotherms

An Intelligent Gravimetric Analyzer (IGA-3 series, Hiden Isochema) was used to measure water vapor adsorption isotherms at 25 ^{o}C and 1 bar. Prior to water adsorption measurements, the samples (~ 30-40 mg) were activated *in situ* until no further weight loss was observed. Two mass flow controllers were used to control the relative humidity (RH) by varying the ratio of saturated air and dry air. Experiments were conducted only up to 80% or 90% RH so that water condensation does not occur in the equipment at higher humidities. The total gas flow rate was set at 200 cm^3/min for all the experiments, and each adsorption/desorption step was given sufficient time (from 15 minutes to 20 hrs) to approach equilibrium for all RH points.

6.3 Results and Discussion

6.3.1 Structure Characterization and Physical Properties

Among the new pillared MOFs synthesized in this work, we could obtain single crystals only for Co-BTTB-DMBPY (Appendix D, Figure D.20). Analysis of Co-BTTB-DMBPY using single crystal XRD shows that this framework has the same topology as the parent M-BTTB-BPY (where M = Co, Zn and BPY = 4,4'-bipyridine) structure synthesized by Karra et al.[65] Hence, metal paddlewheel clusters are connected by BTTB ligands to form 2-D layers, which are further pillared together by DMBPY ligands giving rise to a porous 3D framework (CCDC 992483 contains the CIF). Two identical and independent 3D frameworks interpenetrate (Figure 6.1b, Appendix D, Figure D.1c) with each other forming the 2-fold catenated final structure of this series of MOFs. However, DABCO-based pillared MOFs M-DMOF-TM (where M = Co, Ni, Cu) are non-catenated, similar to the parent Zn-DMOF-TM structure.[67] The phase purity of the as-synthesized

MOF samples was confirmed by comparing PXRD patterns with the simulated patterns from single crystal X-ray diffraction (Appendix D, Figures D.3-D.7). Since we could obtain single-crystal structure only for Co-BTTB-DMBPY, we used simulated patterns of isostructural pillared MOFs Zn-BTTB-BPY[65] and Zn-DMOF-TM[67] for Zn-BTTB-DMBPY and M-DMOF-TM (where M = Co, Ni, Cu) respectively. PXRD patterns of the as-synthesized M-DMOF-TM MOFs confirm that these materials are isostructural to the parent Zn-DMOF-TM structure (Appendix D, Figure D.2). As expected, N_2 adsorption measurements (Appendix D, Figures D.15-D.19) at -196 ^{o}C on the activated MOF samples showed typical Type I behavior according to the IUPAC classification.[4] Furthermore, we observe that methyl functionalization leads to a reduction in porosity (Table 6.1) for M-BTTB-DMBPY (where M = Co, Zn) compared to the parent M-BTTB-BPY (where M = Co, Zn)[65] whereas M-DMOF-TM (where M = Co, Ni, Cu) shows porosity similar to the parent Zn-DMOF-TM[37-38]. TGA analyses of M-DMOF-TM samples show that they all decompose around 310 ^{o}C (Appendix D, Figure D.8, Table 6.1), similar to the parent Zn-DMOF-TM material.[67] However, M-BTTB-DMBPY decomposes at a slightly higher temperature of 340 ^{o}C (Appendix D, Figure D.9, Table 6.1) since catenated crystal structures display higher thermal stability.[68] FTIR spectra (Appendix D, Figures D.10-D.14) for as-synthesized M-DMOF-TM and M-BTTB-DMBPY show peaks around 1680 and 3000 cm^{-1} corresponding to the stretching frequency of C=O bond in DMF/DEF and C−H bond in the methyl moieties attached to the benzene rings respectively. Upon activation peak at 1680 cm^{-1} disappears whereas peaks near 3000 cm^{-1} are retained. Hence, FTIR spectra (Appendix D, Figures D.10-

D.14) of pillared MOFs synthesized in this work confirm the presence of methyl moieties in the framework.

Table 6.1 Comparison of Properties of Water Stable Pillared MOFs Synthesized in This Work.

MOF	Pore Size (Å)	Pore Volume† (cm^3/g)	BET Surface Area* (m^2/g)	Activation Process (under vacuum)	Thermal Stability	Features	BET Surface Area* (after 80% or 90% RH)
Co-DMOF-TM	~3.5‡	0.488	1052	110 ˚ C (1h)	310 ˚C	Non-Catenated	1016
Ni-DMOF-TM	~3.5‡	0.484	1095	110 ˚ C (2h)	310 ˚C	Non-Catenated	1068
Cu-DMOF-TM	~3.5‡	0.461	1041	110 ˚ C (1h)	310 ˚C	Non-Catenated	990
Co-BTTB-DMBPY	4.408#	0.290	809	Chloroform Exchange and 120 ˚ C (12h)	340 ˚C	2-fold-Catenated	807
Zn-BTTB-DMBPY	~4.408	0.269	749	Chloroform Exchange and 120 ˚ C (12h)	340 ˚C	2-fold-Catenated	740

†Obtained from the Dubinin-Astakov model of N_2 adsorption at 77K
‡Zn-DMOF-TM has pore size of 3.5 Å [67]
#Calculated using the approach of Haldoupis et al.[69]
*BET Analysis[66]

6.3.2 Structural Stability Analysis under Humid Environments

The stability of M-DMOF-TM (where M = Co, Ni and Cu) and M-BTTB-DMBPY (where M = Co and Zn) after water exposure (80% or 90% RH) was evaluated using water vapor adsorption isotherms along with PXRD patterns and results from BET modeling[66] of N_2 adsorption isotherms before and after water exposure. Figure 6.3 compares water vapor adsorption at 25 ^oC and 1 bar for M-DMOF-TM with the parent Zn-DMOF-TM. All of these DABCO-based non-catenated pillared MOFs display type V

behavior[70] similar to traditional porous materials such as BPL carbon,[71] SBA-15,[72] and MCM-41[72]. Unlike the parent Zn-DMOF-TM, the Co, Ni, and Cu-based variations of DMOF-TM show varying levels of hysteresis and retain some amount of water even when the stream is switched to dry air (0% RH point in the desorption curve). This is unexpected because in these DABCO-based pillared MOFs, there are no unsaturated metal sites available for water to freely interact with. Recently, Wu et al.[73] showed that framework defects can have significant impact on adsorption properties of MOFs and Canivet et al.[74] suggested that hysteresis in water adsorption isotherms of MOFs can be accredited to framework flexibility. Most likely, M-DMOF-TM (where M = Co, Ni, Cu, and Zn) also have varying levels of flexibility or defects and this creates local heterogeneity in the framework, which eventually drives the water adsorption. Therefore, the pore-filling step in these MOFs occurs at a different relative humidity point even when their pore sizes are similar. Typically, pore-filling step occurs first (at the lowest levels of relative humidity) for the smallest pore material, and last for the largest pore material.[25]

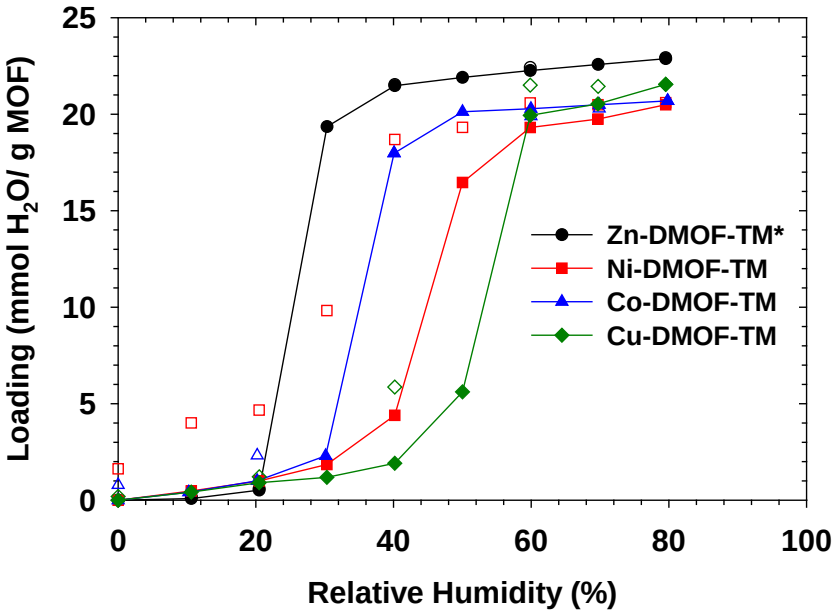

Figure 6.3 Water vapor adsorption isotherms for desolvated compounds of M-DMOF-TM (closed symbols – adsorption, open symbols – desorption). Lines connecting the adsorption points are to faciliate viewing. *Reported from our previous work.[38]

M-DMOF-TM (where M = Co, Ni, Cu) displayed no change in crystallinity (Figure 6.4) or loss of surface area (Table 6.1) after exposure to humid conditions similar to the parent Zn-DMOF-TM material as shown in our previous work (Chapters 3,4).[38,39] The water vapor adsorption capacities at 80% RH are 20.69 mmol/g (37.24 wt %) for Co-DMOF-TM, 20.49 mmol/g (36.88 wt %) for Ni-DMOF-TM, 21.54 mmol/g (38.78 wt %) for Cu-DMOF-TM, and 22.87 mmol/g (41.17 wt %) for Zn-DMOF-TM. The Co, Ni, Cu, and Zn-based variations of the unfunctionalized DMOF structure have been shown to collapse under 60% RH.[21,25,35] However, methyl groups grafted on the benzene dicarboxylate (BDC) ligand in DMOF-TM shield the metal centers from water molecules.[38,39] Hence, Co, Ni, Cu, and Zn-based tetramethyl functionalized variations of

DMOF are remarkably stable even when they have high water vapor adsorption loadings (> 20 mmol/g at 80% RH). Only a few MOFs, such as UiO-66, MIL-100(Fe), and MIL-101(Cr), display such stability after adsorbing large amounts of water.[25,26,48,75]

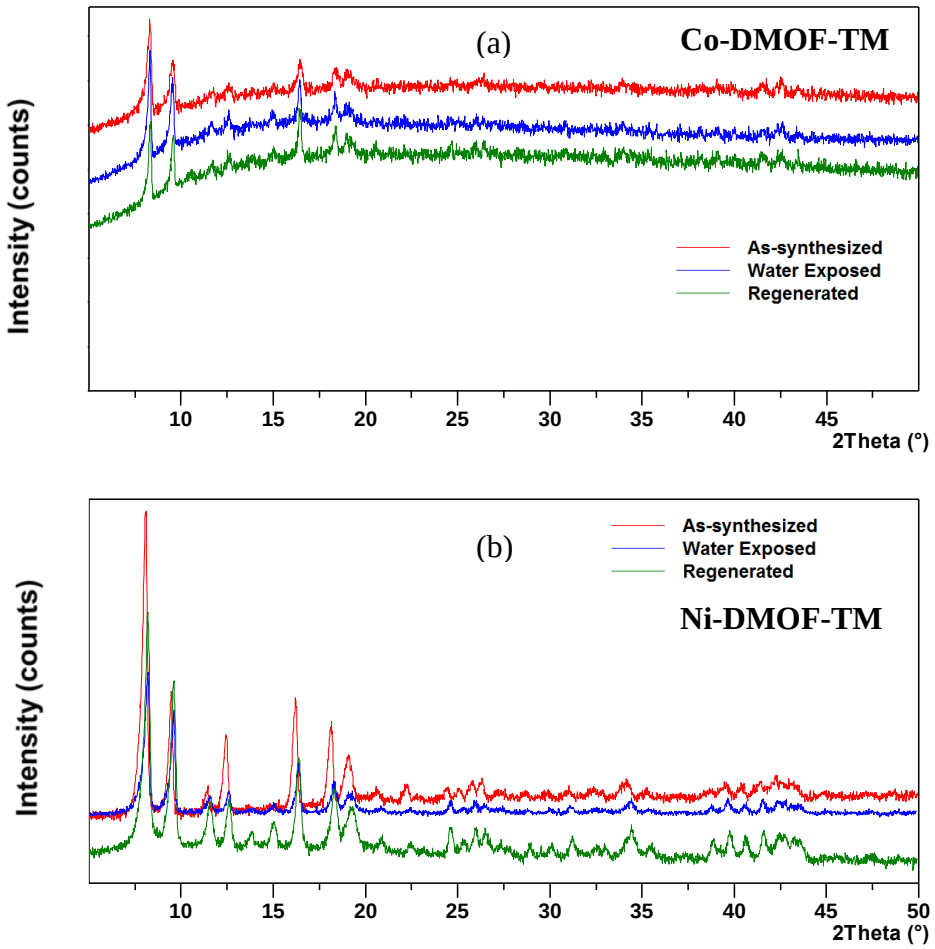

Figure 6.4 PXRD patterns for as-synthesized, water-exposed (after 80% RH), and regenerated (a) Co-DMOF-TM, (b) Ni-DMOF-TM, (c) Cu-DMOF-TM.

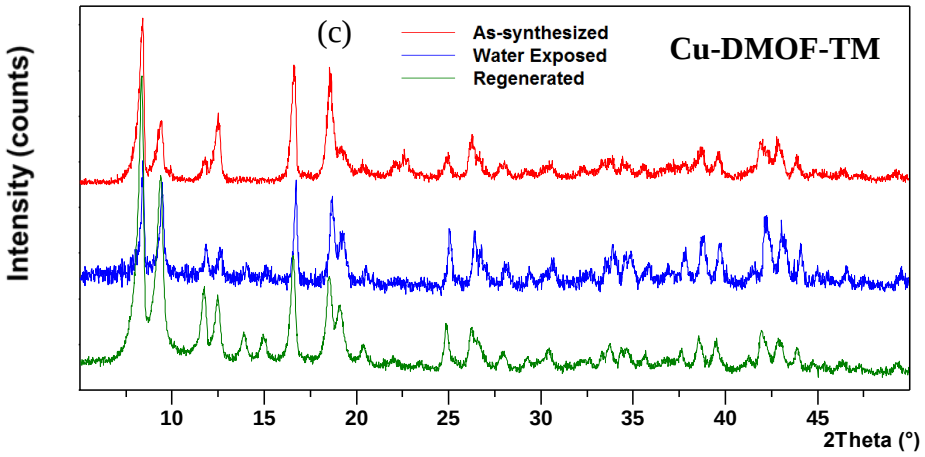

Figure 6.4 Continued.

Figure 6.5 shows the water vapor adsorption isotherms at 25 ^{o}C and 1 bar for the BTTB ligand-based 2-fold catenated pillared MOFs. Up to 70% RH, all of these isostructural pillared MOFs display type VII behavior[70] similar to MOF-508[39] and hence, these materials are very hydrophobic. However, at higher relative humidity, the pore-filling step occurs differently in these MOFs. Furthermore, the desorption branch in their isotherms show varying levels of hysteresis and retain varying amount of water at the 0% RH point in the desorption curve. This is unexpected because these BTTB ligand-based 2-fold catenated pillared MOFs are isostructural and have similar pores. Most likely, along the same lines of M-DMOF-TM (where M = Co, Ni, Cu, and Zn, Figure 6.3), these BTTB ligand-based MOFs also have varying levels of flexibility or defects, which eventually drives the water adsorption.

These BTTB-DMBPY-based catenated pillared MOFs are stable even after exposure to 90% RH as there is negligible change in their surface area and crystallinity (Table 6.1, Figure 6.6) similar to the parent BTTB-BPY-based pillared MOFs.[65]

However, non-catenated pillared MOFs such as DMOF collapses under 60% RH[21,25,35] even when it is synthesized with the DABCO pillar ligand, which is much more basic than the BPY and DMBPY pillar ligands (Table 6.2). It should be noted that the pK_a value of BTTB (Table 6.2) is similar to the BDC ligand (pK_a ~ 3.73)[76] used for the synthesis of DMOF and catenated structures are expected to be more stable.[68] Hence, the stability of these BTTB-based pillared MOFs could be attributed to catenation present in their frameworks similar to MOF-508, which has been reported[39] to be stable too after 90% RH exposure even when the basicity of the pillar ligand is low (Table 6.2). Catenation could make the ligand displacement difficult by locking it in place within the framework.

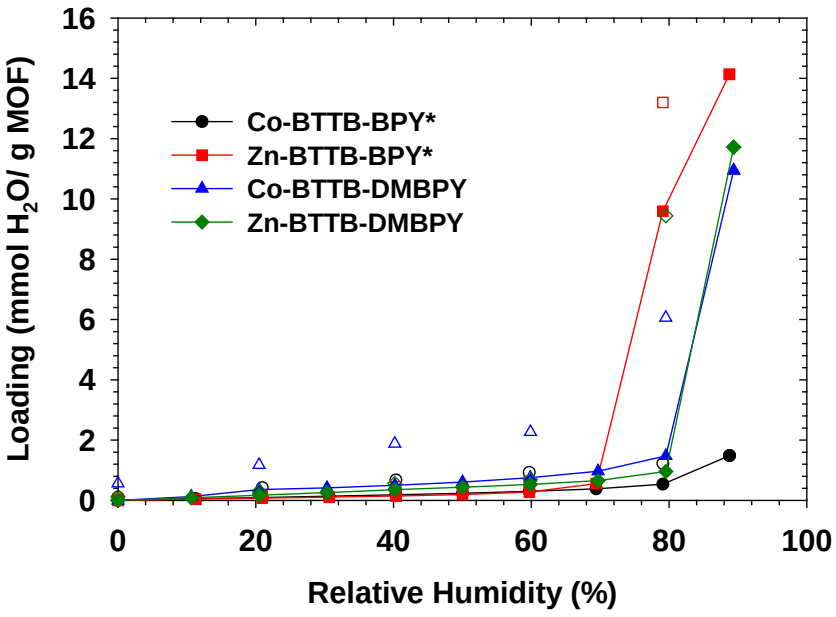

Figure 6.5 Water vapor adsorption isotherms for desolvated compounds of M-BTTB-DMBPY and M-BTTB-BPY* (closed symbols – adsorption, open symbols – desorption). Lines connecting the adsorption points are to faciliate viewing. *Reported from our previous work.[65]

Table 6.2 Comparison of pK_a Values[76] of Ligands Used in the Synthesis of Pillared MOFs.

MOF	Ligand	pK_a
M-DMOF-TM	TMBDC, DABCO	3.80, 8.86
M-BTTB-DMBPY	BTTB, DMBPY	4.01, 5.60
M-BTTB-BPY	BTTB, BPY	4.01, 4.60

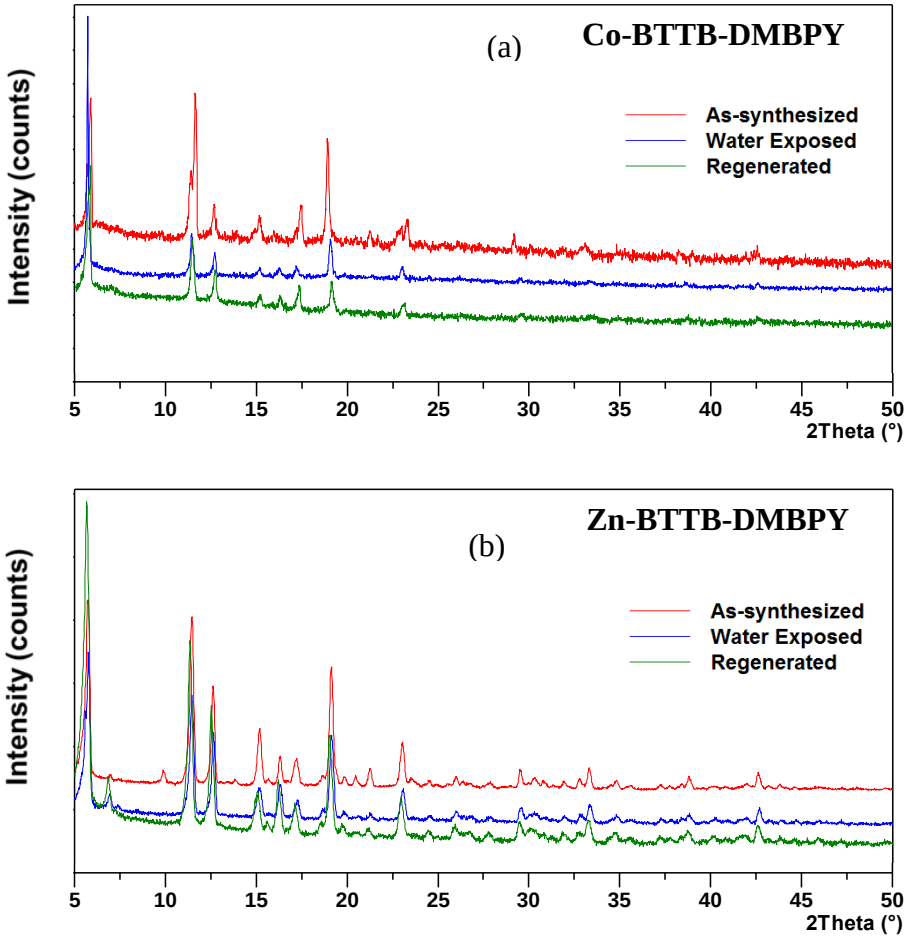

Figure 6.6 PXRD patterns for as-synthesized, water-exposed (after 90% RH), and regenerated (a) Co-BTTB-DMBPY, (b) Zn-BTTB-DMBPY.

6.4 Conclusions

In our previous reports (Chapters 3-5), we have shown that structural factors such as ligand sterics and catenation can enhance MOF stability under humid conditions. In this work, we have used these structural factors to synthesize cobalt, nickel, copper, and zinc-based new water stable pillared MOFs of similar topology. Our study shows that unlike the parent DMOF structure, which collapses under 60% RH, tetramethyl functionalized variations or DMOF-TM are remarkably stable even when they have high water vapor adsorption loadings (> 20 mmol/g at 80% RH). These methyl groups grafted on the BDC ligand shield the metal centers from water molecules. BTTB-based pillared MOFs are synthesized with bipyridyl-based pillar ligands, which have low basicity than DABCO but are still stable after exposure to 90% RH due to the presence of catenation in their frameworks similar to MOF-508, which has been reported to be stable too after 90% RH exposure. The results of this work show that by incorporating specific factors governing structural stability into the framework, we can synthesize new water stable MOFs and hence, can direct the future MOF synthesis efforts.

6.5 References

(1) Garibay, S. J.; Cohen, S. M., Isoreticular synthesis and modification of frameworks with the UiO-66 topology. *Chem Commun (Camb)* **2010,** *46* (41), 7700-2.

(2) Ferey, G., Some suggested perspectives for multifunctional hybrid porous solids. *Dalton Trans* **2009,** (23), 4400-15.

(3) Kuppler, R. J.; Timmons, D. J.; Fang, Q. R.; Li, J. R.; Makal, T. A.; Young, M. D.; Yuan, D. Q.; Zhao, D.; Zhuang, W. J.; Zhou, H. C., Potential applications of metal-organic frameworks. *Coordination Chemistry Reviews* **2009,** *253* (23-24), 3042-3066.

(4) Kitagawa, S.; Kitaura, R.; Noro, S., Functional porous coordination polymers. *Angewandte Chemie* **2004,** *43* (18), 2334-75.

(5) Keskin, S.; van Heest, T. M.; Sholl, D. S., Can metal-organic framework materials play a useful role in large-scale carbon dioxide separations? *ChemSusChem* **2010,** *3* (8), 879-91.

(6) Li, J. R.; Kuppler, R. J.; Zhou, H. C., Selective gas adsorption and separation in metal-organic frameworks. *Chem Soc Rev* **2009,** *38* (5), 1477-504.

(7) Karra, J. R.; Walton, K. S., Effect of open metal sites on adsorption of polar and nonpolar molecules in metal-organic framework Cu-BTC. *Langmuir* **2008,** *24* (16), 8620-6.

(8) Caskey, S. R.; Wong-Foy, A. G.; Matzger, A. J., Dramatic tuning of carbon dioxide uptake via metal substitution in a coordination polymer with cylindrical pores. *J Am Chem Soc* **2008,** *130* (33), 10870-1.

(9) Rowsell, J. L.; Yaghi, O. M., Effects of functionalization, catenation, and variation of the metal oxide and organic linking units on the low-pressure hydrogen adsorption properties of metal-organic frameworks. *J Am Chem Soc* **2006,** *128* (4), 1304-15.

(10) Wang, Z.; Tanabe, K. K.; Cohen, S. M., Tuning hydrogen sorption properties of metal-organic frameworks by postsynthetic covalent modification. *Chemistry* **2010,** *16* (1), 212-7.

(11) Farha, O. K.; Hupp, J. T., Rational design, synthesis, purification, and activation of metal-organic framework materials. *Acc Chem Res* **2010,** *43* (8), 1166-75.

(12) Tanabe, K. K.; Cohen, S. M., Postsynthetic modification of metal-organic frameworks--a progress report. *Chem Soc Rev* **2011,** *40* (2), 498-519.

(13) Eddaoudi, M.; Kim, J.; Rosi, N.; Vodak, D.; Wachter, J.; O'Keeffe, M.; Yaghi, O. M., Systematic design of pore size and functionality in isoreticular MOFs and their application in methane storage. *Science* **2002,** *295* (5554), 469-72.

(14) Zhou, H. C.; Long, J. R.; Yaghi, O. M., Introduction to metal-organic frameworks. *Chem Rev* **2012,** *112* (2), 673-4.

(15) Cook, T. R.; Zheng, Y. R.; Stang, P. J., Metal-organic frameworks and self-assembled supramolecular coordination complexes: comparing and contrasting the design, synthesis, and functionality of metal-organic materials. *Chem Rev* **2013,** *113* (1), 734-77.

(16) Sumida, K.; Rogow, D. L.; Mason, J. A.; McDonald, T. M.; Bloch, E. D.; Herm, Z. R.; Bae, T. H.; Long, J. R., Carbon dioxide capture in metal-organic frameworks. *Chem Rev* **2012,** *112* (2), 724-81.

(17) Czaja, A. U.; Trukhan, N.; Muller, U., Industrial applications of metal-organic frameworks. *Chemical Society Reviews* **2009,** *38* (5), 1284-1293.

(18) Burtch, N. C.; Jasuja, H.; Dubbeldam, D.; Walton, K. S., Molecular-level insight into unusual low pressure CO_2 affinity in pillared metal-organic frameworks. *J Am Chem Soc* **2013,** *135* (19), 7172-80.

(19) DeCoste, J. B.; Peterson, G. W.; Jasuja, H.; Glover, T. G.; Huang, Y. G.; Walton, K. S., Stability and degradation mechanisms of metal-organic frameworks containing the Zr6O4(OH)(4) secondary building unit. *Journal of Materials Chemistry A* **2013,** *1* (18), 5642-5650.

(20) DeCoste, J. B.; Peterson, G. W.; Schindler, B. J.; Killops, K. L.; Browe, M. A.; Mahle, J. J., The effect of water adsorption on the structure of the carboxylate containing metal-organic frameworks Cu-BTC, Mg-MOF-74, and UiO-66. *Journal of Materials Chemistry A* **2013,** *1* (38), 11922-11932.

(21) Tan, K.; Nijem, N.; Canepa, P.; Gong, Q.; Li, J.; Thonhauser, T.; Chabal, Y. J., Stability and Hydrolyzation of Metal Organic Frameworks with Paddle-Wheel SBUs upon Hydration. *Chemistry of Materials* **2012,** *24* (16), 3153-3167.

(22) Greathouse, J. A.; Allendorf, M. D., The interaction of water with MOF-5 simulated by molecular dynamics. *J Am Chem Soc* **2006,** *128* (33), 10678-9.

(23) Li, Y.; Yang, R. T., Gas adsorption and storage in metal-organic framework MOF-177. *Langmuir* **2007,** *23* (26), 12937-44.

(24) Low, J. J.; Benin, A. I.; Jakubczak, P.; Abrahamian, J. F.; Faheem, S. A.; Willis, R. R., Virtual high throughput screening confirmed experimentally: porous coordination polymer hydration. *J Am Chem Soc* **2009,** *131* (43), 15834-42.

(25) Schoenecker, P. M.; Carson, C. G.; Jasuja, H.; Flemming, C. J. J.; Walton, K. S., Effect of Water Adsorption on Retention of Structure and Surface Area of Metal–Organic Frameworks. *Industrial & Engineering Chemistry Research* **2012,** *51* (18), 6513-6519.

(26) Kusgens, P.; Rose, M.; Senkovska, I.; Frode, H.; Henschel, A.; Siegle, S.; Kaskel, S., Characterization of metal-organic frameworks by water adsorption. *Microporous and Mesoporous Materials* **2009,** *120* (3), 325-330.

(27) Cychosz, K. A.; Matzger, A. J., Water stability of microporous coordination polymers and the adsorption of pharmaceuticals from water. *Langmuir* **2010,** *26* (22), 17198-202.

(28) Choi, H. J.; Dinca, M.; Dailly, A.; Long, J. R., Hydrogen storage in water-stable metal-organic frameworks incorporating 1,3-and 1,4-benzenedipyrazolate. *Energy & Environmental Science* **2010,** *3* (1), 117-123.

(29) Cavka, J. H.; Jakobsen, S.; Olsbye, U.; Guillou, N.; Lamberti, C.; Bordiga, S.; Lillerud, K. P., A new zirconium inorganic building brick forming metal organic frameworks with exceptional stability. *J Am Chem Soc* **2008,** *130* (42), 13850-1.

(30) Dietzel, P. D.; Morita, Y.; Blom, R.; Fjellvag, H., An in situ high-temperature single-crystal investigation of a dehydrated metal-organic framework compound and field-induced magnetization of one-dimensional metal-oxygen chains. *Angewandte Chemie* **2005,** *44* (39), 6354-8.

(31) Ma, D.; Li, Y.; Li, Z., Tuning the moisture stability of metal-organic frameworks by incorporating hydrophobic functional groups at different positions of ligands. *Chem Commun (Camb)* **2011,** *47* (26), 7377-9.

(32) Yang, J.; Grzech, A.; Mulder, F. M.; Dingemans, T. J., Methyl modified MOF-5: a water stable hydrogen storage material. *Chem Commun (Camb)* **2011,** *47* (18), 5244-6.

(33) Nguyen, J. G.; Cohen, S. M., Moisture-resistant and superhydrophobic metal-organic frameworks obtained via postsynthetic modification. *J Am Chem Soc* **2010,** *132* (13), 4560-1.

(34) Serre, C., Superhydrophobicity in highly fluorinated porous metal-organic frameworks. *Angewandte Chemie* **2012,** *51* (25), 6048-50.

(35) Liang, Z. J.; Marshall, M.; Chaffee, A. L., CO_2 adsorption, selectivity and water tolerance of pillared-layer metal organic frameworks. *Microporous and Mesoporous Materials* **2010,** *132* (3), 305-310.

(36) Kondo, A.; Daimaru, T.; Noguchi, H.; Ohba, T.; Kaneko, K.; Kanoh, H., Adsorption of water on three-dimensional pillared-layer metal organic frameworks. *J Colloid Interface Sci* **2007,** *314* (2), 422-6.

(37) Jasuja, H.; Huang, Y. G.; Walton, K. S., Adjusting the stability of metal-organic frameworks under humid conditions by ligand functionalization. *Langmuir* **2012,** *28* (49), 16874-80.

(38) Jasuja, H.; Burtch, N. C.; Huang, Y. G.; Cai, Y.; Walton, K. S., Kinetic water stability of an isostructural family of zinc-based pillared metal-organic frameworks. *Langmuir* **2013,** *29* (2), 633-42.

(39) Jasuja, H.; Walton, K. S., Effect of catenation and basicity of pillared ligands on the water stability of MOFs. *Dalton Trans* **2013,** *42* (43), 15421-6.

(40) Decoste, J. B.; Peterson, G. W.; Smith, M. W.; Stone, C. A.; Willis, C. R., Enhanced Stability of Cu-BTC MOF via Perfluorohexane Plasma-Enhanced Chemical Vapor Deposition. *Journal of the American Chemical Society* **2012,** *134* (3), 1486-1489.

(41) Jasuja, H.; Zang, J.; Sholl, D. S.; Walton, K. S., Rational Tuning of Water Vapor and CO_2 Adsorption in Highly Stable Zr-Based MOFs. *J. Phys. Chem. C* **2012,** *116* (44), 23526-23532.

(42) Jasuja, H.; Walton, K. S., Experimental Study of CO_2, CH_4, and Water Vapor Adsorption on a Dimethyl-Functionalized UiO-66 Framework. *The Journal of Physical Chemistry C* **2013,** *117* (14), 7062-7068.

(43) Kaye, S. S.; Dailly, A.; Yaghi, O. M.; Long, J. R., Impact of preparation and handling on the hydrogen storage properties of Zn4O(1,4-benzenedicarboxylate)3 (MOF-5). *J Am Chem Soc* **2007,** *129* (46), 14176-7.

(44) Kang, I. J.; Khan, N. A.; Haque, E.; Jhung, S. H., Chemical and thermal stability of isotypic metal-organic frameworks: effect of metal ions. *Chemistry* **2011,** *17* (23), 6437-42.

(45) Bellarosa, L.; Calero, S.; Lopez, N., Early stages in the degradation of metal-organic frameworks in liquid water from first-principles molecular dynamics. *Physical chemistry chemical physics : PCCP* **2012,** *14* (20), 7240-5.

(46) Han, S. S.; Choi, S. H.; van Duin, A. C., Molecular dynamics simulations of stability of metal-organic frameworks against H2O using the ReaxFF reactive force field. *Chem Commun (Camb)* **2010,** *46* (31), 5713-5.

(47) Colombo, V.; Galli, S.; Choi, H. J.; Han, G. D.; Maspero, A.; Palmisano, G.; Masciocchi, N.; Long, J. R., High thermal and chemical stability in pyrazolate-bridged metal-organic frameworks with exposed metal sites. *Chemical Science* **2011,** *2* (7), 1311-1319.

(48) Soubeyrand-Lenoir, E.; Vagner, C.; Yoon, J. W.; Bazin, P.; Ragon, F.; Hwang, Y. K.; Serre, C.; Chang, J. S.; Llewellyn, P. L., How water fosters a remarkable 5-fold increase in low-pressure CO_2 uptake within mesoporous MIL-100(Fe). *J Am Chem Soc* **2012,** *134* (24), 10174-81.

(49) Wu, T.; Shen, L.; Luebbers, M.; Hu, C.; Chen, Q.; Ni, Z.; Masel, R. I., Enhancing the stability of metal-organic frameworks in humid air by incorporating water repellent functional groups. *Chem Commun (Camb)* **2010,** *46* (33), 6120-2.

(50) Cai, Y.; Zhang, Y. D.; Huang, Y. G.; Marder, S. R.; Walton, K. S., Impact of Alkyl-Functionalized BTC on Properties of Copper-Based Metal-Organic Frameworks. *Crystal Growth & Design* **2012,** *12* (7), 3709-3713.

(51) Taylor, J. M.; Vaidhyanathan, R.; Iremonger, S. S.; Shimizu, G. K., Enhancing water stability of metal-organic frameworks via phosphonate monoester linkers. *J Am Chem Soc* **2012,** *134* (35), 14338-40.

(52) Liu, J.; Benin, A. I.; Furtado, A. M.; Jakubczak, P.; Willis, R. R.; LeVan, M. D., Stability effects on CO_2 adsorption for the DOBDC series of metal-organic frameworks. *Langmuir* **2011,** *27* (18), 11451-6.

(53) Jeremias, F.; Lozan, V.; Henninger, S. K.; Janiak, C., Programming MOFs for water sorption: amino-functionalized MIL-125 and UiO-66 for heat transformation and heat storage applications. *Dalton Trans* **2013**.

(54) Bon, V.; Senkovskyy, V.; Senkovska, I.; Kaskel, S., Zr(iv) and Hf(iv) based metal-organic frameworks with reo-topology. *Chemical Communications* **2012,** *48* (67), 8407-8409.

(55) Yang, C.; Kaipa, U.; Mather, Q. Z.; Wang, X.; Nesterov, V.; Venero, A. F.; Omary, M. A., Fluorous metal-organic frameworks with superior adsorption and hydrophobic properties toward oil spill cleanup and hydrocarbon storage. *J Am Chem Soc* **2011,** *133* (45), 18094-7.

(56) Li, T.; Chen, D.-L.; Sullivan, J. E.; Kozlowski, M. T.; Johnson, J. K.; Rosi, N. L., Systematic modulation and enhancement of CO_2 : N_2 selectivity and water stability in an isoreticular series of bio-MOF-11 analogues. *Chemical Science* **2013,** *4* (4), 1746-1755.

(57) Makal, T. A.; Wang, X.; Zhou, H.-C., Tuning the Moisture and Thermal Stability of Metal–Organic Frameworks through Incorporation of Pendant Hydrophobic Groups. *Crystal Growth & Design* **2013,** *13* (11), 4760-4768.

(58) Liu, H.; Zhao, Y.; Zhang, Z.; Nijem, N.; Chabal, Y. J.; Peng, X.; Zeng, H.; Li, J., Ligand Functionalization and Its Effect on CO_2 Adsorption in Microporous Metal–Organic Frameworks. *Chemistry – An Asian Journal* **2013,** *8* (4), 778-785.

(59) Liu, H.; Zhao, Y. G.; Zhang, Z. J.; Nijem, N.; Chabal, Y. J.; Zeng, H. P.; Li, J., The Effect of Methyl Functionalization on Microporous Metal-Organic Frameworks' Capacity and Binding Energy for Carbon Dioxide Adsorption. *Advanced Functional Materials* **2011,** *21* (24), 4754-4762.

(60) Jiang, H.-L.; Feng, D.; Liu, T.-F.; Li, J.-R.; Zhou, H.-C., Pore Surface Engineering with Controlled Loadings of Functional Groups via Click Chemistry in Highly Stable Metal–Organic Frameworks. *Journal of the American Chemical Society* **2012,** *134* (36), 14690-14693.

(61) Bon, V.; Senkovska, I.; Baburin, I. A.; Kaskel, S., Zr- and Hf-Based Metal–Organic Frameworks: Tracking Down the Polymorphism. *Crystal Growth & Design* **2013,** *13* (3), 1231-1237.

(62) Guillerm, V.; Ragon, F.; Dan-Hardi, M.; Devic, T.; Vishnuvarthan, M.; Campo, B.; Vimont, A.; Clet, G.; Yang, Q.; Maurin, G.; Ferey, G.; Vittadini, A.; Gross, S.; Serre, C., A series of isoreticular, highly stable, porous zirconium oxide based metal-organic frameworks. *Angewandte Chemie* **2012,** *51* (37), 9267-71.

(63) Chen, T.-H.; Popov, I.; Zenasni, O.; Daugulis, O.; Miljanic, O. S., Superhydrophobic perfluorinated metal-organic frameworks. *Chemical Communications* **2013,** *49* (61), 6846-6848.

(64) Li, H.; Shi, W.; Zhao, K.; Li, H.; Bing, Y.; Cheng, P., Enhanced Hydrostability in Ni-Doped MOF-5. *Inorganic Chemistry* **2012,** *51* (17), 9200-9207.

(65) Karra, J. Development of porous metal organic frameworks for gas adsorption applications. Georgia Institute of Technology, Atlanta, 2011.

(66) Walton, K. S.; Snurr, R. Q., Applicability of the BET method for determining surface areas of microporous metal-organic frameworks. *J Am Chem Soc* **2007,** *129* (27), 8552-6.

(67) Chun, H.; Dybtsev, D. N.; Kim, H.; Kim, K., Synthesis, X-ray crystal structures, and gas sorption properties of pillared square grid nets based on paddle-wheel motifs: implications for hydrogen storage in porous materials. *Chemistry* **2005,** *11* (12), 3521-9.

(68) Zhang, J.; Wojtas, L.; Larsen, R. W.; Eddaoudi, M.; Zaworotko, M. J., Temperature and concentration control over interpenetration in a metal-organic material. *J Am Chem Soc* **2009,** *131* (47), 17040-1.

(69) Haldoupis, E.; Nair, S.; Sholl, D. S., Efficient Calculation of Diffusion Limitations in Metal Organic Framework Materials: A Tool for Identifying Materials for Kinetic Separations. *Journal of the American Chemical Society* **2010,** *132* (21), 7528-7539.

(70) Ng, E. P.; Mintova, S., Nanoporous materials with enhanced hydrophilicity and high water sorption capacity. *Microporous and Mesoporous Materials* **2008,** *114* (1-3), 1-26.

(71) Rudisill, E. N.; Hacskaylo, J. J.; Levan, M. D., Coadsorption of Hydrocarbons and Water on Bpl Activated Carbon. *Industrial & Engineering Chemistry Research* **1992,** *31* (4), 1122-1130.

(72) Oh, J. S.; Shim, W. G.; Lee, J. W.; Kim, J. H.; Moon, H.; Seo, G., Adsorption equilibrium of water vapor on mesoporous materials. *Journal of Chemical and Engineering Data* **2003,** *48* (6), 1458-1462.

(73) Wu, H.; Chua, Y. S.; Krungleviciute, V.; Tyagi, M.; Chen, P.; Yildirim, T.; Zhou, W., Unusual and Highly Tunable Missing-Linker Defects in Zirconium Metal–Organic Framework UiO-66 and Their Important Effects on Gas Adsorption. *Journal of the American Chemical Society* **2013,** *135* (28), 10525-10532.

(74) Canivet, J.; Bonnefoy, J.; Daniel, C.; Legrand, A.; Coasne, B.; Farrusseng, D., Structure-property relationships of water adsorption in Metal-Organic Frameworks. *New Journal of Chemistry* **2014** (DOI: 10.1039/C4NJ00076E).

(75) Wiersum, A. D.; Soubeyrand-Lenoir, E.; Yang, Q.; Moulin, B.; Guillerm, V.; Yahia, M. B.; Bourrelly, S.; Vimont, A.; Miller, S.; Vagner, C.; Daturi, M.; Clet, G.; Serre, C.; Maurin, G.; Llewellyn, P. L., An evaluation of UiO-66 for gas-based applications. *Chem Asian J* **2011,** *6* (12), 3270-80.

(76) Hilal, S., Karickhoff, S. W., Carreira, L. A. , A Rigorous Test for SPARC's Chemical Reactivity Models: Estimation of More Than 4300 Ionization pKa's. *Quant. Struc. Act. Rel.* **1995,** *14*, 348.

CHAPTER 7

EVALUATION OF MOFS FOR AIR PURIFICATION AND AIR QUALITY CONTROL APPLICATIONS: AMMONIA REMOVAL FROM AIR

This work was conducted in collaboration with The U.S. Army Edgewood Chemical Biological Center (ECBC) - Gregory W. Peterson, Jared B. Decoste, and Matthew A. Browe.

7.1 Introduction

Activated carbons and zeolites have been a focal point of research in the field of porous materials for decades now due to various uses in applications ranging from petrochemicals and catalysis to adsorption-based selective separations.[1,2] However, limited new developments in synthetic zeolites and difficulties in controlling pore size distributions in activated carbons have led to the emergence of metal-organic frameworks (MOFs) as new contenders in the last 15 years.[3,4] MOFs are made up of metal clusters, which are linked to each other by organic ligands.[3] These hybrid porous materials have record-breaking values of surface areas and pore volumes, uniform pore sizes, and diverse chemical functionalities.[5] Moreover, there are infinite sets of structural possibilities with diverse topologies considering the wide variety of metal groups and organic ligands available to choose from.[6,7] Hence, MOFs are being considered for use in a variety of applications such as air purification, gas storage, gas separation, catalysis, magnetism, photoluminescence, nonlinear optics, gas sensing, and drug delivery.[8-10]

Among the aforementioned applications, air purification and air quality control are important topics, because existing chemical, biological, radiological, and nuclear (CBRN) filters that use an impregnated activated carbon, marketed by Calgon Carbon Corporation,[11] do a poor job of filtering toxic industrial chemicals (TICs) and chemical warfare agents (CWAs) such as ammonia, carbon disulfide, ethylene oxide, and formaldehyde.[12] Ammonia is among the high-hazard gases, has a high vapor pressure of 7600 mm Hg at 25 ^{o}C,[12] and is also one of the most highly-produced inorganic chemicals because of its various usages in commercial and military applications, e.g., ammonia is used in the production of pharmaceuticals, explosives, commercial cleaning products, and fertilizers with the latter alone consumes around 80% of total ammonia produced. There are numerous large-scale ammonia production plants worldwide with China, India, Russia, and the United States as the main contributors.[13] Hence, there is an urgent need for the search of proper adsorbents for improvements in the performance of the current CBRN filters towards TICs such as ammonia. There are a few publications in the literature reporting TIC adsorption in MOFs due to the defense-based nature of this application. Work done by Yaghi et al.[14] on TICs such as sulfur dioxide and ammonia shows that MOFs have a great potential to become next-generation filter media as they outperform the traditional porous materials such as BPL carbon, and zeolite 13X. Cu-BTC (HKUST-1) and Mg-MOF-74 have displayed high ammonia capacities (greater than ~ 5 mmol/g) due to the unsaturated metal centers; nevertheless, their structures collapse upon exposure to humid environments.[15,16] Stability of MOFs under humid environments is a fundamental requirement for their use in CBRN filters. Mu evaluated the effect of functional groups grafted in the pores of MOFs on the adsorptive ammonia removal

through adsorption breakthrough measurements performed at ECBC.[17] MOFs with –COOH and $–NH_2$ functionality were examined for their ammonia adsorption and it was found that the carboxylic functional group (–COOH) is more effective than the amine group ($–NH_2$) because ammonia is basic in nature while –COOH is acidic. However, the best performing MOF (CuBTB, which has one uncoordinated –COOH functional group) in his study is also unstable in humid environments. Quantitative comparison of the performance of these MOFs relative to existing CBRN filter media towards TIC filtration is not available due to the sensitive nature of this application but Schoenecker along with UTRC (United Technologies Research Center) has seen better performance by a variety of MOFs over existing CBRN filter media for TICs such as ammonia, formaldehyde, and methyl amine.[18] Recently, Decoste et al.[19] has reported the first review article summarizing TIC removal from air by using MOFs. It was suggested that functional groups such as $–NH_2$, –OH, and –COOH should be incorporated in the water stable MOF systems as these groups have been shown to interact strongly with ammonia.

To further confirm the effectiveness of –COOH functionality in capturing ammonia, we considered the ZnBTTB (Figure 7.1, which has two uncoordinated –COOH functional groups) MOF synthesized by Karra.[20] However, as discussed in previous Chapters, poor stability under humid conditions has plagued this MOF too. The Zr-based UiO-66 or Zr-BDC MOF (Figure 7.2, Chapter 2 for structural details) possesses exceptional stability[3,21-23] and is a good platform material with potential applications in a wide variety of small molecule gas separations.[23,24] Hence, in this Chapter we have mainly focused on investigating the performance of various functionalized variations of the UiO-66 MOF towards ammonia removal from air. Functionalized variations

considered here are: UiO-66-OH, UiO-66-$(OH)_2$, UiO-66-NO_2, UiO-66-NH_2, UiO-66-SO_3H, and UiO-66-$(COOH)_2$. We expect that the UiO-66 variants with acidic functional group such as –COOH and -SO_3H should have higher interactions with ammonia. We have also considered two water stable DMOFs (DMOF-A, DMOF-TM2) discovered from our systematic water stability studies described in Chapters 3 and 4. The overall goal is to identify ammonia-selective, water stable MOF materials, that can be run in series with existing filters so that now it becomes possible to capture high vapor pressure TICs such as ammonia.

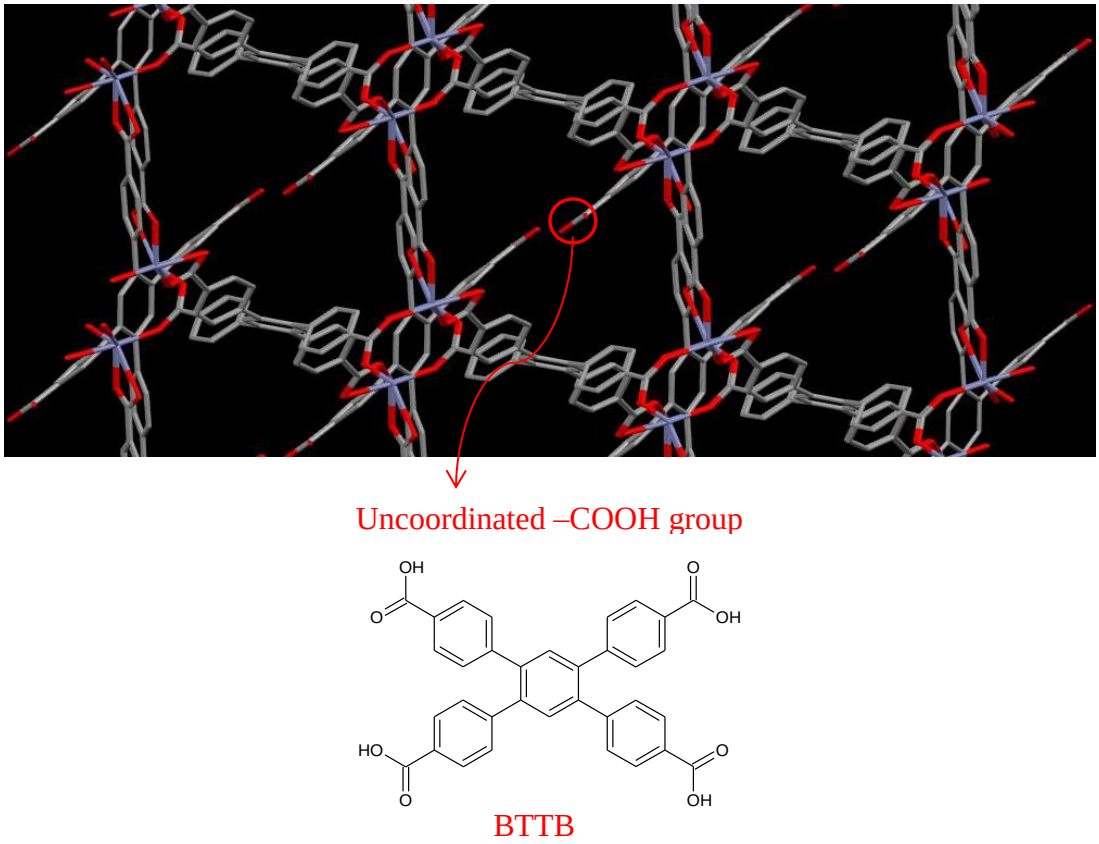

Figure 7.1 Top: Illustration of the ZnBTTB framework structure (C- Grey, Zn- Purple, O- Red, and H- omitted for clarity). Bottom: Structure of BTTB (4,4',4'',4''-benzene-1,2,4,5-tetrayl tetrabenzoic acid) ligand used in the synthesis of ZnBTTB MOF.

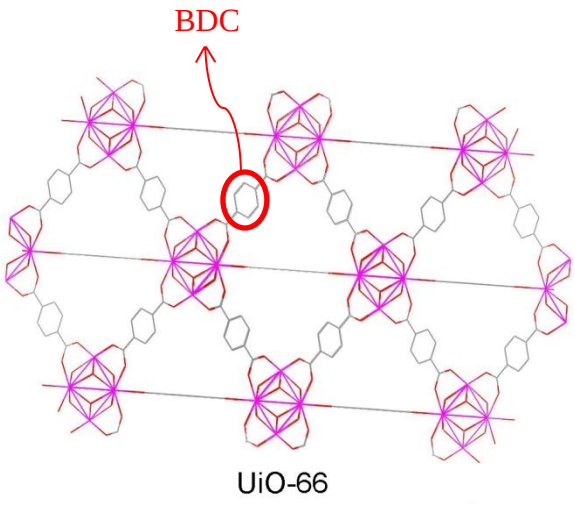

Figure 7.2 Illustration of the UiO-66 framework structure (BDC- 1,4-benzene dicarboxylic acid, C- Grey, Zr- Pink, O- Red, and H- omitted for clarity).

7.2 Experimental Section

7.2.1 Materials

All the commercially available solvents and chemicals were used as received without further purification. All the MOFs were synthesized solvothermally. Ligands used in the synthesis of the UiO-66 analogues are shown in Figure 7.3.

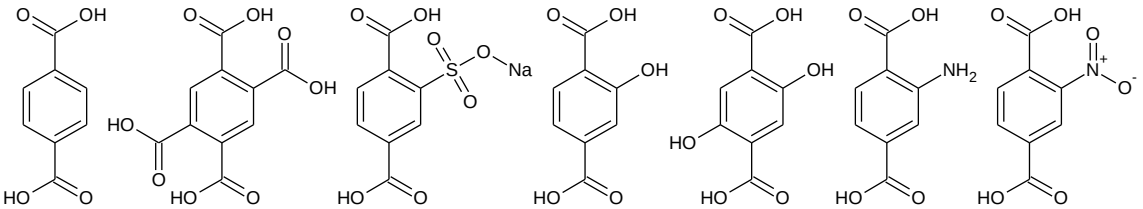

Figure 7.3 Ligands utilized in synthesis of the UiO-66 analogues.

ZnBTTB. Synthesis of this MOF was performed as reported by Karra,[20] i.e., $Zn(NO_3)_2 \cdot 6H_2O$ (59.4 mg, 0.2 mmol), BTTB (55.8 mg, 0.1 mmol) were mixed in 2 mL of N,N′-diethylformamide (DEF), 2 mL of ethanol, 1 mL of water, and 2 drops of 1N HCl. This resulting mixture was sealed in a 23 mL Teflon-lined stainless steel reactor and heated at 100 °C for 4 days. The solution was then cooled to room temperature in air, and the resulting solid was filtered and repeatedly washed with DEF. Activated sample of ZnBTTB was prepared by heating the as-synthesized sample at 250 °C for 2 h under vacuum.

DMOF-A and DMOF-TM2. Synthesis and activation of both of these MOFs was carried out as explained in Chapter 3.

UiO-66. UiO-66 was synthesized as reported by Peterson et al.,[25] i.e., 19.068 mmoles of zirconium (IV) chloride and 19.068 mmoles of 1,4-benzenedicarboxylic acid were mixed in 742 mL of dimethyl formamide (DMF) at room temperature in a glass beaker. The resulting mixture was divided in equal parts into three 500 mL glass jars. The jars were placed in a pre-heated oven at 120°C for 24 hours. The solution was cooled to room temperature, and the resulting solid was repeatedly washed with DMF. The dried as-synthesized sample was activated by heating it at 200 ^oC under vacuum overnight.

UiO-66-NO_2 and UiO-66-NH_2. UiO-66-NO_2 and UiO-66-NH_2 were synthesized in a similar fashion as reported by Cohen et al.,[3] i.e., equal molar amounts (0.35 mmol) of $ZrCl_4$ and ligand [UiO-66-NO_2: 2-nitro-1,4-benzenedicarboxylic acid (BDC-NO_2), UiO-66-NH_2: 2-amino-1,4-benzenedicarboxylic acid (BDC-NH_2)] were combined in 4 mL DMF and the resulting mixture was heated in a Teflon lined autoclave at 120 ^oC for 24 hrs. After the solution was cooled to room temperature in air, the resulting solid was

filtered and repeatedly washed with DMF. The dried as-synthesized samples of UiO-66-NO_2 and UiO-66-NH_2 were activated by heating them overnight at 170 ^oC and 200 ^oC respectively under vacuum.

UiO-66-X (where X = -OH, -$(OH)_2$, -SO_3H, -$(COOH)_2$). UiO-66-X variants were synthesized as reported by Biswas et al.,[26] i.e., equal molar amounts (0.31 mmol) of $ZrOCl_2.8H_2O$ and ligand [UiO-66-OH: 2-hydroxy-1,4-benzenedicarboxylic acid (BDC-OH), UiO-66-$(OH)_2$: 2,5-dihydroxy-1,4-benzenedicarboxylic acid (BDC-$(OH)_2$), UiO-66-SO_3H: 2-sulfo-1,4-benzenedicarboxylic acid monosodium salt (BDC-SO_3Na, protonates during synthesis due to an acidic reaction medium), and UiO-66-$(COOH)_2$: 1,2,4,5-benzenetetracarboxylic acid (BDC-$(COOH)_2$)] were combined in 3 mL of N,N′-dimethylacetamide (DMA) and 1.2 mL of formic acid. The resulting mixture was transferred to Teflon lined stainless steel reactors and heated in a programmable oven to 150 °C at a rate of 2.2 °C min^{-1}, held at this temperature for 24 h, then cooled to room temperature at a rate of 2.2 °C min^{-1}. The as-synthesized samples of UiO-66-X were washed with acetone and DMF followed by solvent exhange with methanol. These solvent exchanged samples were activated by heating them overnight at 65 ^oC under vacuum.

Before shipping these MOFs to our collaborator's facility in Maryland for breakthrough measurements, structures of these MOFs were confirmed via PXRD and BET modelling of N_2 adsorption at 77 K.

7.2.2 Powder X-Ray Diffraction

Powder X-ray diffraction patterns (PXRD) were recorded on a X'Pert X-ray PANalytical diffractometer with an X'celerator module using Cu Kα (λ = 1.5418 Å)

radiation at room temperature, with a step size of 0.02˚ in two theta (2θ) over a range of 5-50 degrees. Zero-background sample holders were used to minimize background scattering. PXRD patterns of as-synthesized UiO-66-X (where X = $-NH_2$, $-NO_2$, -OH, $-(OH)_2$, $-SO_3H$, $-(COOH)_2$) are compared with pattern simulated from the single-crystal structure of UiO-66 (Figure 7.4). Figure 7.4 confirms that the UiO-66-X variants are crystalline and isostructural to the parent UiO-66 MOF.

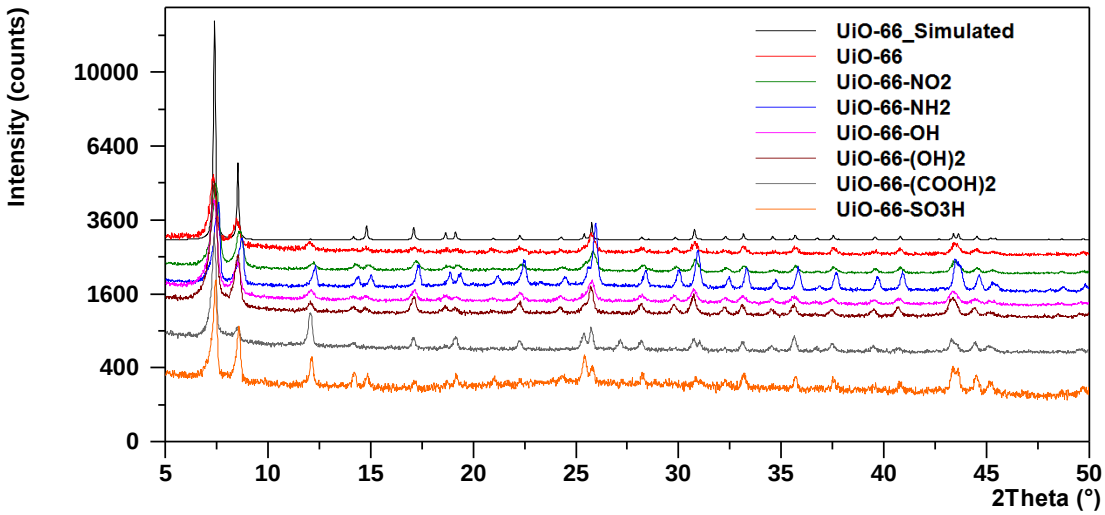

Figure 7.4 Comparison between PXRD patterns of as-synthesized UiO-66, UiO-66-X variants, and theoretical pattern of UiO-66 simulated from single crystal data.

7.2.3 Nitrogen Adsorption Measurements

Nitrogen adsorption isotherms were measured at 77 K for each activated MOF sample using a Quadrasorb system from Quantachrome instruments. To calculate specific surface areas, BET analysis was performed in the low pressure range ($P/P_o < 0.05$) as suggested by Walton et. al[27] for MOFs. Samples were activated overnight at their

respective activation temperatures as mentioned in section 7.2.1. As expected, BET analysis of N_2 adsorption at 77 K on the activated UiO-66-X samples show that functionalization leads to reduced porosity (Table 7.1) compared to the parent MOF. Entry to the internal pores of the parent UiO-66 MOF is limited by triangular windows of 6 Å.[20] However, in the UiO-66-X (where X = $-NH_2$, $-NO_2$, -OH, $-(OH)_2$, $-SO_3H$, $-(COOH)_2$) variants functionalization should further reduce the window opening.

7.2.4 Ammonia Breakthrough Measurements

Samples were shipped to our collaborator's facility in Maryland, USA for breakthrough measurements and were evaluated against ammonia in a microbreakthrough system, which has been detailed elsewhere.[14b] Testing was conducted under dry (0% RH) and humid (80% RH) conditions at 20 ^{o}C. All samples were activated for 1 hour under flowing air at their respective activation temperatures. For the humid tests, samples were subsequently pre-equilibrated at 80% RH for 2 hours. A chemical ballast was pressurized with a known amount of ammonia such that when mixed with a diluent stream at 0% RH and atmospheric pressure, a concentration of 1,000 or 2,000 mg/m^3 (1,438 or 2,876 ppm) resulted. A feed flow rate of 20 mL/min was used for all the breakthrough experiments. Adsorbents were packed in a 4 mm i.d. glass fritted tube to a constant height of approximately 4 mm, resulting in equivalent volumes of material tested. The effluent concentration was monitored continuously using a Hewlett Packard (HP) 5890 gas chromatograph equipped with a photoionization detector.

Breakthrough curves were integrated to determine the ammonia loading/capacity on each sample. It is important to note that, although we refer to these as "breakthrough" curves, they do not represent the mass transfer that will be associated with an end item

filter since samples used in this work are in powder form. These tests are used as a quick screening tool to determine a capacity, which should be similar to a single isotherm point. Desorption is then performed to determine the type of interaction between the material and adsorbate, with all samples desorbed to below 20% of their saturated breakthrough values. Calculated ammonia capacities typically have an error of approximately 10 % associated with the system. Screening is conducted to identify materials exhibiting substantial capacity for ammonia and/or other toxic chemicals. The current goal of the air purification program is to identify materials with capacities of 0.1 g of chemical per g of adsorbent; for ammonia, this equates to approximately 6 mmol/g.

7.3 Results and Discussion

Figures 7.5 and 7.6 present ammonia breakthrough curves at a feed concentration of 1,000 mg/m^3 (1,438 ppm) under dry and humid (80% RH) conditions respectively. Under dry conditions, ZnBTTB MOF shows ammonia capacity of ~4.6 mmol/g (higher than CuBTB,[17] which has one uncoordinated –COOH group, Table 7.1) even though it has a BET surface area of ~ 450 m^2/g. Most likely, this is because of two uncoordinated –COOH groups grafted in the pores whereas DMOF-A & DMOF-TM2 showed negligible capacity (< 0.5 mmol/g, Table 7.1) for ammonia as there is no functional site for ammonia to adsorb. It should be noted that higher interactions of ammonia with the water-unstable CuBTB and ZnBTTB MOFs under dry conditions could also be due to ammonia chemically reacting with the framework similar to MOF-5 and MOF-177.[28] However, we did not characterize MOFs post ammonia exposure in this work. Their ammonia capacities increased to ~20 mmol/g, ~1 mmol/g, and ~4.6 mmol/g respectively under humid conditions possibly due to ammonia chemically reacting with the

frameworks of the water unstable ZnBTTB MOF[20] and kinetically stable MOFs DMOF-A and DMOF-TM2 (Chapters 3 and 4). Unusual shapes (additional steps, Figure 7.6) of breakthrough curves qualitatively infer that MOFs such as DMOF-TM2 and ZnBTTB decompose in the humid ammonia stream.

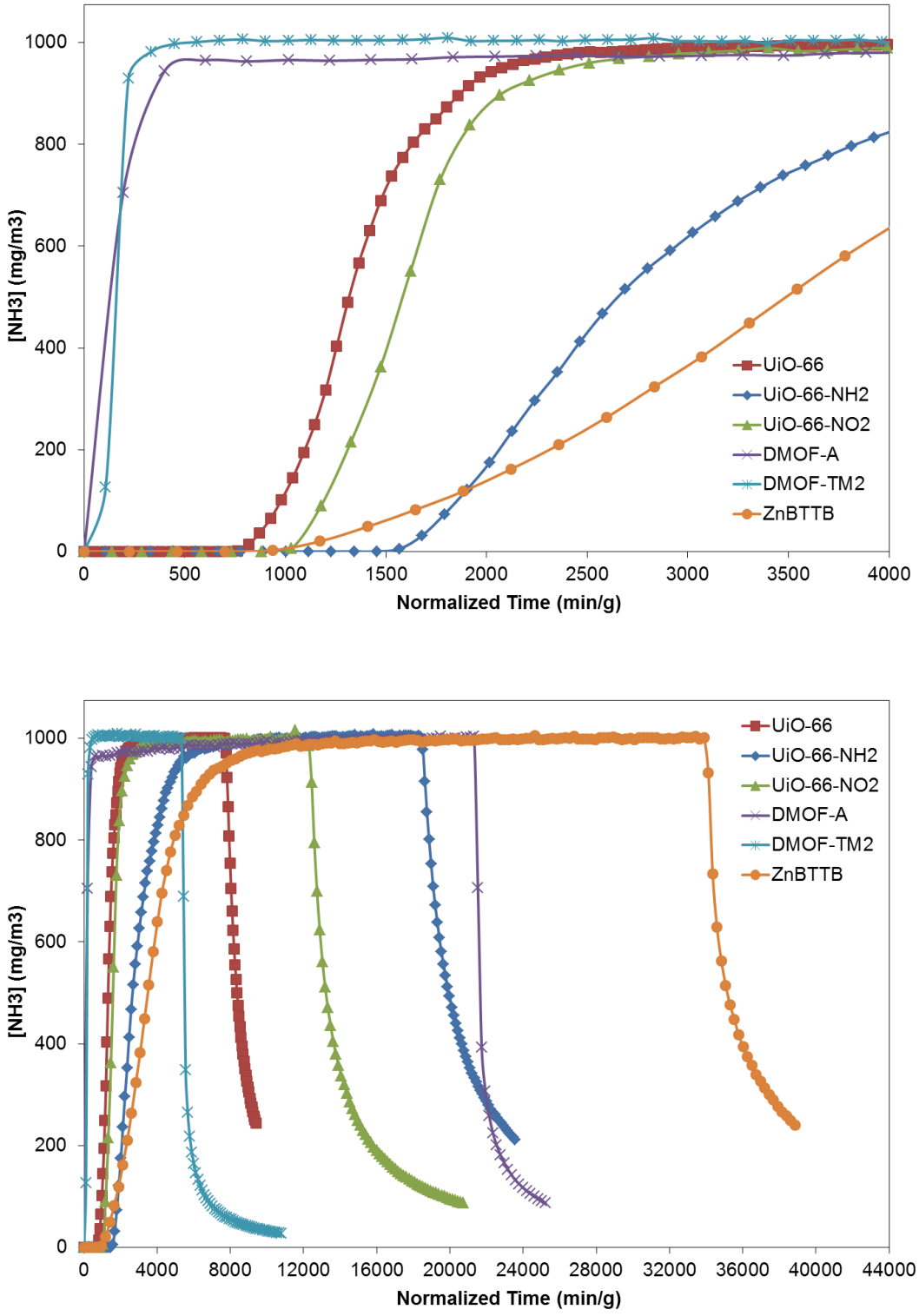

Figure 7.5 NH_3 breakthrough curves (top: time up to 4,000 min/g, bottom: whole time range) under dry air conditions at feed concentration of 1,000 mg/m^3 (1,438 ppm).

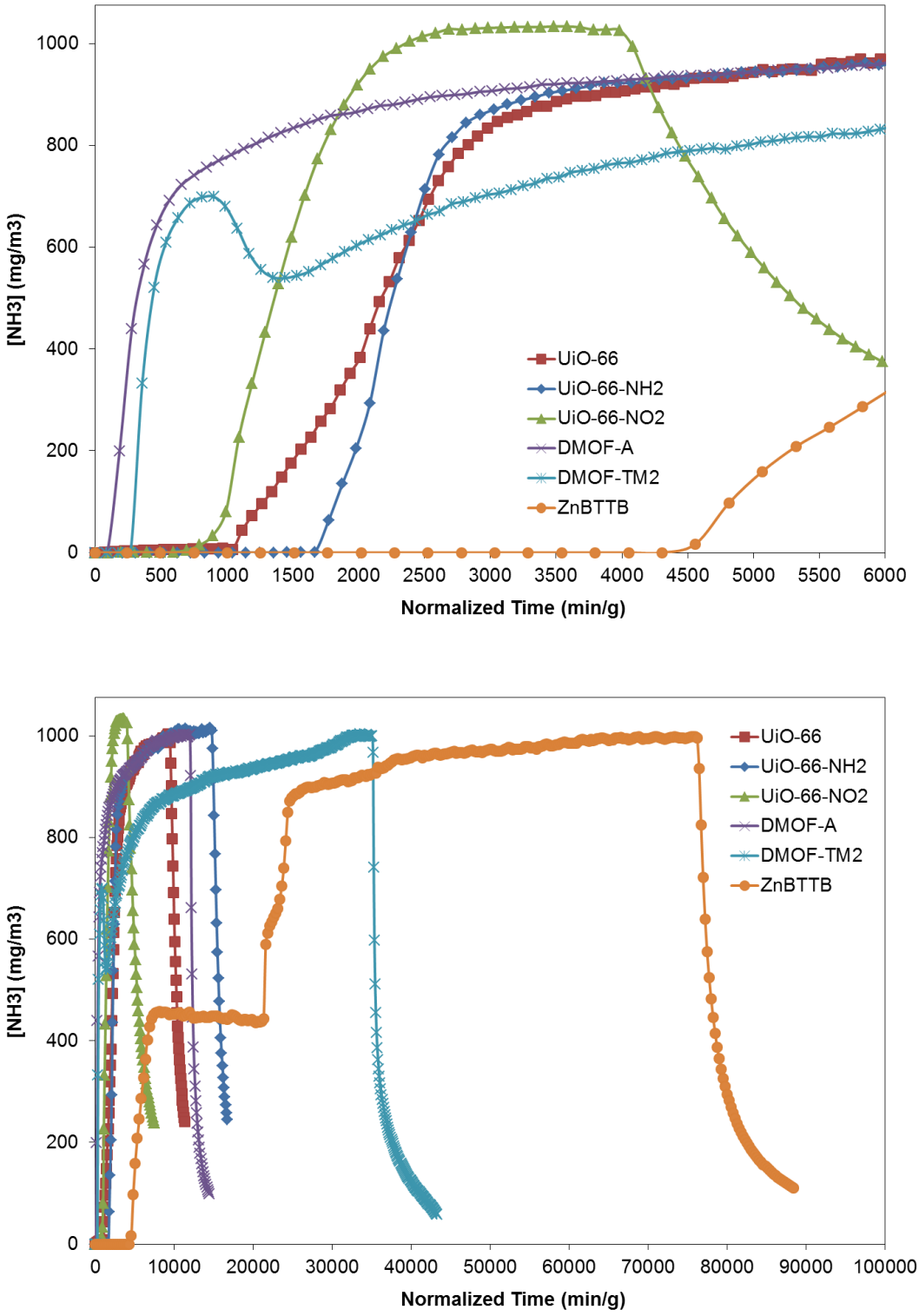

Figure 7.6 NH_3 breakthrough curves (top: time up to 6,000 min/g, bottom: whole time range) under humid (80% RH) air conditions at feed concentration of 1,000 mg/m^3 (1,438 ppm).

As mentioned before, these breakthrough tests are used as a quick screening tool to determine a capacity, similar to a single isotherm point. Hence, our collaborators increased the feed concentration to 2,000 mg/m^3, because it quickens the turnaround time for samples and capacities should be relatively unaffected. Our collaborators have tested a few different materials such as UiO-66 and UiO-66-NH_2 at 2,000 mg/m^3, and obtained capacities similar to those reported in Table 7.1 for UiO-66, UiO-66-NH_2 at 1,000 mg/m^3.[29] Figures 7.7 and 7.8 present ammonia breakthrough curves for UiO-66-OH, UiO-66-$(OH)_2$, UiO-66-SO_3H, and UiO-66-$(COOH)_2$ at a feed concentration of 2,000 mg/m^3 (2,876 ppm) under dry and humid (80% RH) conditions, respectively.

Table 7.1 Structural Summary of MOFs and Their Ammonia Capacities.

Sample	Metal	Ligand	Functional Group	Pore size (Å)	Surface area (m^2/g)	Capacity for ammonia	
						Dry (mmol/g)	Wet (mmol/g)
*DMOF	Zn	BDC, DABCO	-	7.5, 3.2	2000	0.27	5.56
*CuBTB	Cu (UMCs)	H_3BTB	Carboxylic (-COOH)	12.5, 8, 5.4	600	2.19	5.95
ZnBTTB	Zn	H_4BTTB	Dicarboxylic $(-COOH)_2$	4.468	446	4.59	20.26
DMOF-A	Zn	ADC, DABCO	-	−, 4.8 ×3.2, 4.8×3.2	760	0.48	1.18
DMOF-TM2	Zn	TMBDC, DABCO	-	3.5,−, −	1050	0.15	4.57
UiO-66	Zr	BDC	-	~6	1100-1250	1.79	2.75
UiO-66-NH_2	Zr	NH_2-BDC	Amino ($-NH_2$)	<6	1096	3.56	3.01
UiO-66-NO_2	Zr	NO_2-BDC	Nitro ($-NO_2$)	<6	729	1.98	1.60
UiO-66-OH	Zr	HO-BDC	Hydroxy (-OH)	<6	946	5.69	2.77
UiO-66-$(OH)_2$	Zr	$(OH)_2$-BDC	Dihydroxy $(-OH)_2$	<6	814	2.29	2.16
UiO-66-SO_3H	Zr	SO_3H-BDC	Sulphonic ($-SO_3H$)	<6	323	2.24	1.45
UiO-66-$(COOH)_2$	Zr	$(COOH)_2$-BDC	Dicarboxylic $(-COOH)_2$	<6	221	2.83	1.83

*Data is reported from literature[15]

Non-highlighted and highlighted rows are for the ammonia breakthrough runs at feed concentrations of 1,000 mg/m^3 and 2,000 mg/m^3 respectively.

Based on chemical intuition, we expected acidic functional groups ($-SO_3H$ and -COOH) to interact more strongly with ammonia than other functional groups. However, dry ammonia capacities of UiO-66-SO_3H and UiO-66-$(COOH)_2$ were found to be lower (< 3 mmol/g, Table 7.1) than UiO-66-OH and UiO-66-NH_2, which showed higher capacities of ~5.7 and ~3.6 mmol/g respectively. This clearly shows that functionalization of the UiO-66 framework is limited by the pore space and grafting

bulky functional groups such as –COOH and -SO_3H will lead to significant reduction in its porosity (surface area and pore volume) and ammonia adsorption capacity. The -OH group is less bulky than -NH_2 and a –OH---NH_3 hydrogen bond is stronger than a –NH_2---NH_3. Moreover, Snurr and coworkers have computationally shown that the binding energy of ammonia with –OH group is higher (almost double) than –NH_2.[30,31] Hence, these are likely the reasons why UiO-66-OH has a higher capacity of ~5.7 mmol/g for ammonia under dry conditions and it also shows that the high ammonia capacities of MOFs result from the interplay of various different factors (functional group, surface area, and pore size).

Weak forces such as hydrogen bonding are probably responsible for the ammonia removal capabilities of both materials (UiO-66-OH and UiO-66-NH_2) because after feed termination they display significant desorption (Figures 7.5, 7.7). High ammonia capacity (~5.7 mmol/g, close to current target) of UiO-66-OH makes this material interesting for ammonia filtration. However, unlike the MOFs ZnBTTB, DMOF-A, and DMOF-TM2 we observed a decrease in the ammonia capacities of functionalized UiO-66 variations under humid conditions (Table 7.1). This shows that water and ammonia both are competing for adsorption on these functionalized active sites, hindering access for ammonia molecules. Moreover, here we also think that ammonia is not chemically reacting considering the superior stability of the UiO-66 framework.[29] This is further supported by the fact that the shape of the breakthrough curves for the UiO-66 analogues is not unusual (no additional steps, Figures 7.6, 7.8). Conversely, for the parent material UiO-66, we observed an increase in its ammonia capacity in humidity conditions because of the solubility of ammonia in water. Schoenecker et al.[22b] observed that the adsorption

isotherm for UiO-66-NH_2 shows more Type I behavior below 20% RH compared to the parent material. Hence, similarly in the case of the functionalized UiO-66 variations (more hydrophilic) too, it is very likely that water fills the pores more extensively than for UiO-66 leaving no or little space for ammonia to adsorb.

Based on the aforementioned observation, we propose that the effect of water adsorption can be reduced by using a physical mixture of UiO-66-OH (hydrophilic) and monomethyl- (UiO-66-MM), dimethyl- (UiO-66-DM) functionalized variations (hydrophobic) of UiO-66. Moreover, these hydrophobic methyl functionalized analogues have shown higher affinity for polar CO_2 gas molecule than UiO-66 in the low pressure region under dry conditions (refer to next Chapter for details). In the future, before evaluating the performance of the physical mixture of hydrophilic and hydrophobic analogues of UiO-66 for ammonia capture, ammonia breakthrough capacity for mono- and dimethyl-functionalized variations of UiO-66 should also be measured. Moreover, functionalization of other water stable MOFs (e.g., MIL-100, MIL-101)[32,33] with larger pore space should also be explored in the future as it seems that there is not adequate pore space within the UiO-66 framework for complex functionalization to be effective.

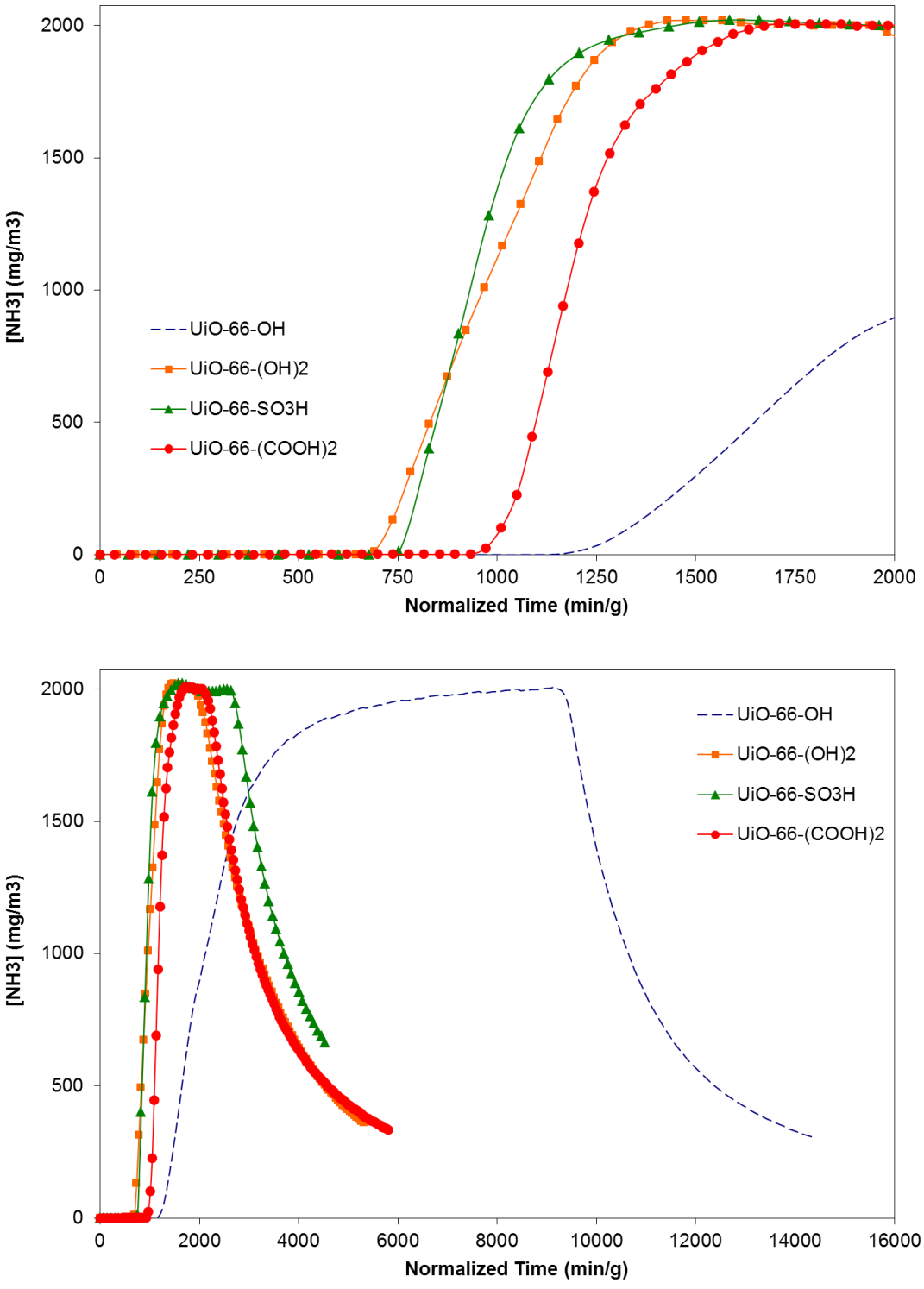

Figure 7.7 NH_3 breakthrough curves (top: time up to 2,000 min/g, bottom: whole time range) under dry air conditions at feed concentration of 2,000 mg/m^3 (2,876 ppm).

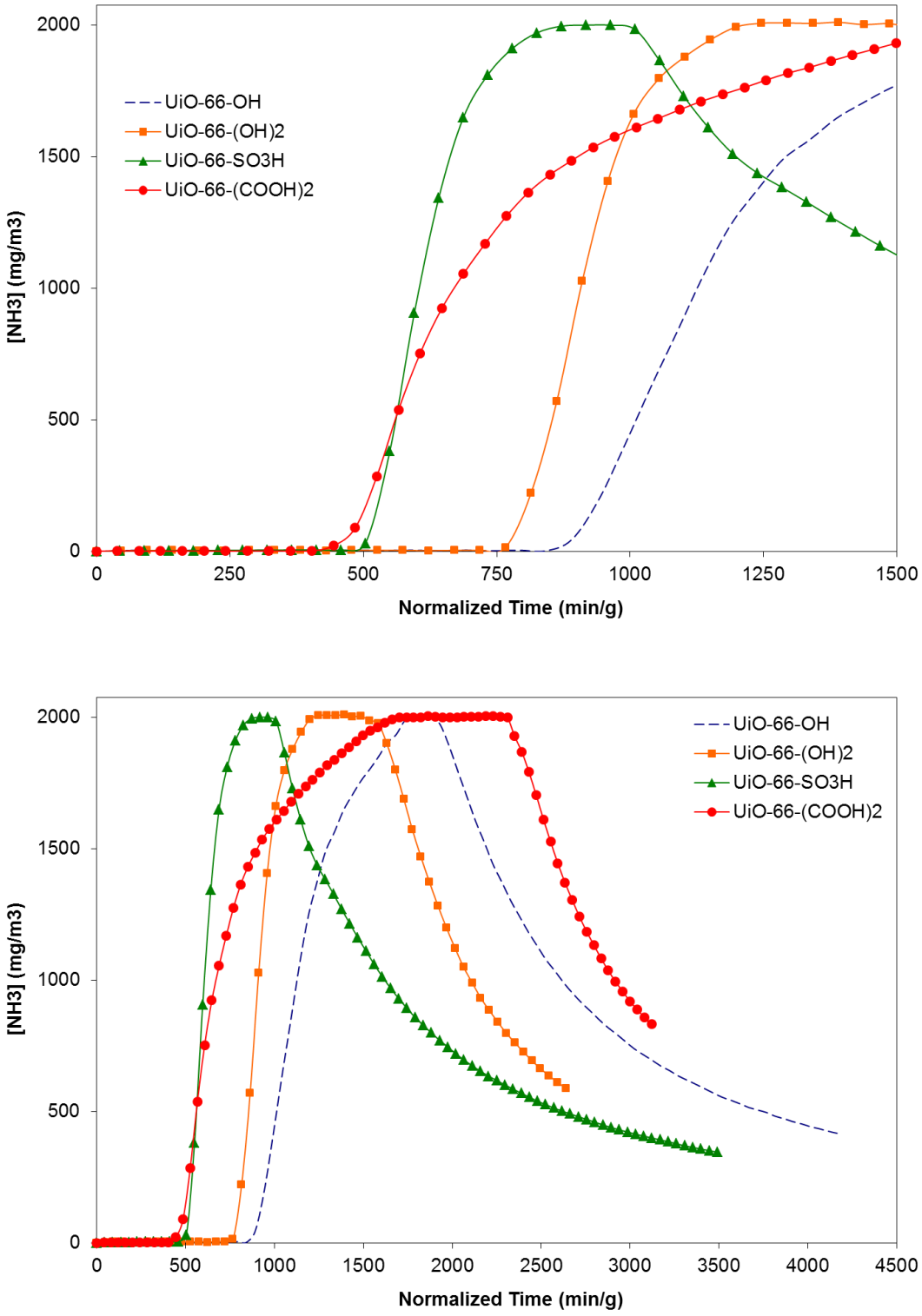

Figure 7.8 NH_3 breakthrough curves (top: time up to 1,500 min/g, bottom: whole time range) under humid (80% RH) air conditions at feed concentration of 2,000 mg/m^3 (2,876 ppm).

7.4 Conclusions

In conclusion, using already reported "one-pot" synthesis methods, 10 MOFs were successfully synthesized in the required quantities (~100 mg) and shipped to our collaborator's facility in Maryland for ammonia breakthrough measurements under dry and wet (80% RH) conditions. Overall, a functionalized Zr-based UiO-66 material (e.g., UiO-66-OH) is promising, as it could offer a method for targeting the removal of specific chemical threats in an environmentally-stable framework that does not degrade in the presence of water, a well-known issue with MOFs. These materials, however, fall short of the ammonia removal goal of 0.1 g /g MOF (or ~ 6 mmol/g) loading especially under humid conditions, and it seems that there is not adequate pore space within the UiO-66 framework for complex functionalization to be effective. Hence, functionalization of other water stable MOFs (e.g., MIL-100, MIL-101) with larger pore space should be explored in the future.

7.5 References

(1) Davis, M. E. Ordered Porous Materials for Emerging Applications. *Nature* **2002**, *417*, 813-821.

(2) Ferey, G. Hybrid Porous Solids: Past, Present, Future. *Chem. Soc. Rev.* **2008**, *37*, 191-214.

(3) Garibay, S. J.; Cohen, S. M. Isoreticular Synthesis and Modification of Frameworks with the UiO-66 Topology. *Chem. Commun.* **2010**, *46*, 7700-7702.

(4) Ferey, G.; Mellot-Draznieks, C.; Serre, C.; Millange, F. Crystallized Frameworks with Giant Pores: Are There Limits to the Possible? *Acc. Chem. Res.* **2005**, *38*, 217-225.

(5) Li, J.-R.; Kuppler, R. J.; Zhou, H.-C. Selective Gas Adsorption and Separation in Metal-Organic Frameworks. *Chem. Soc. Rev.* **2009**, *38*, 1477-1504.

(6) Eddaoudi, M.; Kim, J.; Rosi, N.; Vodak, D.; Wachter, J.; O'Keeffe, M.; Yaghi, O. M. Systematic Design of Pore Size and Functionality in Isoreticular MOFs and Their Application in Methane Storage. *Science* **2002**, *295*, 469-472.

(7) Karra, J. R.; Walton, K. S. Effect of Open Metal Sites on Adsorption of Polar and Nonpolar Molecules in Metal-Organic Framework Cu-BTC. *Langmuir* **2008**, *24*, 8620-8626.

(8) Keskin, S.; Van Heest, T. M.; Sholl, D. S. Can Metal-Organic Framework Materials Play a Useful Role in Large-Scale Carbon Dioxide Separations? *ChemSusChem* **2010**, *3*, 879-891.

(9) Keskin, S.; Kizilel, S. Biomedical Applications of Metal Organic Frameworks. *Ind. Eng. Chem. Res.* **2011**, *50*, 1799-1812.

(10) Kitagawa, S.; Kitaura, R.; Noro, S. Functional Porous Coordination Polymers. *Angew. Chem.-Int. Edit.* **2004**, *43*, 2334-2375.

(11)http://www.calgoncarbon.com/media/images/site_library/46_RespiratorsHP_10223w.pdf , last accessed on 02/12/2014.

(12) Karwacki, C. J., Jones P. Toxic Industrial Chemicals Assessment of NBC Filter Performance, Edgewood Chemical Biological Center, 2000.

(13) http://minerals.usgs.gov/minerals/pubs/commodity/nitrogen/nitromcs05.pdf. last accessed on 02/12/2014.

(14) (a) Britt, D.; Tranchemontagne, D.; Yaghi, O. M., Metal-organic frameworks with high capacity and selectivity for harmful gases. *Proc. Natl. Acad. Sci. U.S.A.* **2008,** *105* (33), 11623-11627; (b) Glover, T. G.; Peterson, G. W.; Schindler, B. J.; Britt, D.; Yaghi, O., MOF-74 building unit has a direct impact on toxic gas adsorption. *Chem. Eng. Sc.* **2011,** *66* (2), 163-170.

(15) Peterson, G. W.; Wagner, G. W.; Balboa, A.; Mahle, J.; Sewell, T.; Karwacki, C. J., Ammonia Vapor Removal by Cu3(BTC)2 and Its Characterization by MAS NMR. *J. Phys. Chem. C* **2009,** *113* (31), 13906-13917.

(16) DeCoste, J. B.; Peterson, G. W.; Schindler, B. J.; Killops, K. L.; Browe, M. A.; Mahle, J. J., The effect of water adsorption on the structure of the carboxylate

containing metal-organic frameworks Cu-BTC, Mg-MOF-74, and UiO-66. *J. Mater. Chem. A* **2013,** *1* (38), 11922-11932.

(17) Mu, B.: Synthesis and gas adsorption study of porous metal-organic framework materials, Ph.D. Thesis, Georgia Institute of Technology, Atlanta, GA, 2011.

(18) Schoenecker, P. M.: High-throughput synthesis and application development of water-stable mofs, Ph.D. Thesis, Georgia Institute of Technology, Atlanta, GA, 2012.

(19) DeCoste, J. B.; Peterson, G. W. Metal-Organic Frameworks for Air Purification of Toxic Chemicals. Chem. Rev. **2014**, (DOI: 10.1021/cr4006473).

(20) Karra, R. J.: Development of porous metal-organic frameworks for gas adsorption applications, Ph.D. Thesis, Georgia Institute of Technology, Atlanta, GA, 2011.

(21) Cavka, J. H.; Jakobsen, S.; Olsbye, U.; Guillou, N.; Lamberti, C.; Bordiga, S.; Lillerud, K. P. A New Zirconium Inorganic Building Brick Forming Metal Organic Frameworks with Exceptional Stability. *J. Am. Chem. Soc.* **2008**, *130*, 13850-13851.

(22) Kandiah, M.; Nilsen, M. H.; Usseglio, S.; Jakobsen, S.; Olsbye, U.; Tilset, M.; Larabi, C.; Quadrelli, E. A.; Bonino, F.; Lillerud, K. P. Synthesis and Stability of Tagged UiO-66 Zr-MOFs. *Chem. Mater.* **2010**, *22*, 6632-6640.

(23) (a) Cmarik, G. E.; Kim, M.; Cohen, S. M.; Walton, K.S. Tuning the Adsorption Properties of UiO-66 via Ligand Functionalization. *Langmuir* **2012,** *28*, 15606-15613. (b) Schoenecker, P. M.; Carson, C. G.; Jasuja, H.; Flemming, C. J. J.; Walton, K. S. Effect of Water Adsorption on Retention of Structure and Surface Area of Metal–Organic Frameworks. *Ind. Eng. Chem. Res.* **2012**, *51*, 6513-6519.

(24) Yang, Q. Y.; Wiersum, A. D.; Jobic, H.; Guillerm, V.; Serre, C.; Llewellyn, P. L.; Maurin, G. Understanding the thermodynamic and kinetic behavior of the CO_2/CH_4 gas mixture within the porous zirconium terephthalate UiO-66(Zr): a joint experimental and modeling approach. *J. Phys. Chem. C* **2011,** *115* (28), 13768-13774.

(25) Peterson, G. W.; DeCoste, J. B.; Glover, T. G.; Huang, Y.; Jasuja, H.; Walton, K. S., Effects of pelletization pressure on the physical and chemical properties of the

metal–organic frameworks Cu3(BTC)2 and UiO-66. *Microporous and Mesoporous Mater.* **2013,** *179* (0), 48-53.

(26) Biswas, S.; Van Der Voort, P., A General Strategy for the Synthesis of Functionalised UiO-66 Frameworks: Characterisation, Stability and CO_2 Adsorption Properties. *Eur. J. Inorg. Chem.* **2013,** *2013* (12), 2154-2160.

(27) Walton, K. S.; Snurr, R. Q., Applicability of the BET method for determining surface areas of microporous metal-organic frameworks. *J Am Chem Soc* **2007,** *129* (27), 8552-6.

(28) Saha, D.; Deng, S., Ammonia adsorption and its effects on framework stability of MOF-5 and MOF-177. *Journal of Colloid and Interface Science* **2010,** *348* (2), 615-620.

(29) Peterson, G. W.; DeCoste, J. B.; Fatollahi-Fard, F.; Britt, D. K., Engineering UiO-66-NH2 for Toxic Gas Removal. *Ind. Eng. Chem. Res.* **2013,** *53* (2), 701-707.

(30) Yu, D.; Ghosh, P.; Snurr, R. Q., Hierarchical modeling of ammonia adsorption in functionalized metal-organic frameworks. *Dalton Transactions* **2012,** *41* (14), 3962-3973.

(31) Kim, K. C.; Yu, D.; Snurr, R. Q., Computational Screening of Functional Groups for Ammonia Capture in Metal–Organic Frameworks. *Langmuir* **2013,** *29* (5), 1446-1456.

(32) Jeremias, F.; Khutia, A.; Henninger, S. K.; Janiak, C., MIL-100(Al, Fe) as water adsorbents for heat transformation purposes-a promising application. *J. Mater. Chem.* **2012,** *22* (20), 10148-10151.

(33) Hartmann, M.; Fischer, M., Amino-functionalized basic catalysts with MIL-101 structure. *Microporous and Mesoporous Mater.* **2012,** *164* (0), 38-43.

CHAPTER 8

RATIONAL TUNING OF WATER VAPOR AND CO_2 ADSORPTION IN HIGHLY STABLE ZR-BASED MOFS

8.1 Introduction

Rapidly increasing CO_2 emissions due to burning of fossil fuels has led to increasing attention to methods that will effectively capture CO_2 from various gas streams. Natural gas is a desirable fuel because it burns more cleanly than any other fossil fuel such as gasoline or coal. Moreover, its main constituent CH_4 has a higher hydrogen to carbon (H/C) ratio than any other hydrocarbon fuel.[1] However, natural gas coming from landfills and biogas plants is of low quality, i.e., it is comprised of 50-85% CH_4 with impurities such as CO_2 (20-35%), N_2, H_2O and H_2S.[2] Thus, pre-combustion CO_2 capture from natural gas streams is of great importance as its presence reduces the energy content and can corrode pipelines.[3] Likewise, post combustion CO_2 sequestration from power plant flue gas (where the main component is water-saturated N_2) is also a tremendous challenge to curb greenhouse gas emissions.[4]

Pressure swing adsorption (PSA) employs porous adsorbents and is a potentially viable alternative to highly energy intensive amine scrubbing processes that have been extensively investigated for CO_2 capture.[5] The ideal adsorbent should possess characteristics such as high porosity, reversible adsorption, structural stability, and

capability for surface modification for systematic tuning of host-guest interactions. However, conventional porous materials such as zeolites, mesoporous silicas, and impregnated carbons are relatively difficult to modify according to the requirements of the separation system, and effective regeneration often requires significant heating.[5] For example, zeolite 13X is the adsorbent employed commercially for CO_2 separation from gas streams as it has been shown to provide high CO_2 adsorption capacity under dry conditions.[6,7] However, it has a high affinity for moisture and must be regenerated at high temperature (350°C) to retain its high CO_2 adsorption capacity.[7]

Intense interest in new adsorbents for adsorption applications has led to the development of a new class of porous structures known as metal-organic frameworks (MOFs).[8] MOFs are fascinating crystalline materials comprised of organic ligands and metal-containing nodes or secondary building units (SBUs), which are connected to each other to form the extended porous networks. They are attractive materials for applications such as gas separations/ storage, chemical sensing, drug delivery, and catalysis because of their extremely high porosities, crystalline nature, uniform pore sizes, and chemical functionalities.[9,10] Pore sizes and chemical functionalities can be tuned by altering the metal node or organic ligand.[11,12]

Despite the many advantages that MOFs offer, usage of MOFs in many commercial applications such as gas separation depends on their stability upon exposure to water vapor.[13,14,15,16,17,18,19,20] MOFs based on Zr-based SBUs show great promise for usage in the aforementioned applications as they possess unprecedented thermal, chemical, and mechanical stability. This stability has been accredited to highly charged oxophilic Zr^{4+} cations and high nuclearity of the Zr(IV)-based SBU $[Zr_6O_4(OH)_4]$.[21,22,23]

Since, the discovery of the first member (UiO-66[21]) of this family in 2008, Lillerud et al.,[24] Cohen et al.,[22,25] and Behrens et al.[23] have independently worked towards the development of more Zr(IV)-based MOFs. Llewellyn et al.[5] reported that highly stable UiO-66 is of interest for CO_2 capture from CO_2/CH_4 gas mixtures, as under dry conditions it has shown good selectivity, high working capacity, and low-cost regenerability. However, Schoenecker et al.[26] showed that UiO-66 has a strong affinity for water, which can be detrimental to the separation process since water vapor is usually present in CO_2-containing streams such as flue gas and natural gas. Consequently, water will adsorb preferentially, leading to lower adsorption of CO_2.[19, 27]

Functionalization of MOFs with polar groups (-NH_2, -SO_3H, -CO_2H, -OH) has been extensively used to enhance CO_2 capture.[28,29,30] These functionalized MOFs have high affinity and reactivity towards water, which is unfavorable for the efficient separation.[26,27, 31] Little has been done regarding the use of hydrophobic or nonpolar functional groups to improve the efficiency of separation.[32] Researchers have shown that it is possible to enhance the water stability of MOFs by incorporating hydrophobic functional groups into the pores.[33,34,35,36,37] However, a few studies have been reported on the ability of such functionalized MOFs to separate CO_2 from flue gas or natural gas streams. Cai et al.[38a] reported that at low pressure, alkyl-functionalized BTC-based copper MOFs have significantly lower water vapor loading compared to HKUST-1, while they have comparable CO_2 and CH_4 loadings. Cmarik et al.[38b] evaluated CO_2, CH_4, N_2, and water vapor adsorption in several polar and non-polar variants of UiO-66. The nonpolar naphthyl-functionalized material was found to suppress water adsorption compared to the parent MOF, but the CO_2 loadings were also lowered. Burtch et al.[38c]

showed that the addition of methyl and other non-polar functional groups on the benzene dicarboxylate (BDC) linker in the pillared DMOF structure provide the greatest increase in low pressure CO_2 affinity whereas polar groups such as nitro, hydroxyl, chlorine, fluorine and bromine produce little to no improvement.

Here we report a detailed experimental study of CO_2, CH_4, and water vapor adsorption on the new monomethyl and dimethyl-functionalized variations of UiO-66 (UiO-66-MM, UiO-66-DM). These MOFs were synthesized by pre-synthesis functionalization of the BDC ligand (Figure 8.1) and characterized using a series of techniques including PXRD, FTIR, N_2 adsorption, NMR, and TGA. UiO-66-DM was also developed simultaneously and independently by Huang et al.,[39] and our procedure is distinct from their report. In their work, it was reported that UiO-66-DM has higher affinity for CO_2 compare to the parent material in the low pressure region. However, the water effect on the structure was only qualitatively examined, and no CH_4 adsorption data were reported. We show that by modulating the number of methyl groups on the BDC ligand we can rationally tune both the water vapor and low pressure CO_2, CH_4 adsorption. As expected, water vapor loadings follow the order: UiO-66-DM < UiO-66-MM < UiO-66. In fact, the water adsorption loading for UiO-66-DM is now even less than the water vapor loadings for commercial adsorbents such as zeolites 5A and 13X.[26] Moreover, as expected, this mono and dimethyl functionalization do not render any adverse effect on the high stability of UiO-66 framework. However, under dry conditions and low coverage both UiO-66-DM and UiO-66 have a low CO_2/CH_4 selectivity while UiO-66-MM has a much higher CO_2/CH_4 selectivity. Taking both hydrophilicity and

selectivity factors into account, we believe that both UiO-66-MM and UiO-66-DM will exhibit superior performance over the parent MOF in humid gas separations.

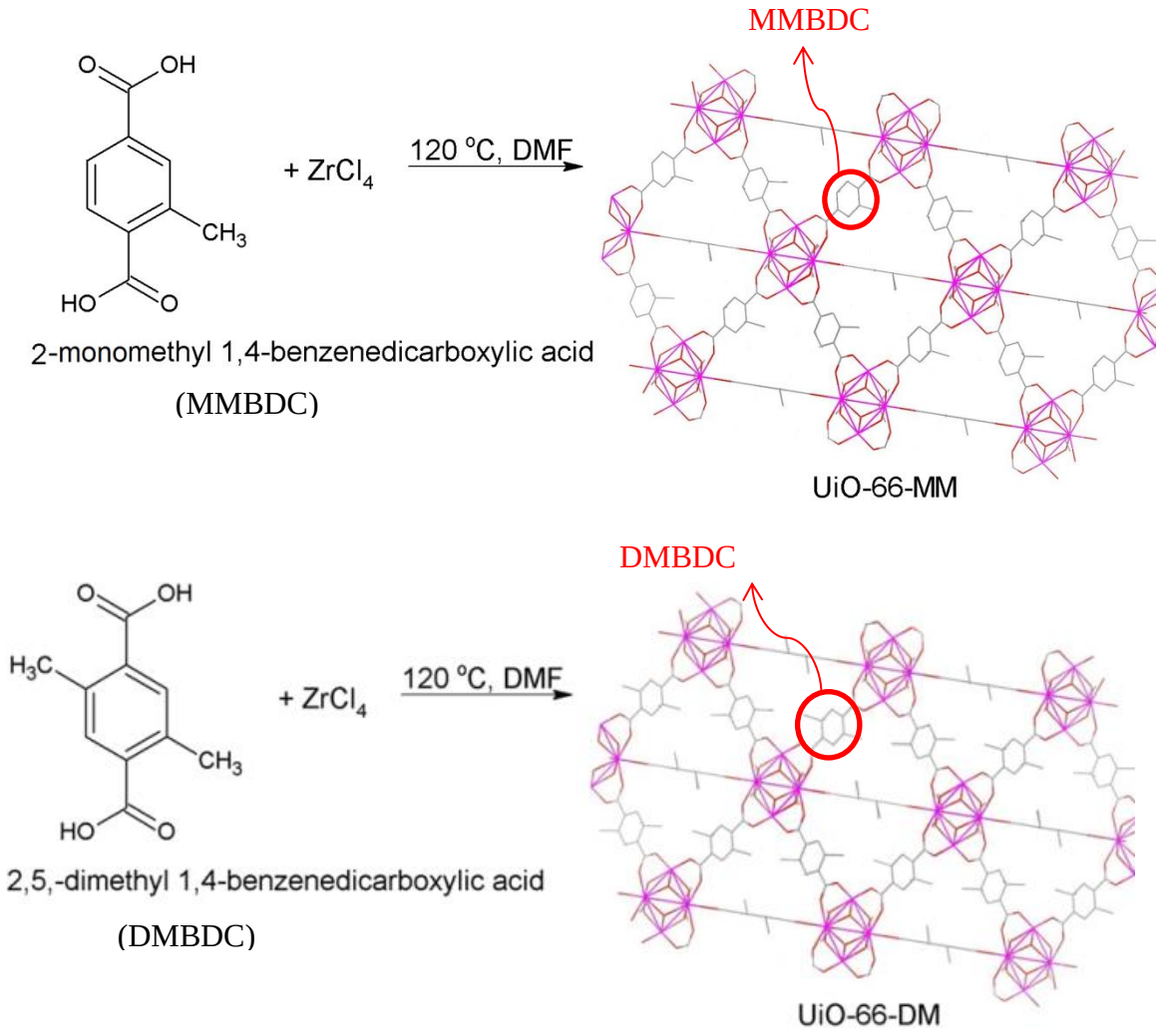

Figure 8.1 Synthesis of monomethyl and dimethyl-functionalized UiO-66 framework (UiO-66-MM and UiO-66-DM).

8.2 Materials and Methods

All the employed chemicals were commercially available and used as-received by following sources: Sigma-Aldrich, N,N′-dimethylformamide (DMF), zirconium (IV)

chloride ($ZrCl_4$); Combi-Blocks, 2-monomethyl 1,4-benzene-dicarboxylic acid (MMBDC); TCI America, 2,5-dimethyl 1,4-benzenedicarboxylic acid (DMBDC); Acros, chloroform ($CHCl_3$), 1,4-benzene-dicarboxylic acid (BDC).

8.2.1 MOF Synthesis and Activation

UiO-66. UiO-66 was synthesized as reported by Schoenecker et al.[26] and activated at 200 ^oC overnight in the degasser.

UiO-66-MM. UiO-66-MM is synthesized in a similar fashion as reported for amino-, bromo-, nitro-, and naphthalene-functionalized UiO-66 by Cohen et al.,[22] i.e., equal molar amounts (0.35 mmol) of $ZrCl_4$ and mono-methyl benzene dicarboxylic acid (MMBDC) are combined in 4 mL DMF and the resulting mixture is heated in a Teflon lined autoclave at 120 ^oC for 24 hrs. After the solution was cooled to room temperature in air, the resulting solid was filtered and repeatedly washed with DMF. The dried as-synthesized sample is then soaked in chloroform ($CHCl_3$) for three days at room temperature to remove DMF and unreacted MMBDC. Finally, it is filtered off and dried followed by its activation at 200 ^oC overnight in the degasser.

UiO-66-DM. Synthesis of UiO-66-DM was performed using a slightly modified procedure of Cavka et al.[21] reported for the parent UiO-66 MOF. UiO-66-DM was synthesized by dissolving 0.681 mmol of zirconium (IV) chloride ($ZrCl_4$) and 0.681 mmol of 2,5-dimethyl-1,4-benzenedicarboxylic acid (DMBDC) in 26.5 mL of DMF at room temperature. The resulting mixture was divided equally into two 20 mL scintillation vials. These vials were kept in a sand bath inside an oven at 120 ^oC for 24 h. The final product was cooled to room temperature and then washed with DMF three times to remove the unreacted reactants before overnight activation at 200 ^oC.

8.2.2 Powder X-Ray Diffraction

Powder X-ray diffraction patterns (PXRD) were measured using an X'Pert X-ray PANalytical diffractometer with an X'celerator module using Cu Kα (λ = 1.5418 Å) radiation at room temperature, with a step size of 0.02˚ in two theta (2θ). PXRD patterns of as-synthesized samples were also compared with patterns of water-exposed samples and with samples obtained after activating/ regenerating the water-exposed samples to determine the stability of the methyl functionalized UiO-66 MOFs under humid conditions.

8.2.3 Nitrogen Adsorption Measurements

Nitrogen adsorption isotherms (Appendix E, Figures E.7-E.10.) were measured at 77 K for activated MOF samples before and after water exposure using a Quadrasorb system from Quantachrome instruments. Specific surface areas were determined by applying BET model to these isotherms. BET theory was applied over the pressure range as suggested by Walton et. al[40a] for MOFs, i.e., the BET analysis was performed in low pressure range ($P/P_o < 0.05$). N_2 isotherms showed typical Type I behavior as per the IUPAC classification.[9]

8.2.4 Thermal Gravimetric Analysis

Thermo gravimetric analysis (TGA) was carried out in the temperature range of 30-700 ˚C on a NETZSCH STA 449 F1 Jupiter® under helium with a heating rate of 5 ˚C / min. Figure 8.7 shows that increasing the number of methyl groups on the BDC ligand reduces the amount of physisorbed water, i.e., increases hydrophobicity.

8.2.5 Fourier Transform Infrared Spectroscopy

Fourier transform Infrared (FTIR) spectrum of UiO-66-MM and UiO-66-DM was recorded with PerkinElmer Spectrum One as KBr pellets in the range 400 – 4000 cm^{-1}. Figures 8.3 and 8.5 confirm the presence of monomethyl and dimethyl moieties in the frameworks of UiO-66-MM and UiO-66-DM respectively.

8.2.6 Nuclear Magnetic Resonance

A Bruker DSX300 solid-state NMR spectrometer was used to record the ^{13}C CP-MAS NMR spectrum of as-synthesized UiO-66-MM. The instrument was operating at a 1H frequency of 300 MHz, spinning speed was 10 kHz, the repetition delay between scans was 4s, and contact time for the cross-polarization was 2ms. A total of 4096 scans were accumulated. A total of 4096 scans were accumulated. δ = 20-30 ppm (carbon C7 from methyl group), ~170 ppm (carbon C8 & C10 from carbonyl group). Refer Figure 8.4. Two peaks ~ 170 ppm strongly hint that they corresponds to coordinated and uncoordinated carbonyl of MMBDC. Hence, there is unreacted MMBDC ligand in the pores. As a result of this, we also observe three peaks for CH_3 (20-30 ppm) as CH_3 is close to carbonyl, so coordinated/ uncoordinated mode of the carbonyl can cause shifts of the CH_3 peak.

Varian Mercury Vx 300 was used to record the ^1H NMR spectrum of activated UiO-66-DM. A portion of the activated (under vacuum at 200 ^oC, 12 hrs.) UiO-66-DM was digested with NaOH in D_2O and subjected to ^1H NMR measurements. ^1H NMR (300 MHz, D_2O, 25 ^oC, TMS): δ = 6.95 ppm (H connected to carbon of benzene ring), 2.10 ppm (H from methyl group). Refer Figure 8.6.

8.2.7 Water Vapor Adsorption Isotherm

Water vapor sorption isotherms were obtained using an Intelligent Gravimetric Analyzer (IGA-3 series, Hiden Isochema). Dry air was used as carrier gas and a percentage of it was effervesced through a vessel filled with deionized water to generate the saturated air. The relative humidity (RH) was controlled by varying the ratio of saturated air and dry air through two mass flow controllers. Experiments were conducted only up to 90% RH due to water condensation in the equipment at higher humidities. The total gas flow rate used was 200 cm^3/min and typical equilibrium times ranged from 15 minutes to 24 h for each adsorption/desorption point in the isotherm. Before starting the adsorption measurement, samples were activated in order to remove the solvent molecules, until no further weight loss was observed. Samples were regenerated/ reactivated after the water adsorption isotherm and prior to PXRD and BET analysis. The regeneration was conducted at the initial activation temperature and under dynamic vacuum for 12 hrs.

8.2.8 Pure Component Gas Adsorption Isotherm Measurements and Analysis

CO_2 and CH_4 adsorption isotherms were measured at 30 ^oC and for a pressure range of 0 to 20,000 mbar using an Intelligent Gravimetric Analyzer (IGA-1 series, Hiden Isochema). Sample size used for the measurement was around 25 mg. Before starting the adsorption measurements, samples were activated at 200 ^oC until no further weight loss was observed in order to remove the solvent / guest molecules. After activation, the system was retained under vacuum, and the temperature was adjusted to 30 ^oC. Maximum equilibrium time of 30 minutes was set for each point in the isotherm.

Toth Model fits nicely to the experimental adsorption isotherms of CO_2 and CH_4 (Appendix E, Figures E.11-E.13). The Toth Model is given by[40b]

$$C = C_s \frac{bP}{[1 + (bP)^t]^{1/t}}$$

where C is the adsorption loading, C_s is the maximum loading corresponding to a complete monolayer coverage, t is a parameter, which is typically < 1. More the parameter t deviates from unity; more heterogeneous is the system. The parameters b and t are specific for adsorbate-adsorbent pairs. Toth model is generally applied to fit the experimental adsorption data as it is simple in form and thermodynamically consistent at low and high pressures. The Toth model parameters obtained from fitting the experimental data are used to calculate Henry's constants (K_H) for each adsorbate-MOF pair (Table 8.2). Values of Henry's constants provide information on the strength of interaction between the adsorbate and the adsorbent.

8.3 Results and Discussion

8.3.1 Structure Characterization and Physical Properties

Similar to the other functionalized UiO-66 frameworks, both UiO-66-MM and UiO-66-DM crystallize as intergrown crystals that are too small for structure determination by single crystal diffraction. Hence, PXRD patterns of as-synthesized UiO-66, UiO-66-MM, and UiO-66-DM are compared with pattern simulated from the single-crystal structure of UiO-66 (Figure 8.2). Figure 8.2 confirms that UiO-66-MM and UiO-66-DM are crystalline and isostructural to the parent UiO-66 MOF. Thus, in the 3D structure of UiO-66-MM and UiO-66-DM, Zr(IV)-based SBU $[Zr_6O_4(OH)_4]$ is bridged by twelve MMBDC and DMBDC ligands respectively. Evidence of the presence of the

monomethyl and dimethyl moieties on the BDC linker was obtained by characterizing the UiO-66-MM and UiO-66-DM with FTIR and NMR spectroscopy.

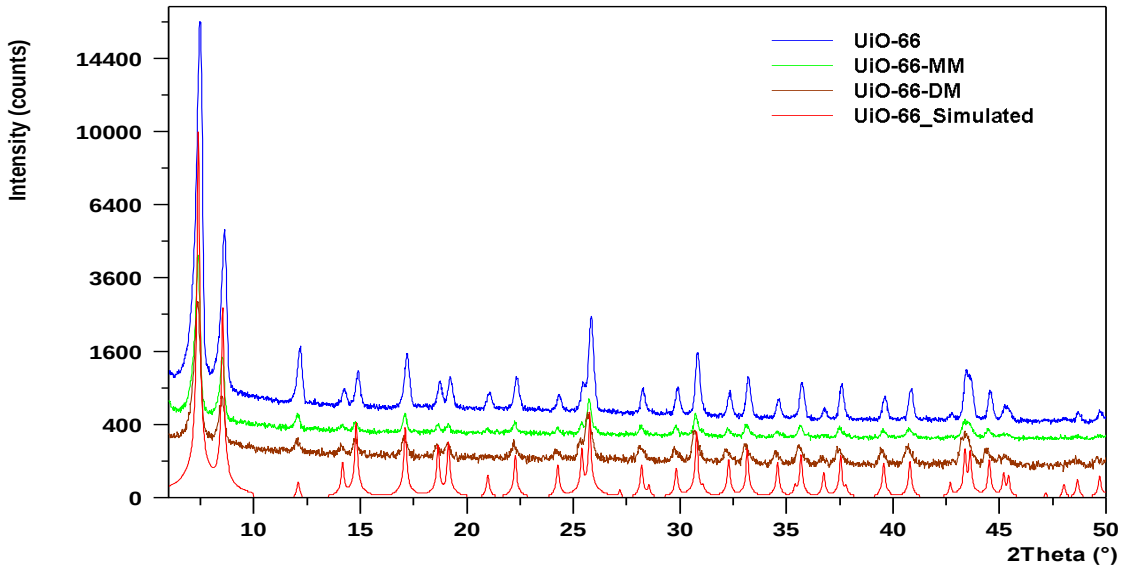

Figure 8.2 Comparison between PXRD patterns of as-synthesized UiO-66, UiO-66-MM, UiO-66-DM, and theoretical pattern of UiO-66 simulated from single crystal data.

Figure 8.3 shows a peak at 1665 cm^{-1} in the FTIR spectra of as-synthesized and directly activated (under vacuum at 200 ^{o}C, 12 hrs.) samples of UiO-66-MM. This peak corresponds to C=O in DMF and unreacted MMBDC ligand. The ^{13}C NMR spectrum obtained for as-synthesized UiO-66-MM confirms the presence of unreacted MMBDC ligand in the pores (Figure 8.4, section 8.2.6). Moreover, this peak at 1650 cm^{-1} disappears (Figure 8.3) when UiO-66-MM sample is activated after solvent exchange with $CHCl_3$. Hence, solvent exchange with $CHCl_3$ is necessary for the removal of unreacted MMBDC ligand, and heating the solvent-exchanged UiO-66-MM sample at 200 ^{o}C under vacuum is appropriate for activation. For activated samples, peak at 3430

cm^{-1} (corresponding to O-H in both the SBU $[Zr_6O_4(OH)_4]$ and physisorbed water) has not disappeared completely instead has only decreased in intensity. This shows that activated material rehydoxylates or physisorbs water as it is getting exposed to moisture present in air during its pelletization/ transfer of pellet into the sample holder to run FTIR. Furthermore, we always see a peak at 2910 cm^{-1}, which corresponds to the stretching frequency of C-H bond in methyl moieties of the MMBDC ligand. Thus, FTIR spectroscopy proves the presence of the methyl group on the benzene ring of MMBDC ligand. Similarly, FTIR spectrum (Figure 8.5) of as-synthesized UiO-66-DM also shows peaks at 1660 cm^{-1} and 3430 cm^{-1}. However, there is no peak at 1660 cm^{-1} in the FTIR spectrum of activated UiO-66-DM and this confirms the removal of DMF molecules from the pores of as-synthesized sample. Moreover, this also shows that there is no unreacted DMBDC ligand present in the pores of as-synthesized UiO-66-DM. A peak is also observed at 2930 cm^{-1} that corresponds to the stretching frequency of the C-H bond in the dimethyl moieties attached to the benzene ring, which confirms the presence of DMBDC ligand in this MOF. Similarly, ^1H NMR spectrum of activated UiO-66-DM displayed resonances associated with the DMBDC ligand (Figure 8.6).

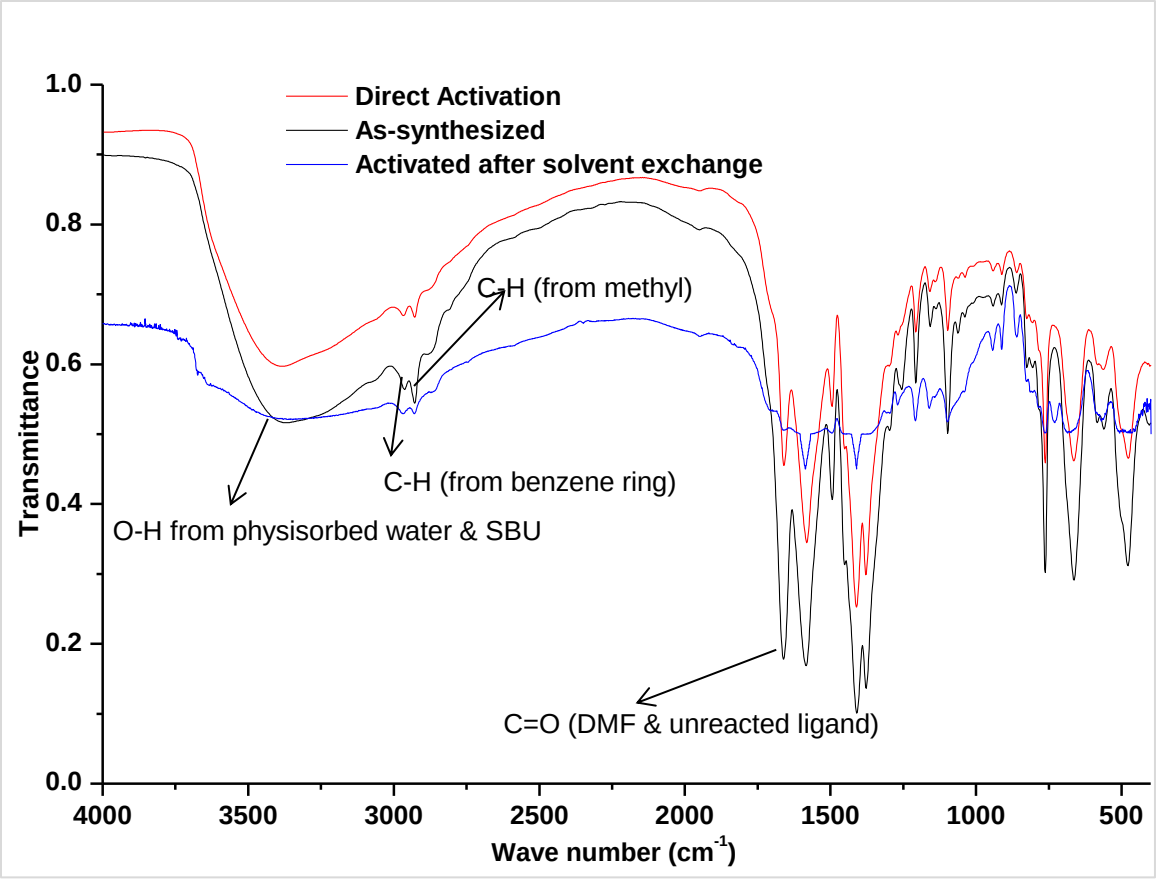

Figure 8.3 FTIR spectra of UiO-66-MM, Top: directly activated (under vacuum at 200 ^{o}C, 12 hrs.), middle: as-synthesized, and bottom: activated (under vacuum at 200 ^{o}C, 12 hrs.) after solvent ($CHCl_3$) exchange.

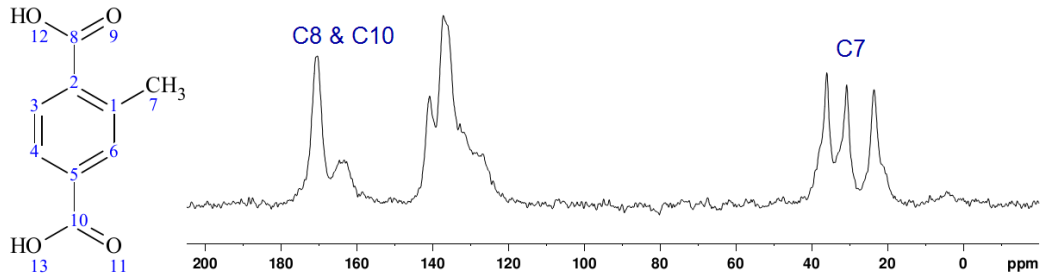

Figure 8.4 Solid state ^{13}C NMR spectrum of as-synthesized UiO-66-MM.

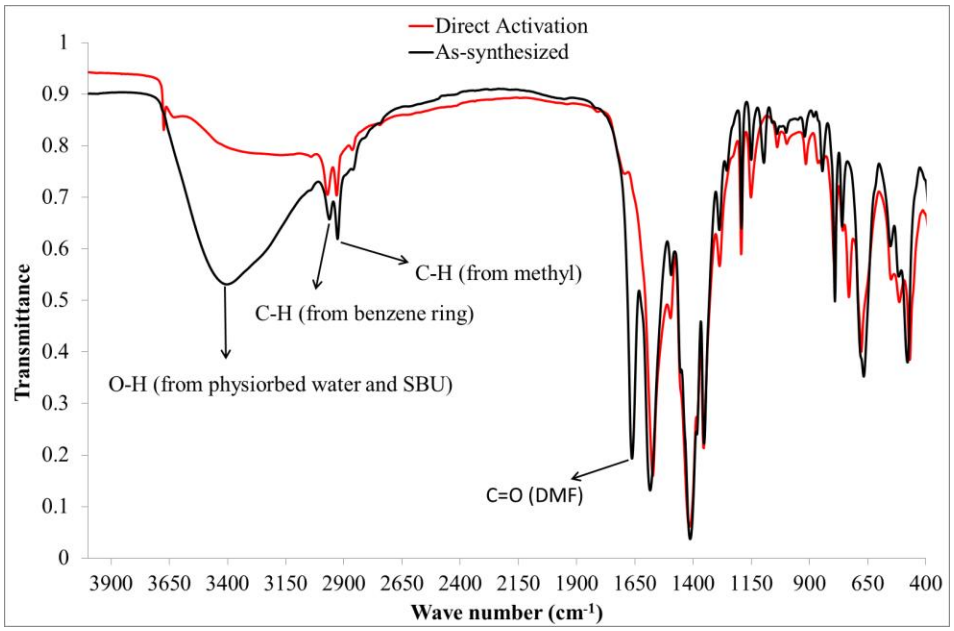

Figure 8.5 FTIR spectra of UiO-66-DM, Top: directly activated (under vacuum at 200 ^{o}C, 12 hrs.) and bottom: as-synthesized.

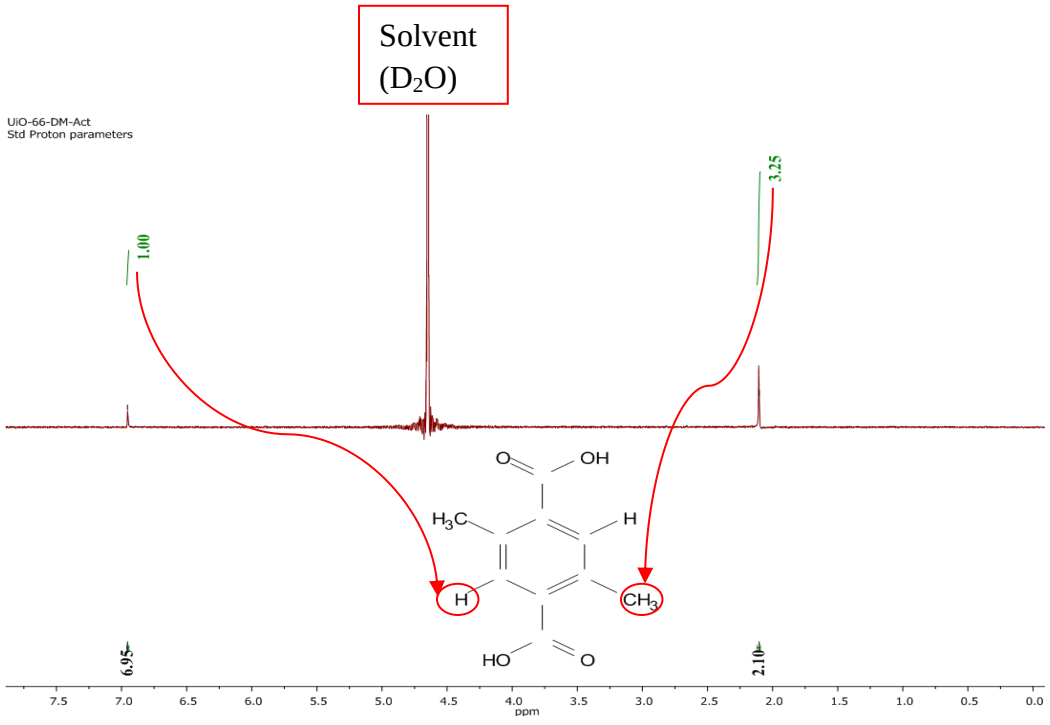

Figure 8.6 NMR spectrum of activated UiO-66-DM (values labeled in green color are the areas under the peaks (positions labeled in black) of different types of ^{1}H present).

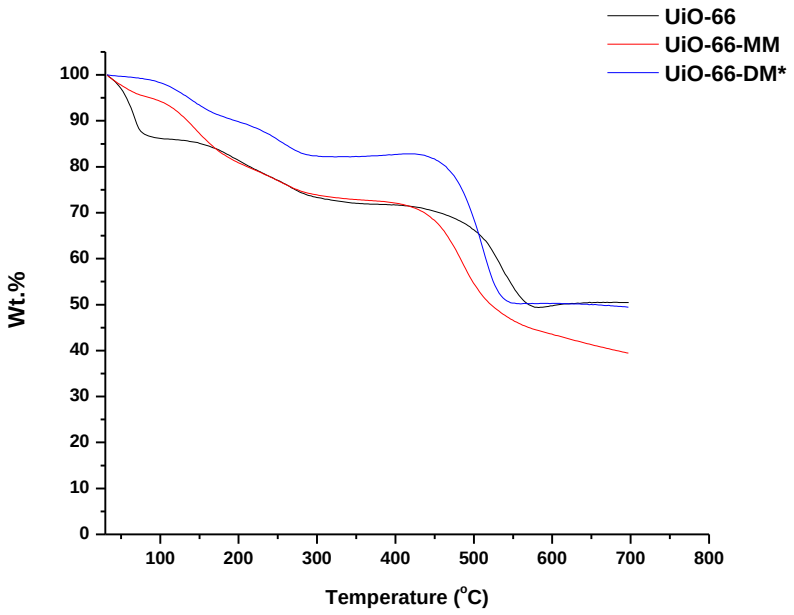

Figure 8.7 TGA curves of as-synthesized UiO-66, UiO-66-MM, and UiO-66-DM in helium flux.

The thermal stability of UiO-66-MM and UiO-66-DM was examined using TGA. Figure 8.7 shows that both UiO-66-MM and UiO-66-DM decomposes at approximately 450 ^{o}C, which is less than the reported decomposition temperature of UiO-66 (540 ^{o}C)[21] but still higher than the typical value of 350 ^{o}C observed for many other MOFs.[21] Yang et al.[34] synthesized methyl functionalized MOF-5, and also observed a similar decrease in the thermal stability. UiO-66-NH_2 and UiO-66-NO_2 have also been shown to decompose at a lower temperature compared to UiO-66.[24] However, the origin of the differences in these thermal stabilities is still unclear. Similar to UiO-66,[41] the TGA curves for as-synthesized UiO-66-MM and UiO-66-DM in Figure 8.7 show three weight loss regions before framework decomposition that corresponds to dehydration (physisorbed water, T < 100 ^{o}C), solvent removal (DMF, 100 ^{o}C < T < 180 ^{o}C), and dehydroxylation of the

$Zr_6O_4(OH)_4$ cornerstone into Zr_6O_6 (180 ^oC < T < 280 ^oC). Figure 8.7 also shows that as the number of methyl group on the BDC ligand increases, the amount of physisorbed water also reduces, i.e., hydrophobicity increases.

As expected, N_2 adsorption (Appendix E, Figures E.7, E,9) at 77 K on the activated UiO-66-MM and UiO-66-DM samples show that functionalization by the methyl moieties leads to reduced porosity (Table 8.1) compared to the parent MOF. Entry to the internal pores of the parent UiO-66 MOF is limited by triangular windows of 6 Å.[21,39] However, in UiO-66-MM and UiO-66-DM, functionalization by the methyl moieties should further reduce the window opening.

Table 8.1. Adsorption Loadings at 90% Relative Humidity and BET Surface Areas Before and After Water Exposure.

Material	Pore Volume† (cm^3/g)	Pore Diameter (Å)	Loading, 90% RH (cm^3 H_2O/g)	Surface Area* (m^2/g)		
				Before	After	% Loss
‡UiO-66	0.52	~ 6	0.43	1160	1136	2
UiO-66-MM	0.51	< 6	0.34	1065	1020	4
UiO-66-DM	0.40	< 6	0.24	811	797	2

*BET Analysis
†Obtained from the Dubinin-Astakov model of N_2 adsorption at 77K
‡Reported from literature[26]

8.3.2 High Structural Stability

The sensitivity of MOFs under humid conditions is well known, but water adsorption studies on MOFs are still lacking compared to other adsorbates.[14,15,17,37,42,43] Recently, we measured the water vapor adsorption isotherms of several well-known

MOFs including UiO-66 and it's several variants and found that this family of MOFs is uniformly stable in the presence of water.[26,38b] In the current study, water vapor adsorption measurements for UiO-66-MM, UiO-66-DM and subsequent stability tests were performed to compare with UiO-66.

Figure 8.8 shows that increase in the number of methyl groups on the BDC ligand directly improves the hydrophobicity of these MOFs. Moreover, TG analyses (Figure 8.7) of these as-synthesized UiO-66-type MOFs also show that the amount of physisorbed water ($T < 100\ ^{o}C$) lost is highest in UiO-66 and lowest in UiO-66-DM, which is in good agreement with our water adsorption results. UiO-66-DM shows significantly lower water adsorption loadings compared to UiO-66 and, is also even lower than the water vapor loadings for traditional porous materials such as zeolites 5A and 13X and BPL carbon.[26] Among the UiO-66 variants studied by Cmarik et al.,[38b] the naphthyl functionalized MOF displayed the lowest water adsorption loadings but still adsorbed approximately 13 mmol/g at 40% RH compared to only 6 mmol/g adsorbed in UiO-66-DM under the same conditions. The desorption isotherms of these Zr-MOFs exhibit hysteresis with a portion of the water being retained. At 0% RH, UiO-66, UiO-66-MM, and UiO-66-DM retain 2.42 mmol/g, 1.54 mmol/g, and 1.75 mmol/g, respectively. For comparison, UiO-66-NO_2 was shown to retain almost 6 mmol/g of water after desorption,[38b] and UiO-66-NH_2 retains approximately 3.3 mmol/g.[26] Wiersum et al.[49] showed that the amount of water retained by UiO-66 after the first adsorption cycle corresponds to partial rehydroxylation of the sample, and full rehydroxylation was possible only after the third cycle. Thus, the same explanation of partial rehydroxylation can be extended to the functionalized UiO-66 MOFs as well. However, we do expect a

different extent of rehydroxylation to occur after the first cycle for UiO-66-NO_2, −NH_2, −MM and −DM compared to UiO-66 because the amount retained at 0 % RH appears to be related to the polarity or hydrophilicity of the functional group. Thus, the amount of water retained in the MOFs at 0% RH follows the trend UiO-66-NO_2 > −NH_2 > −DM ~ −MM ~ −Naphthyl ~ parent structure.

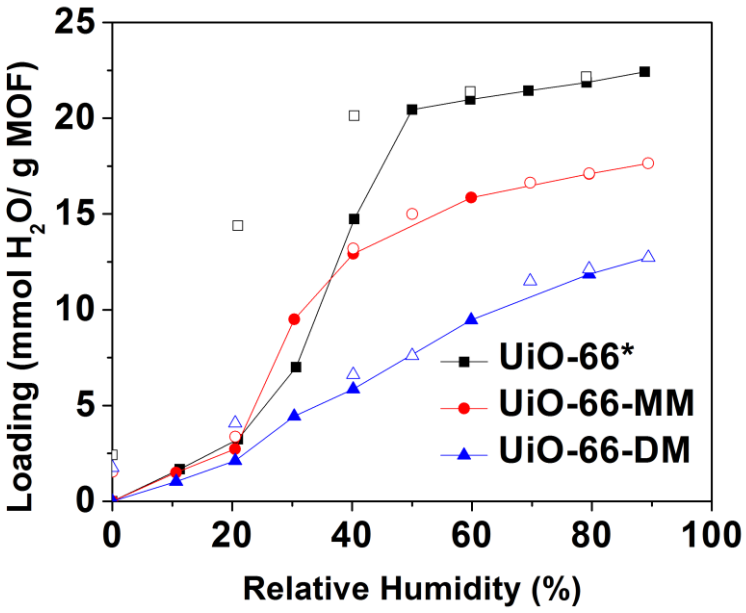

Figure 8.8 Water vapor sorption/desorption isotherms (at 25 °C) for desolvated compounds of UiO-66, UiO-66-MM, and UiO-66-DM (closed symbols – adsorption, open symbols – desorption). Lines connecting the adsorption points are to faciliate viewing. *Reported from our previous work.[26]

PXRD patterns for UiO-66-MM and UiO-66-DM before and after water exposure are shown in Figure 8.9. Similar to the previously studied variants,[38b,26] both of these MOFs also does not lose its crystallinity and are quite robust as there is negligible loss in their BET surface area (shown in Table 8.1) even after exposure to high levels of

humidity. The volumetric water loadings (cm^3/g) at 90% RH are shown in Table 8.1. It is expected that water should completely fill the pores at saturation, but for UiO-66, the water volume is slightly lower than the pore volume obtained from nitrogen adsorption. This may be due to fact that only during water adsorption does the Zr inorganic unit undergo rehydroxylation from $[Zr_6O_6]$ to $[Zr_6O_4(OH)_4]$. Thus, it is difficult to directly compare pore volumes obtained from water adsorption with those obtained by N_2 adsorption. The water volume obtained for UiO-66-MM and UiO-66-DM is 33% and 40% lower respectively than the pore volume obtained by N_2 adsorption. Similar to UiO-66, this decrease in volume relative to the N_2 pore volume will have contributions from the rehydroxylation process. However, adsorption saturation has not been reached at 90% RH, so water does not fully fill the pores. Thus, the volume should be much lower than the N_2 volume.

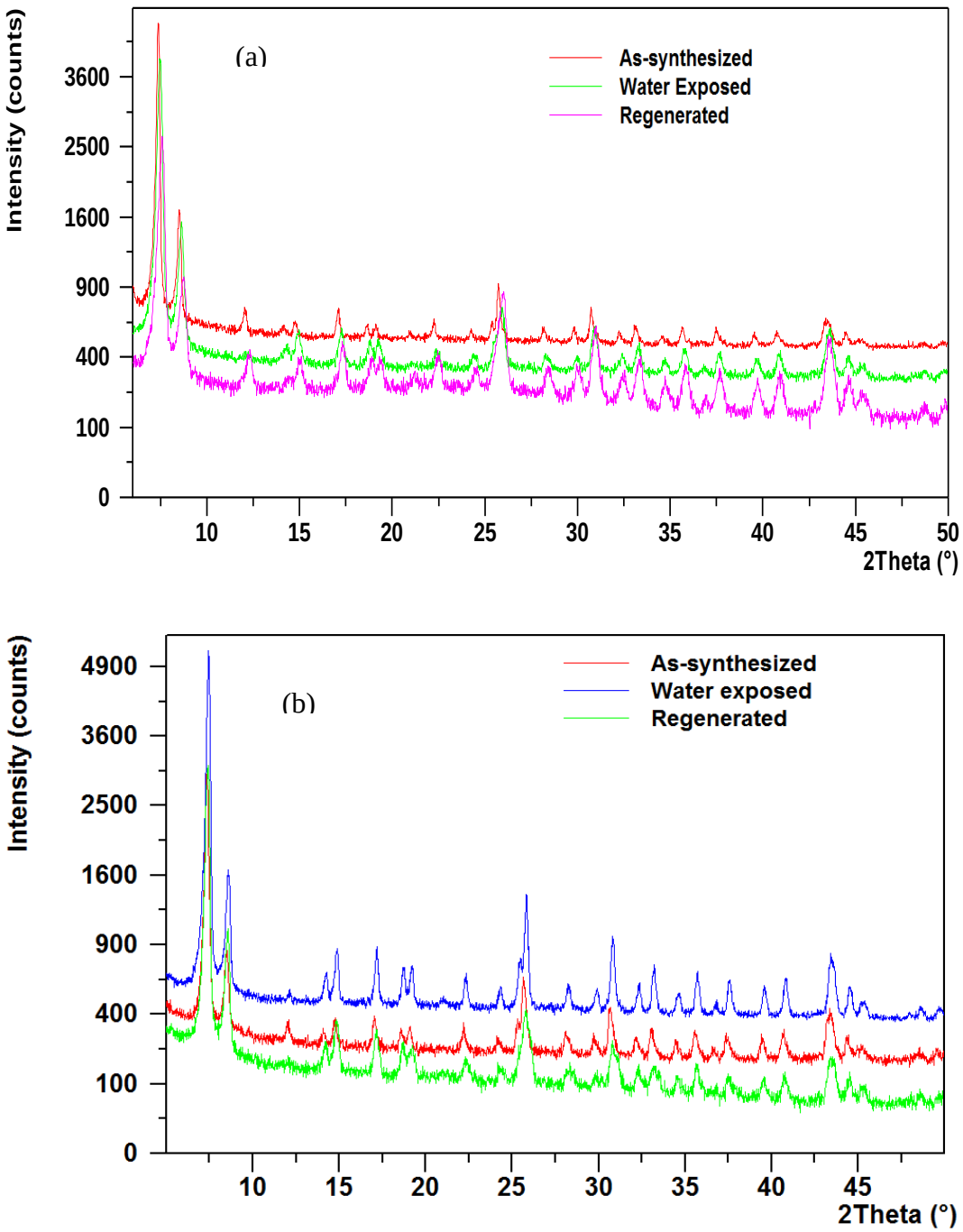

Figure 8.9. PXRD patterns for as-synthesized (middle), water vapor-exposed (top), and regenerated (bottom) (a) UiO-66-MM and (b) UiO-66-DM.

Zeolite 13X has often been employed commercially for CO_2 separation from gas streams due to its high CO_2 adsorption capacity under dry conditions, but also must be regenerated at high temperature (350 ^oC) to retain this capacity and has a high affinity for moisture.[6,7] Counter to this, UiO-66-MM and UiO-66-DM can be regenerated at relatively lower temperatures (200 ^oC). Moreover, at 28 % RH zeolite 13X[7] adsorbs 15.11 mmol H_2O/g, which is ~1.5 times and ~ 3.5 times more than the water adsorption in UiO-66-MM and UiO-66-DM respectively at 30 % RH. Since the pore volume and surface area of zeolite 13X (0.25 cm^3/g, 725 m^2/g)[44,45] are lower than UiO-66-MM and UiO-66-DM (Table 8.1), we expect these methyl functionalized variations of UiO-66 to have a higher capacity for gases such as CO_2 at higher pressures and outperform zeolite 13X, especially under humid environments. Water adsorption studies on other MOFs, e.g., the DMOF family,[46,47] also show much lower water loadings than zeolite 13X, but many of these MOFs lose their crystallinity after exposure to humidity, with the exception of the tetramethyl and anthracene derivatives. In general, the key to developing high performance adsorbents is finding a balance between adsorption capacity and selectivity for the target; these two characteristics are often inverse related.

8.3.3 CO_2 and CH_4 Adsorption

Inspired by the high stability and significantly low water loadings of UiO-66-MM and UiO-66-DM, pure-component CO_2 and CH_4 adsorption isotherms were measured at 30 ^oC. The CO_2 and CH_4 adsorption isotherms for UiO-66, UiO-66-MM, and UiO-66-DM shown in Figure 8.10 exhibit type I isotherms with no hysteresis. CO_2 is more strongly adsorbed than CH_4 because it has a relatively high quadrupole moment while CH_4 is nonpolar. At high pressure (Figure 8.10b), the adsorption loadings are

higher for the parent material since it has a higher pore volume. However, Figure 8.10a shows that CO_2 and CH_4 loadings at low pressures are slightly enhanced in UiO-66-MM and UiO-66-DM due to the presence of increased van der Waals interactions from the methyl moieties. This can be more easily seen by comparing the values of Henry's constants (K_H) for CH_4 and CO_2 adsorption on UiO-66-MM, UiO-66-DM, and UiO-66 in Table 8.2. The Toth parameters (section 8.2.8)[40b] were used to calculate Henry's constants as Toth model fits nicely to the experimental isotherms (Appendix E, E.11-E.13). Results show that increasing the number of methyl groups on the BDC ligand is directly correlated to the henry's constant (Table 8.2) for CH_4 adsorption on these isostructural MOFs. However, it is unclear why same trend is not seen for CO_2, i.e., henry's constant for CO_2 follows the order UiO-66-MM > UiO-66-DM > UiO-66. One possible explanation[48] could be that there are two opposing and competitive effects brought on by methyl functionalization: 1. Enhancement due to increase in quadrupole-π electron interactions. 2. Decline due to the reduction in surface area and pore volume. For UiO-66-MM enhancement effect dominates whereas for UiO-66-DM decline effect dominates. However, molecular simulations are needed to provide further atomistic insight into the phenomena governing the interesting low pressure CO_2 and CH_4 adsorption behavior in this series of MOFs. After we published our work described here in the Journal of Physical Chemistry C, Biswas et al.[50] also recently showed the enhanced CO_2 capture by the CH_3-functionalized UiO-66 MOFs compared to UiO-66. The most basic way of predicting the CO_2/CH_4 selectivity (Table 8.2) at low coverage is by taking the ratio of henry constants; this approach is exact in the limit of low partial pressures for both gases.[51] Accordingly, selectivity is lowest in UiO-66-DM (1.39) but is highest in

UiO-66-MM (15.64) because UiO-66-DM and UiO-66-MM respectively has the highest interactions with CH_4 and CO_2 molecules. These results are different than the behavior observed for UiO-66-Naphthyl where the Henry's constant is essentially unchanged compared to the parent material.[38b] Thus, there is a tradeoff between the hydrophobicity/ hydrophilicity of a MOF and its CO_2/CH_4 selectivity. Taking both hydrophilicity and selectivity factors into account, we believe that both UiO-66-MM and UiO-66-DM will exhibit superior performance over the parent MOF in humid gas separations. In the future, $CO_2/CH_4/H_2O$, $CO_2/N_2/H_2O$, and $NH_3/Air/H_2O$ breakthrough measurements at various relative humidities would be performed in our group to check the performance of these methyl functionalized UiO-66 frameworks compared to the parent structure.

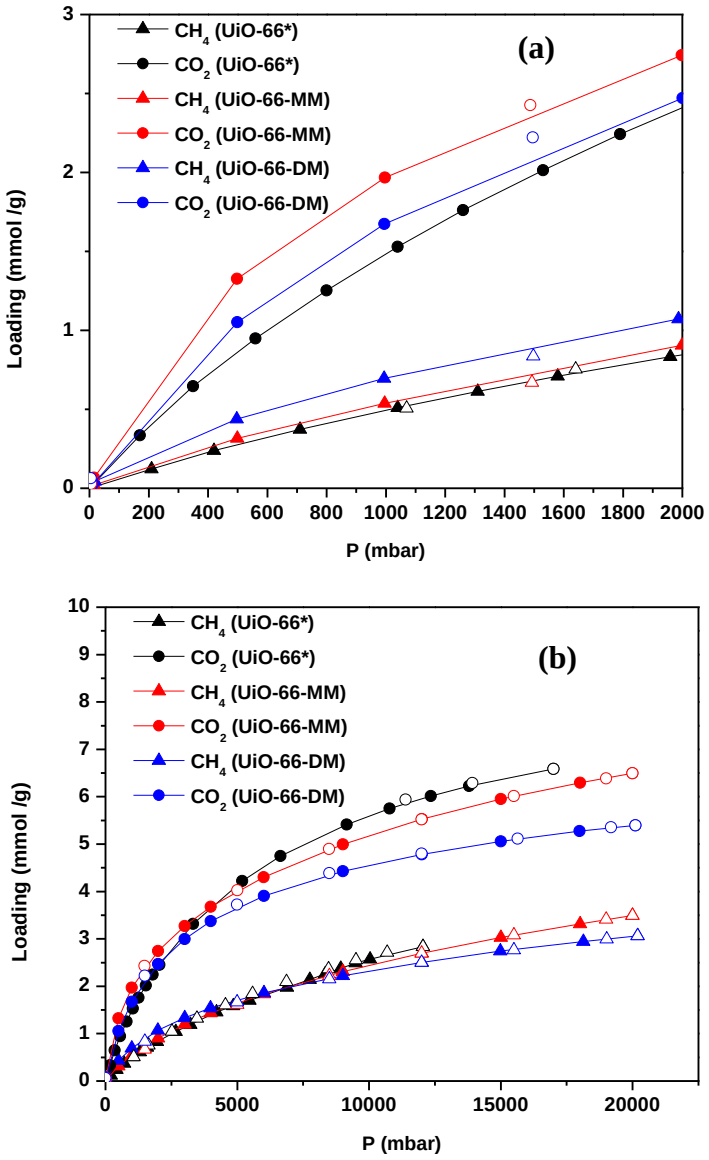

Figure 8.10 Adsorption isotherms for CO_2 and CH_4 in UiO-66, UiO-66-MM, and UiO-66-DM at 30 ^{o}C (closed symbols-adsorption; open symbols-desorption): (a) 0−2000 mbar and (b) 0−20,000 mbar. Lines connecting the adsorption points are to faciliate viewing. *Reported from literature.[49]

Table 8.2 Toth Model Parameters, Henry's Constants (K_H), and Low Coverage CO_2/ CH_4 Selectivities at 30 ^oC for UiO-66 Type MOFs.

MOF	CO_2			CH_4			$K_H^{CO_2} = C_s*b$ (mmol/g*mbar)	$K_H^{CH_4} = C_s*b$ (mmol/g*mbar)	Low coverage Selectivity (CO_2/CH_4)
	C_s	b	t	C_s	b	t			
[53]UiO-66	10.1061	2.06E-04	0.7654	42.9466	2.28E-05	0.3478	2.08E-03	9.78E-04	02.12
UiO-66-MM	21.1144	8.55E-04	0.3008	17.9681	6.42E-05	0.3936	1.08E-02	1.15E-03	15.64
UiO-66-DM	07.7105	4.92E-04	0.6120	10.5325	2.58E-04	0.3570	3.79E-03	2.72E-03	01.39

8.4 Conclusions

In summary, the synthesis and characterization of new water resistant, highly robust monomethyl- and dimethyl-functionalized UiO-66 analogues (UiO-66-MM and UiO-66-DM) have been carried out. Our study shows that functionalization by methyl moieties significantly reduces the water loading compared to UiO-66 without altering the high stability of the framework. Moreover, the water adsorption loadings and regeneration temperature of UiO-66-MM and UiO-66-DM are significantly lower than the benchmark material zeolite 13X. While amine groups have been a topic of intense focus for CO_2 separations, this work shows that nonpolar functional groups may also play an important role in enhancing CO_2 adsorption while lowering interactions with water. The methyl functionalized UiO-66 MOFs have lower affinity for water (UiO-66-DM < UiO-66-MM < UiO-66) compared to UiO-66. However, under dry conditions and low coverage both UiO-66-DM and UiO-66 have a low CO_2/CH_4 selectivity while UiO-66-

MM has a much higher CO_2/CH_4 selectivity. Taking both hydrophilicity and selectivity factors into account, we believe that both UiO-66-MM and UiO-66-DM will exhibit superior performance over the parent MOF in humid gas separations. In general, understanding the trade-offs between water adsorption behavior and high selectivity and high capacity for the target will be key to developing new adsorbents for CO_2 capture.

8.5 References

(1) Burchell, T.; Rogers, M. *SAE Tech. Pap. Ser.* **2000**, 2000-01-2205.

(2) Herout M.; Malaťák J.; Kučera L.; Dlabaja T. *Res. Agr. Eng.*, **2011,** 57, 137–143.

(3) Millward, A. R.; Yaghi, O. M. *J. Am. Chem. Soc.* **2005**, 127 (51), 17998-17999.

(4) D'Alessandro, D. M.; Smit, B.; Long, J. R. *Angew. Chem.-Int. Edit.* **2010,** *49* (35), 6058-6082.

(5) Yang, Q. Y.; Wiersum, A. D.; Jobic, H.; Guillerm, V.; Serre, C.; Llewellyn, P. L.; Maurin, G. *J. Phys. Chem. C* **2011,** *115* (28), 13768-13774.

(6) Cavenati, S.; Grande, C. A.; Rodrigues, A. E. *J. Chem. Eng. Data* **2004,** *49* (4), 1095-1101.

(7) Franchi, R. S.; Harlick, P. J. E.; Sayari, A. *Ind. Eng. Chem. Res.* **2005,** *44* (21), 8007-8013.

(8) Ferey, G.; Mellot-Draznieks, C.; Serre, C.; Millange, F. *Acc. Chem. Res.* **2005,** *38* (4), 217-225.

(9) Kitagawa, S.; Kitaura, R.; Noro, S. *Angew. Chem.-Int. Edit.* **2004,** *43* (18), 2334-2375.

(10) Keskin, S.; van Heest, T. M.; Sholl, D. S. *ChemSusChem* **2010,** *3* (8), 879-891.

(11) Eddaoudi, M.; Kim, J.; Rosi, N.; Vodak, D.; Wachter, J.; O'Keeffe, M.; Yaghi, O. M. *Science* **2002,** *295* (5554), 469-472.

(12) Karra, J. R.; Walton, K. S. *Langmuir* **2008,** *24* (16), 8620-8626.

(13) Han, S.; Huang, Y.; Watanabe, T.; Dai, Y.; Walton, K. S.; Nair, S.; Sholl, D. S.; Meredith, J. C. *ACS Comb. Sci.***2012,** *14* (4), 263-267.

(14) Low, J. J.; Benin, A. I.; Jakubczak, P.; Abrahamian, J. F.; Faheem, S. A.; Willis, R. R. *J. Am. Chem. Soc.* **2009,** *131* (43), 15834-15842.

(15) Greathouse, J. A.; Allendorf, M. D. *J. Am. Chem. Soc.* **2006,** *128* (33), 10678-10679.

(16) Cychosz, K. A.; Matzger, A. J. *Langmuir* **2010,** *26* (22), 17198-17202.

(17) Li, Y.; Yang, R. T. *Langmuir* **2007,** *23* (26), 12937-12944.

(18) Nalaparaju, A.; Zhao, X. S.; Jiang, J. W. *J. Phys. Chem. C* **2010,** *114* (26), 11542-11550.

(19) Kizzie, A. C.; Wong-Foy, A. G.; Matzger, A. J. *Langmuir* **2011,** *27* (10), 6368-6373.

(20) Saha, D.; Deng, S. *J. Phy. Chem. Lett.* **2010,** *1* (1), 73-78.

(21) Cavka, J. H.; Jakobsen, S.; Olsbye, U.; Guillou, N.; Lamberti, C.; Bordiga, S.; Lillerud, K. P. *J. Am. Chem. Soc.* **2008,** *130* (42), 13850-13851.

(22) Garibay, S. J.; Cohen, S. M. *Chem. Commun.* **2010,** *46* (41), 7700-7702.

(23) Wissmann, G.; Schaate, A.; Lilienthal, S.; Bremer, I.; Schneider, A. M.; Behrens, P. *Microporous and Mesoporous Mater.* **2012,** *152,* 64-70.

(24) Kandiah, M.; Nilsen, M. H.; Usseglio, S.; Jakobsen, S.; Olsbye, U.; Tilset, M.; Larabi, C.; Quadrelli, E. A.; Bonino, F.; Lillerud, K. P. *Chem. Mater.* **2010,** *22* (24), 6632-6640.

(25) Kim, M.; Cohen, S. M. *Crystengcomm* **2012,** *14* (12), 4096-4104.

(26) Schoenecker, P. M.; Carson, C. G.; Jasuja, H.; Flemming, C. J. J.; Walton, K. S. *Ind. Eng. Chem. Res.* **2012**, *51*, 6513.

(27) Soubeyrand-Lenoir, E.; Vagner, C.; Yoon, J. W.; Bazin, P.; Ragon, F.; Hwang, Y. K.; Serre, C.; Chang, J.-S.; Llewellyn, P. L. *J. Am. Chem. Soc.* **2012,** *134* (24), 10174-10181.

(28) Choi, S.; Watanabe, T.; Bae, T.-H.; Sholl, D. S.; Jones, C. W. *J. Phy. Chem. Lett.* **2012,** *3* (9), 1136-1141.

(29) Yang, Q.; Wiersum, A. D.; Llewellyn, P. L.; Guillerm, V.; Serred, C.; Maurin, G. *Chem. Commun.* **2011,** *47* (34), 9603-9605.

(30) Zhao, Y. G.; Wu, H. H.; Emge, T. J.; Gong, Q. H.; Nijem, N.; Chabal, Y. J.; Kong, L. Z.; Langreth, D. C.; Liu, H.; Zeng, H. P.; Li, J. *Chem. Eur. J.* **2011,** *17* (18), 5100-5108.

(31) Yang, C.; Kaipa, U.; Mather, Q. Z.; Wang, X.; Nesterov, V.; Venero, A. F.; Omary, M. A. *J. Am. Chem. Soc.* **2011,** *133* (45), 18094-18097.

(32) Serre, C. *Angew. Chem.-Int. Edit.* **2012,** *51* (25), 6048-6050.

(33) Wu, T.; Shen, L.; Luebbers, M.; Hu, C.; Chen, Q.; Ni, Z.; Masel, R. I. *Chem. Commun.* **2010,** *46* (33).

(34) Yang, J.; Grzech, A.; Mulder, F. M.; Dingemans, T. J. *Chem. Commun.* **2011,** *47* (18), 5244-5246.

(35) Nguyen, J. G.; Cohen, S. M. *J. Am. Chem. Soc.* **2010,** *132* (13), 4560-+.

(36) Paranthaman, S.; Coudert, F.-X.; Fuchs, A. H. *Phys. Chem. Chem. Phys.* **2010,** *12* (28), 8123-8129.

(37) Ma, D.; Li, Y.; Li, Z. *Chem. Commun.* **2011,** *47* (26), 7377-7379.

(38) (a)Cai, Y.; Zhang, Y. D.; Huang, Y. G.; Marder, S. R.; Walton, K. S. *Crystal Growth & Design* **2012,** *12* (7), 3709-3713. (b) Cmarik, G. E.; Kim, M.; Cohen, S. M.; Walton, K. S. *Langmuir* **2012,** *28* (44), 15606-13. (c) Burtch, N. C.; Jasuja, H.; Dubbeldam, D.; Walton, K. S. *J Am Chem Soc* **2013,** *135* (19), 7172-80.

(39) Huang, Y.; Qin, W.; Li, Z.; Li, Y. *Dalton Trans.* **2012,** *41* (31), 9283-9285.

(40) (a) Walton, K. S.; Snurr, R. Q. *J Am Chem Soc* **2007,** *129* (27), 8552-6. (b) Duong, D. D. *Imperial College Press, London* **1998**.

(41) Valenzano, L.; Civalleri, B.; Chavan, S.; Bordiga, S.; Nilsen, M. H.; Jakobsen, S.; Lillerud, K. P.; Lamberti, C. *Chem. Mater.* **2011**, *23*, 1700-1718.

(42) Kaye, S. S.; Dailly, A.; Yaghi, O. M.; Long, J. R. *J. Am. Chem. Soc.* **2007**, *129*, 14176-14177.

(43) Kondo, A.; Daimaru, T.; Noguchi, H.; Ohba, T.; Kaneko, K.; Kanob, H. *J. Colloid Interface Sci.* **2007**, *314*, 422-426.

(44) Cortes, F. B.; Chejne, F.; Carrasco-Marin, F.; Moreno-Castilla, C.; Perez-Cadenas, A. F. *Adsorption* **2010**, *16*, 141-146.

(45) Lee, J. S.; Kim, J. H.; Kim, J. T.; Suh, J. K.; Lee, J. M.; Lee, C. H. *J. Chem. Eng. Data* **2002**, *47*, 1237-1242.

(46) Jasuja, H.; Huang, Y.; Walton, K. S. *Langmuir* **2012**, *28*, 16874-16880.

(47) Jasuja, H.; Burtch, N. C.; Huang, Y.; Cai, Y.; Walton, K. S. *Langmuir* **2012,** *29*, 633-642.

(48) Liu, H.; Zhao, Y.; Zhang, Z.; Nijem, N.; Chabal, Y. J.; Peng, X.; Zeng, H.; Li, J. *Chemistry – An Asian Journal* **2013,** *8* (4), 778-785.

(49) Wiersum, A. D.; Soubeyrand-Lenoir, E.; Yang, Q. Y.; Moulin, B.; Guillerm, V.; Ben Yahia, M.; Bourrelly, S.; Vimont, A.; Miller, S.; Vagner, C.; Daturi, M.; Clet, G.; Serre, C.; Maurin, G.; Llewellyn, P. L. *Chem. Asian J.* **2011,** *6* (12), 3270-3280.

(50) Biswas, S.; Van Der Voort, P. *Eur. J. Inorg. Chem.* **2013,** *2013* (12), 2154-2160.

(51) Van Heest, T.; Teich-McGoldrick, S. L.; Greathouse, J. A.; Allendorf, M. D.; Sholl, D. S. *J. Phys. Chem. C* **2012,** *116* (24), 13183-13195.

CHAPTER 9

METAL-ORGANIC FRAMEWORK SCALE-UP: EFFECT OF SOLVENT REDUCTION ON THE SYNTHESIS OF THE HIGHLY ROBUST ZR-BDC (UIO-66) MOF

This work was conducted in collaboration with Deonte Fletcher (undergraduate researcher of the Walton group).

9.1 Introduction

Activated carbons and zeolite molecular sieves have been used commercially as adsorbents, catalysts, and ion exchangers for many decades.[1,2] However, now metal-organic frameworks or MOFs have emerged as a new competitor. MOFs are crystalline porous materials consisting of metal-containing nodes and organic ligands, which are connected to each other.[3] MOFs possess various attractive features such as high values of porosity (surface area and pore volume), uniform pore sizes which are easily tunable, chemically functionalized adsorption sites, and potential for post-synthetic modification (PSM).[4] Hence, MOFs are currently at the forefront of research into new fuel-tanks for adsorptive methane and hydrogen storage, catalysis, and gas separation.[5] Over the next 10-15 years, advances in MOF chemistry should lead to a revolution in the field of microporous materials.

In spite of the numerous desirable attributes of MOFs, their commercial and industrial applications have been hindered by issues with stability under humid conditions and difficulties in the scale-up of synthesis methods. As discussed in Chapters 3-6 and 8 various recent publications have emerged reporting MOFs capable of

withstanding water exposure without any loss in their crystallinity and porosity. However, the scale-up of MOFs has not been widely studied. There are a few publications on MOF scale-up in the literature with varying level of details. Solvothermal synthesis of HKUST-1 or Cu-BTC on an 80 g scale using a batch reactor by Wang et al.[6] is the first study reported in this context followed by the synthesis of MOF-5 on a 50 g scale by Mueller et al.[7] Recently Seo et al.[8] reported the synthesis of MIL-100 (Fe) on a 15.6 kg scale per batch using a 200 L Hastalloy C-276 reactor vessel. MOFs are normally synthesized using batch solvothermal reactions similar to zeolites. However, there have been some publications reporting continuous-flow solvothermal MOF synthesis processes.[9-11] On the industrial scale, continuous-flow through reactors can reduce MOF production cost significantly and increase material production immensely via reduced downtime.

For the MOF syntheses scale-up and crystallization process design, the following matters need to be considered[12]: (i) accessibility and prices of the raw materials (metal precursor and organic ligand), (ii) accomplishing high yields (measured using space-time yield or STY- kg of MOF product per m^3 of reaction mixture per day of synthesis), (iii) evading large quantities of impurities, (iv) operating conditions for synthesis and (v) eliminating use of large amounts of organic solvents. Metal precursors such as nitrate salts and chloride salts should be avoided as they are explosive and corrosive respectively. Otherwise, sophisticated materials (e.g., Hastalloy C-276 used for MIL-100 (Fe)[8] synthesis from iron nitrate) have to be used for the reactor design, which in turn will increase the cost of MOF production. The elimination of the large usage of organic solvents required in most solvothermal MOF syntheses can be extremely

important for MOF scale-up since it can reduce the raw material costs, waste disposal costs, filtration costs, and environmental concerns.

BASF is the only major company known to be working towards the industrial-scale synthesis of MOFs. Their patent applications cover non-conventional MOF synthesis techniques including microwave,[13] electrochemical,[14] and organic solvent free synthesis.[15,16] Cu-BTC or HKUST-1 has been produced on the industrial scale by BASF under the name Basolite C300 using the continuous electrochemical synthesis.[14] The electrochemical method omits anions such as nitrates and chlorides that are problematic from the process control point of view. However, the electrochemical synthesis can be costly for MOF production when the metal anodes required in the synthesis are more expensive than metal salts required in solvothermal synthesis. Hence, this technique has not been applied to a wide range of MOFs unlike solvothermal synthesis, which is usually used for MOF production. Majano et al.[17] has used copper (II) hydroxide, which is an appealing alternative to metal nitrates or metal chlorides for the large scale (reaction volume~ 3.7 L) solvothermal synthesis (STY~ 1842 kg/m^3day^{-1}) of HKUST-1 in aqueous ethanolic solution at room temperature. Hence, use of harmful solvents such as DMF (dimethylformamide), DEF (dimethylformamide), and DMSO (dimethylsulfoxide) has now been avoided. Huo et al.[18] synthesized HKUST-1 using water as a solvent (reaction volume~ 1.2 L) at room temperature with a STY of 1791 kg/m^3day^{-1}, much higher than the STY of 225 kg/m^3day^{-1} for Basolite C300. Similarly, BASF has reported synthesis of the Al-fumarate MOF (Basolite A520)[16,19] from aluminum sulfate instead of nitrate or chloride salt as metal precursor in aqueous solution with the STY greater than 3600 kg/m^3day^{-1} at moderate temperature (room temperature to 60 ^oC) and ambient pressure.

BASF has also made industrial scale synthesis of Mg-MOF (Basolite M050, STY greater than 3000 kg/m^3day^{-1})[15] attractive by using a solvent-free approach since in this case the ligand (formic acid) plays the role of solvent. However, some organic ligands such as BDC (benzene dicarboxylic acid) are difficult to maintain in liquid state.[20] Hence, this technique has also not been applied to a wide range of MOFs unlike solvothermal synthesis, which is usually used for MOF production.

Thus, 6 BASF MOFs (Basolite A100 or MIL-53(Al), Basolite C300 or HKUST-1, Basolite F300 or Fe-BTC, Basolite M050 or Mg-Formate, Basolite A520 or Al-Fumarate, and Basolite Z1200 or ZIF-8)[5,14,19,21] can be obtained commercially through Sigma Aldrich with prices up to ~ 30 $/g MOF.[22] With such a high price, MOFs cannot compete in the 3 billion dollar adsorbent market,[23] and their synthesis cost must be reduced. Moreover, only Al-based Basolite MOFs (A100, A520) and Basolite Z1200 are stable under humid conditions.[5] Hence, currently only three water stable MOFs are commercially available, and there is a lot of opportunity for the scale-up of other water stable MOFs.

MOF synthesis by techniques such as microwave, sonochemical, and mechanochemical methods are still in their formative stages and will take more time to become fully established.[24] Hence, in this Chapter, the scale-up of the UiO-66 MOF (Figure 9.1, refer Chapter 2 for structural details) has been examined using the batch solvothermal reaction. More specifically, the effect of solvent reduction on the solvothermal synthesis of UiO-66 has been studied. As mentioned before, the elimination of the large usage of DMF solvent required for UiO-66 synthesis can reduce the raw material costs, waste disposal costs, filtration costs, and environmental concerns

significantly at the industrial scale. A cost analysis (raw material prices of 24th Feb. 2014 were used) of a 5 gallon reaction volume for UiO-66 synthesis using a three times concentrated recipe (3X) than the original recipe (1X) of Cavka et al.[25] shows that ~92 % of the total material cost (~725 USD) is due to the DMF solvent. Moreover, minimization of the solvent amount used means maximization of the STY. Usually, small scale MOF syntheses reported in the literature are not optimized and have a STY in the range of 0.1-1 kg/m^3day^{-1}.[5] With such small values of the STY, MOF syntheses cannot be economical because large size reactors will now be required or more reactors will be needed to synthesize a certain quantity of MOF in a given time period.

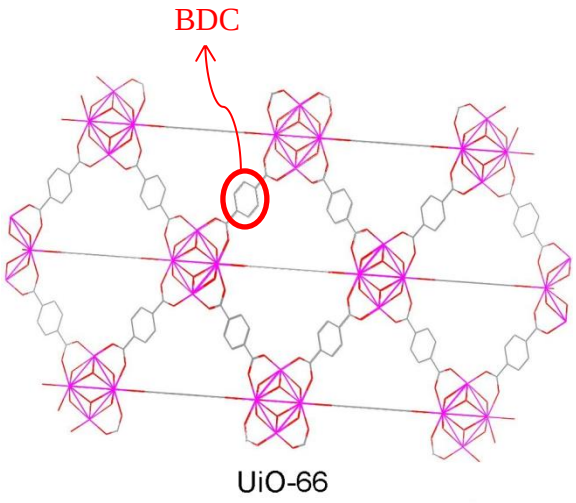

Figure 9.1 Illustration of UiO-66 framework structure (C- Grey, Zr- Pink, O- Red, and H- omitted for clarity).

UiO-66 is selected for this work because it has shown unprecedented thermal ($T_{decomp.}$ = 540 ^oC), chemical (stable in solvents such as water, acetone, and benzene), and mechanical (pressure up to 10,000 kg/cm^2 or ~9800 bar) stability.[25] This stability has

been attributed to the oxophilicity and high nuclearity of the zirconium (IV) based inorganic brick [$Zr_6O_4(OH)_4$]. Moreover, as mentioned in Chapters 7 and 8, UiO-66 is shown to be exceedingly amenable to isoreticular functionalization without losing its high hydrothermal and chemical stabilities. Hence, the current study should provide a platform for the future scale-up efforts for various functionalized variations of UiO-66, which have shown good performance towards ammonia removal from air (refer to Chapter 7 for details).

9.2 Experimental Section

9.2.1 Materials

All the chemicals were commercially available and employed as-received: Sigma-Aldrich, N,N′-dimethylformamide (DMF), zirconium (IV) chloride ($ZrCl_4$); Acros, 1,4-benzene-dicarboxylic acid (BDC), zirconium (IV) chloride ($ZrCl_4$).

The original recipe of Cavka et al.[25] for UiO-66 synthesis reports heating of an equimolar (0.227 mmol) mixture of $ZrCl_4$ and BDC precursors in 26.5 mL of DMF solvent (reactant concentration = 0.0085 M, we call it 1X) at 120 ˚C for 24 hr in a sealed glass vial or Teflon lined autoclave. After synthesis, the solution was cooled to room temperature; the resulting solid was filtered and washed with DMF three times. This gives a yield of ~0.050 g (STY of 1.89 kg/$m^3$$day^{-1}$) of white colored as-synthesized UiO-66 powder. Cohen et al.[3] has successfully synthesized UiO-66 at 120 ˚C and in 24 hr with 0.35 mmol of reactants in 4 mL DMF, i.e., ten times (10X) higher concentration. Moreover, the solubility of BDC in DMF at 25 ^oC is 0.3677 M (44X).[26] Thus, there is room for optimizing the solvent amount used with respect to the product yield and for further increasing the STY of the UiO-66 synthesis. Here, UiO-66 has been synthesized

with increasing reactant concentrations in 26.5 mL DMF, and the quality and yield of the product were studied. Further, by using the refined synthesis recipe UiO-66 synthesis has been scaled-up to 50 g (STY of 180 kg/m^3day^{-1}) per batch. Quality is assessed using powder XRD and BET analysis of N_2 adsorption isotherms.

9.2.2 Powder X-Ray Diffraction

Powder X-ray diffraction (PXRD) patterns were recorded on a X'Pert X-ray PANalytical diffractometer with an X'celerator module using Cu Kα (λ = 1.5418 Å) radiation at room temperature, with a step size of 0.02˚ in 2θ.

9.2.3 BET Surface Area Analysis

Nitrogen adsorption isotherms at 77 K were measured using a Quadrasorb system from Quantachrome instruments to evaluate the porosity of the synthesized UiO-66 samples. To calculate BET surface areas, the report of Walton et al.[27] was followed to accurately fit the BET model to nitrogen adsorption isotherms in the low pressure range ($P/P_0 < 0.05$).

9.3 Results and Discussion

Before starting the reactant concentration optimization, the scalability of UiO-66 at 3X concentration was evaluated at by simply increasing the reaction volume from 26.5 mL to 742 mL at synthesis conditions of 120 ˚C and 24 hr (Table 1, concentration = 0.0255 M, 3 times (3X) of Cavka et al.[25]). PXRD patterns of samples from all the batches match well with the simulated XRD pattern obtained from the CIF of UiO-66 (Figure 9.2). N_2 adsorption was performed on the activated (under vacuum at 200℃ for 12-18 hrs.) samples from all the batches, which gave BET surface area in the range of 1075-

1385 m^2/g. It was observed that as the reaction volume increases surface area first decreases and then becomes constant (Figure 9.3). This might be due to more time needed for crystallization in large volume batches or more extensive washing required post MOF synthesis, for the large quantities of UiO-66 produced. It was also noticed that the yield of the activated MOF (Figure 9.3) increases linearly with the reaction volume, which is a nontrivial first step in MOF scale-up. This result was encouraging enough to move on to the reactant concentration optimization idea. Concentration optimization (solvent minimization) should bring down cost of MOF production significantly.

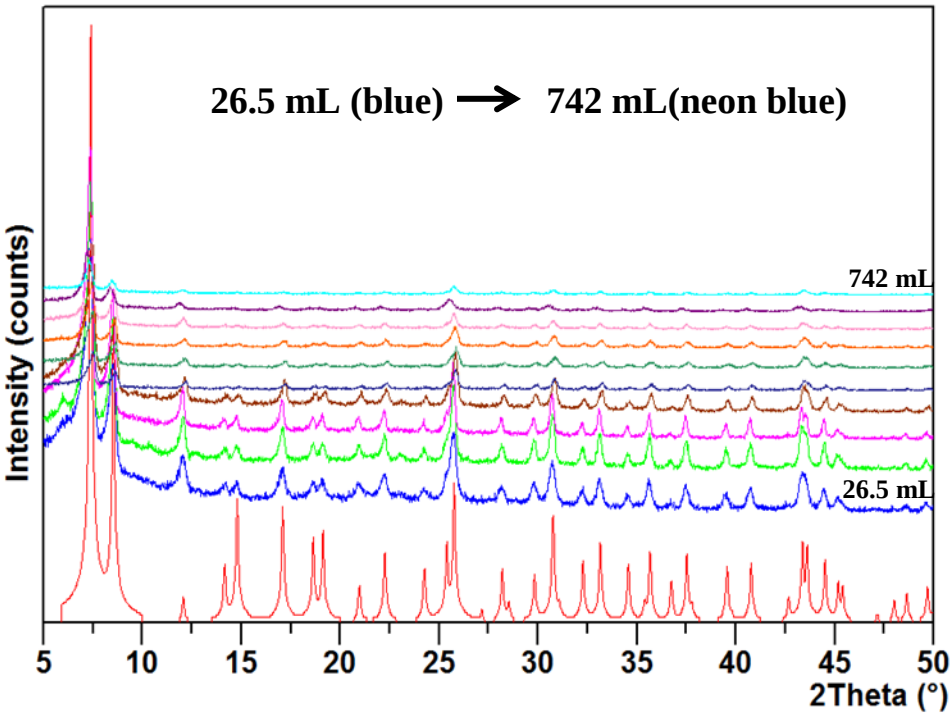

Figure 9.2 PXRD patterns of UiO-66 synthesized at 3X concentration using various reaction volumes (red- simulated pattern, blue-26.5 mL, neon blue- 742 mL).

Table 9.1 Data of UiO-66 Scale-Up Experiments at Concentration = 0.0255 M, 3X of Cavka et al.[25]

Volume of DMF (mL)	Reactants (mmoles)	BET Surface Area (m^2/g)	Weight of activated UiO-66 produced (g)
26.5	0.681	1370	0.1560
53	1.362	1385	0.3565
79.5	2.043	1350	0.5310
106	2.724	1340	0.7165
212	5.448	1240	1.4285
318	8.172	1235	1.9790
424	10.896	1160	2.9515
530	13.620	1085	3.3630
636	16.344	1075	4.3200
742	19.068	1080	5.0270

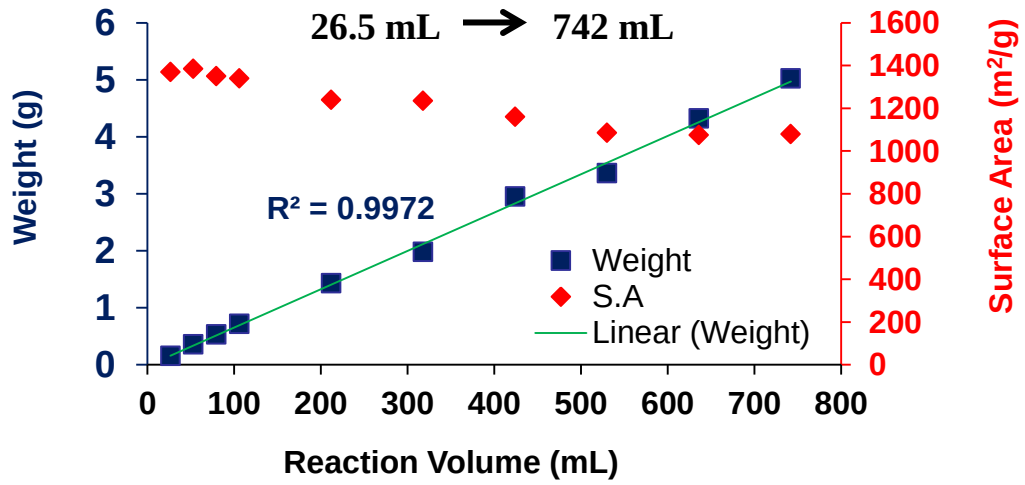

Figure 9.3 Yield and BET surface area (S.A.) of activated UiO-66 as a function of reaction volume at 3X concentration

After confirming the scalability of UiO-66 at 3X concentration, conditions for the batch synthesis of UiO-66 were optimized by following a three-step approach:

1. Synthesize UiO-66 with increasing reactant amounts in 26.5 mL DMF (reactant concentration also increases) at 120 ^{o}C for 24 hr.
2. Increase the synthesis time for concentrations higher than the optimum concentration from step 1.
3. Reduce the synthesis time by increasing the synthesis temperature.

Thus, the optimum conditions required to obtain the high yield of high quality UiO-66 in the shortest possible time with the minimum use of solvent can be found.

It was observed that the yield of UiO-66 increases linearly up to 0.0765 M (9X) concentration of reactants (Figure 9.4 and Table 9.2) used in the synthesis at 120 ^{o}C, 24 hr and thus, high quality material (good crystallinity-Figure 9.6, surface area > 1000 m^2/g) in high yield is obtained from the same amount of DMF (26.5 mL). However, upon jumping to 15X concentration from 9X concentration, the synthesis time was doubled to 48 hr and concentrated HCl (12.4 M, same mmoles as of BDC ligand) was also added. It was observed that HCl improved the solubility of precursor chemicals and crystallization rate. Hence, in the 24 hr synthesis and without adding HCl, low quality product in low yield was obtained due to insufficient time available for the crystallization of UiO-66 crystals with a reactant concentration higher than 9X. Due to this reason, the synthesis with 9X concentration for 48 hr showed an increase in the yield and BET surface area compared to the 24 hr synthesis (Table 9.2). Moreover, there were issues in filtration with 15X concentration during the 24 hr synthesis, i.e., after synthesis MOF particles were passing through the filter paper even upon using finer filter paper (Fisherbrand™, P2, P4

grade)[28] than the filter paper (Fisherbrand™, P8 grade)[28] typically used in our labs to filter MOF precipitate after synthesis. There were no filtration issues at all after adding HCl and increasing the synthesis time to 48 hr for concentrations higher than 15X. Farha et al.[29] have recently supported our observation since they also observed that HCl speeds up the crystallization during the synthesis of UiO-66 or UiO-67. Moreover, adding HCl will neutralize the amine impurities present inherently in the reagent grade DMF obtained from Sigma Aldrich.[30] In fact, the rotten fish smell of DMF is due to amine impurities present, and purified (distilled) DMF should not have any smell.

Ideally, particle size distributions should have been measured for samples obtained under various synthesis conditions in this study. However, UiO-66 and its other functionalized analogues crystallize as intergrown crystals that are too small to be visualized under an electron microscope such as TEM (transmission electron microscope). Furthermore, the use of techniques such as dynamic light scattering (DLS) have issues of particle agglomeration in the solvent used for DLS. Due to these reasons, Dr. Schoenecker from our group could not measure particle size distribution during his PhD project of scaling up the UiO-66-NH_2 MOF in a flow-through reactor.[9] However, work done by Schaate et al.[31] has shown that by using modulators such as acetic acid and benzoic acid, the crystal size of UiO-66 could be increased (single crystal could be picked now) as these modulators slow down MOF formation and hence now it becomes possible to measure particle size distribution using DLS. In this work, the use of modulators was not considered during the UiO-66 synthesis since the main goal was to showcase that the amount of DMF used with respect to yield obtained could be reduced

further compared to Cavka et al.[25] and it is possible to use the optimized synthesis conditions for UiO-66 scale-up.

Upon further increasing the reactant concentration (Figure 9.5) in the 48 hr synthesis with HCl addition, the yield of good quality (good crystallinity- Figure 9.6, surface area > 1000 m^2/g) UiO-66 again increases linearly up to 35X concentration. Approximately 3 g of the as-synthesized UiO-66 (Figure 9.7-left) can be obtained from 26.5 mL DMF by using 35X reactant concentration with a STY of 55 kg/m^3day^{-1} (Table 9.2). However, except Basolite F300, which has STY of 20 kg/m^3day^{-1}, the STY for all the other Basolite materials is greater than 55 kg/m^3day^{-1}.[5,21] Hence, to increase the STY the synthesis time was reduced by increasing the synthesis temperature. At the same time, Guillerm et al.[32] reported the synthesis of MIL-140-A, a polymorph of UiO-66 (Table 9.3), by heating a high concentration of reactants (~ 39X concentration for BDC ligand and ~ 19.5X concentration for $ZrCl_4$) in 125 mL DMF (no HCl addition) at 220 ^oC for 16 hrs. Hence, we modified the recipe of Guillerm et al.[32] and tried the synthesis of UiO-66 with HCl addition (12.4 M, equimolar to the BDC ligand) and 39X concentration of both reactants in 26.5 mL DMF at 200 ^oC for 16 hrs in the Teflon lined autoclave reactors from Parr.[33] Now, glass jars or vials cannot handle the build-up of pressure at such high reaction temperatures due to boiling of the solvent. To our delight, good quality (good crystallinity- Figure 9.6, surface area > 1000 m^2/g) material was produced, and the yield obtained was higher than values obtained with the syntheses using concentration lower than or equal to 35X at 120 ^oC for 2 days, and moreover, the STY has now increased to 179 kg/m^3day^{-1} (Table 9.2).

Upon further increasing the reactant concentration the yield again increases linearly up to 44X concentration (Figure 9.8). Hence, it is now possible to synthesize ~ 3.5 g of good quality UiO-66 from 26.5 mL DMF in just 16 hr at 200 ^{o}C by using the 44X concentration (the solubility limit of BDC in DMF at 25 ^{o}C) and achieve a STY of 196 kg/m^{3}day^{-1}. This STY is higher than that of most of the zeolites (STY ~ 50-150 kg/m^{3}day^{-1}) and BASF MOFs such as Basolite F300 (STY ~ 20 kg/m^{3}day^{-1}), Basolite Z1200 (STY ~ 100 kg/m^{3}day^{-1}), and Basolite A100 (STY ~ 160 kg/m^{3}day^{-1}).[21] Similarly, the synthesis at 200 ^{o}C, 16 hr for other lower reactant concentrations (20X, 25X, 30X, 35X, Figure 9.7- right) were also performed. Yields and MOF quality obtained in 16 hr at 200 ^{o}C are similar to values obtained with the synthesis at 120 ^{o}C for 2 days but STY will now be increased three-fold. Moreover, combining the yield data for lower reactant concentrations (20X, 25X, 30X, 35X) with higher reactant concentrations (39X, 40X, 44X) it was observed that the yield again increases linearly for syntheses at 200 ^{o}C, 16 hr (Figure 9.9). While writing this Chapter, Ragon et al.[34] independently published a report describing the UiO-66 scale-up with rather high STY of ~ 490 kg/m^{3}day^{-1} since they used extremely large quantities (19 times higher molar ratio of HCl to ligand compared to this work) of HCl, which in turn speeds up the crystallization.

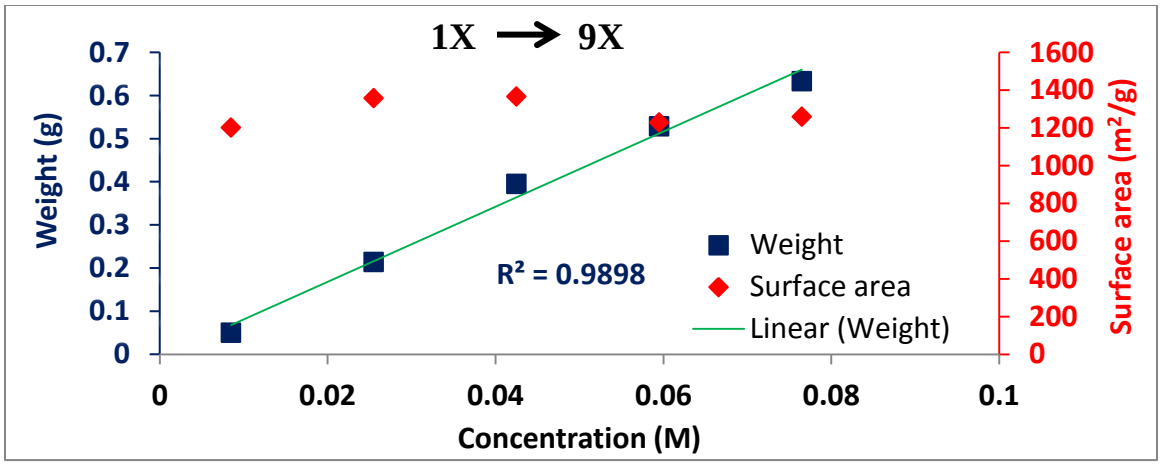

Figure 9.4 Yield and BET surface area of as-synthesized UiO-66 as a function of reactant concentrations at 120 ^{o}C and 24 hrs.

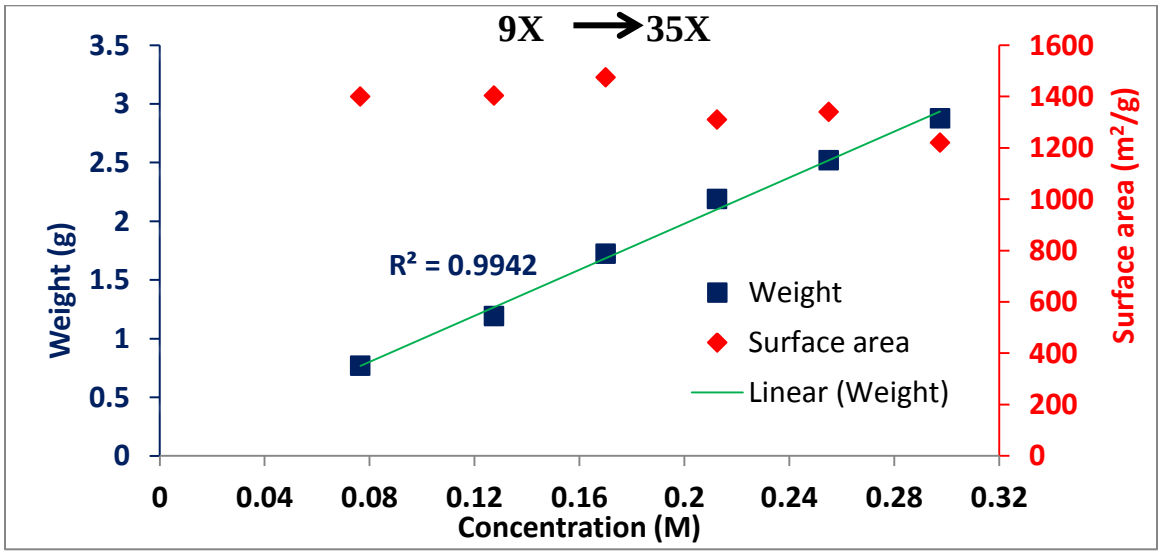

Figure 9.5 Yield and BET surface area of as-synthesized UiO-66 as a function of reactant concentrations at 120 ^{o}C and 48 hr.

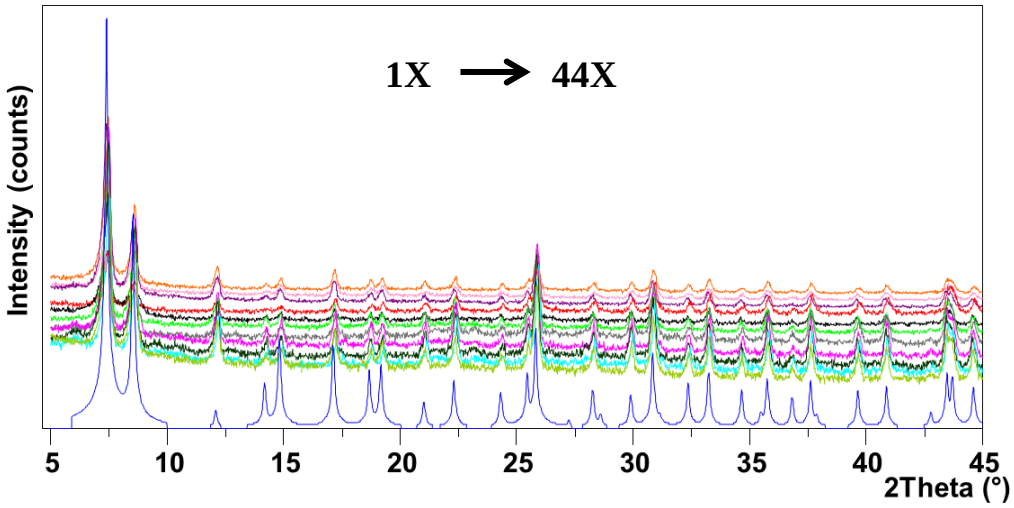

Figure 9.6 PXRD patterns of UiO-66 synthesized with increasing reactant concentrations in a 26.5 mL reaction volume (blue- simulated pattern, green- 1X, orange- 44X, PXRD patterns for 3X and 39X are not shown here).

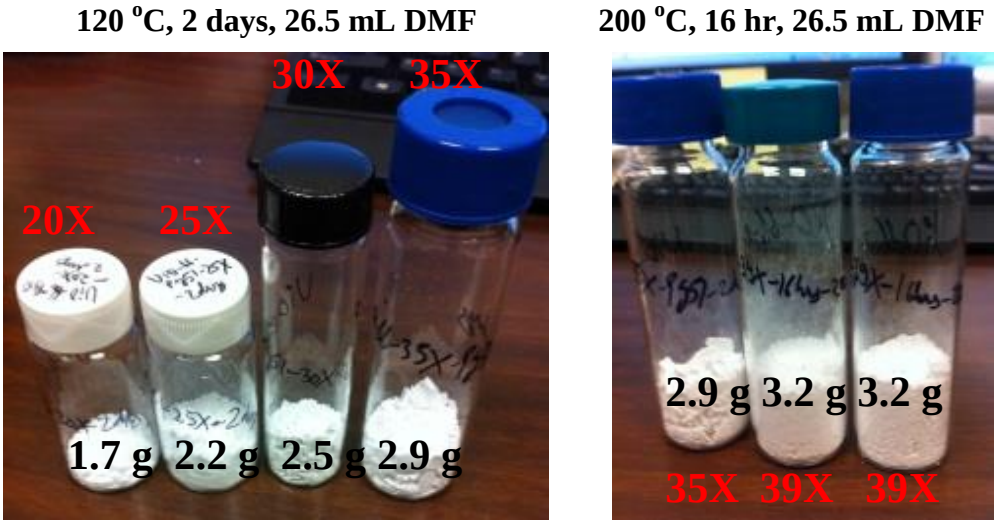

Figure 9.7 Vials demonstrating increase in the yield of as-synthesized UiO-66 as a function of reactant concentrations, left: at 120 °C, 2 days, and 26.5 mL DMF, right: at 200 °C, 16 hrs, and 26.5 mL DMF.

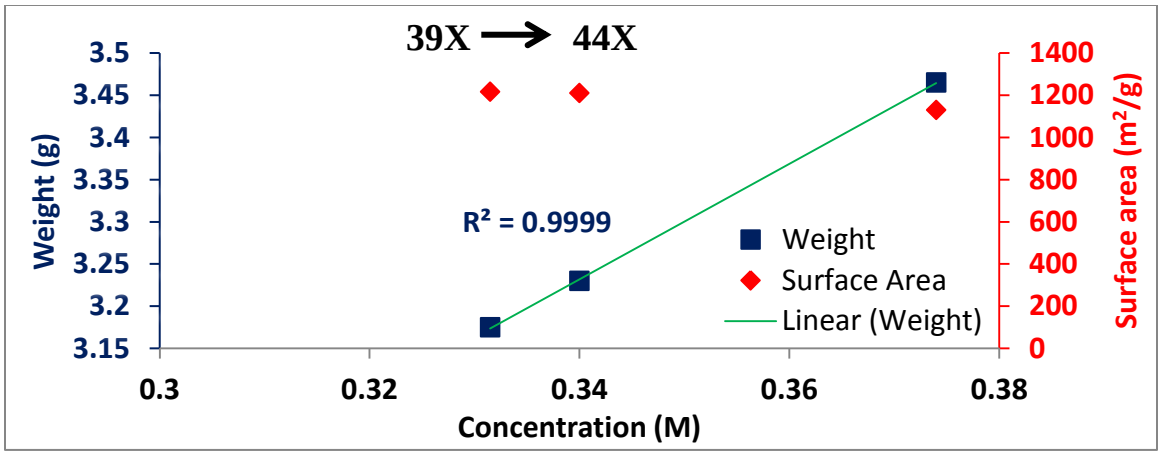

Figure 9.8 Yield and BET surface area of as-synthesized UiO-66 as a function of reactant concentrations at 200 ^{o}C and 16 hr.

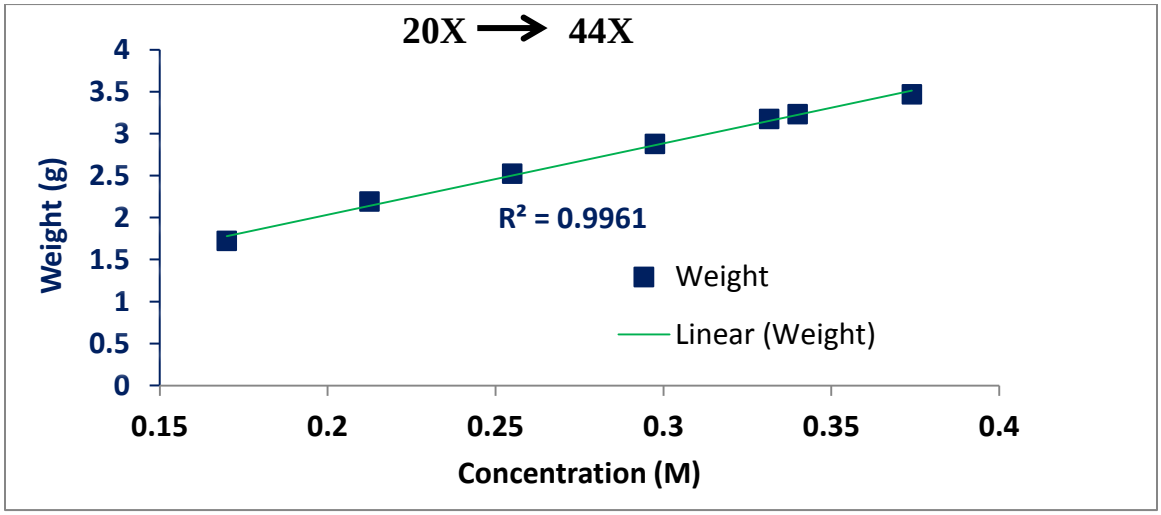

Figure 9.9 Yield of as-synthesized UiO-66 as a function of reactant concentrations at 200 ^{o}C and 16 hr.

Synthesis temperatures lower than Guillerm et al.[32] were attempted since it was reported that MIL-140-A is the thermodynamic phase (forms at higher temperature) whereas UiO-66 is the kinetic phase (forms at lower temperature). Upon aging $ZrCl_4$

hydrolyzes to form ZrO_2, which is an integral part of the SBU of MIL-140-A. Hence, it was observed that if the $ZrCl_4$ bottle is old (exposed to moisture present in the lab air various times) then even at 200 ^oC there is a small impurity of MIL-140-A (shown as ✦) present in the UiO-66 sample (Figure 9.10 and BET surface is slightly decreased i.e., 955 m^2/g). However, when fresh $ZrCl_4$ was used, pure UiO-66 (Figure 9.11 and BET surface area of 1183 m^2/g) was obtained. Similarly, it was also noticed that if the Teflon liners used for synthesis are not properly cleaned and have some impurity of MIL-140-A from the previous run then also MIL-140-A is preferred due to a seeding effect during crystallization (Figure 9.12). Hence, old $ZrCl_4$ or improperly cleaned Teflon liners will lead to impurities of MIL-140-A in the synthesized UiO-66 sample.

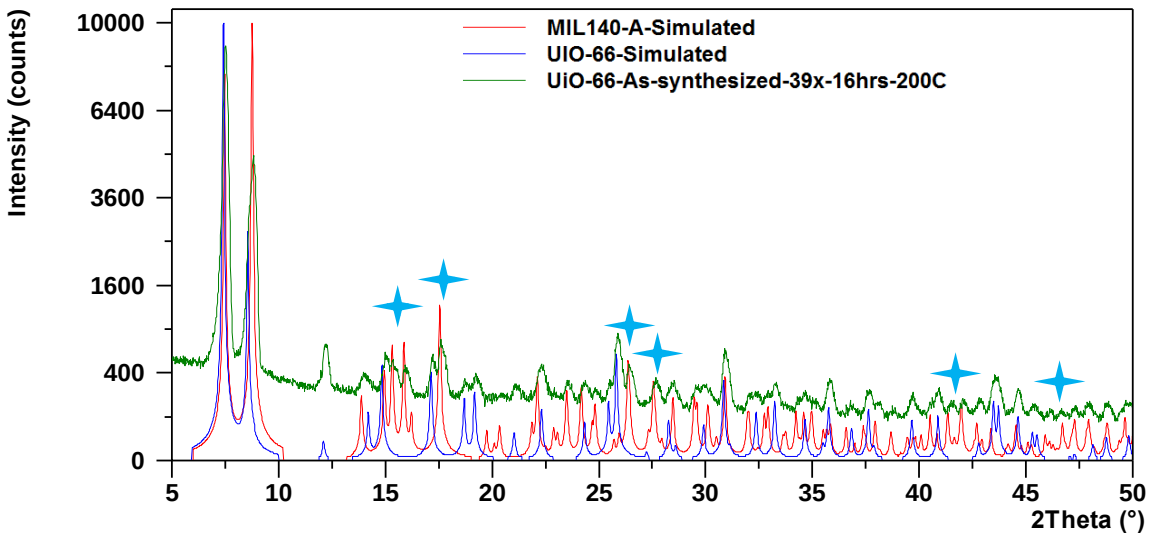

Figure 9.10 PXRD pattern of UiO-66 with MIL-140-A impurity (shown as ✦), synthesized with 39X concentration of reactants (old $ZrCl_4$ bottle) in 26.5 mL reaction volume at 200 ^oC and 16 hr (blue- simulated pattern of UiO-66, red- simulated pattern of MIL-140-A).

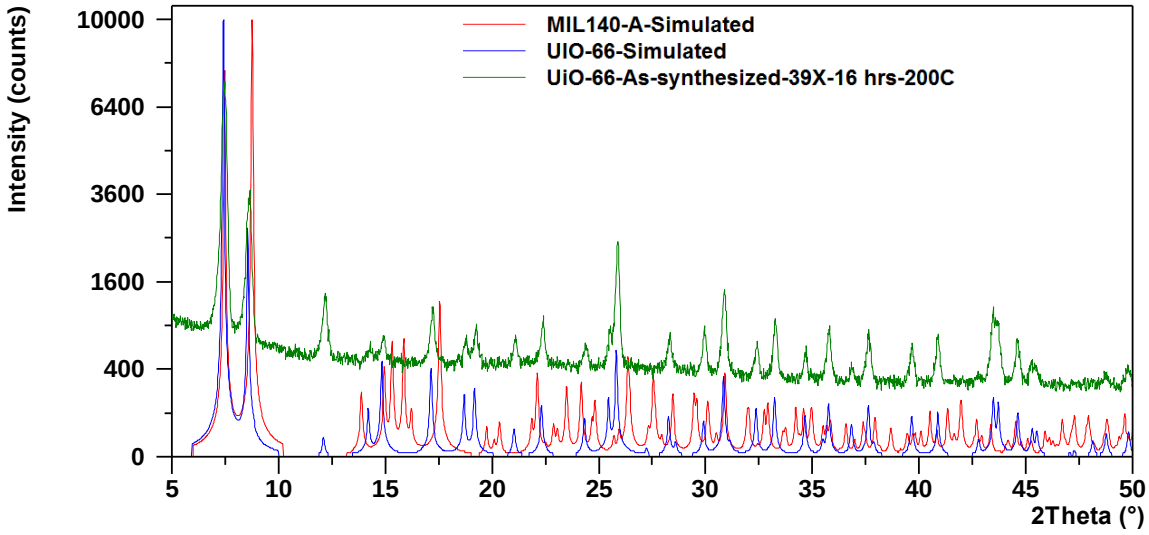

Figure 9.11 PXRD pattern of UiO-66 without MIL-140-A impurity, synthesized with 39X concentration of reactants (fresh $ZrCl_4$ bottle) in 26.5 mL reaction volume at 200 ^oC and 16 hr (blue- simulated pattern of UiO-66, red- simulated pattern of MIL-140-A).

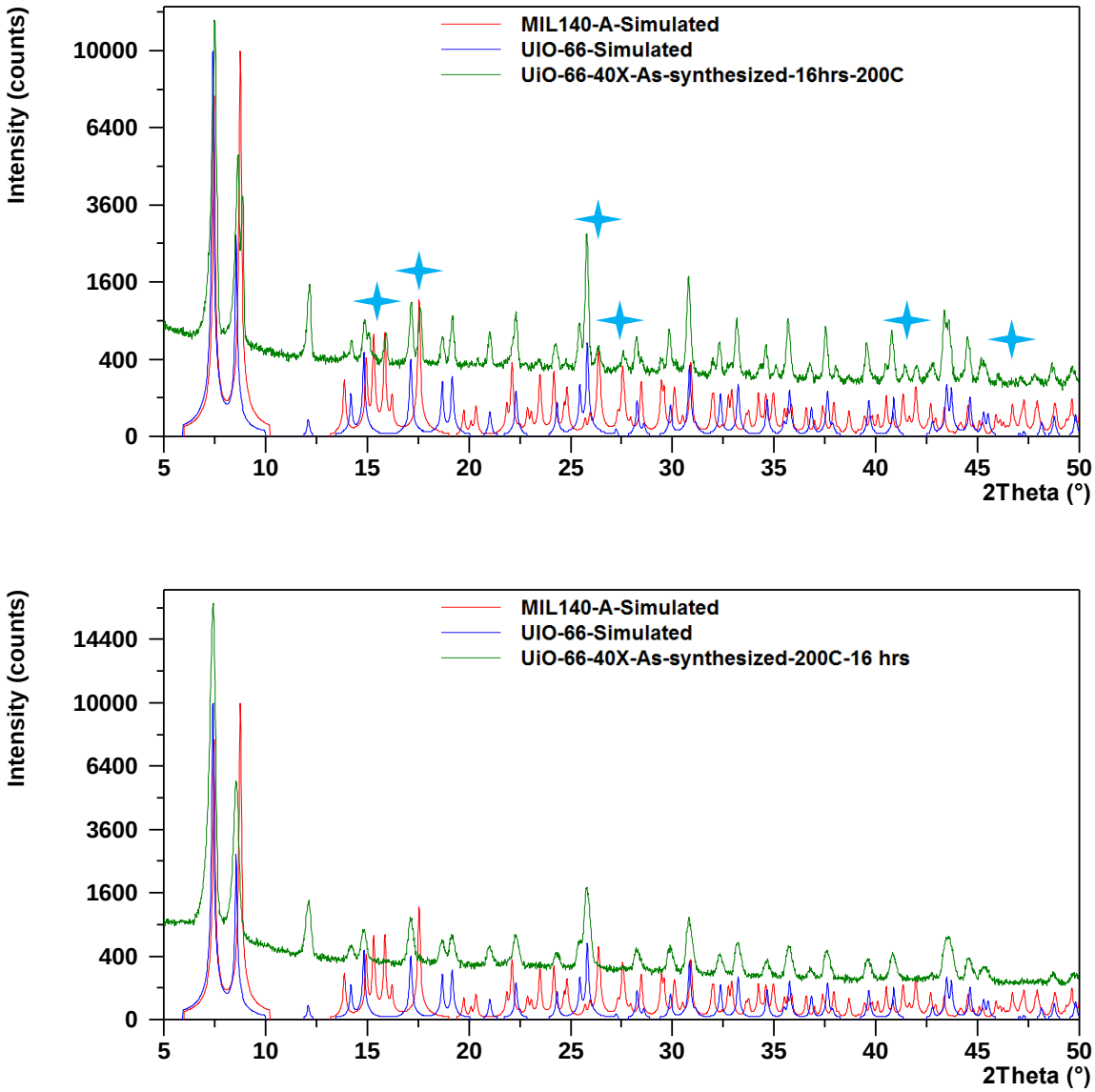

Figure 9.12 PXRD pattern of UiO-66, top: with MIL-140-A impurity (shown as ✦, with dirty Teflon liner), bottom: without MIL-140-A impurity (new clean Teflon liner), synthesized with 40X concentration of reactants in 26.5 mL reaction volume at 200 ^{o}C and 16 hr (blue- simulated pattern of UiO-66, red- simulated pattern of MIL-140-A).

Table 9.2 Data of Yield of UiO-66 with the Increasing Amounts of Reactants in 26.5 mL DMF.

Label	Concentration (M)	Yield[#] (g)	BET Surface Area (m^2/g)	Time (hr)	Space-Time Yield (STY, $kg/m^3 day^{-1}$)	Solvent Cost ($/ g UiO-66)
1X*	0.0085	0.050	1200	24	1.89	18.73
3X	0.0255	0.214	1356	24	8.07	4.38
5X	0.0425	0.395	1365	24	14.89	2.37
7X	0.0595	0.528	1228	24	19.92	1.77
9X	0.0765	0.633	1258	24	23.89	1.47
9X	0.0765	0.767	1400	48	14.48	1.22
15X	0.1275	1.190	1404	48	22.46	0.78
20X	0.1700	1.723	1474	48	32.50	0.54
25X	0.2125	2.190	1310	48	41.33	0.42
30X	0.2550	2.520	1340	48	47.55	0.37
35X	0.2975	2.877	1220	48	54.29	0.32
[ł]39X	0.3315	3.175	1216	16	179.72	0.29
[ł]40X	0.3400	3.230	1210	16	182.83	0.29
[ł]44X	0.3740	3.465	1130	16	196.13	0.27

HCl (12.4 M, equimolar to the BDC ligand) was added for concentrations greater than or equal to 15X. The synthesis with 9X concentration for 48 hr showed an increase in the yield and BET surface area compared to the 24 hr synthesis.
*Original recipe of Cavka et al.[25]
[ł]In Teflon lined bomb reactors at 200 ^{o}C for 16 hrs.
[#]Weight is of as-synthesized (unactivated) material and is averaged over 2-3 batches.

To showcase that even these high reactant concentration recipes are also scalable, the reaction volume of 39X concentration were scaled-up by 10 times and 15 times. 39X

concentration was now run in 265 mL and 400 mL DMF at 200 ^{o}C in a 2000 mL Teflon lined autoclave (Figure 9.13) for 16 hr. To ensure safe operation, MOF synthesis was performed using an oven kept under a canopy hood (Figure 9.13- right). Now, the yield again increases linearly with increase in the reaction volume (Figure 9.14, Table 9.4). PXRD patterns for 265 mL and 400 mL batches match well with the simulated XRD pattern obtained from the CIF of UiO-66 (Figure 9.15), and there is no MIL-140-A impurity. N_2 adsorption was performed on the activated (under vacuum at 200℃ for 12-18 hrs.) samples from 265 mL and 400 mL batches, which gave BET surface areas of 1186 and 975 m^2/g respectively (Table 9.4). It was observed that as reaction volume increases, surface area decreases (Figure 9.14). This might be due to more extensive washing (not focused on in this work) being required post-MOF synthesis to remove impurities (Figure 9.15) from the large quantities of UiO-66 produced. Seo et al.[8] developed extensive washing steps and showed their importance in the purification of the as-synthesized MIL-100(Fe) material obtained on large scale using a 200 L Hastalloy C-276 reactor. Hence, using this high concentration (39X) recipe 50 g of UiO-66 can be produced from just ~425 mL DMF whereas upon using Cavka et al.'s[25] recipe 26.5 L DMF would have been required considering the linear increase in the yield with the reaction volume. This is an enormous cost savings from a scale-up point of view. As shown in Table 9.2 , solvent cost for MOF production with 1X concentration is ~ 19 USD/ g UiO-66 whereas for high concentrations such as 39X it is only ~ 0.30 USD/ g UiO-66 (20 L drum of DMF from Sigma Aldrich costs ~707 USD).[30]

Table 9.3 Comparison of Properties of Zr-BDC-Based Polymorphs.

MOF	Pore Size (Å)	Pore Volume (g)	BET Surface area (m^2/g)	Remarks
[9,25]UiO-66	6	0.52	1100	3D pore, SBU is $[Zr_6O_4(OH)_4]$ surrounded by 12 BDC ligands
[32]MIL-140A	3.2	0.18	415	1D pore, SBU is complex ZrO_2 chains surrounded by 6 BDC ligands

Table 9.4 Data of UiO-66 Scale-Up Experiments at Concentration = 0.3315 M, 39X of Cavka et al.[25]

Volume of DMF (mL)	Mili-moles of reactants	BET Surface Area (m^2/g)	Weight of as-synthesized UiO-66 produced (g)
26.5	8.83	1216	3.175
265	88.3	1186	29.907
400	132.45	975	47.500

Figure 9.13 Left: Teflon lined autoclaves of different sizes (23 mL, 46 mL, 125 mL, and 2000 mL) used for synthesis at high temperatures. Right: Iso-thermal oven kept under a canopy hood in the neighboring lab of Dr. Kohl in the Bunger Henry building.

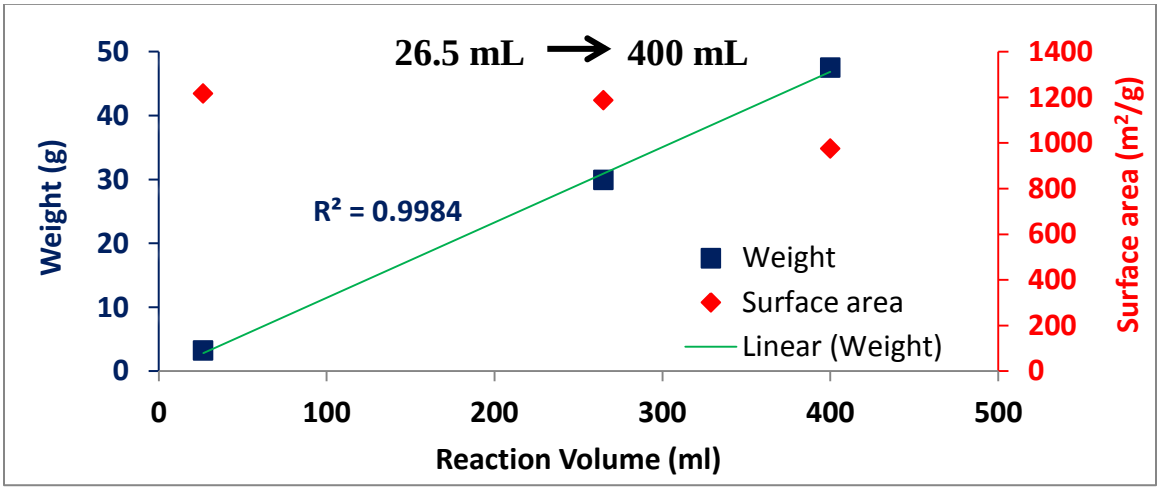

Figure 9.14 Yield and BET surface area of as-synthesized UiO-66 as a function of reaction volume at 39X concentration, 200 ^{o}C and 16 hr.

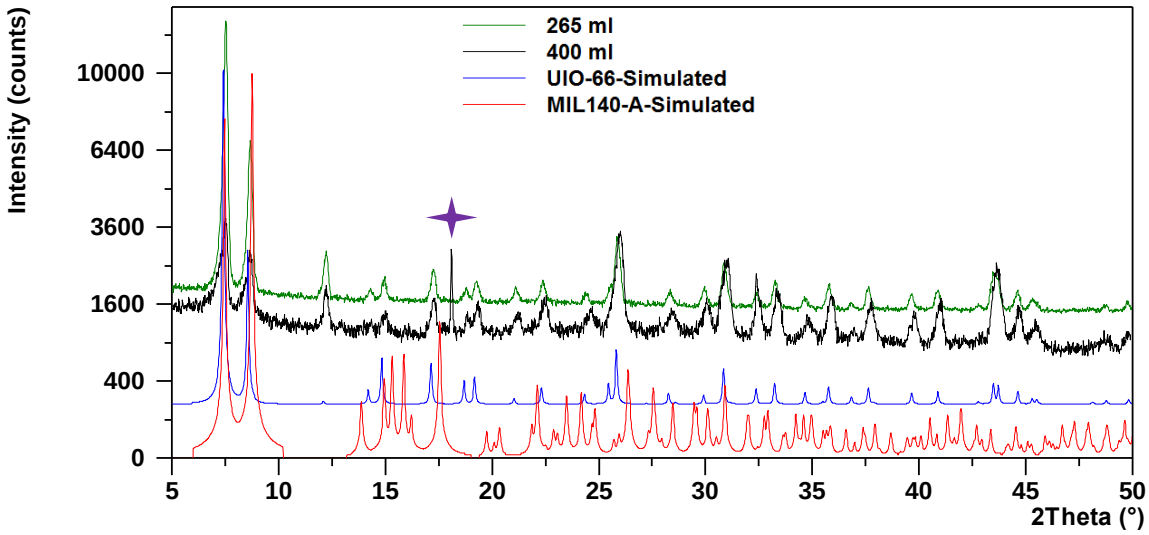

Figure 9.15 PXRD patterns of UiO-66 synthesized at 39X concentration using various reaction volumes (red- simulated pattern of MIL-140-A, blue- simulated pattern of UiO-66, black- 400 mL, green- 265 mL). ✦ show signs of impurity in the 400 mL batch, which should be removed via extensive washing.

One of the challenges faced while carrying out syntheses of UiO-66 with high reactant concentrations in the 2000 mL Teflon lined autoclave was drying the large quantities of UiO-66 produced. Drying MOFs would require more space and attention (separate dedicated fume hoods or canopy hoods) than zeolites considering their high porosities, high surface areas, and organic solvents used in their syntheses. Generally, spray dryers or rotary evaporators are used for drying purposes in the industrial scale production of solids (e.g., Basolite A520[16] was dried using a spray dyer).[35] Considering the strong interest of the Walton group in the scale-up of various MOFs, an effective solution to dry large quantities of as-synthesized MOFs quickly should be explored in the future.

9.4 Conclusions

Despite the various desirable attributes of MOFs, their commercialization has been hindered by difficulties in the scale-up of MOF synthesis methods. The solvothermal technique is the most frequently used method for MOF synthesis. However, this method suffers from the use of large amounts of solvents and hence, it cannot address prominent cost and environmental concerns. In this work, the effect of solvent reduction on the solvothermal synthesis of the highly robust UiO-66 MOF was studied. UiO-66 was synthesized with increasing reactant amounts in a fixed solvent volume of 26.5 mL, i.e., with increasing reactant concentrations, and the quality and yield of the product were studied. Quality was evaluated using PXRD and BET analysis of N_2 adsorption isotherms. It was observed that the yield of UiO-66 increases with the reactant concentrations up to 44X, which is the solubility limit of BDC in DMF at 25 ^{o}C. UiO-66 synthesis methods have been refined such that it is now possible to produce 70 times higher yield than obtained from the original synthesis report using the same solvent volume. Hence, space time yield (STY) has now increased to 196 kg/m^3day^{-1}, higher than that of most of the zeolites (STY ~ 50-150 kg/m^3day^{-1}) and BASF MOFs such as Basolite F300 (STY ~ 20 kg/m^3day^{-1}), Basolite Z1200 (STY ~ 100 kg/m^3day^{-1}), and Basolite A100 (STY ~ 160 kg/m^3day^{-1}). This would result in a significant reduction of the MOF production cost at the industrial scale. Further, by using the refined synthesis recipe the UiO-66 synthesis has been scaled-up to ~ 50 g per batch.

9.5 References

(1) Davis, M. E., Ordered porous materials for emerging applications. *Nature* **2002,** *417* (6891), 813-21.

(2) Ferey, G., Hybrid porous solids: past, present, future. *Chem Soc Rev* **2008,** *37* (1), 191-214.

(3) Garibay, S. J.; Cohen, S. M., Isoreticular synthesis and modification of frameworks with the UiO-66 topology. *Chem Commun (Camb)* **2010,** *46* (41), 7700-2.

(4) Kitagawa, S.; Kitaura, R.; Noro, S., Functional porous coordination polymers. *Angewandte Chemie* **2004,** *43* (18), 2334-75.

(5) Yilmaz, B.; Trukhan, N.; MÜLler, U., Industrial Outlook on Zeolites and Metal Organic Frameworks. *Chinese Journal of Catalysis* **2012,** *33* (1), 3-10.

(6) Min Wang, Q.; Shen, D.; Bülow, M.; Ling Lau, M.; Deng, S.; Fitch, F. R.; Lemcoff, N. O.; Semanscin, J., Metallo-organic molecular sieve for gas separation and purification. *Microporous and Mesoporous Materials* **2002,** *55* (2), 217-230.

(7) Mueller, U.; Schubert, M.; Teich, F.; Puetter, H.; Schierle-Arndt, K.; Pastre, J., Metal-organic frameworks - prospective industrial applications. *Journal of Materials Chemistry* **2006,** *16* (7), 626-636.

(8) Seo, Y.-K.; Yoon, J. W.; Lee, J. S.; Lee, U. H.; Hwang, Y. K.; Jun, C.-H.; Horcajada, P.; Serre, C.; Chang, J.-S., Large scale fluorine-free synthesis of hierarchically porous iron(III) trimesate MIL-100(Fe) with a zeolite MTN topology. *Microporous and Mesoporous Materials* **2012,** *157* (0), 137-145.

(9) Schoenecker, P. M.: High-throughput synthesis and application development of water-stable MOFs, Ph.D. Thesis, Georgia Institute of Technology, Atlanta, GA, 2012.

(10) Gimeno-Fabra, M.; Munn, A. S.; Stevens, L. A.; Drage, T. C.; Grant, D. M.; Kashtiban, R. J.; Sloan, J.; Lester, E.; Walton, R. I., Instant MOFs: continuous synthesis of metal-organic frameworks by rapid solvent mixing. *Chemical Communications* **2012,** *48* (86), 10642-10644.

(11) Arnau, C.-S.; Inhar, I.; Mary, C.-S.; Daniel, M., A spray-drying strategy for synthesis of nanoscale metal–organic frameworks and their assembly into hollow superstructures. *Nature Chemistry* **2013,** *5* (3), 203-211.

(12) Stock, N.; Biswas, S., Synthesis of Metal-Organic Frameworks (MOFs): Routes to Various MOF Topologies, Morphologies, and Composites. *Chemical Reviews* **2011,** *112* (2), 933-969.

(13) Ni, Z.; Masel, R. I. *United States Patent Application Publication* **2009**, *11/785,102*.

(14) Mueller, U.; Puetter, H.; Hesse, M.; Wessel, H. WO 2005/049892.

(15) Leung E, Müller U, Cox G. WO 2010/106121 A1. 2010.

(16) Leung E, Müller U, Cox G, Mattenheimer H, Blei S. EP Patentanmeldung 10183283.0, 2010.

(17) Majano, G.; Pérez-Ramírez, J., Scalable Room-Temperature Conversion of Copper(II) Hydroxide into HKUST-1 (Cu3(btc)2). *Advanced Materials* **2013,** *25* (7), 1052-1057.

(18) Huo, J.; Brightwell, M.; El Hankari, S.; Garai, A.; Bradshaw, D., A versatile, industrially relevant, aqueous room temperature synthesis of HKUST-1 with high space-time yield. *Journal of Materials Chemistry A* **2013,** *1* (48), 15220-15223.

(19) Gaab, M.; Trukhan, N.; Maurer, S.; Gummaraju, R.; Müller, U., The progression of Al-based metal-organic frameworks – From academic research to industrial production and applications. *Microporous and Mesoporous Materials* **2012,** *157* (0), 131-136.

(20) Lucchesi CA, Lewis WT. Latent heat of sublimation of terephthalic acid from differential thermal analysis data. *J. Chem. Eng. Data* **1968**, 13(3), 389.

(21) Czaja, A. U.; Trukhan, N.; Muller, U., Industrial applications of metal-organic frameworks. *Chemical Society Reviews* **2009,** *38* (5), 1284-1293.

(22) http://www.sigmaaldrich.com/catalog/product/aldrich/688614?lang=en&region=US, LA on 24th Feb. 2014.

(23) Cychosz K. A., Ahmad R., Matzger A. J. Liquid phase separations by crystalline microporous coordination polymers. Chem. Sci. Sep 2010;1(3):293-302.

(24) Meek, S. T.; Greathouse, J. A.; Allendorf, M. D., Metal-organic frameworks: a rapidly growing class of versatile nanoporous materials (adv. Mater. 2/2011). *Advanced materials (Deerfield Beach, Fla.)* **2011,***23* (2), 141.

(25) Cavka, J. H.; Jakobsen, S.; Olsbye, U.; Guillou, N.; Lamberti, C.; Bordiga, S.; Lillerud, K. P., A new zirconium inorganic building brick forming metal organic frameworks with exceptional stability. *Journal of the American Chemical Society* **2008,** *130* (42), 13850-13851.

(26) Qing L. D., Chu L. J., Zhuang L. D., Wang F. A. Solubilities of terephthalaldehydic, p-toluic, benzoic, terephthalic and isophthalic acids in N,N-dimethylformamide from 294.75 to 370.45 K Fluid Phase Equilib., 200, (2002) 69-74.

(27) Walton, K. S.; Snurr, R. Q. Applicability of the BET Method for Determining Surface Areas of Microporous Metal-Organic Frameworks. J. Am. Chem. Soc. 2007, 129(27), 8552−8556.

(28)https://www.fishersci.com/ecomm/servlet/cmstatic?storeId=10652&href=index.jsp&store=Scientific&segment=scientificStandard, LA on Feb. 24th 2014.

(29) Katz, M. J.; Brown, Z. J.; Colon, Y. J.; Siu, P. W.; Scheidt, K. A.; Snurr, R. Q.; Hupp, J. T.; Farha, O. K., A facile synthesis of UiO-66, UiO-67 and their derivatives. *Chemical Communications* **2013,** *49* (82), 9449-9451.

(30) http://www.sigmaaldrich.com/catalog/product/sial/319937?lang=en&region=US, LA on 24th Feb. 2014.

(31) Schaate, A.; Roy, P.; Godt, A.; Lippke, J.; Waltz, F.; Wiebcke, M.; Behrens, P., Modulated synthesis of Zr-based metal-organic frameworks: from nano to single crystals. *Chemistry* **2011,** *17* (24), 6643-51.

(32) Guillerm, V.; Ragon, F.; Dan-Hardi, M.; Devic, T.; Vishnuvarthan, M.; Campo, B.; Vimont, A.; Clet, G.; Yang, Q.; Maurin, G.; Ferey, G.; Vittadini, A.; Gross, S.; Serre, C., A series of isoreticular, highly stable, porous zirconium oxide based metal-organic frameworks. *Angewandte Chemie* **2012,** *51* (37), 9267-71.

(33) http://www.parrinst.com/products/sample-preparation/acid-digestion/, LA on 24th Feb. 2014.

(34) Ragon, F.; Horcajada, P.; Chevreau, H.; Hwang, Y. K.; Lee, U. H.; Miller, S. R.; Devic, T.; Chang, J.-S.; Serre, C., In Situ Energy-Dispersive X-ray Diffraction for the Synthesis Optimization and Scale-up of the Porous Zirconium Terephthalate UiO-66. *Inorganic Chemistry* **2014,** *53* (5), 2491-2500.

(35) Stiles A B, Koch T A. Catalyst Manufacture. 2nd Ed. New York: Marcel Dekker, Inc. 1995.

CHAPTER 10

CONCLUSIONS AND RECOMMENDATIONS

10.1 Water Stability of MOFs (Chapters 3-6)

Performance of MOFs in humid or aqueous environments is a topic of great significance for the commercialization of this class of materials for a variety of applications ranging from adsorption separations to controlled storage and release. Poor water stability of MOFs compared to zeolites and activated carbons is well known, and there is a critical need to perform systematic water stability studies and characterize MOFs comprehensively post water exposure. The effects of porosity, metal-ligand coordination, metal type, and ligand character must be decoupled to allow elucidation of the degradation mechanisms of MOFs in humid environments. The systematic approach that is necessary for such a study requires a variety of isostructural families of MOFs. Using these systematic studies we can isolate the specific factors governing structural stability of MOFs and direct the future synthesis efforts towards the construction of new water stable MOFs. Hence, in this work (Chapters 3-6), I have shown that structural factors such as shielding of the metal, pK_a (basicity) of ligand, and catenation are important contributors to MOF water stability or instability and we can synthesize novel MOFs after incorporating these structural factors into the framework.

In Chapter 3,[1] the goal has been to understand the influence of the ligand functionalization on the relative stabilities of MOFs belonging to same family of isostructural, non-catenated pillared DMOFs $[Zn(L)(DABCO)_{0.5}]$, where L is the functionalized BDC (1,4-benzenedicarboxylic acid) ligand. Incorporating a broad range

of functional groups on the BDC ligand provides different extent of shielding to metal. The resulting MOFs have varying surface areas, pore sizes, and pore volumes. Stability is assessed through water vapor adsorption isotherms combined with powder X-Ray diffraction (PXRD) experiments and surface area analyses. Our study demonstrates that integration of polar functional groups (e.g. nitro, bromo, chloro, hydroxy etc.) on the dicarboxylate linker renders these MOFs water unstable compared to the parent MOF as these polar functional groups have a negative shielding effect, i.e., they facilitate hydrolysis. On the other hand, placing non-polar groups (e.g., methyl) on the BDC ligand results in structurally robust MOFs because metal is effectively shielded from attack by water molecules. Therefore, the anthracene- and tetramethyl-BDC MOFs do not lose crystallinity or surface area after water exposure, in spite of the large amount of water adsorption due to pore-filling at ~ 20 % relative humidity (RH). This has been observed rarely in the MOF literature. The results of this work show that by ligand functionalization, it is possible to adjust the water stability of a pillared MOF both in the positive and negative directions by proper shielding and, thus, provide an important step towards understanding the water adsorption behavior of MOFs.

In Chapter 4,[2] shielding concept has been extended by synthesizing four novel isostructural DMOFs with methyl functional groups at different positions on the BDC ligand along with already reported fluorine (polar) and methyl (non-polar) functionalized DMOF analogues. This work is distinctly different from previous reports where the apparent water stability is improved through the inclusion of functional groups such as -CH_3, -C_2H_5, and -CF_3, which only serve to prevent significant amounts of water from adsorbing into the pores. In this study, we present the first demonstration of tuning of the

inherent kinetic stability of MOF structures in the presence of large amounts of adsorbed water. Notably, we demonstrate that while the parent DMOF structure is unstable, the DMOF variation containing the tetramethyl BDC ligand remains fully stable after adsorbing large amounts of water vapor during cyclic water adsorption cycles. These trends cannot be rationalized in terms of hydrophobicity alone; experimental water isotherms show that MOFs containing the same number of methyl groups per unit cell will have different kinetic stabilities and that the precise placements of the methyl groups on the BDC ligand is therefore critically important in determining their stability in the presence of water. We present the water adsorption isotherms, PXRD patterns, and BET surface areas before and after water exposure in order to illustrate these trends. Furthermore, pK_a values for the functionalized ligands are compared to investigate whether the difference in structural stability among members of this isostructural, pillared family under humid conditions is thermodynamic or kinetic in nature. Molecular simulations are also used to provide insight into the structural characteristics governing these trends in kinetic water stability.

In Chapter 5,[3] we have examined two important contributors to MOF stability or instability: basicity (pK_a value) of the pillar ligand and catenation of the framework. Catenation is the interpenetration or interweaving of two or more identical and independent frameworks. We demonstrate that, using catenation in combination with a pillaring strategy, it is possible to obtain water stable MOFs even when the pillar ligand has lower basicity (pK_a value). This study shows that after 90% RH exposure, comparing Zn-BDC-DABCO (DMOF) and Zn-BDC-BPY (MOF-508), MOF-508 is stable due to its two-fold interpenetration that prevents significant water adsorption. In contrast,

comparing non-catenated isostructural pillared MOFs Zn-TMBDC-DABCO (DMOF-TM) and Zn-TMBDC-BPY (MOF-508-TM), MOF-508-TM is unstable since BPY is less basic (lower pK_a) and less rigid than DABCO.

In Chapter 6,[4] we have extended our previous work (Chapter 3-5)[1-3] on the systematic water stability studies of MOFs and synthesized new cobalt, nickel, copper, and zinc-based water stable pillared MOFs by incorporating structural factors such as ligand sterics and catenation into the framework. As expected, our study demonstrates that unlike the parent DMOF structures (based on various metals such as Co, Ni, Cu, and Zn), which all collapse under 60% RH, their corresponding tetramethyl functionalized variations or DMOF-TM structures are remarkably stable even when adsorbing more than 20 mmol H_2O/g MOF at 80% RH. This behavior is due to shielding provided to the metal centers by the methyl groups grafted on the BDC ligand from water molecules as shown in our previous work,[1,2] for Zn-based DMOF-TM. Moreover, BTTB (4,4',4'',4''-benzene-1,2,4,5-tetrayl tetrabenzoic acid)-based pillared MOFs (based on Co and Zn metals) are also found to be stable after 90% RH exposure even when the basicity of the bipyridyl-based pillar ligand is low. This is due to the presence of catenation in their frameworks similar to MOF-508, which has been reported to be stable too after 90% RH exposure.[3]

In summary, the impact of water adsorption and its subsequent effect on the thermodynamic stability of MOF structures can be defined by the acid-base effects of metal centers and ligands respectively. Similarly, hydrophobicity and steric factors (around both metal and ligand) can also be important in defining the kinetic stability of MOFs as they can increase the activation energy barrier for the hydrolysis reaction.[5]

Hence, in the near future, novel water stable MOFs based on lanthanides metal series should be synthesized and tested for their stability under humid environments. Here, our hypothesis is based on the structural factors such as high metal coordination number, which prevents water clustering near the metal centers.[6] Water stability of various MOFs such as UiO-66,[7,8] MIL-125,140,[8,9] DUT-51,67-69,[10,11] PCN-56-59,222,224,225,[12-15] MOF-525,545,[16] and LaBTB[17] can be correlated with the high metal coordination number. Techniques such as plasma-enhanced chemical vapor deposition,[18] carbon-coating,[19] ligand functionalization,[20-23] core-shell models,[24] and post-synthetic cation exchange,[25] which have been used to enhance the stability of MOF-5 (IRMOF-1), Cu-BTC (HKUST-1), and BiO-MOF-11 should be applied to other unstable MOF systems too. Moreover, long-term stability (aging) studies in controlled humidity chambers should also be explored in the future as these studies can be extremely useful to simulate the conditions faced by adsorbents in industrial applications.

In the literature, there are mainly reports of using *ex situ* techniques to characterize MOFs post water exposure. Hence, in the future, we need more *in situ* characterization studies under controlled humidity environments to help us understand the breakdown mechanisms of MOFs. For example, *in situ* PXRD is a easy technique to implement from the sample preparation and analysis point of view and will point us to the exact point (% RH) where long range-order of MOF structure starts changing. Similarly, *in situ* solid-state NMR[26,27] can be extremely valuable since it probes short-range ordering and local structure around the target nucleus and hence, it can provide information complementary to XRD. Another important but relatively unexplored topic is the effect of structural defects on the MOF water stability. Therefore, this should also be

explored in the future using techniques such as positronium annihilation lifetime spectroscopy (PALS),[28] atomic force microscopy (AFM),[29,30] and confocal fluorescence microscopy.[31] Electron microscopy techniques such as transmission electron microscopy (TEM), scanning electron microscopy (SEM) can also provide instrumental information about structural defects and surface selective information due to the high-resolving power of electrons. However, one has to be careful while using electron microscopy techniques as many porous materials including MOFs can be electrical insulators, which creates the problem of sample charging and can also be electron beam sensitive.[30]

10.2 Ammonia Adsorption in MOFs (Chapter 7)

UiO-66 is the first MOF based on the Zr-based secondary building unit (SBU) and is being highly investigated for a wide variety of small molecule gas separations since it possess unprecedented thermal, chemical, and mechanical stability.[32] In this Chapter,[33] we have mainly investigated the performance of various functionalized variations of UiO-66 (UiO-66-OH, UiO-66-$(OH)_2$, UiO-66-NO_2, UiO-66-NH_2, UiO-66-SO_3H, and UiO-66-$(COOH)_2$) towards ammonia removal from air. Ammonia breakthrough measurements showed that a hydroxyl functionalized Zr-based UiO-66 material or UiO-66-OH is promising as it could offer a method for targeting the removal of specific chemical threats in a chemically stable framework that does not degrade in the presence of water. However, this material falls short of the ammonia removal goal of 0.1 g /g MOF (or ~ 6 mmol/g) loading under humid conditions.

The hydrophobic mono- and di-methyl functionalized analogues of UiO-66 (UiO-66-MM and UiO-66-DM) have shown higher affinity for polar CO_2 gas molecule than UiO-66 in the low pressure region under dry conditions (refer to Chapter 8 for

details).[34,35] Hence, we believe that the effect of water adsorption can be reduced by using a physical mixture of UiO-66-OH (hydrophilic) and methyl-functionalized hydrophobic variations (UiO-66-MM and UiO-66-DM) of UiO-66. However, in the future, before evaluating the performance of the aforementioned physical mixture for ammonia capture, ammonia breakthrough capacity for UiO-66-MM and UiO-66-DM should also be measured and compared with UiO-66. Other important strategies for attaining high ammonia loadings that should be explored in the future are: (1) functionalization of other water stable MOFs (e.g., MIL-100, MIL-101)[36,37,38] with larger pore space as it seems that there is not adequate pore space within the UiO-66 framework for complex functionalization to be effective, (2) post-synthetic modification of hydroxyl or carboxylic functional groups grafted in the pores of MOFs to generate metal alkoxides since Snurr and coworkers[39] have shown extremely high binding energies of ammonia with metal alkoxides.

10.3 Rational Tuning of Water Vapor and CO_2 (Chapter 8)

In Chapter 8,[34,35] we have reported the synthesis of novel, highly robust, monomethyl- and dimethyl-functionalized Zr-based MOFs (UiO-66-MM and UiO-66-DM) by pre-synthesis functionalization of the BDC ligand. Both MOFs have a topology similar to that of UiO-66 and are characterized using a series of techniques including PXRD, FTIR, N_2 adsorption, NMR, and TGA. By modulating the number of methyl groups on the BDC ligand we have rationally tuned both the water vapor and low pressure CO_2/CH_4 uptakes in this isostructural family of Zr-based MOFs. As expected, water vapor loadings follow the order: UiO-66-DM < UiO-66-MM < UiO-66. However, under dry conditions and low coverage both UiO-66-DM and UiO-66 have a low

CO_2/CH_4 selectivity while UiO-66-MM has a much higher CO_2/CH_4 selectivity. Taking both hydrophilicity and selectivity factors into account, we believe that both UiO-66-MM and UiO-66-DM will exhibit superior performance over the parent MOF in humid gas separations. Hence, in the future, $CO_2/CH_4/H_2O$, $CO_2/N_2/H_2O$, and $NH_3/Air/H_2O$ breakthrough measurements at various relative humidities should be performed to evaluate the performance of these methyl functionalized UiO-66 frameworks compared to the parent structure under humid environments. Moreover, molecular simulations similar to Burtch et al.[40] should also be performed to provide insight into the structural characteristics governing aforementioned trends of CO_2/CH_4 selectivity.

10.4 MOF Scale-Up (Chapter 9)

In Chapter 9,[41] we have studied the effect of solvent reduction on the solvothermal synthesis of the UiO-66 MOF as elimination of the large usage of organic solvents required in most solvothermal syntheses can reduce the raw material costs, filtration costs, waste disposal costs, and environmental concerns. I have mentored an undergraduate researcher on this topic. Together, we have refined UiO-66 synthesis methods such that we are now able to produce more than 70 times the yield obtained from the original synthesis report of Cavka et al.[42] using the same reactor volume. Hence, space time yield (STY) has now increased to 196 kg/m^3day^{-1}, higher than that of most of the zeolites (STY ~ 50-150 kg/m^3day^{-1}) and BASF MOFs such as Basolite F300 (STY ~ 20 kg/m^3day^{-1}), Basolite Z1200 (STY ~ 100 kg/m^3day^{-1}), and Basolite A100 (STY ~ 160 kg/m^3day^{-1}).[43] Further, by using the refined synthesis recipe, the UiO-66 synthesis has been scaled-up to ~ 50g per batch from the typical MOF syntheses at the mg scale per

batch. Now, 50g of UiO-66 can be synthesized with just 425 mL (vs. 26.5 L) DMF. This is an enormous cost savings from a scale-up point of view.

In the future, attention should be paid towards solvent recycling and developing extensive washing steps to remove impurities from the large quantities of MOF produced via scaled-up batches. Similarly, drying large quantities of MOFs would require commercial dryers and separate dedicated fume hoods or canopy hoods (safety requirements) considering their high porosities and hazardous organic solvents used in their syntheses. Moreover, before scaling-up the synthesis of other MOFs, it would be prudent to refine their synthesis recipes (reactant concentration, modulator concentration, synthesis time, and synthesis temperature) at the small scale. This should be ideally done using an automatic high throughput machine (e.g., Symyx Core Module robot)[44] since it would save lot of man-hours. After the successful scale-up of MOF syntheses, another important aspect for the future is to explore the formation of engineered MOF particles (granules, extrudates, or monoliths) via pressurization or use of binders and evaluate the performance of MOFs in engineered forms.[45]

10.5 References

(1) Jasuja, H.; Huang, Y. G.; Walton, K. S., Adjusting the stability of metal-organic frameworks under humid conditions by ligand functionalization. *Langmuir* **2012,** *28* (49), 16874-80.

(2) Jasuja, H.; Burtch, N. C.; Huang, Y. G.; Cai, Y.; Walton, K. S., Kinetic water stability of an isostructural family of zinc-based pillared metal-organic frameworks. *Langmuir* **2013,** *29* (2), 633-42.

(3) Jasuja, H.; Walton, K. S., Effect of catenation and basicity of pillared ligands on the water stability of MOFs. *Dalton Trans* **2013,** *42* (43), 15421-6.

(4) Jasuja, H.; Jiao, Y.; Burtch, N. C.; Huang, Y.; Walton, K. S., Synthesis of Novel Cobalt, Nickel, Copper, and Zinc-based Water Stable Pillared Metal-Organic Frameworks, *Langmuir* 2014, (In Preparation).

(5) Burtch N. C.; Jasuja, H.; Walton, K. S., Water Stability and Adsorption in Metal-Organic Frameworks, *Chem. Rev.* 2014, (In Preparation).

(6) Low, J. J.; Benin, A. I.; Jakubczak, P.; Abrahamian, J. F.; Faheem, S. A.; Willis, R. R., Virtual high throughput screening confirmed experimentally: porous coordination polymer hydration. J Am Chem Soc **2009**, *131 (43)*, 15834-42.

(7) DeCoste, J. B.; Peterson, G. W.; Schindler, B. J.; Killops, K. L.; Browe, M. A.; Mahle, J. J., The effect of water adsorption on the structure of the carboxylate containing metal-organic frameworks Cu-BTC, Mg-MOF-74, and UiO-66. *Journal of Materials Chemistry A* **2013,** *1* (38), 11922-11932.

(8) Jeremias, F.; Lozan, V.; Henninger, S. K.; Janiak, C., Programming MOFs for water sorption: amino-functionalized MIL-125 and UiO-66 for heat transformation and heat storage applications. *Dalton Transactions* **2013,** *42* (45), 15967-15973.

(9) Guillerm, V.; Ragon, F.; Dan-Hardi, M.; Devic, T.; Vishnuvarthan, M.; Campo, B.; Vimont, A.; Clet, G.; Yang, Q.; Maurin, G.; Ferey, G.; Vittadini, A.; Gross, S.; Serre, C., A Series of Isoreticular, Highly Stable, Porous Zirconium Oxide Based Metal-Organic Frameworks. *Angew. Chem.-Int. Edit.* **2012,** *51* (37).

(10) Bon, V.; Senkovska, I.; Baburin, I. A.; Kaskel, S., Zr- and Hf-Based Metal-Organic Frameworks: Tracking Down the Polymorphism. *Crystal Growth & Design* **2013,** *13* (3), 1231-1237.

(11) Bon, V.; Senkovskyy, V.; Senkovska, I.; Kaskel, S., Zr(iv) and Hf(iv) based metal-organic frameworks with reo-topology. *Chemical Communications* **2012,** *48* (67), 8407-8409.

(12) Jiang, H.-L.; Feng, D.; Liu, T.-F.; Li, J.-R.; Zhou, H.-C., Pore Surface Engineering with Controlled Loadings of Functional Groups via Click Chemistry in Highly Stable Metal–Organic Frameworks. *Journal of the American Chemical Society* **2012,** *134* (36), 14690-14693.

(13) Feng, D.; Gu, Z.-Y.; Li, J.-R.; Jiang, H.-L.; Wei, Z.; Zhou, H.-C., Zirconium-Metalloporphyrin PCN-222: Mesoporous Metal–Organic Frameworks with

Ultrahigh Stability as Biomimetic Catalysts. *Angewandte Chemie International Edition* **2012,** *51* (41), 10307-10310.

(14) Jiang, H.-L.; Feng, D.; Wang, K.; Gu, Z.-Y.; Wei, Z.; Chen, Y.-P.; Zhou, H.-C., An Exceptionally Stable, Porphyrinic Zr Metal–Organic Framework Exhibiting pH-Dependent Fluorescence. *Journal of the American Chemical Society* **2013,** *135* (37), 13934-13938.

(15) Feng, D.; Chung, W.-C.; Wei, Z.; Gu, Z.-Y.; Jiang, H.-L.; Chen, Y.-P.; Darensbourg, D. J.; Zhou, H.-C., Construction of Ultrastable Porphyrin Zr Metal–Organic Frameworks through Linker Elimination. *Journal of the American Chemical Society* **2013,** *135* (45), 17105-17110.

(16) Morris, W.; Volosskiy, B.; Demir, S.; Gandara, F.; McGrier, P. L.; Furukawa, H.; Cascio, D.; Stoddart, J. F.; Yaghi, O. M., Synthesis, Structure, and Metalation of Two New Highly Porous Zirconium Metal-Organic Frameworks. *Inorganic Chemistry* **2012,** *51* (12), 6443-6445.

(17) Duan, J.; Higuchi, M.; Horike, S.; Foo, M. L.; Rao, K. P.; Inubushi, Y.; Fukushima, T.; Kitagawa, S., High CO_2/CH_4 and C2 Hydrocarbons/CH_4 Selectivity in a Chemically Robust Porous Coordination Polymer. *Advanced Functional Materials* **2013,** *23* (28), 3525-3530.

(18) Decoste, J. B.; Peterson, G. W.; Smith, M. W.; Stone, C. A.; Willis, C. R., Enhanced Stability of Cu-BTC MOF via Perfluorohexane Plasma-Enhanced Chemical Vapor Deposition. *Journal of the American Chemical Society* **2012,** *134* (3), 1486-1489.

(19) Yang, S. J.; Park, C. R., Preparation of Highly Moisture-Resistant Black-Colored Metal Organic Frameworks. *Advanced Materials* **2012,** *24* (29), 4010-4013.

(20) Yang, J.; Grzech, A.; Mulder, F. M.; Dingemans, T. J., Methyl modified MOF-5: a water stable hydrogen storage material. *Chem Commun* **2011,** *47* (18), 5244-6.

(21) Wu, T.; Shen, L.; Luebbers, M.; Hu, C.; Chen, Q.; Ni, Z.; Masel, R. I., Enhancing the stability of metal-organic frameworks in humid air by incorporating water repellent functional groups. *Chem Commun* **2010,** *46* (33), 6120-2.

(22) Nguyen, J. G.; Cohen, S. M., Moisture-resistant and superhydrophobic metal-organic frameworks obtained via postsynthetic modification. *J Am Chem Soc* **2010,** *132* (13), 4560-1.

(23) Cai, Y.; Zhang, Y. D.; Huang, Y. G.; Marder, S. R.; Walton, K. S., Impact of Alkyl-Functionalized BTC on Properties of Copper-Based Metal-Organic Frameworks. *Crystal Growth & Design* **2012,** *12* (7), 3709-3713.

(24) Li, T.; Sullivan, J. E.; Rosi, N. L., Design and Preparation of a Core–Shell Metal–Organic Framework for Selective CO_2 Capture. *Journal of the American Chemical Society* **2013,** *135* (27), 9984-9987.

(25) Li, H.; Shi, W.; Zhao, K.; Li, H.; Bing, Y.; Cheng, P., Enhanced Hydrostability in Ni-Doped MOF-5. *Inorganic Chemistry* **2012,** *51* (17), 9200-9207.

(26) Sutrisno, A.; Huang, Y., Solid-state NMR: A powerful tool for characterization of metal–organic frameworks. *Solid State Nuclear Magnetic Resonance* **2013,** *49–50* (0), 1-11.

(27) Hoffmann, H.; Debowski, M.; Müller, P.; Paasch, S.; Senkovska, I.; Kaskel, S.; Brunner, E., Solid-State NMR Spectroscopy of Metal–Organic Framework Compounds (MOFs). *Materials* **2012,** *5* (12), 2537-2572.

(28) Liu, M.; Wong-Foy, A. G.; Vallery, R. S.; Frieze, W. E.; Schnobrich, J. K.; Gidley, D. W.; Matzger, A. J., Evolution of Nanoscale Pore Structure in Coordination Polymers During Thermal and Chemical Exposure Revealed by Positron Annihilation. *Adv. Mater.* **2010,** *22* (14), 1598-1601.

(29) Sindoro, M.; Jee, A.-Y.; Granick, S., Shape-selected colloidal MOF crystals for aqueous use. *Chemical Communications* **2013,** *49* (83), 9576-9578.

(30) Liu, Z.; Fujita, N.; Miyasaka, K.; Han, L.; Stevens, S. M.; Suga, M.; Asahina, S.; Slater, B.; Xiao, C.; Sakamoto, Y.; Anderson, M. W.; Ryoo, R.; Terasaki, O., A review of fine structures of nanoporous materials as evidenced by microscopic methods. *Microscopy* **2013,** *62* (1), 109-146.

(31) Ameloot, R.; Vermoortele, F.; Hofkens, J.; De Schryver, F. C.; De Vos, D. E.; Roeffaers, M. B. J., Three-Dimensional Visualization of Defects Formed during the Synthesis of Metal–Organic Frameworks: A Fluorescence Microscopy Study. *Angewandte Chemie International Edition* **2013,** *52* (1), 401-405.

(32) (a) Cmarik, G. E.; Kim, M.; Cohen, S. M.; Walton, K.S. Tuning the Adsorption Properties of UiO-66 via Ligand Functionalization. *Langmuir* **2012,** *28*, 15606-15613. (b) Schoenecker, P. M.; Carson, C. G.; Jasuja, H.; Flemming, C. J. J.;

Walton, K. S. Effect of Water Adsorption on Retention of Structure and Surface Area of Metal–Organic Frameworks. *Ind. Eng. Chem. Res.* **2012**, *51*, 6513-6519.

(33) Jasuja, H.; Peterson G. W.; Decoste, J. B.; Browe, M. A.; Walton, K. S., Evaluation of MOFs for Air Purification and Air Quality Control Applications: Ammonia Removal from Air, *Microporous Mesoporous Mater.* 2014, (In Preparation).

(34) Jasuja, H.; Zang, J.; Sholl, D. S.; Walton, K. S., Rational Tuning of Water Vapor and CO_2 Adsorption in Highly Stable Zr-Based MOFs. *J. Phys. Chem. C* **2012,** *116* (44), 23526-23532.

(35) Jasuja, H.; Walton, K. S., Experimental Study of CO_2, CH4, and Water Vapor Adsorption on a Dimethyl-Functionalized UiO-66 Framework. *J. Phys. Chem. C* **2013,** *117* (14), 7062-7068.

(36) Jeremias, F.; Khutia, A.; Henninger, S. K.; Janiak, C., MIL-100(Al, Fe) as water adsorbents for heat transformation purposes-a promising application. *J. Mater. Chem.* **2012,** *22* (20), 10148-10151.

(37) Hartmann, M.; Fischer, M., Amino-functionalized basic catalysts with MIL-101 structure. *Microporous and Mesoporous Mater.* **2012,** *164* (0), 38-43.

(38) Soubeyrand-Lenoir, E.; Vagner, C.; Yoon, J. W.; Bazin, P.; Ragon, F.; Hwang, Y. K.; Serre, C.; Chang, J. S.; Llewellyn, P. L., How water fosters a remarkable 5-fold increase in low-pressure CO_2 uptake within mesoporous MIL-100(Fe). *J Am Chem Soc* **2012,** *134* (24), 10174-81.

(39) Kim, K. C.; Yu, D.; Snurr, R. Q., Computational Screening of Functional Groups for Ammonia Capture in Metal–Organic Frameworks. *Langmuir* **2013,** *29* (5), 1446-1456.

(40) Burtch, N. C.; Jasuja, H.; Dubbeldam, D.; Walton, K. S., Molecular-level insight into unusual low pressure CO_2 affinity in pillared metal-organic frameworks. *J Am Chem Soc* **2013,** *135* (19), 7172-80.

(41) Jasuja, H.; Fletcher, D.; Walton, K. S., Metal-Organic Framework Scale-Up: Effect of Solvent Reduction on the Synthesis of the Highly Robust Zr-BDC (UiO-66) MOF, *AIChE J.* 2014, (In Preparation).

(42) Cavka, J. H.; Jakobsen, S.; Olsbye, U.; Guillou, N.; Lamberti, C.; Bordiga, S.; Lillerud, K. P., A new zirconium inorganic building brick forming metal organic frameworks with exceptional stability. *J Am Chem Soc* **2008,** *130* (42), 13850-1.

(43) Czaja, A. U.; Trukhan, N.; Muller, U., Industrial applications of metal-organic frameworks. *Chemical Society Reviews* **2009,** *38* (5), 1284-1293.

(44) Chandler, W.; Carlson, E.; Busacca, B.; Rust, W.; Hajduk, D.; Han, H.; Brown, J., The Extended Core Module Robot: A Flexible, Modular Platform for High-Throughput Development Workflows. *Journal of the Association for Laboratory Automation* **2005,** *10* (6), 418-422.

(45) DeCoste, J. B.; Peterson, G. W., Metal–Organic Frameworks for Air Purification of Toxic Chemicals. *Chemical Reviews* **2014 (DOI: 10.1021/cr4006473)**.

APPENDIX A

ADJUSTING THE STABILITY OF METAL–ORGANIC FRAMEWORKS UNDER HUMID CONDITIONS BY LIGAND FUNCTIONALIZATION

A.1 Synthesis Procedure for MOFs

Preparation of Zn-1,4-NDC-DABCO

Synthesis of Zn-1,4-NDC-DABCO was done as per the literature procedure,[1] i.e., by mixing $Zn(NO_3)_2.6H_2O$ (0.6 mmol), NDC (0.6 mmol) and DABCO (0.3 mmol) in DMF (9 mL) at room temperature in a glass beaker and the resulting slurry was stirred for 3 hrs. After filtering the white precipitate, the resulting solution was poured into a glass vial, which was placed in a sand bath and finally sand bath was kept in a preheated oven at 120 ^oC for 48 hrs. After the solution was cooled to room temperature in air, the resulting solid was filtered and repeatedly washed with DMF. The resulting brick-shaped colorless crystals obtained after drying were transferred to a vial. Activated samples for gas adsorption measurements were prepared by heating the as-synthesized compound at 110 ^oC overnight in the degasser.

Preparation of Zn-ADC-DABCO

Zn-ADC-DABCO was synthesized according to literature procedure,[2] i.e., $Zn(NO_3)_2.6H_2O$ (1 mmol), ADC (1 mmol), were dissolved in DMF (5 mL) at room temperature in a glass beaker. After DABCO (0.5 mmol) and MeOH (5 mL) were added to the mixture, resulting slurry was stirred for 12-18 hrs. After filtering the white

precipitate, the filtrate was poured into a Teflon autoclave, which was kept in a preheated oven at 120 ^{o}C for 48 hrs. After the solution was left to cool to room temperature in air, the resulting solid was filtered and repeatedly washed with DMF. The yellowish brick-shaped crystals obtained after drying were transferred to a vial. Crystals of Zn-ADC-DABCO were activated by heating the as-synthesized compound at 110 ^{o}C overnight in the degasser.

Preparation of Zn-BDC-TMBDC-DABCO

Synthesis of Zn-BDC-TMBDC-DABCO was performed following literature procedure,[1] i.e., $Zn(NO_3)_2.6H_2O$ (0.6 mmol), BDC (0.3 mmol), TMBDC (0.3 mmol) and DABCO (0.3 mmol) were mixed in DMF (9 mL) at room temperature in a glass beaker and resulting slurry was stirred for 3 hrs. The white precipitate was filtered and the resulting solution was poured into a glass vial, which was placed in a sand bath and finally sand bath was kept in a preheated oven at 120 ^{o}C for 48 hrs. Solution was cooled to room temperature in air followed by filtering the resulting solid, which was repeatedly washed with DMF. The resulting colorless brick-shaped crystals obtained after drying was transferred to a vial. Activated samples for gas adsorption measurements were prepared by heating the as-synthesized compound at 110 ^{o}C overnight in the degasser.

Preparation of Zn-TMBDC-DABCO

Zn-TMBDC-DABCO was prepared in a similar manner as described by Chun et. al.[1] Therefore, $Zn(NO_3)_2.6H_2O$ (0.63 mmol), TMBDC (0.63 mmol) and DABCO (0.31 mmol) were mixed in 15 mL of DMF in a glass beaker at room temperature and then the mixture was homogenized by stirring for 2-3 hrs. The resulting solution was transferred to Teflon-lined stainless steel bomb reactor, kept in a preheated oven at 120 ^{o}C for 48 hrs.

In the end, solution was allowed to cool to room temperature in air and then the resulting white colored solid was filtered and repeatedly washed with DMF. Crystals of Zn-TMBDC-DABCO were activated by heating the as-synthesized compound at 110 ^{o}C overnight in the degasser.

Preparation of Zn-BDC-NO_2-DABCO

The yellow crystals of Zn-BDC-NO_2-DABCO were synthesized in a similar fashion as reported by Uemura et. al.,[3] i.e., by mixing $Zn(NO_3)_2.6H_2O$ (2 mmol), BDC-NO_2 (2 mmol) and DABCO (1 mmol) in DMF (30 mL) at room temperature and resulting slurry was stirred for 5-10 minutes . The solution was transferred into a Teflon autoclave and then it was kept in a preheated oven at 120 ^{o}C for 48 hrs. After the reaction, the product was filtered and repeatedly washed with DMF. Activated samples for gas adsorption measurements were prepared by heating the as-synthesized compound at 110 ^{o}C overnight in the degasser.

Preparation of Zn-BDC-Br-DABCO

Synthesis of Zn-BDC-Br-DABCO was performed following literature procedure,[4] i.e., $Zn(NO_3)_2.6H_2O$ (2 mmol), BDC-Br (2 mmol) and DABCO (1 mmol) were mixed in 30 mL of DMF at room temperature in a glass beaker and resulting slurry was stirred for 5-10 minutes. Subsequently, solution was poured into a Teflon autoclave, which was kept in a preheated oven at 120 ^{o}C for 48 hrs. Solution was cooled to room temperature in air and then the resulting solid was filtered and repeatedly washed with DMF. The resulting brick-shaped colorless crystals obtained after drying, were transferred to a vial. Crystals of Zn-BDC-Br-DABCO were activated by heating the as-synthesized compound at 110 ^{o}C overnight in the degasser.

Preparation of Zn-BDC-Cl_2-DABCO

The crystals of Zn-BDC-Cl_2-DABCO were synthesized in a similar fashion as reported by Uemura et. al.,[4] i.e., by mixing $Zn(NO_3)_2.6H_2O$ (2 mmol), BDC-Cl_2 (2 mmol) and DABCO (1 mmol) in 30 mL of DMF in a glass beaker at room temperature and subsequently, homogenized by stirring for 5-10 minutes. The resulting solution was transferred to Teflon-lined stainless still bomb reactor, kept in a preheated oven at 120 ^oC for 48 hrs. In the end, solution was allowed to cool to room temperature in air and then the resulting white colored solid was filtered and repeatedly washed with DMF. Activated samples for gas adsorption measurements were prepared by heating the as-synthesized compound at 110 ^oC overnight in the degasser.

Preparation of Zn-BDC-OH-DABCO

The colorless crystals of Zn-BDC-OH-DABCO were synthesized according to literature procedure,[5] i.e., by mixing $Zn(NO_3)_2.6H_2O$ (1 mmol), BDC-OH (1 mmol) and DABCO (0.5 mmol) in 10 mL DMF at room temperature and resulting slurry was stirred for 5-10 minutes . The solution was transferred into a Teflon autoclave and then it was kept in a preheated oven at 110 ^oC for 24 hrs. After the reaction, the product was filtered and repeatedly washed with DMF. Crystals of Zn-BDC-OH-DABCO were activated by heating the as-synthesized compound at 110 ^oC overnight in the degasser.

A.2 PXRD (Powder X-Ray Diffraction)

Powder X-ray diffraction patterns (PXRD) were collected using an X'Pert X-ray PANalytical diffractometer with an X'celerator module using Cu Kα (λ = 1.5418 Å) radiation at room temperature, with a step size of 0.02˚ in two theta (2θ). From these

patterns, the phase purity of as-synthesized samples can be confirmed by comparison with the simulated patterns from single crystal X-ray diffraction (Figures A.1-A.8).

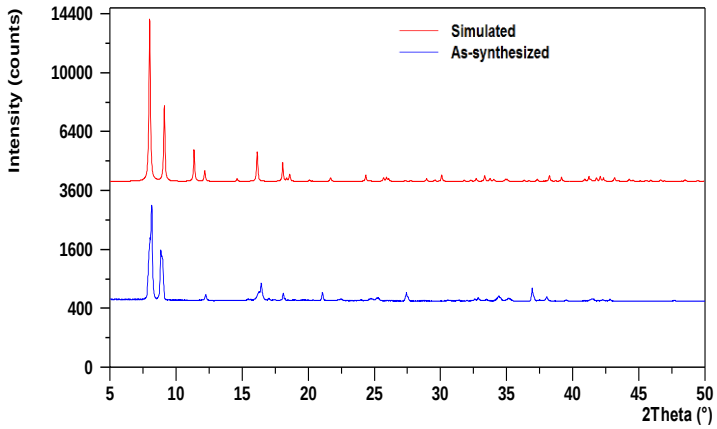

Figure A.1 Comparison of PXRD pattern for as-synthesized Zn-1,4-NDC-DABCO or DMOF-N and its theoretical pattern from single crystal data.

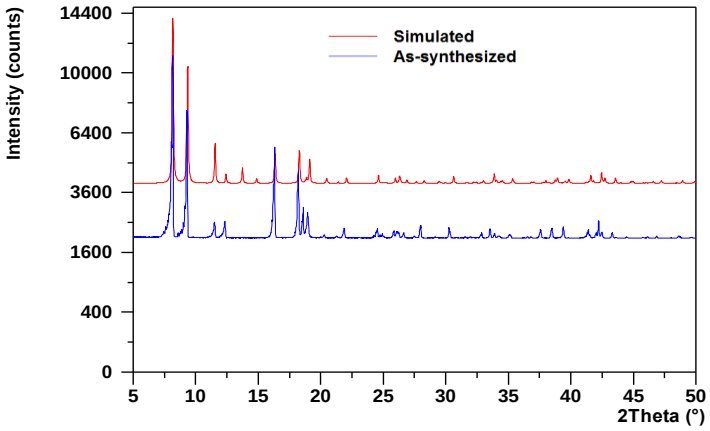

Figure A.2 Comparison of PXRD pattern for as-synthesized Zn-ADC-DABCO or DMOF-A and its theoretical pattern from single crystal data.

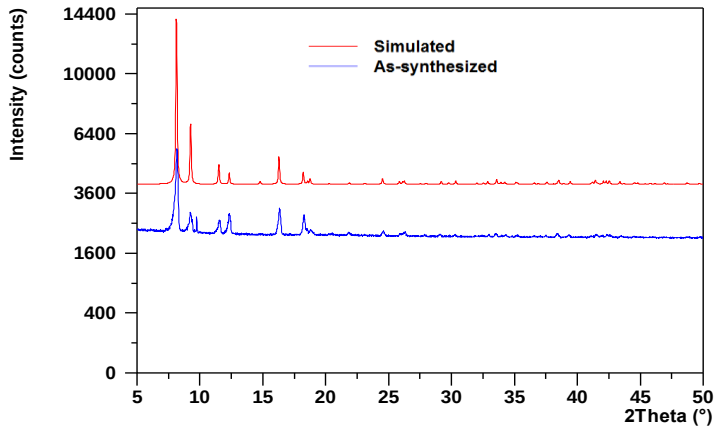

Figure A.3 Comparison of PXRD pattern for as-synthesized Zn-BDC-TMBDC-DABCO or DMOF-TM1 and its theoretical pattern from single crystal data.

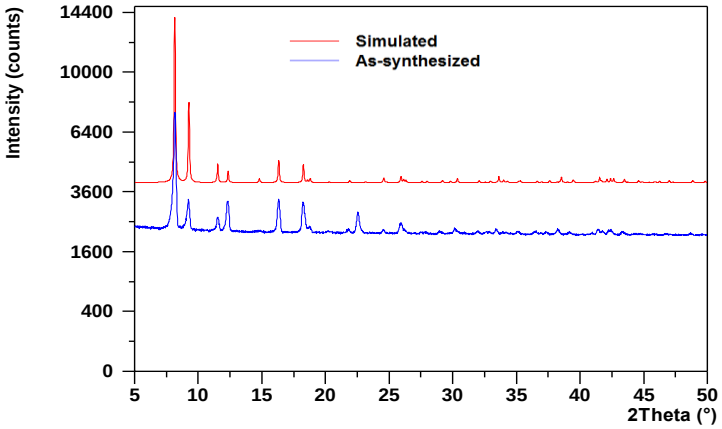

Figure A.4 Comparison of PXRD pattern for as-synthesized Zn-TMBDC-DABCO or DMOF-TM2 and its theoretical pattern from single crystal data.

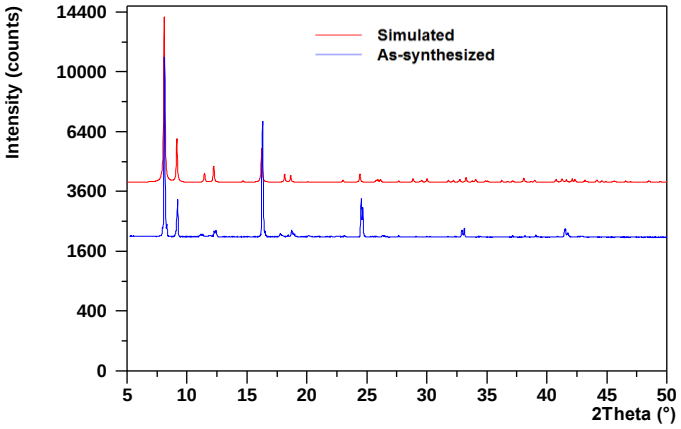

Figure A.5 Comparison of PXRD pattern for as-synthesized Zn-BDC-NO_2-DABCO or DMOF-NO_2 and its theoretical pattern from single crystal data.

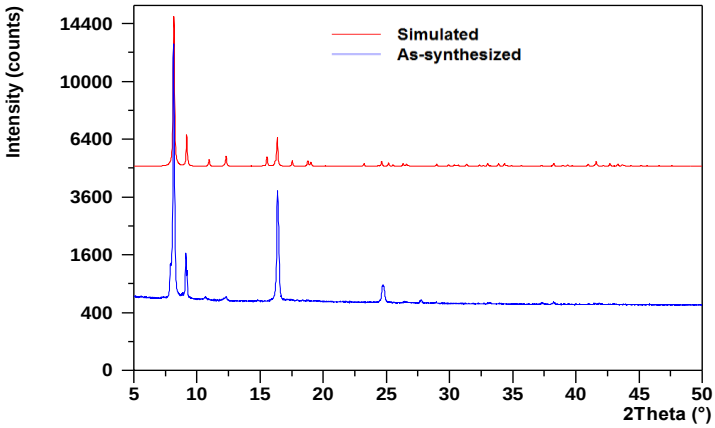

Figure A.6 Comparison of PXRD pattern for as-synthesized Zn-BDC-Br-DABCO or DMOF- Br and its theoretical pattern from single crystal data.

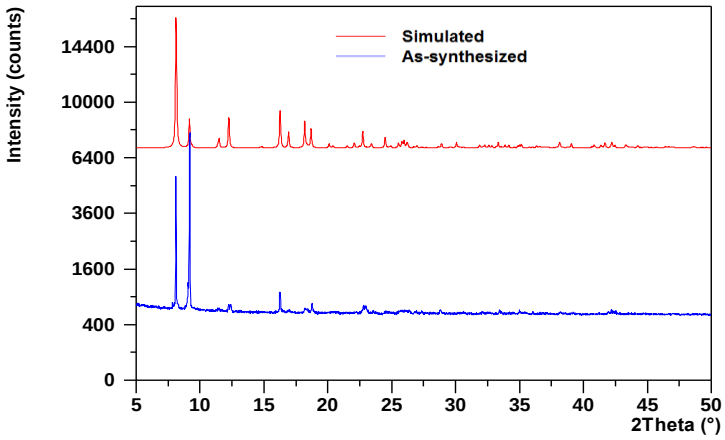

Figure A.7 Comparison of PXRD pattern for as-synthesized Zn-BDC-Cl_2-DABCO or DMOF- Cl_2 and its theoretical pattern from single crystal data.

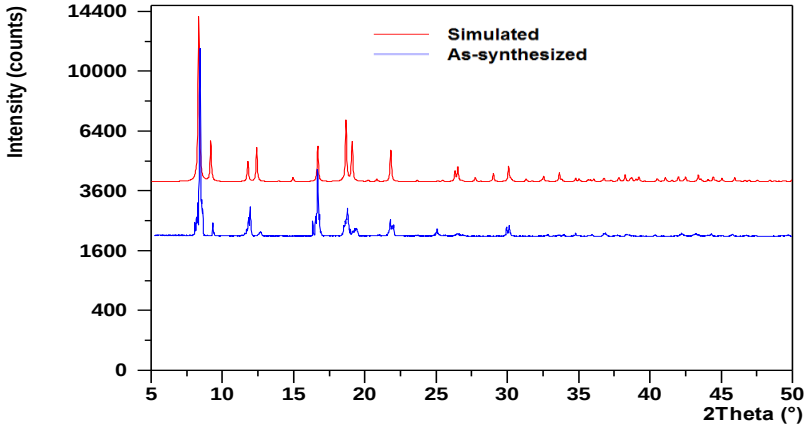

Figure A.8 Comparison of PXRD pattern for as-synthesized Zn-BDC-OH-DABCO or DMOF- OH and its theoretical pattern from single crystal data.

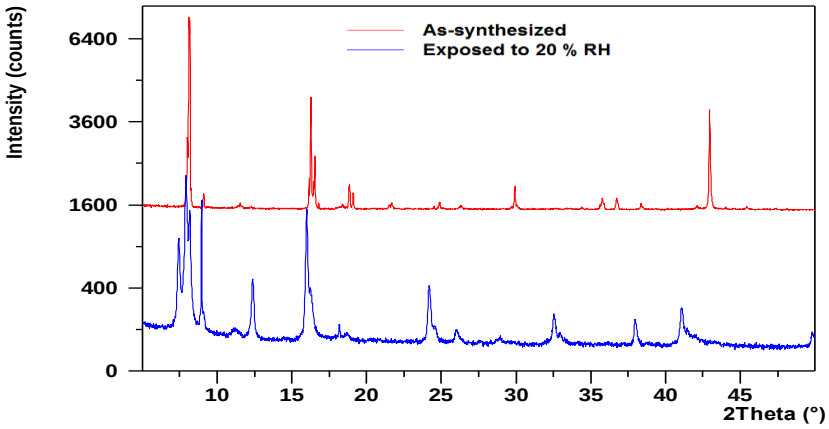

Figure A.9 PXRD patterns for as-synthesized, and water exposed (only up to 20% RH) Zn-BDC-OH-DABCO or DMOF-OH.

A.3 Surface Area Analysis

Specific surface areas were determined by applying the BET model to nitrogen adsorption isotherms (Figures A.10-A.17) measured at 77 K for each activated MOF using a Quadrasorb system from Quantachrome Instruments.

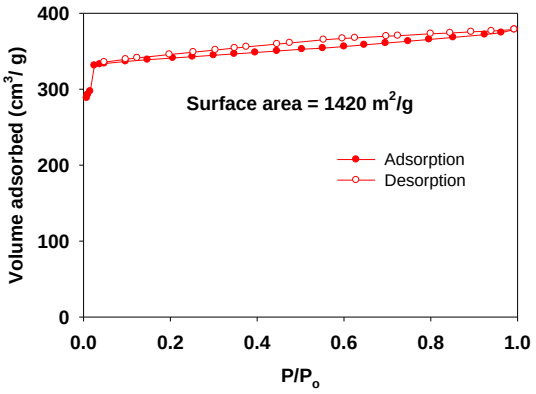

Figure A.10 Nitrogen isotherm of activated Zn-1,4-NDC-DABCO or DMOF- N at 77 K (closed symbols – adsorption, open symbols – desorption).

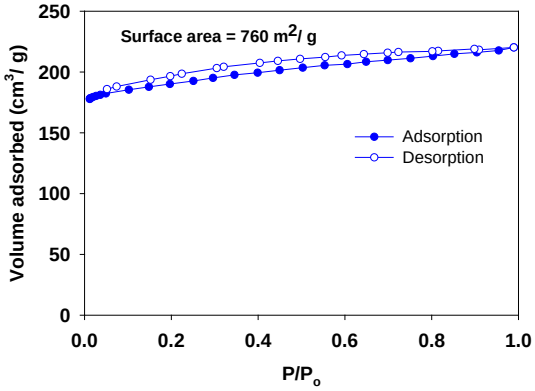

Figure A.11 Nitrogen isotherm of activated Zn-ADC-DABCO or DMOF- A at 77 K (closed symbols – adsorption, open symbols – desorption).

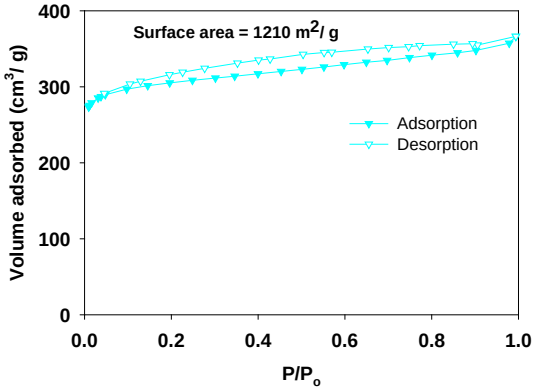

Figure A.12 Nitrogen isotherm of activated Zn-BDC-TMBDC-DABCO or DMOF- TM1 at 77 K (closed symbols – adsorption, open symbols – desorption).

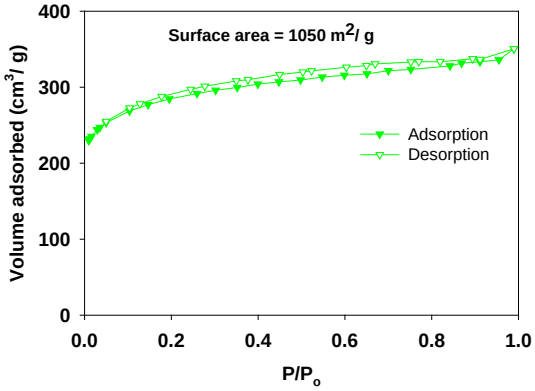

Figure A.13 Nitrogen isotherm of activated Zn-TMBDC-DABCO or DMOF- TM2 at 77 K (closed symbols – adsorption, open symbols – desorption).

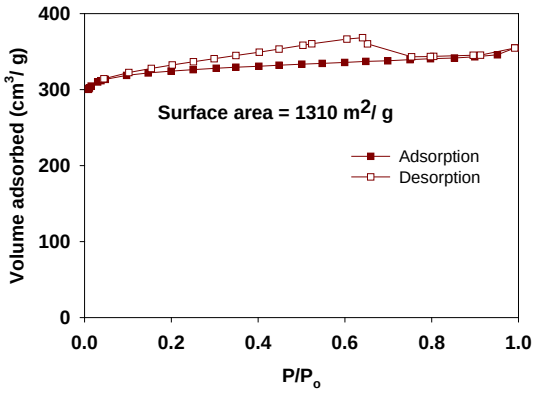

Figure A.14 Nitrogen isotherm of activated Zn-BDC-NO_2-DABCO or DMOF- NO_2 at 77 K (closed symbols – adsorption, open symbols – desorption).

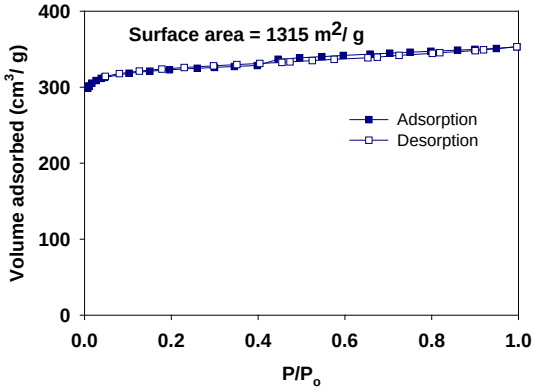

Figure A.15 Nitrogen isotherm of activated Zn-BDC-Br-DABCO or DMOF- Br at 77 K (closed symbols – adsorption, open symbols – desorption).

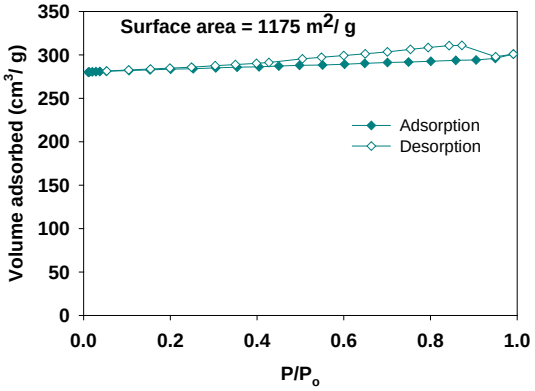

Figure A.16 Nitrogen isotherm of activated Zn-BDC-Cl_2-DABCO or DMOF- Cl_2 at 77 K (closed symbols – adsorption, open symbols – desorption).

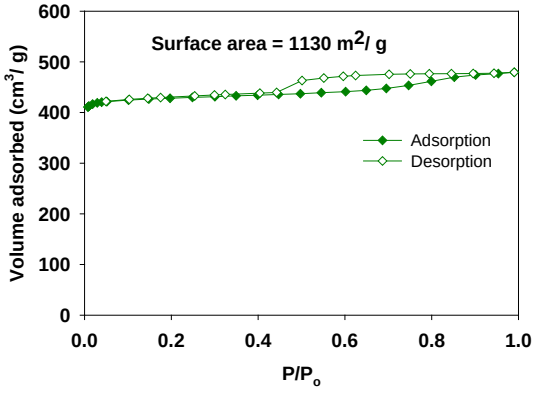

Figure A.17 Nitrogen isotherm of activated Zn-BDC-OH-DABCO or DMOF- OH at 77 K (closed symbols – adsorption, open symbols – desorption).

A.4 Water Vapor Adsorption Isotherm Measurements

A few of the MOFs, DMOF-TM2, DMOF-N, and DMOF-Cl2 were evaluated for repeatability as these provide examples of stable, partially stable, and unstable MOFs, respectively. Measurements on samples from the same batch of material exhibit good repeatability (Figure A.18). Samples from different batches lead to slight variations in the total adsorption loadings at saturation (Figure A.19). However, the water isotherm shape and location at which pore-filling occurs remains consistent between samples. The stability or instability of the MOF does not appear to impact the repeatability of the results.

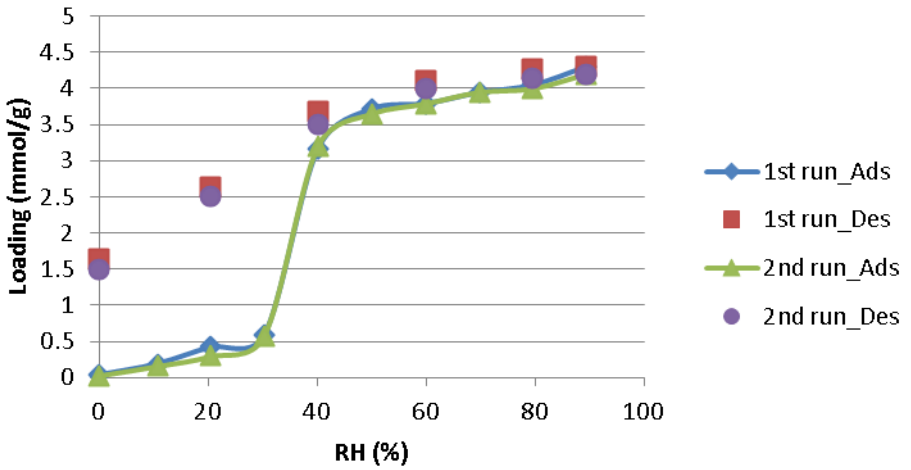

Figure A.18 Water vapor adsorption isotherms at 25C for DMOF-Cl2 measured on two samples from the same batch.

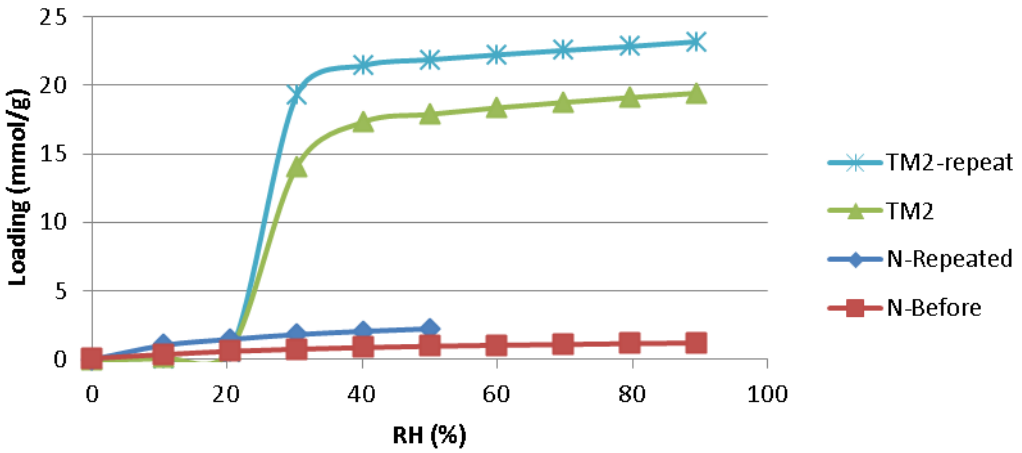

Figure A.19 Water vapor adsorption isotherms at 25C for DMOF-TM2 and DMOF-N measured on two samples from different batches.

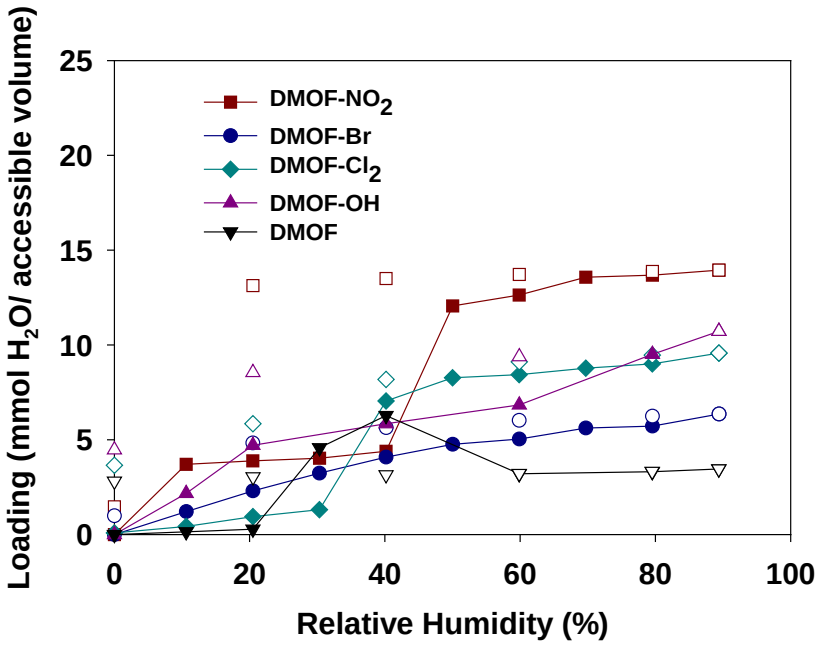

Figure A.20 Water adsorption isotherms plotted on a pore volume basis (cm^3) for DMOF with polar functional groups.

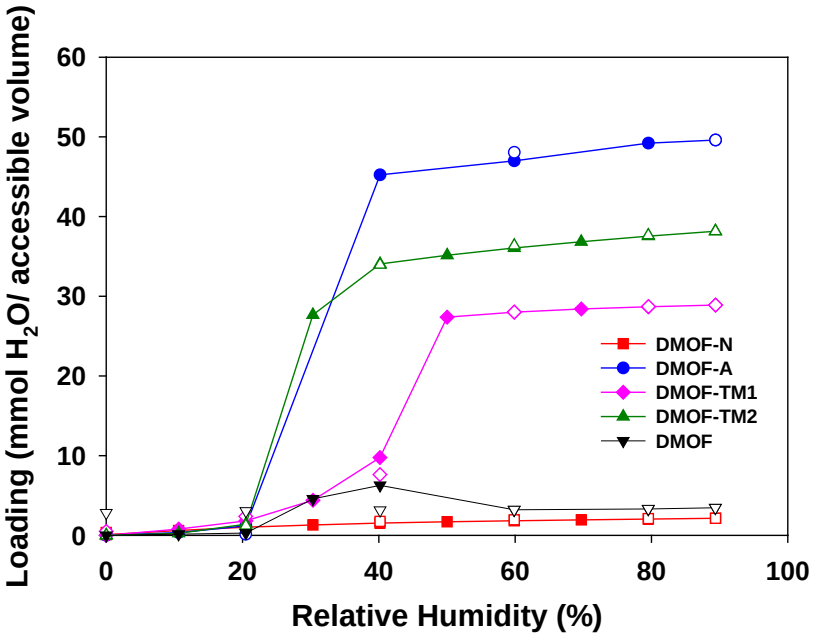

Figure A.21 Water adsorption isotherms plotted on a pore volume basis (cm^3) for DMOF with non-polar functional groups.

A.5 References

(1) Chun, H.; Dybtsev, D. N.; Kim, H.; Kim, K., Synthesis, X-ray crystal structures, and gas sorption properties of pillared square grid nets based on paddle-wheel motifs: implications for hydrogen storage in porous materials. *Chem. –Eur. J.* **2005,** *11* (12), 3521-9.

(2) Tanaka, D.; Horike, S.; Kitagawa, S.; Ohba, M.; Hasegawa, M.; Ozawa, Y.; Toriumi, K., Anthracene array-type porous coordination polymer with host-guest charge transfer interactions in excited states. *Chem. Commun.* **2007,** (30), 3142-4.

(3) Uemura, K.; Onishi, F.; Yamasaki, Y.; Kita, H., Syntheses, crystal structures, and water adsorption behaviors of jungle-gym-type porous coordination polymers containing nitro moieties. *J. Solid State Chem.* **2009,** *182* (10), 2852-2857.

(4) Uemura, K.; Yamasaki, Y.; Onishi, F.; Kita, H.; Ebihara, M., Two-step adsorption on jungle-gym-type porous coordination polymers: dependence on hydrogen-bonding capability of adsorbates, ligand-substituent effect, and temperature. *Inorg. Chem.* **2010,** *49* (21), 10133-43.

(5) Chen, Z.; Xiang, S.; Arman, H. D.; Li, P.; Zhao, D.; Chen, B., Significantly Enhanced CO_2/CH_4 Separation Selectivity within a 3D Prototype Metal-Organic Framework Functionalized with OH Groups on Pore Surfaces at Room Temperature. *Eur. J. Inorg. Chem.* **2011,** (14), 2227-2231.

APPENDIX B

KINETIC WATER STABILITY OF AN ISOSTRUCTURAL FAMILY OF ZINC-BASED PILLARED METAL–ORGANIC FRAMEWORKS

B.1 Synthesis Procedure for MOFs

Preparation of Zn-BDC-MMBDC-DABCO (DMOF-MM1)

Synthesis of Zn-BDC-MMBDC-DABCO was done after slightly modifying the reported procedure[1] for DMOF-TM1, i.e., by mixing $Zn(NO_3)_2.6H_2O$ (180 mg), BDC (48 mg), MMBDC (54.06 mg) and DABCO (36 mg) in DMF (9 mL) at room temperature in a glass beaker and the resulting slurry was stirred for 3 hrs. After filtering the white precipitate, the resulting solution was poured into a Teflon-lined stainless steel bomb reactor, which was placed in a preheated oven at 120 ^oC for 48 hrs. After the solution was cooled to room temperature in air, the resulting solid was filtered and repeatedly washed with DMF. The resulting colorless crystals obtained after drying were transferred to a vial. Activated (guest free) samples for adsorption measurements were prepared by heating the as-synthesized compound at 110^oC overnight in the degasser.

Preparation of Zn-MMBDC-DABCO (DMOF-MM2)

To synthesize Zn-MMBDC-DABCO, we replaced TMBDC ligand by MMBDC in the recipe reported by Chun et al.,[1] i.e., $Zn(NO_3)_2.6H_2O$ (189 mg), MMBDC (113.53 mg) and DABCO (35 mg) were mixed in 15 mL of DMF in a glass beaker at room temperature and then the mixture was homogenized by stirring for 2-3 hrs. After filtering the white precipitate, the filtrate was poured into a Teflon autoclave, which was kept in a

preheated oven at 120 ^{o}C for 48 hrs. Solution was cooled to room temperature in air and then the resulting solid was filtered and repeatedly washed with DMF. Crystals of Zn-MMBDC-DABCO were activated by heating the as-synthesized compound at 110℃ overnight in the degasser.

Preparation of Zn-BDC-DMBDC-DABCO (DMOF-DM1)

Synthesis of Zn-BDC-DMBDC-DABCO was performed in the exact same fashion as of DMOF-MM1, i.e., $Zn(NO_3)_2.6H_2O$ (180 mg), BDC (48 mg), DMBDC (58.25 mg) and DABCO (36 mg) were mixed in DMF (9 mL) at room temperature in a glass beaker and resulting slurry was stirred for 3 hrs. The white precipitate was filtered and the resulting solution was poured into a glass vial, which was placed in a sand bath and finally sand bath was kept in a preheated oven at 120 ^{o}C for 48 hrs. Solution was cooled to room temperature in air followed by filtering the resulting solid, which was repeatedly washed with DMF. The resulting colorless brick-shaped crystals obtained after drying was transferred to a vial. Activated samples for adsorption measurements were prepared by heating the as-synthesized compound at 110^{o} overnight in the degasser.

Preparation of Zn-DMBDC-DABCO (DMOF-DM2)

The crystals of Zn-DMBDC-DABCO were synthesized in a similar fashion as reported by Chun et al.,[1] i.e., by mixing $Zn(NO_3)_2.6H_2O$ (189 mg), DMBDC (122.33 mg) and DABCO (35 mg) were mixed in 15 mL of DMF in a glass beaker at room temperature and then the mixture was homogenized by stirring for 2-3 hrs. The resulting solution was transferred to Teflon-lined stainless steel bomb reactor, kept in a preheated oven at 120 ^{o}C for 48 hrs. In the end, solution was allowed to cool to room temperature in air and then the resulting white colored solid was filtered and repeatedly washed with

DMF. Crystals of Zn-TMBDC-DABCO were activated by heating the as-synthesized compound at 110℃ overnight in the degasser.

Preparation of Zn-BDC-TMBDC-DABCO (DMOF-TM1)

Synthesis of Zn-BDC-TMBDC-DABCO was performed after slightly modifying the reported procedure,[1] i.e., $Zn(NO_3)_2.6H_2O$ (180 mg), BDC (48 mg), TMBDC (66 mg) and DABCO (36 mg) were mixed in 9 mL DMF at room temperature and resulting slurry was stirred for 3 hrs. The white precipitate was filtered and the resulting solution was poured into a glass vial, which was placed in a sand bath and finally sand bath was kept in a preheated oven at 120 ^oC for 48 hrs. Solution was cooled to room temperature in air followed by filtering the resulting solid, which was repeatedly washed with DMF. The resulting colorless brick-shaped crystals obtained after drying was transferred to a vial. Activated samples for adsorption measurements were prepared by heating the as-synthesized compound at 110^o overnight in the degasser.

Preparation of Zn-TMBDC-DABCO (DMOF-TM2)

Zn-TMBDC-DABCO was prepared in a similar fashion as reported by Dybstev et al.,[1] i.e., $Zn(NO_3)_2.6H_2O$ (189 mg), TMBDC (140 mg) and DABCO (35 mg) were mixed in 15 mL of DMF at room temperature and then the mixture was homogenized by stirring for 2-3 hrs. The resulting solution was transferred to Teflon-lined stainless steel bomb reactor, kept in a preheated oven at 120 ^oC for 48 hrs. Finally, solution was allowed to cool to room temperature in air and then the resulting white colored solid was filtered and repeatedly washed with DMF. Samples of Zn-TMBDC-DABCO were activated by heating the as-synthesized material at 110℃ overnight in the degasser.

Preparation of Zn-TFBDC-DABCO (DMOF-TF)

Zn-TFBDC-DABCO was prepared in a similar manner as described by Chun et al.,[1] i.e., $Zn(NO_3)_2.6H_2O$ (119 mg) and TFBDC (96 mg) were dissolved in 5 mL methanol. After that DABCO (22 mg) and DMF (1.2 mL) were added to the metal-carboxylate ligand mixture and the resulting solution was stirred for 1 h at room temperature. The white precipitate was filtered and the resulting solution was transferred to Teflon-lined stainless steel bomb reactor, kept in a preheated oven at 95 ^{o}C for 7 hrs. The final product was washed with DMF and methanol. Activated samples for adsorption measurements were prepared by heating the as-synthesized compound at 95 ^{o}C overnight in the degasser. Synthesis of this MOF is sensitive, i.e., on using glass vials instead of Teflon lined bomb reactor, we were unsuccessful in synthesizing it.

B.2 PXRD (Powder X-Ray Diffraction)

Powder X-ray diffraction patterns (PXRD) were collected using an X'Pert X-ray PANalytical diffractometer with an X'celerator module using Cu Kα (λ = 1.5418 Å) radiation at room temperature, with a step size of 0.02˚ in two theta (2θ). From these patterns, the phase purity of as-synthesized samples can be confirmed by comparison with the simulated patterns from single crystal X-ray diffraction (Figures B.1-B.7).

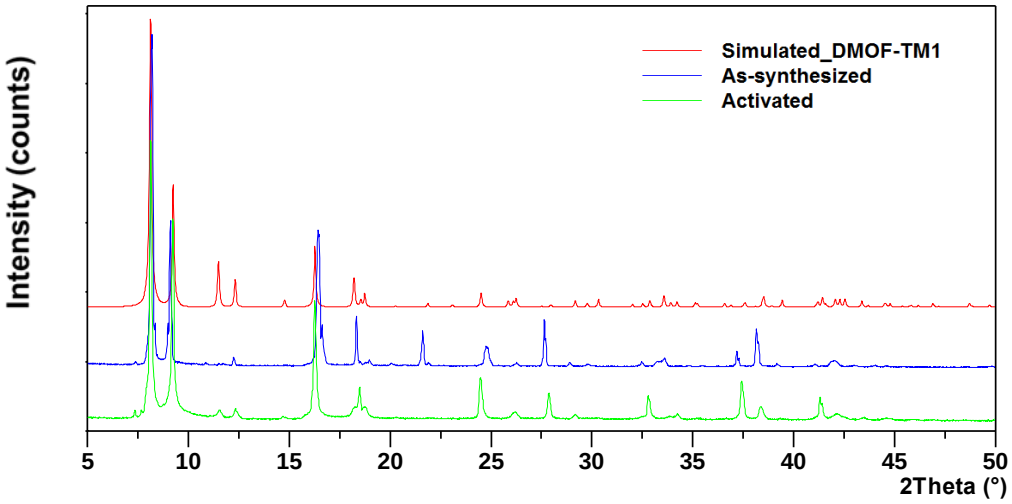

Figure B.1 Comparison of PXRD patterns for as-synthesized, activated DMOF-MM1 and theoretical pattern of DMOF-TM1 from single crystal data.

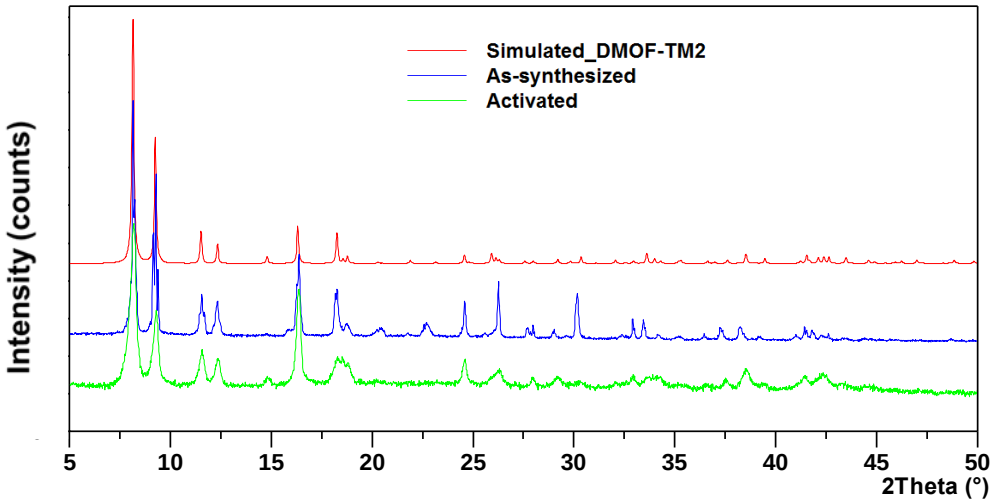

Figure B.2 Comparison of PXRD patterns for as-synthesized, activated DMOF-MM2 and theoretical pattern of DMOF-TM2 from single crystal data.

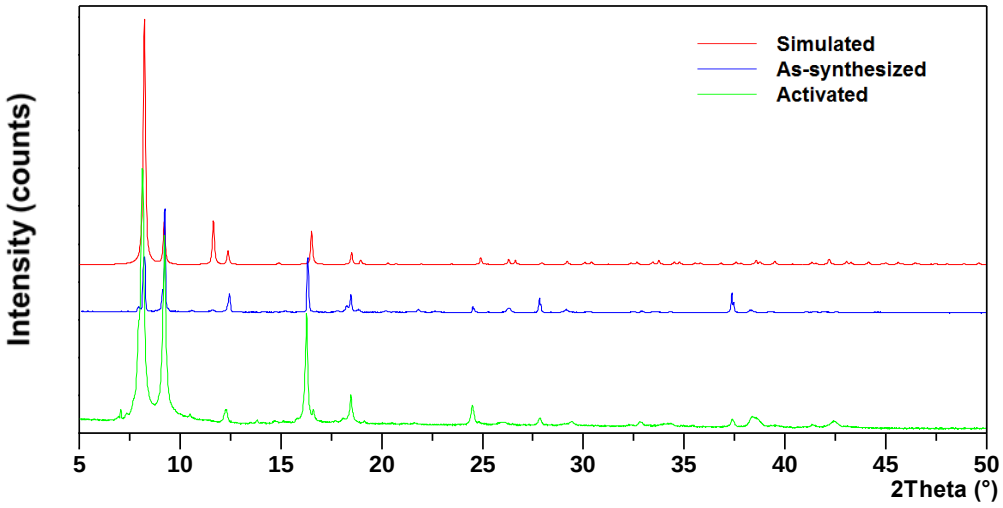

Figure B.3 Comparison of PXRD patterns for as-synthesized, activated DMOF-DM1 and its theoretical pattern from single crystal data.

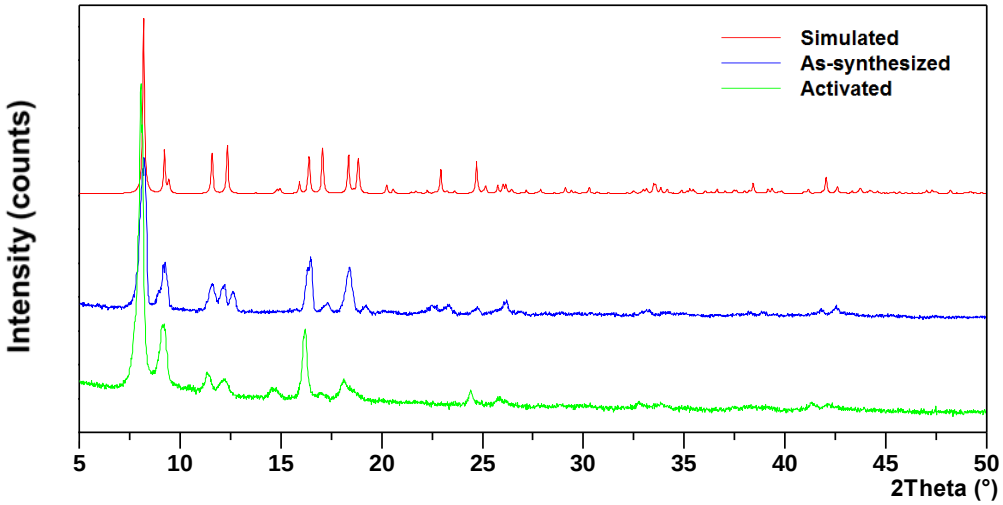

Figure B.4 Comparison of PXRD patterns for as-synthesized, activated DMOF-DM2 and its theoretical pattern from single crystal data.

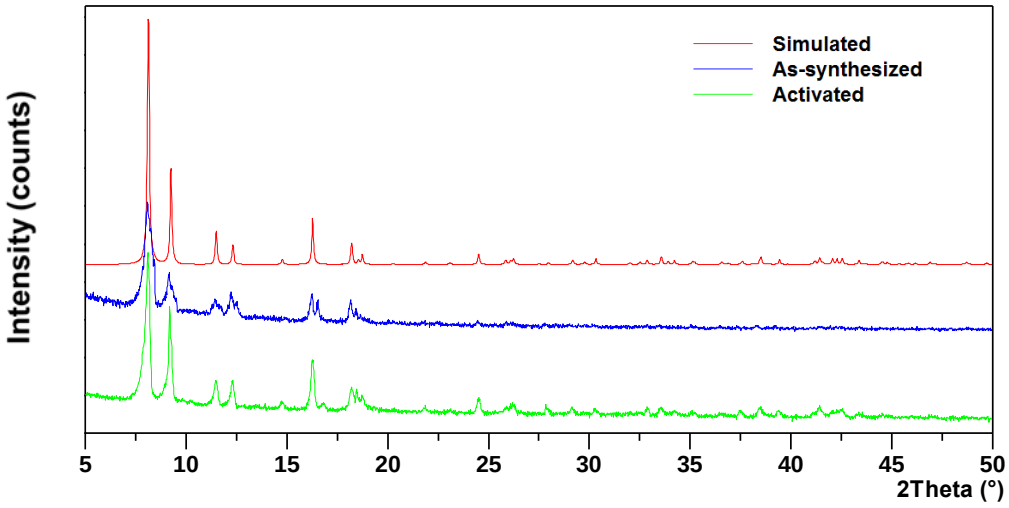

Figure B.5 Comparison of PXRD patterns for as-synthesized, activated DMOF-TM1 and its theoretical pattern from single crystal data.

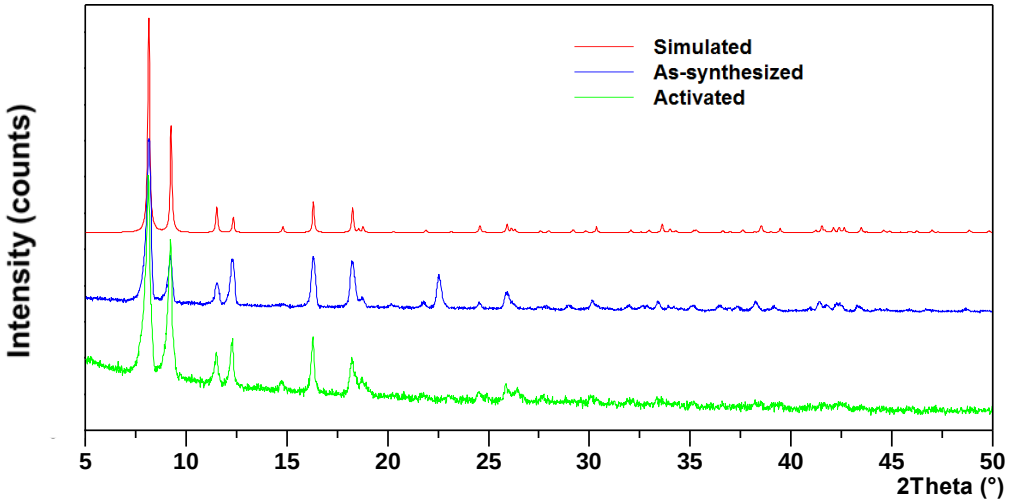

Figure B.6 Comparison of PXRD patterns for as-synthesized, activated DMOF-TM2 and its theoretical pattern from single crystal data.

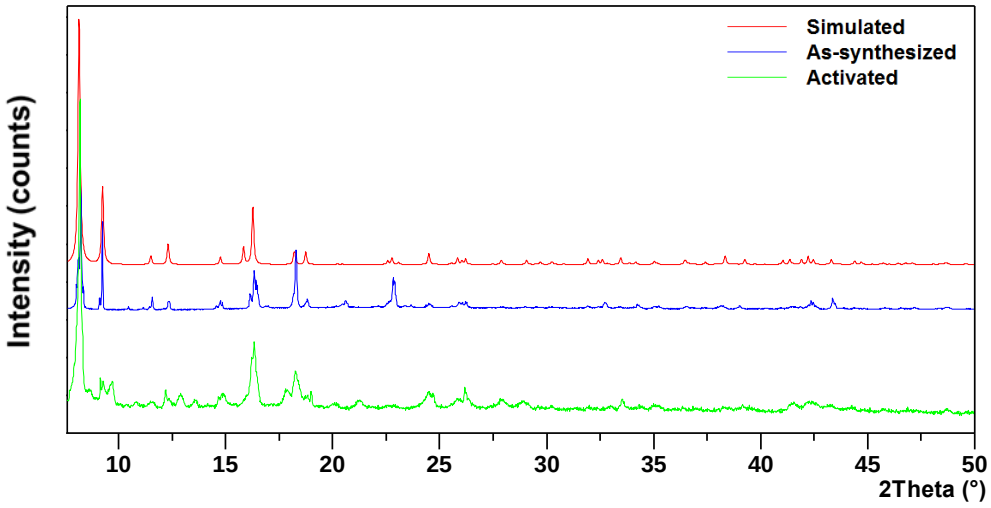

Figure B.7 Comparison of PXRD patterns for as-synthesized, activated DMOF-TF and its theoretical pattern from single crystal data.

B.3 BET Analysis of N_2 adsorption isotherms

Specific surface areas were determined by applying the BET model to nitrogen adsorption isotherms (Figures B.8-B.14) measured at 77 K for each activated MOF using a Quadrasorb system from Quantachrome Instruments.

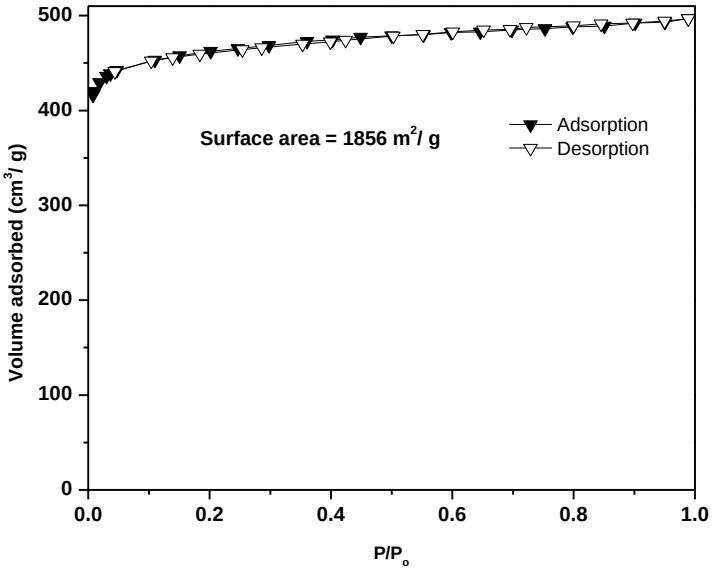

Figure B.8 Nitrogen isotherm of activated DMOF-MM1 at 77 K (closed symbols – adsorption, open symbols – desorption).

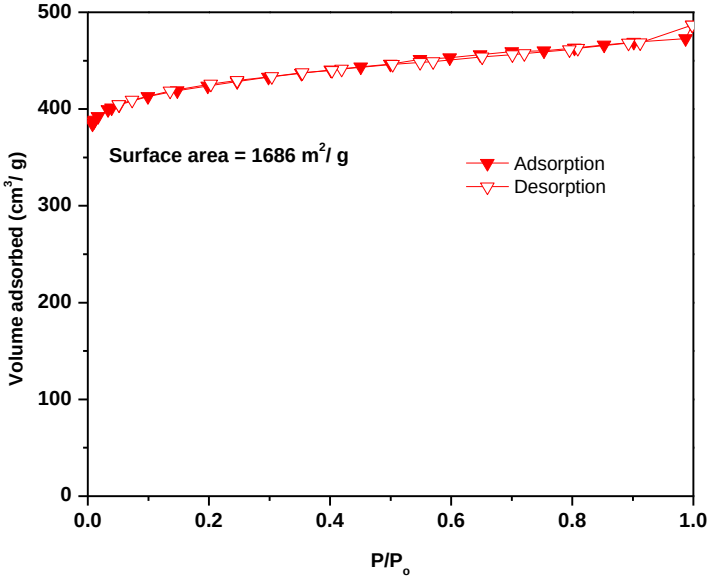

Figure B.9 Nitrogen isotherm of activated DMOF-MM2 at 77 K (closed symbols – adsorption, open symbols – desorption).

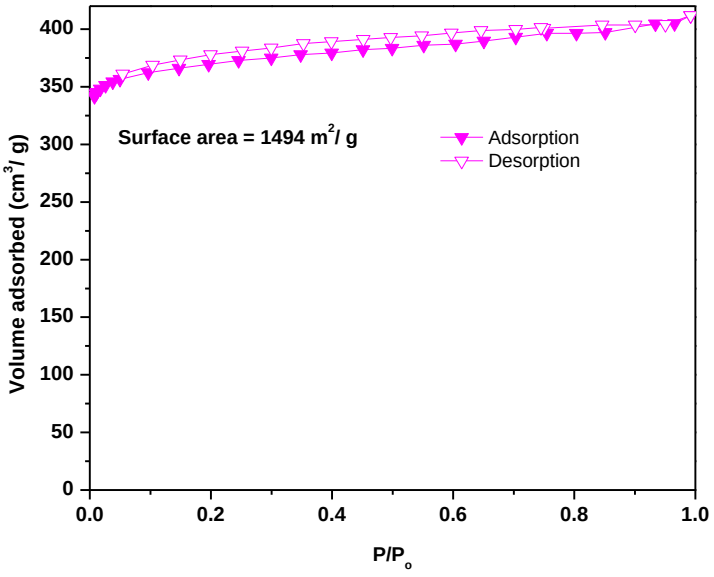

Figure B.10 Nitrogen isotherm of activated DMOF-DM1 at 77 K (closed symbols – adsorption, open symbols – desorption).

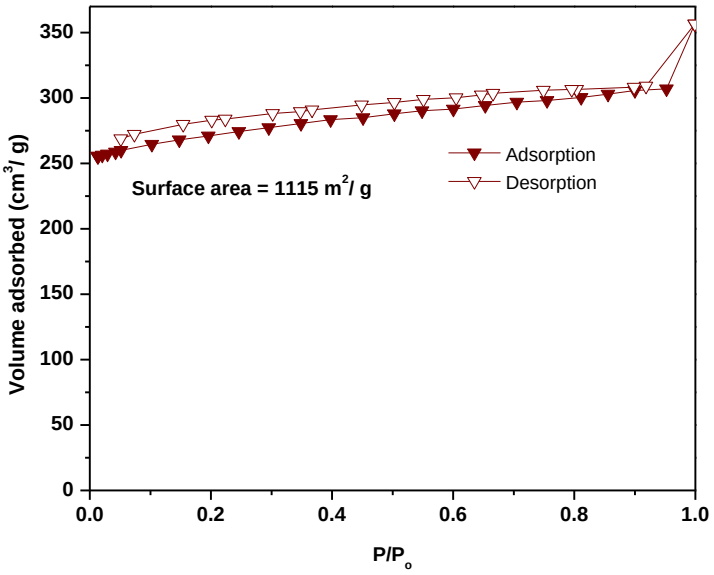

Figure B.11 Nitrogen isotherm of activated DMOF-DM2 at 77 K (closed symbols – adsorption, open symbols – desorption).

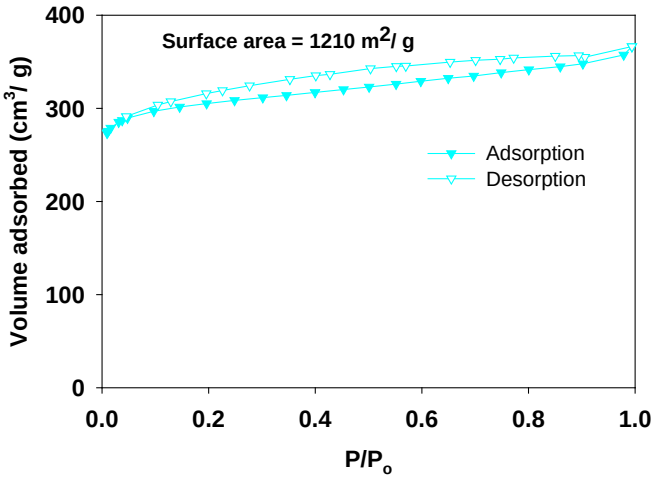

Figure B.12 Nitrogen isotherm of activated DMOF-TM1 at 77 K (closed symbols – adsorption, open symbols – desorption).

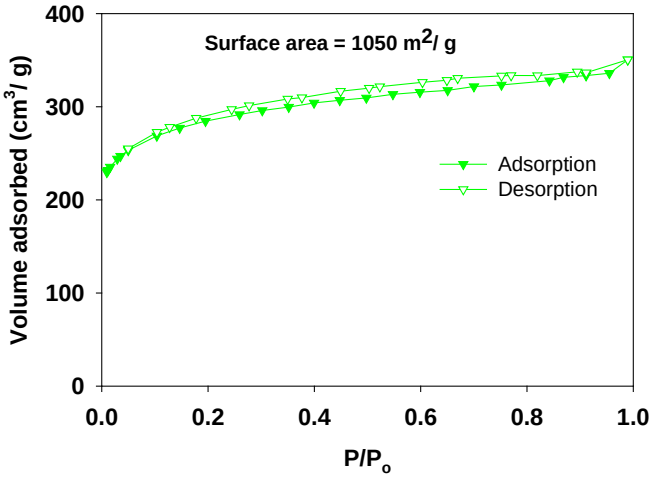

Figure B.13 Nitrogen isotherm of activated DMOF-TM2 at 77 K (closed symbols – adsorption, open symbols – desorption).

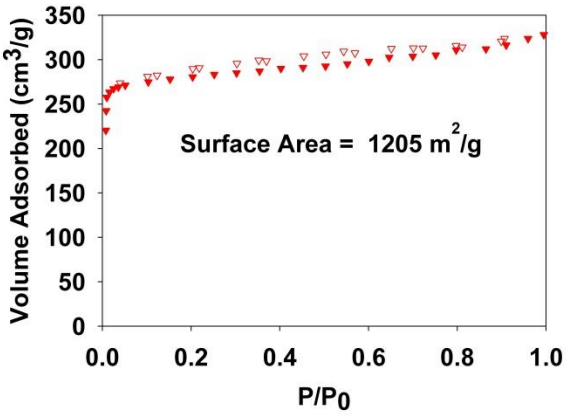

Figure B.14 Nitrogen isotherm of activated DMOF-TF at 77 K (closed symbols – adsorption, open symbols – desorption).

B.4 Simulation Details

Table B.1 DREIDING[2] Lennard-Jones Parameters for Framework Atoms.

Atom	**L-J Parameters**	
	σ (Å)	ε/k_B (K)
Zn	4.04	62.39
O	3.03	48.16
C	3.47	47.86
H	2.85	7.65
N	3.26	38.95
F	3.09	36.48

Table B.2 Partial Charges (e) for Each of the Frameworks, Using Label Definitions Given in Figure B.15.

Atom	DMOF	DMOF-TF	DMOF-TM2
Zn	0.89	0.90	0.87
O	-0.60	-0.58	-0.58
N	-0.14	-0.14	-0.14
H	0.09	0.10	0.10
C1	0.68	0.71	0.70
C2	-0.07	-0.26	-0.22
C3	-0.09	0.20	0.10
C4	-0.07	-0.08	-0.07
H1	0.10	---	0.12
F	---	-0.13	---
C5	---	---	-0.37

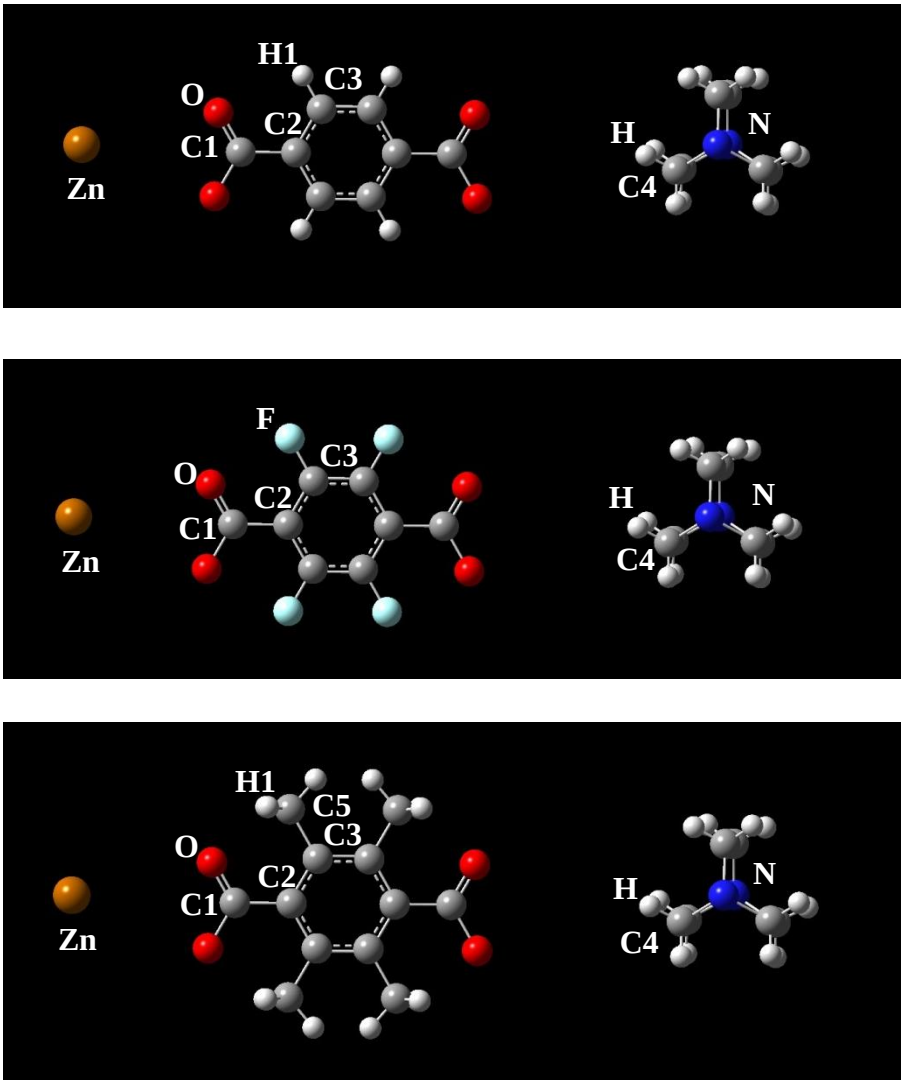

Figure B.15 Labelling of atoms in the isostructural DMOF variations. Labels are referenced in Table B.2, above.

Table B.3 Lennard-Jones Parameters and Partial Charges for Tip4p-Ew[3], Using Label Definitions Given in Figure B.16.

Atom	L-J Parameters		Charge
	σ (Å)	ε/k_B (K)	q(*e*)
O	3.164	81.899	---
H	---	----	0.524
Site 1	---	----	-1.048

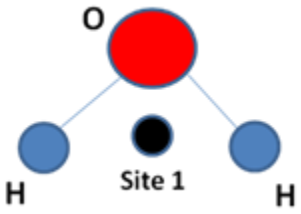

Figure B.16 Labelling of atoms in the water molecule. Labels are referenced in Table B.3, above.

B.5 References

(1) Chun, H.; Dybtsev, D. N.; Kim, H.; Kim, K., Synthesis, X-ray Crystal Structures, and Gas Sorption Properties of Pillared Square Grid Nets Based on Paddle-Wheel Motifs: Implications for Hydrogen Storage in Porous Materials. *Chem. – Eur. J.* **2005,** *11* (12), 3521-3529.

(2) Mayo, S. L.; Olafson, B. D.; Goddard, W. A., DREIDING - a generic force-field for molecular simulations. *J. Phys. Chem.* **1990,** *94* (26), 8897-8909.

(3) Horn, H. W.; Swope, W. C.; Pitera, J. W.; Madura, J. D.; Dick, T. J.; Hura, G. L.; Head-Gordon, T., Development of an improved four-site water model for biomolecular simulations: TIP4P-Ew. *J. Chem. Phys.***2004,** *120* (20), 9665-9678.

APPENDIX C

EFFECT OF CATENATION AND BASICITY OF PILLARED LIGANDS ON THE WATER STABILITY OF MOFS

C.1 PXRD (Powder X-Ray Diffraction)

Powder X-ray diffraction patterns (PXRD) were collected using an X'Pert X-ray PANalytical diffractometer with an X'celerator module using Cu Kα (λ = 1.5418 Å) radiation at room temperature, with a step size of 0.02˚ in two theta (2θ). From these patterns, the phase purity of as-synthesized samples can be confirmed by comparison with the simulated patterns from single crystal X-ray diffraction (Figures C.1-C.4).

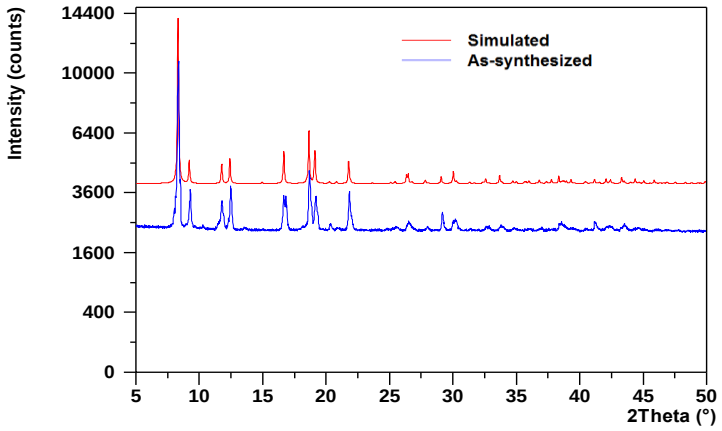

Figure C.1 Comparison of PXRD pattern for as-synthesized Zn-BDC-DABCO or DMOF and its theoretical pattern from single crystal data.

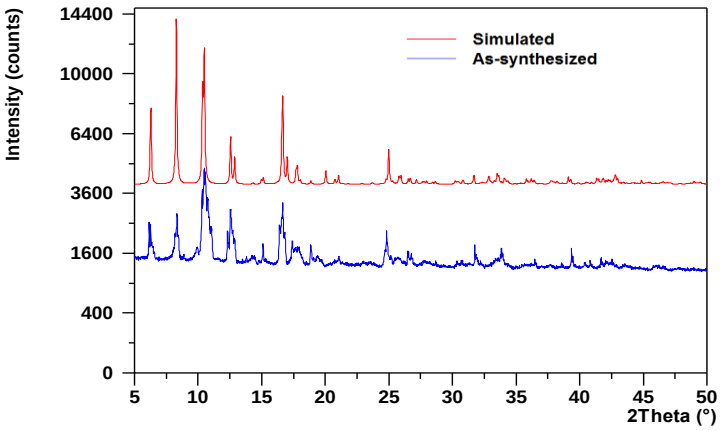

Figure C.2 Comparison of PXRD pattern for as-synthesized Zn-BDC-BPY or MOF-508a and its theoretical pattern from single crystal data.

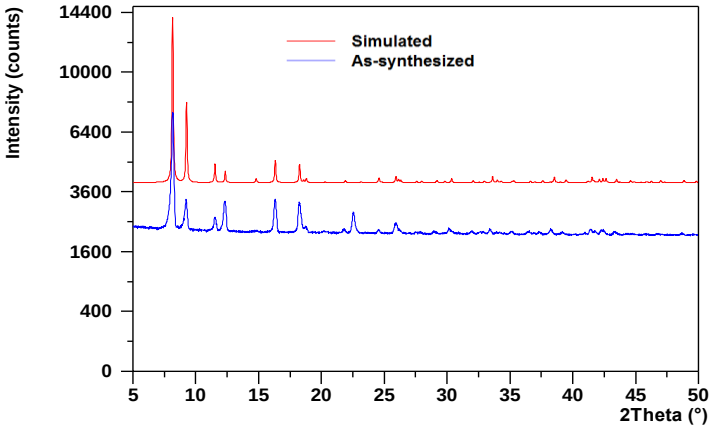

Figure C.3 Comparison of PXRD pattern for as-synthesized Zn-TMBDC-DABCO or DMOF-TM and its theoretical pattern from single crystal data.

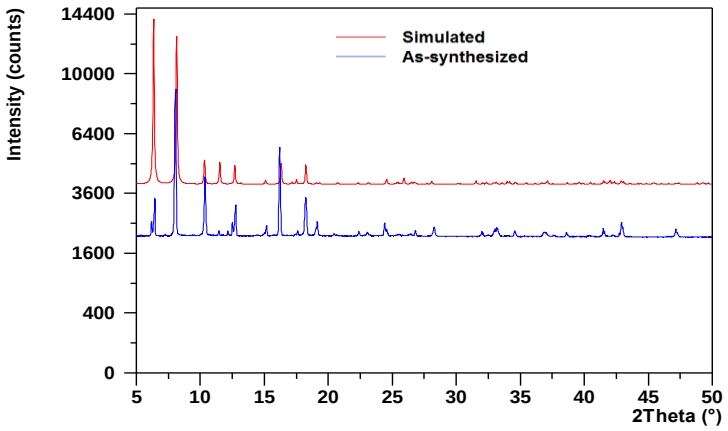

Figure C.4 Comparison of PXRD pattern for as-synthesized Zn-TMBDC-BPY or MOF-508-TM and its theoretical pattern from single crystal data.

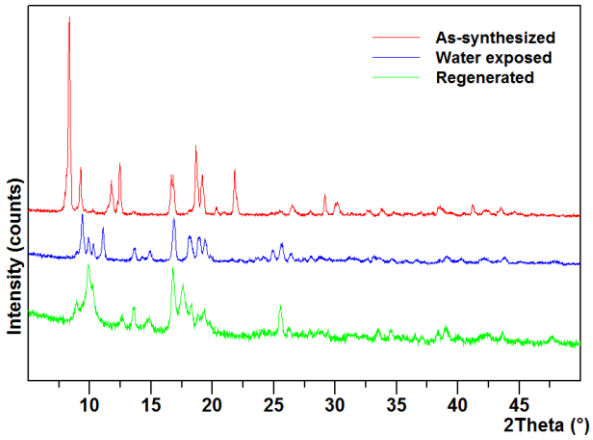

Figure C.5 PXRD patterns as-synthesized (top), water exposed (upon 90% RH, middle) and regenerated (bottom) Zn-BDC-DABCO or DMOF.[1]

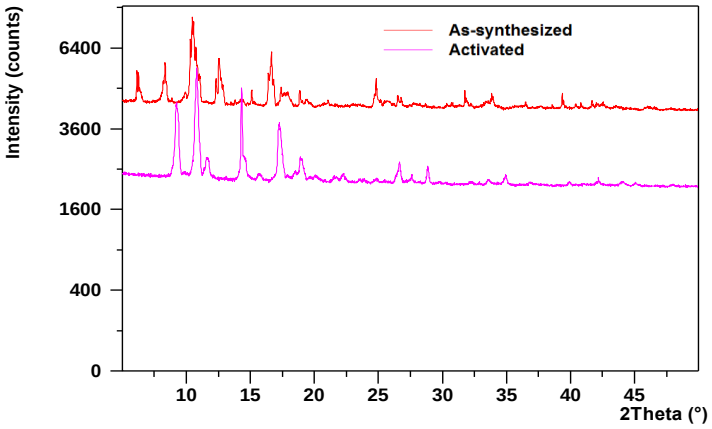

Figure C.6 PXRD patterns for as-synthesized Zn-BDC-BPY or MOF-508a and activated Zn-BDC-BPY or MOF-508b displaying shifting of peaks towards right on activation, which was also observed by Chen et. al.[2]

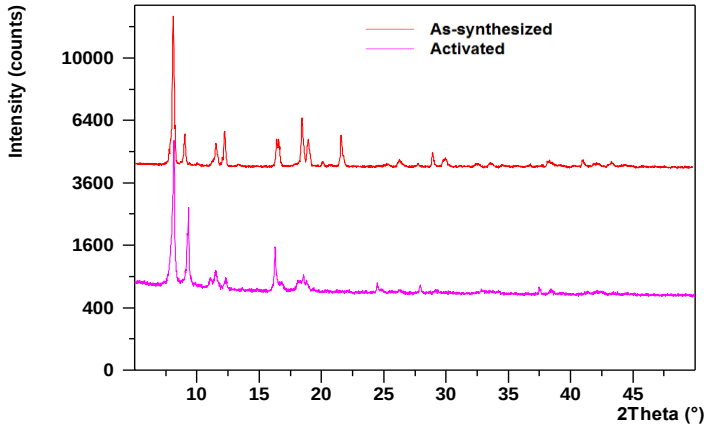

Figure C.7 PXRD patterns for as-synthesized and activated Zn-BDC-DABCO or DMOF displaying no change up on activation, which was also observed by Lee et. al.[3]

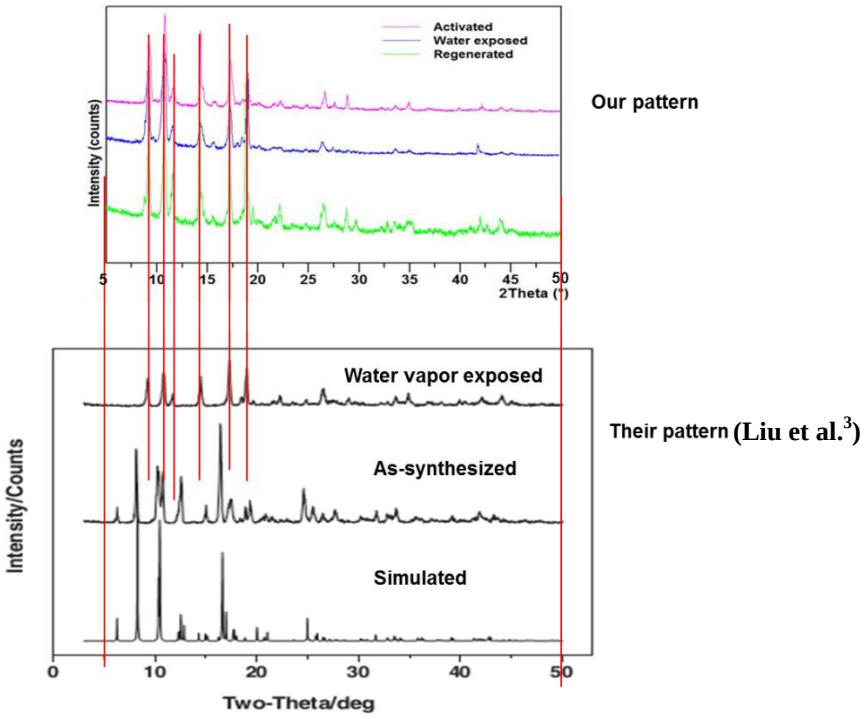

Figure C.8 Comparison of PXRD patterns for water exposed MOF-508 sample obtained in our work and reported by Liu et al.[4]

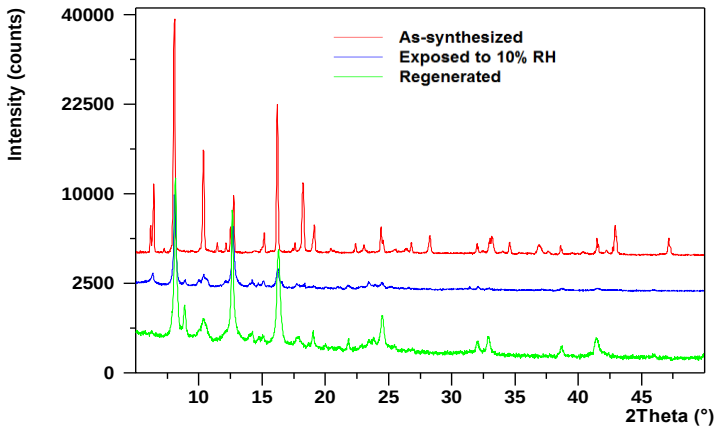

Figure C.9 PXRD patterns as-synthesized (top), water exposed (only up to 10% RH, middle) and regenerated (bottom) Zn-TMBDC-BPY or MOF-508-TM.

C.2 Surface Area Analysis

Specific surface areas were determined by applying the BET model to nitrogen adsorption isotherms (Figures C.10-C.13) measured at 77 K for each activated MOF using a Quadrasorb system from Quantachrome Instruments.

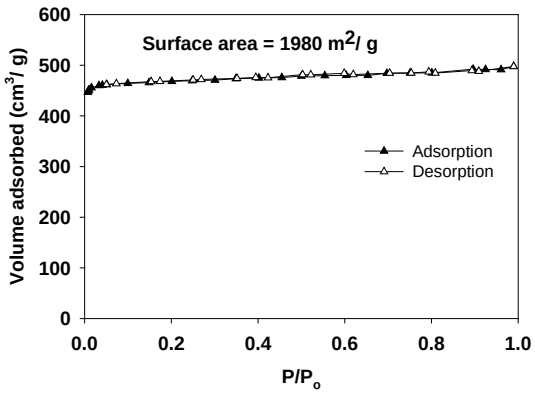

Figure C.10 Nitrogen isotherm of activated Zn-BDC-NO_2-DABCO or DMOF- NO_2 at 77 K (closed symbols – adsorption, open symbols – desorption).

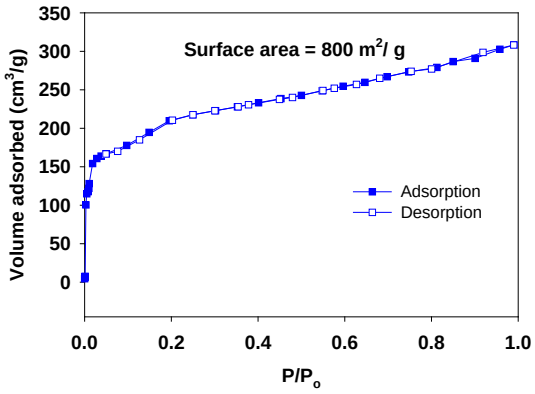

Figure C.11 Nitrogen isotherm of activated Zn-BDC-BPY or MOF-508b at 77 K (closed symbols – adsorption, open symbols – desorption).

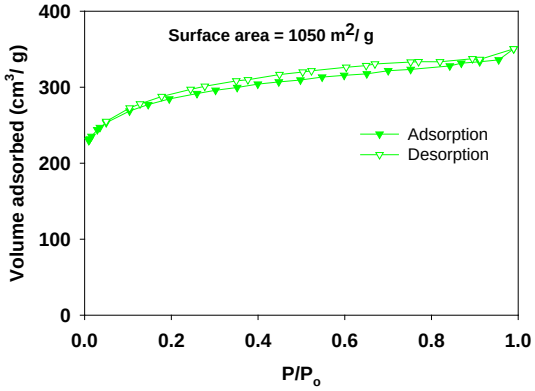

Figure C.12 Nitrogen isotherm of activated Zn-TMBDC-DABCO or DMOF-TM at 77 K (closed symbols – adsorption, open symbols – desorption).

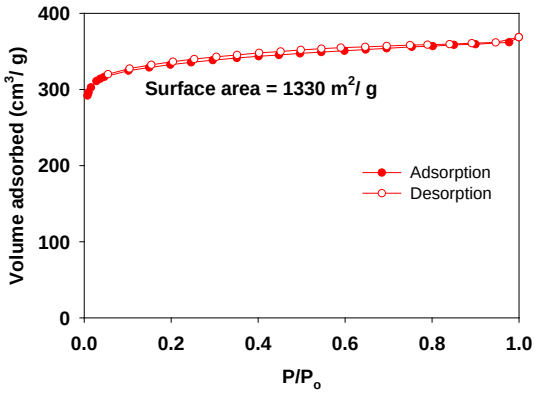

Figure C.13 Nitrogen isotherm of activated Zn-TMBDC-BPY or MOF-508-TM at 77 K (closed symbols – adsorption, open symbols – desorption).

C.3 References

(1) P. M. Schoenecker, C. G. Carson, H. Jasuja, C. J. J. Flemming and K. S. Walton, *Ind. Eng. Chem. Res.*, 2012, **51**, 6513-6519.

(2) B. L. Chen, C. D. Liang, J. Yang, D. S. Contreras, Y. L. Clancy, E. B. Lobkovsky, O. M. Yaghi and S. Dai, *Angew. Chem., Int. Ed.*, 2006, **45**, 1390-1393.

(3) J. Y. Lee, D. H. Olson, L. Pan, T. J. Emge and J. Li, *Adv. Funct. Mater.*, 2007, **17**, 1255-1262.

(4) H. Liu, Y. G. Zhao, Z. J. Zhang, N. Nijem, Y. J. Chabal, H. P. Zeng and J. Li, Adv. Funct. Mater. 2011, **21** (24), 4754-4762.

APPENDIX D

SYNTHESIS OF NOVEL COBALT, NICKEL, COPPER, AND ZINC-BASED WATER STABLE PILLARED METAL-ORGANIC FRAMEWORKS

D.1 3D Structures of Pillared MOFs

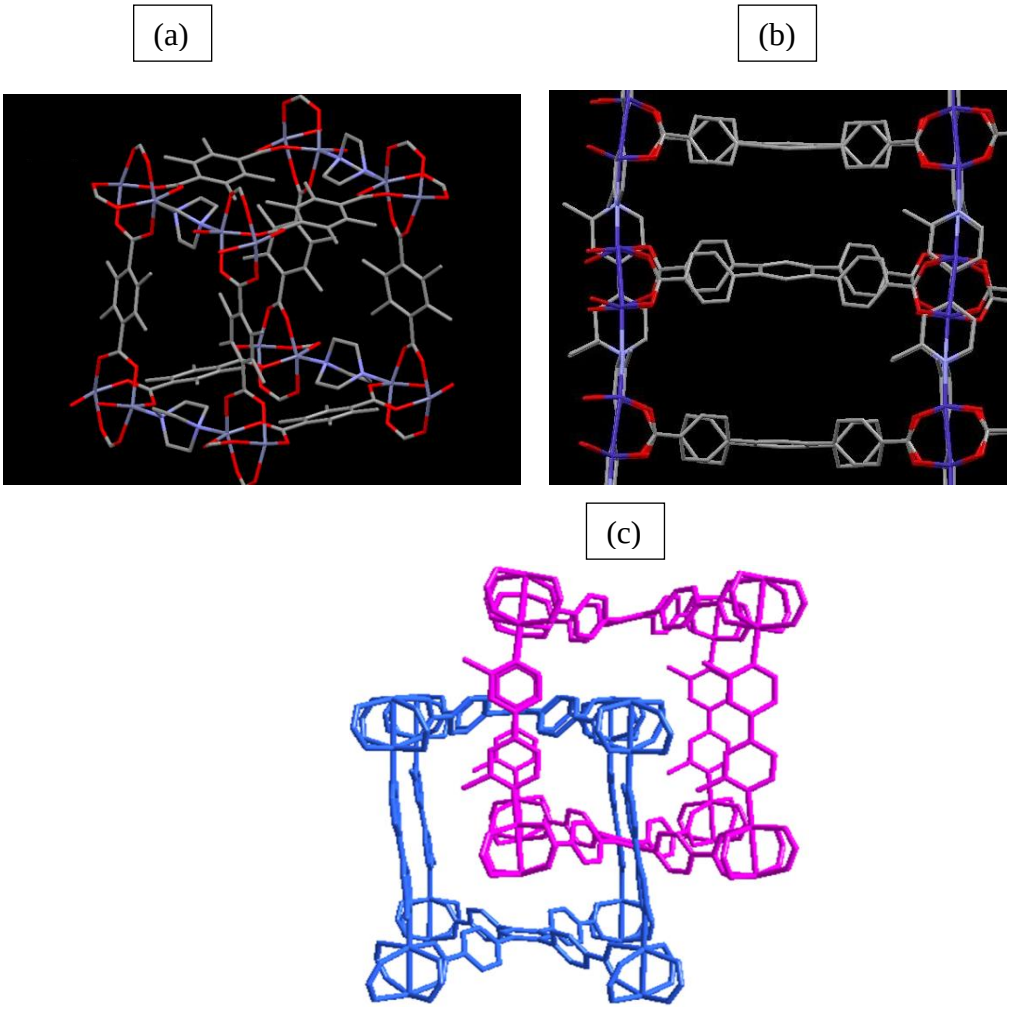

Figure D.1 Structure of pillared MOFs (a) M-TMBDC-DABCO (where M = Co, Ni, Cu), (b) M-BTTB-DMBPY (where M = Co, Zn), (c) 2-fold catenation in M-BTTB-DMBPY. Hydrogen atoms are omitted for clarity.

D.2 PXRD (Powder X-Ray Diffraction)

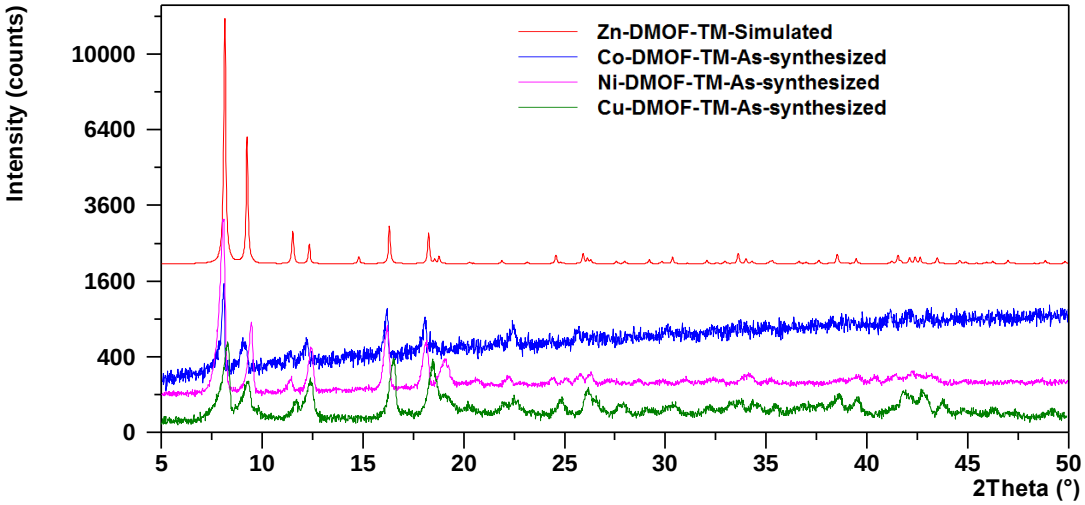

Figure D.2 Comparison of PXRD patterns for as-synthesized M-DMOF-TM (where M = Co, Ni, & Cu) and theoretical pattern of Zn-DMOF-TM* from single crystal data. *Reported from Chun et al.[1]

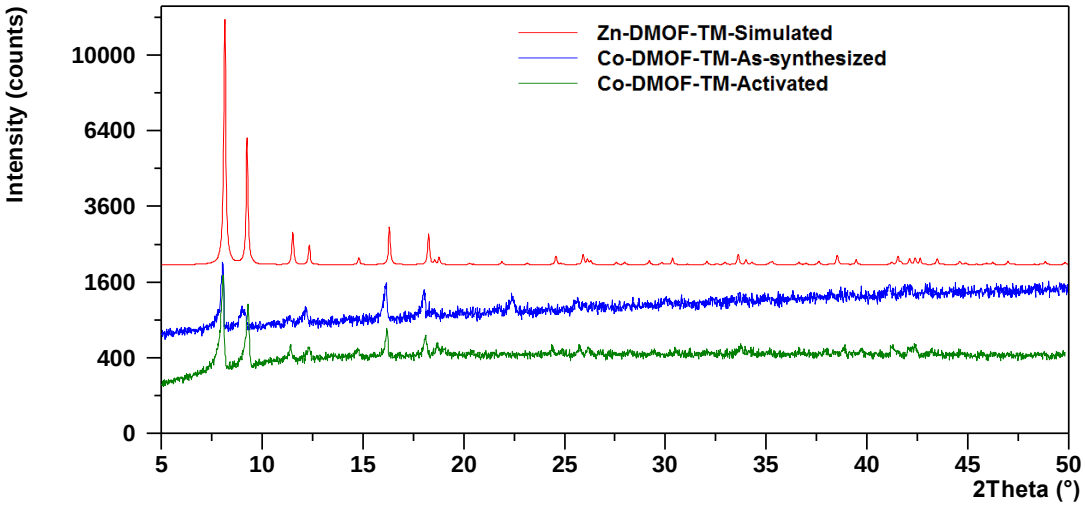

Figure D.3 Comparison of PXRD patterns for as-synthesized, activated Co-DMOF-TM and theoretical pattern of Zn-DMOF-TM* from single crystal data. *Reported from Chun et al.[1]

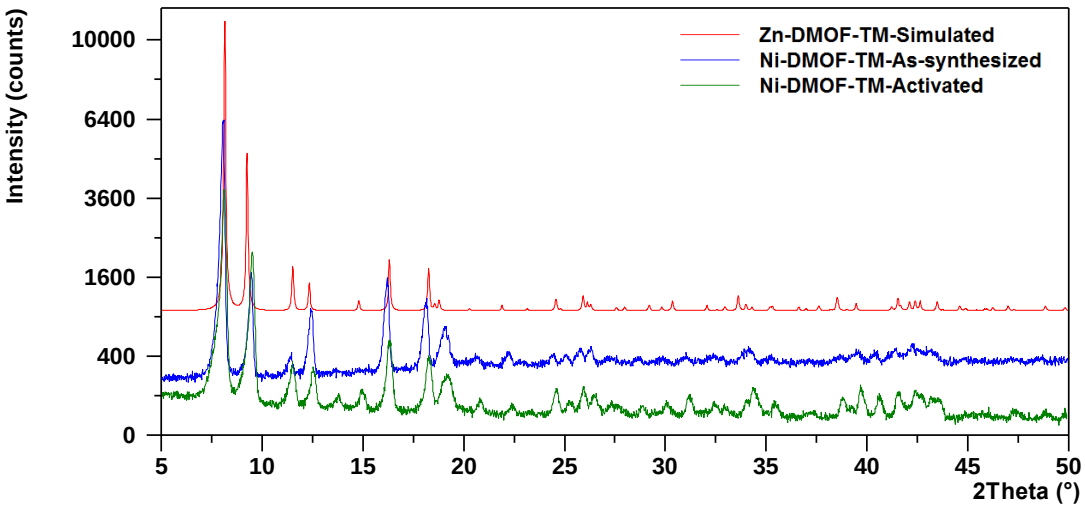

Figure D.4 Comparison of PXRD patterns for as-synthesized, activated Ni-DMOF-TM and theoretical pattern of Zn-DMOF-TM* from single crystal data. *Reported from Chun et al.[1]

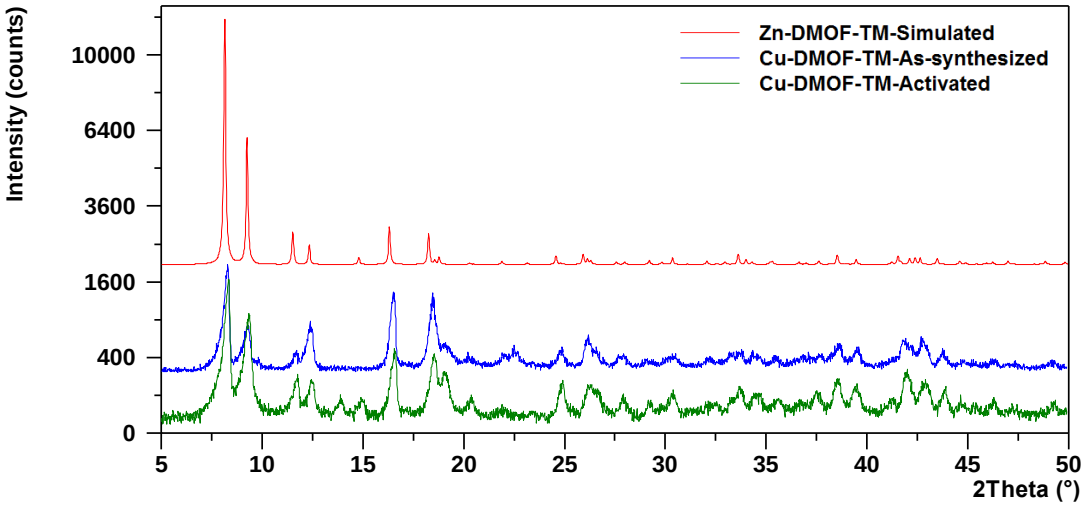

Figure D.5 Comparison of PXRD patterns for as-synthesized, activated Cu-DMOF-TM and theoretical pattern of Zn-DMOF-TM* from single crystal data. *Reported from Chun et al.[1]

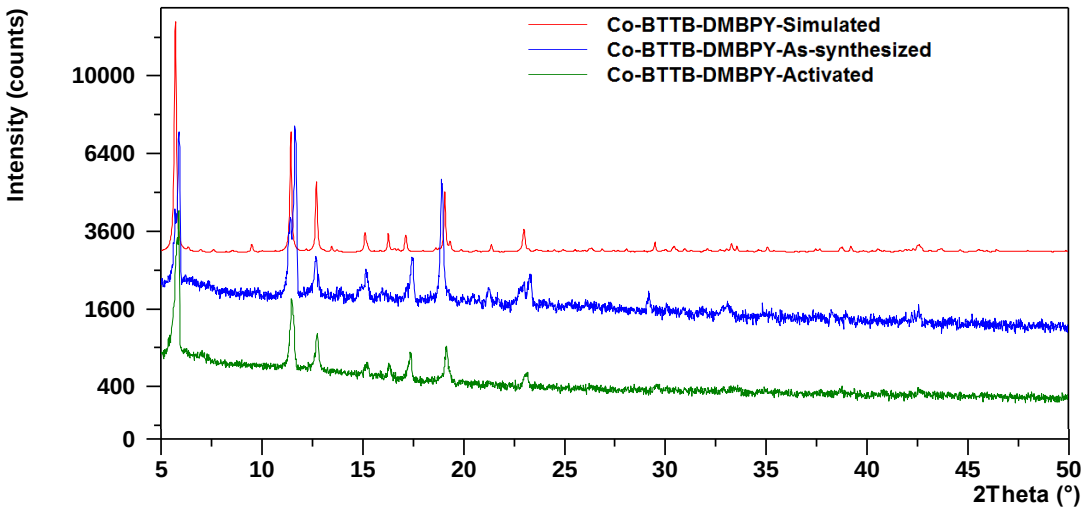

Figure D.6 Comparison of PXRD patterns for as-synthesized, activated Co-BTTB-DMBPY and its theoretical pattern from single crystal data (CCDC 992483 contains the crystallographic information file-CIF)

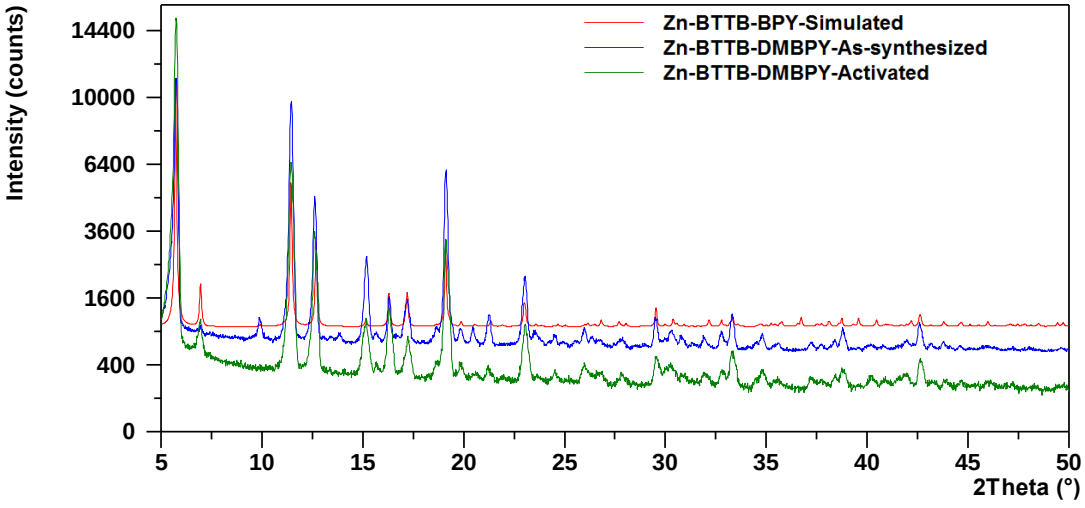

Figure D.7 Comparison of PXRD patterns for as-synthesized, activated Zn-BTTB-DMBPY and theoretical pattern of Zn-BTTB-BPY* from single crystal data. *Reported from our previous work.[2]

D.3 Thermo-gravimetric Analysis (TGA)

(a)

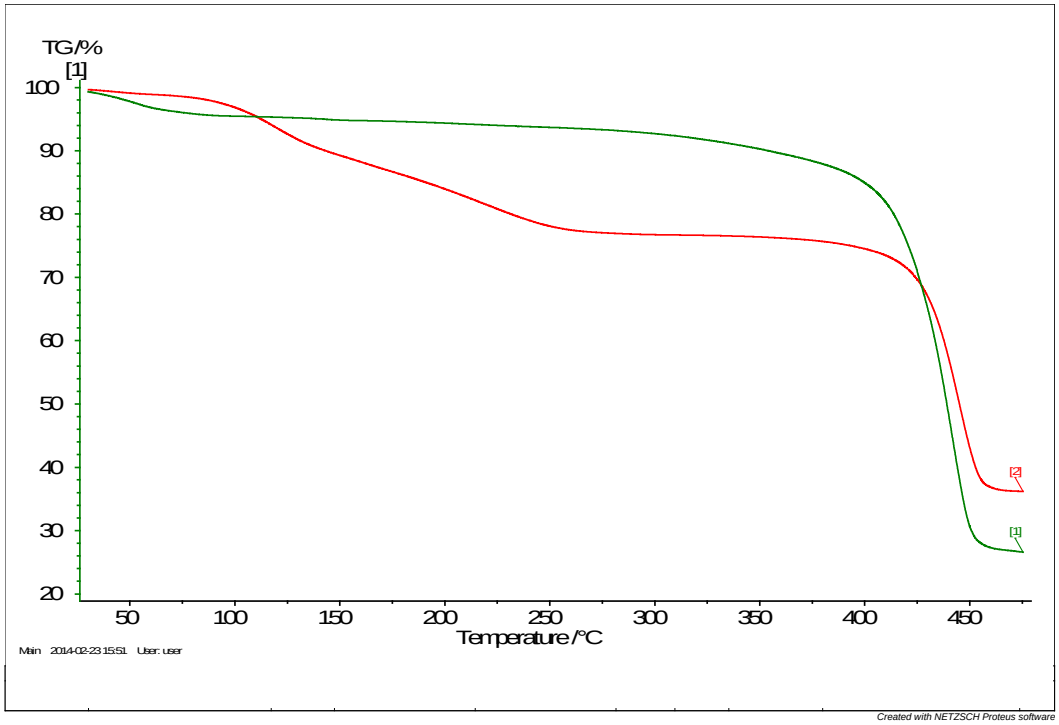

Figure D.8 TGA curves of as-synthesized (red) and activated (green) (a) Co-DMOF-TM, (b) Ni-DMOF-TM, and (c) Cu-DMOF-TM in helium flux.

(b)

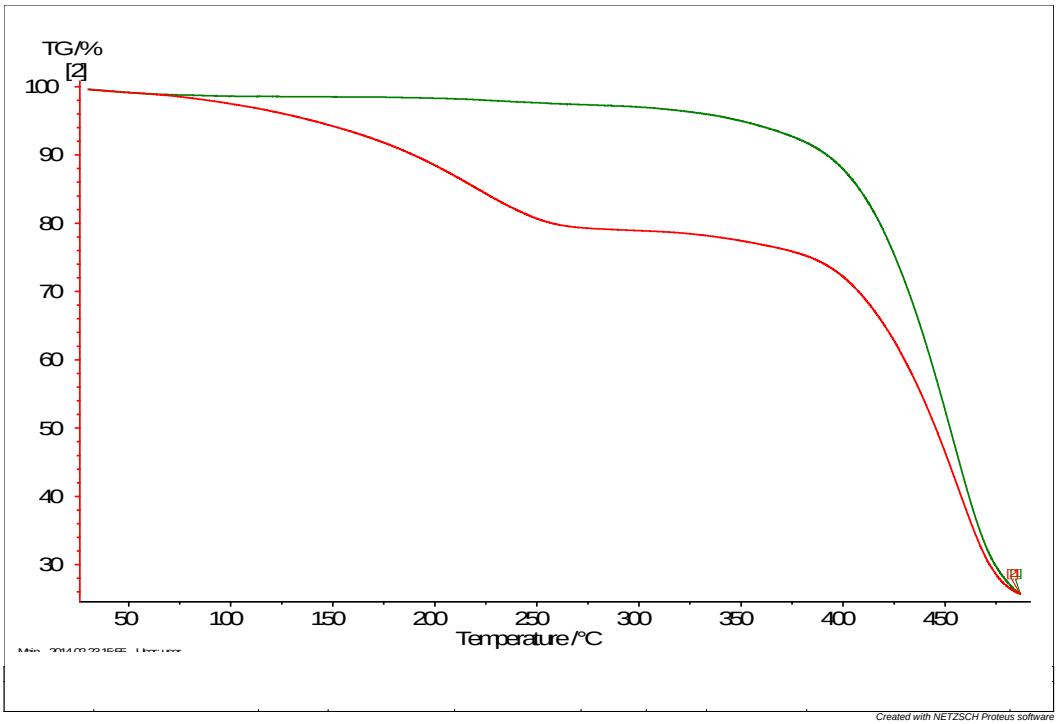

(c)

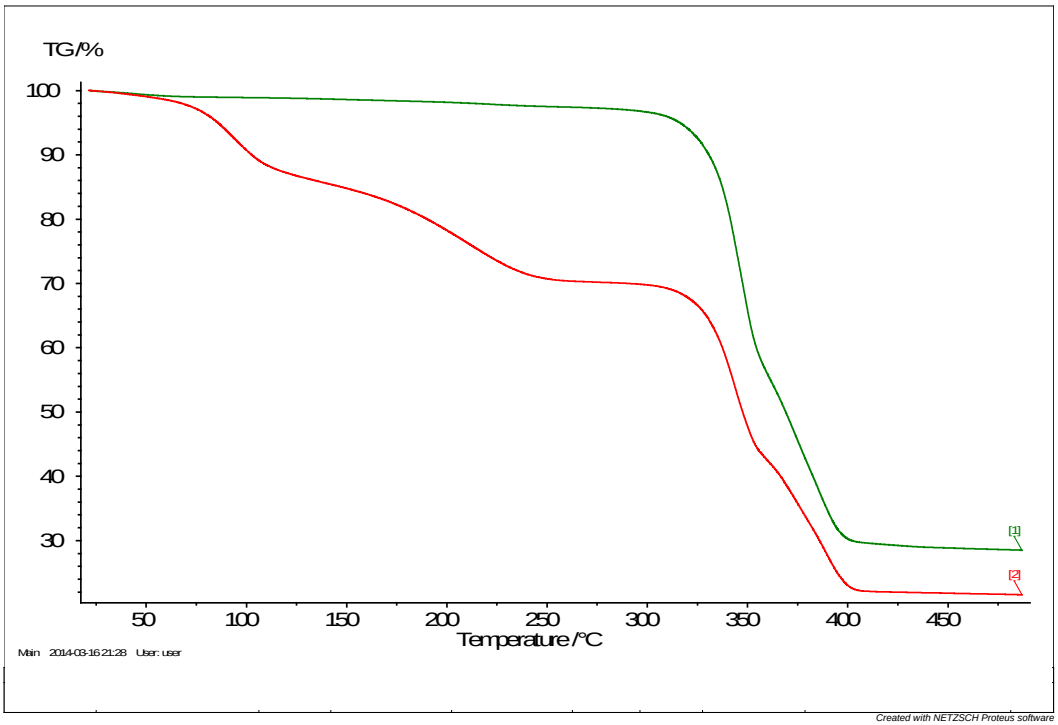

Figure D.8 Continued.

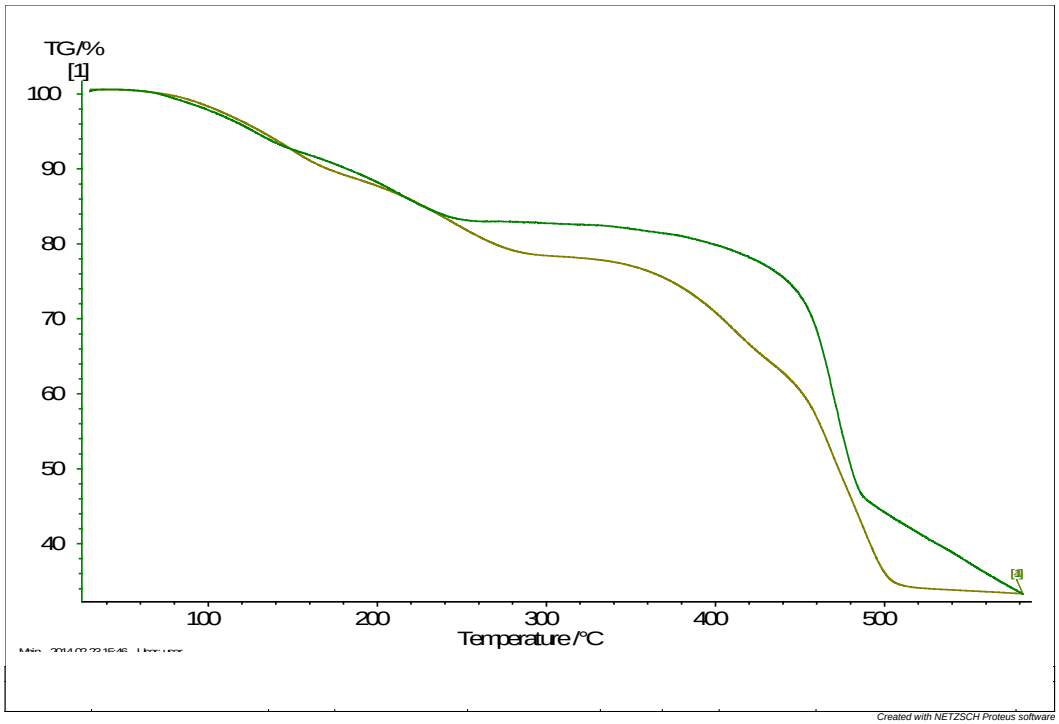

Figure D.9 TGA curves of as-synthesized Co-BTTB-DMBPY (green) and Zn-BTTB-DMBPY (gold) in helium flux.

D.4 Fourier Transform Infrared (FTIR) Spectroscopy

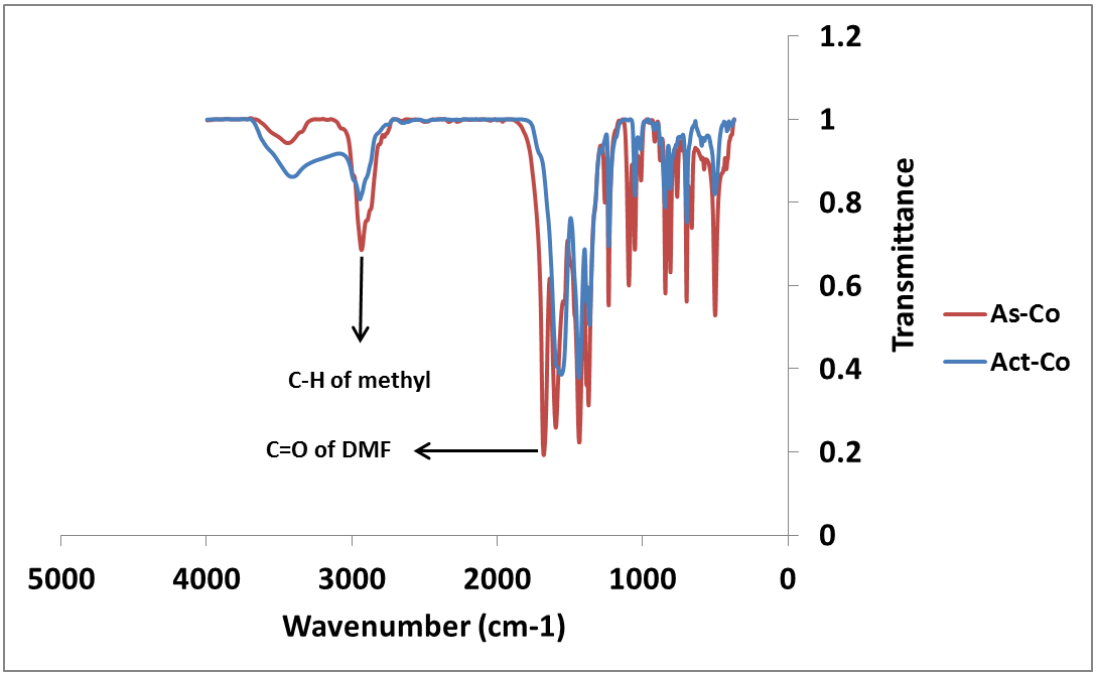

Figure D.10 FTIR spectra of as-synthesized (maroon) and activated (blue) Co-DMOF-TM.

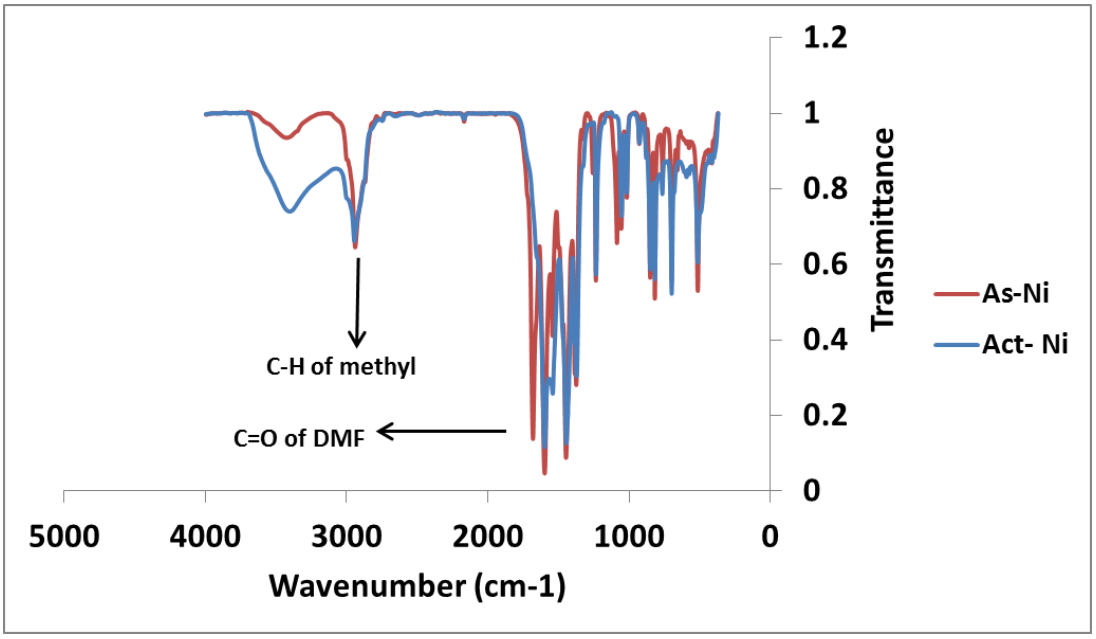

Figure D.11 FTIR spectra of as-synthesized (maroon) and activated (blue) Ni-DMOF-TM.

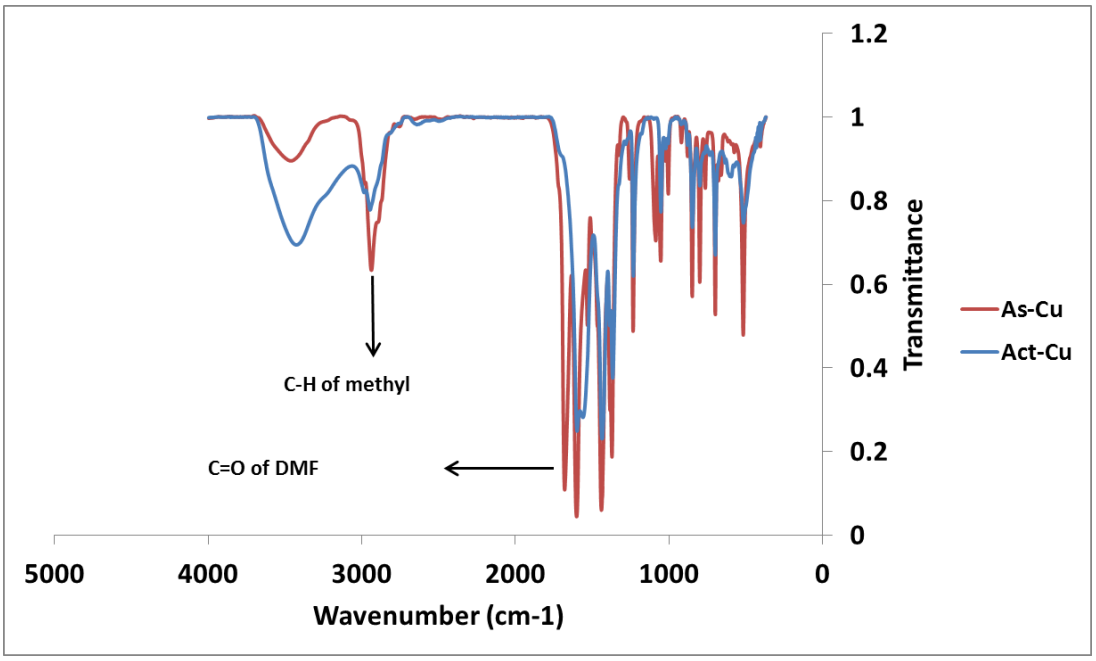

Figure D.12 FTIR spectra of as-synthesized (maroon) and activated (blue) Cu-DMOF-TM.

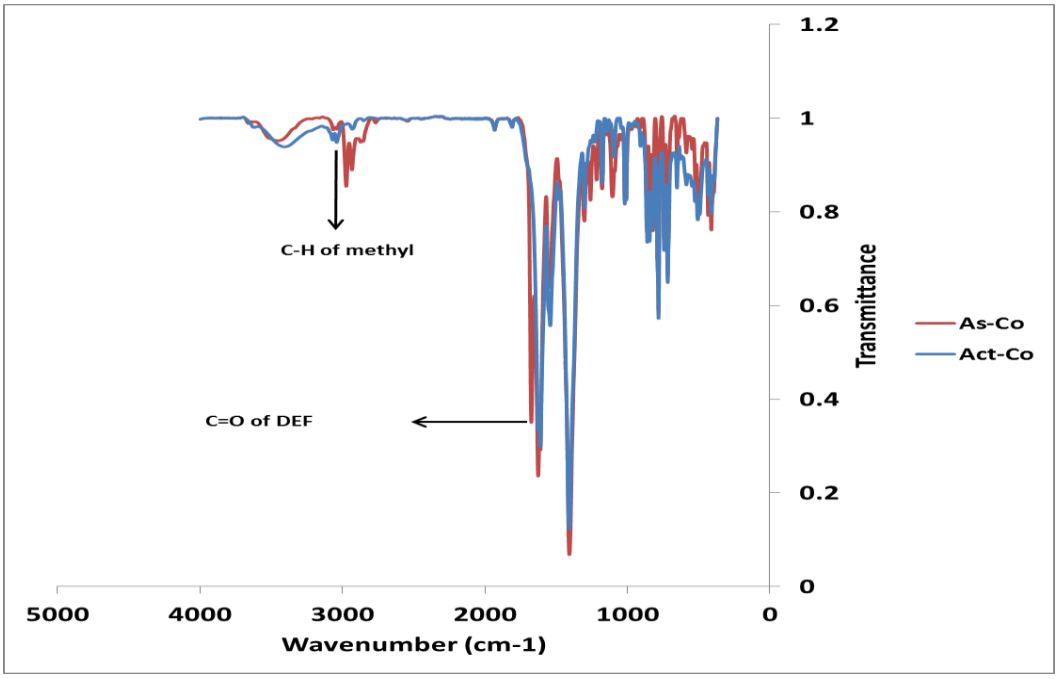

Figure D.13 FTIR spectra of as-synthesized (maroon) and activated (blue) Co-BTTB-DMBPY.

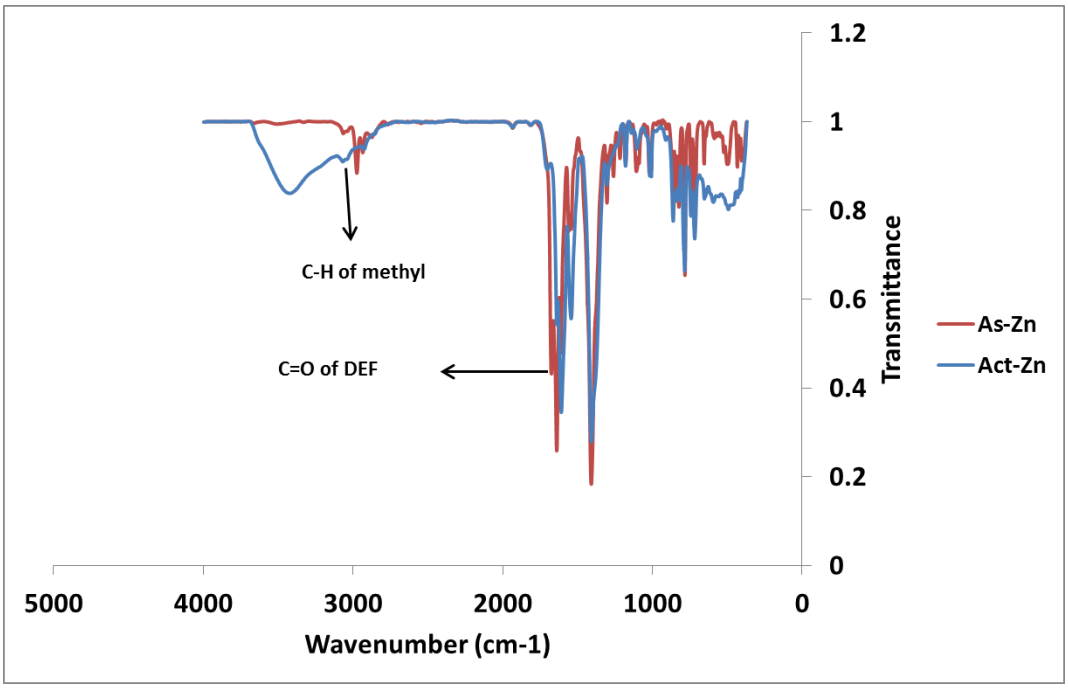

Figure D.14 FTIR spectra of as-synthesized (maroon) and activated (blue) Zn-BTTB-DMBPY.

D.5 BET Analysis of N_2 Adsorption Isotherms

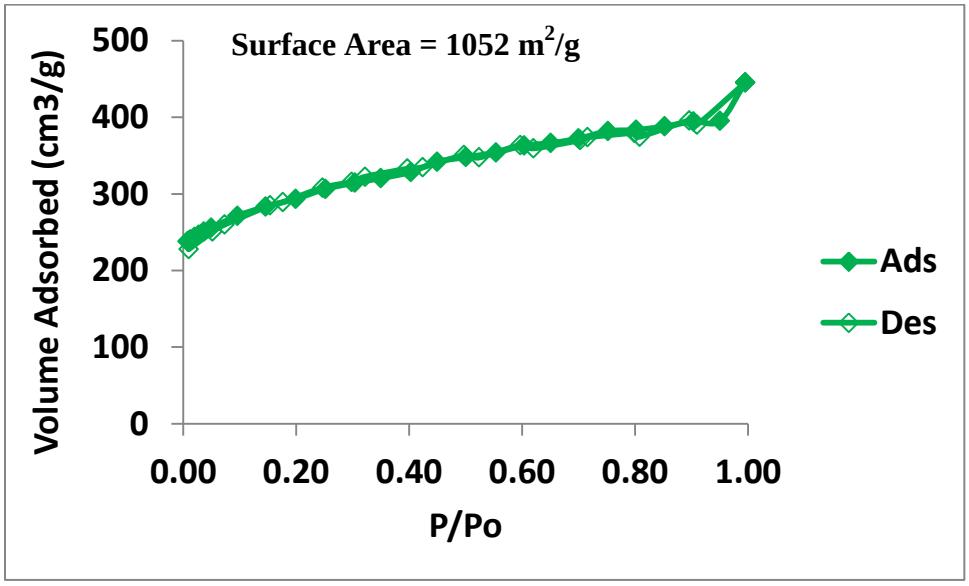

Figure D.15 Nitrogen isotherm of activated Co-DMOF-TM at 77 K (closed symbols – adsorption, open symbols – desorption).

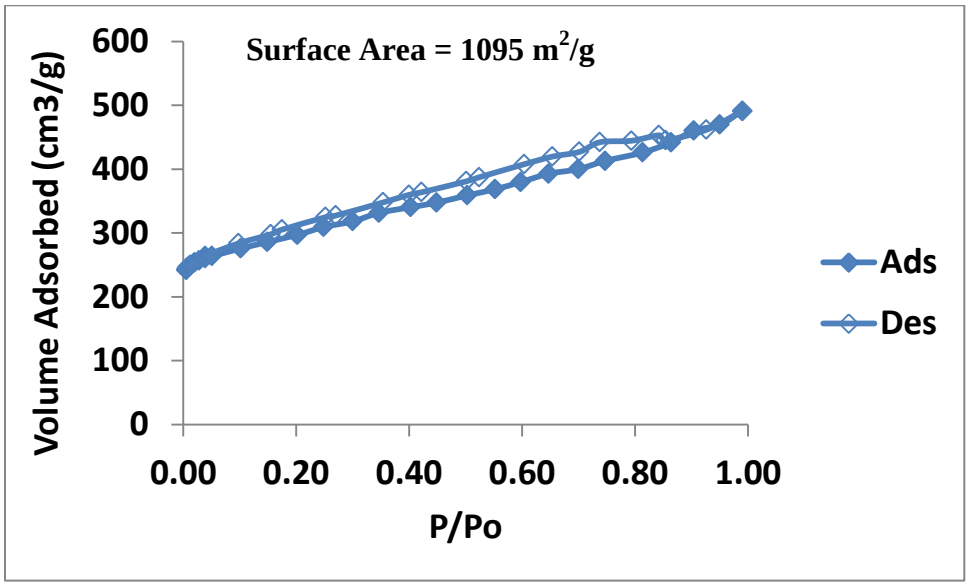

Figure D.16 Nitrogen isotherm of activated Ni-DMOF-TM at 77 K (closed symbols – adsorption, open symbols – desorption).

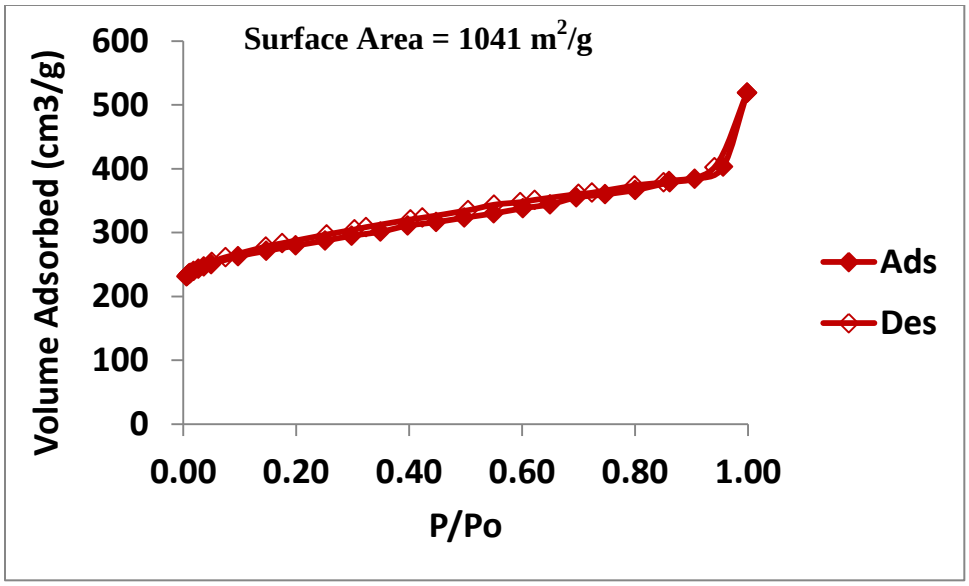

Figure D.17 Nitrogen isotherm of activated Cu-DMOF-TM at 77 K (closed symbols – adsorption, open symbols – desorption).

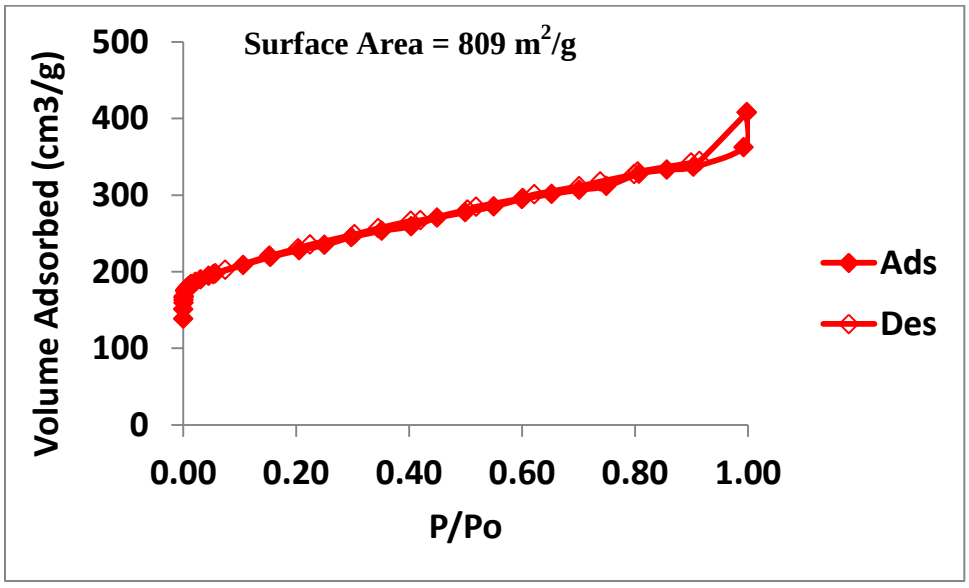

Figure D.18 Nitrogen isotherm of activated Co-BTTB-DMBPY at 77 K (closed symbols – adsorption, open symbols – desorption).

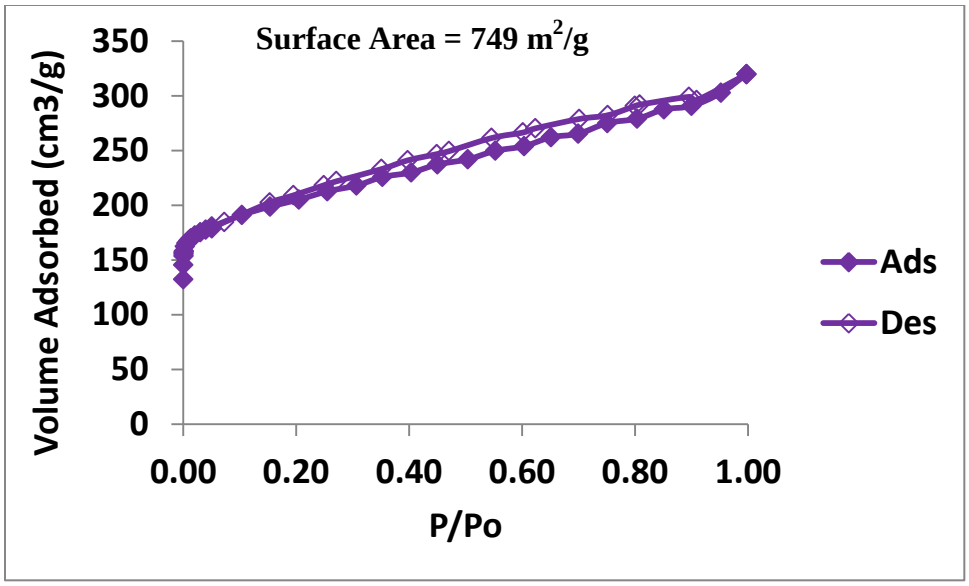

Figure D.19 Nitrogen isotherm of activated Zn-BTTB-DMBPY at 77 K (closed symbols – adsorption, open symbols – desorption).

D.6 Crystallographic data

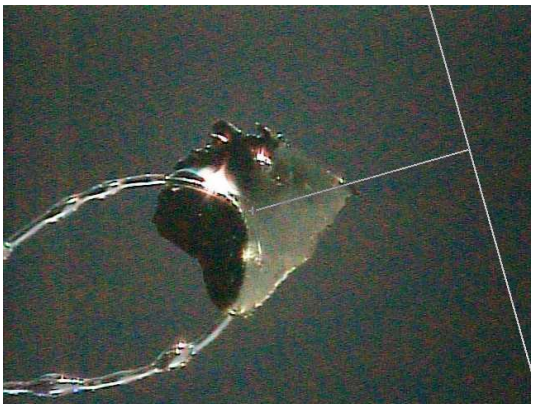

Figure D.20 Photograph of single crystal of Co-BTTB-DMBPY (size (mm) – 0.128 x 0.536 x 0.555).

Table D.1 Crystallographic Data for Co-BTTB-DMBPY.

Compound	Co-BTTB-DMBPY
Formula	$C_{46}H_{30}Co_2N_2O_8$
Fw	856.58
Crystal size(mm)	0.128 x 0.536 x 0.555
Space group	*Pbcm*
a = (Å)	11.632(2)
b =(Å)	27.860(6)
c(Å)	31.017(7)
V(Å^3)	10052(4)
Z	8
λ(*Mo K*α)(Å)	0.71073
D_c(g/cm^3)	1.132
μ(mm^{-1})	0.706
T(K)	296(2)
*R*int	0.0683
parameters	531
R_1, *w*R(I > 2σ(I))[a]	0.0630, 0.1517
R_1, *w*R(all data)[b]	0.0914, 0.1625
w=1/〔 $\sigma^2(F_0^2)+(aP)^2+bP$〕	a= 0.065, b=15.9005
Goodness-of-fit-on F^2	1.071
$\Delta\rho_{min}$ and $\Delta\rho_{max}$(e Å^{-3})	-0.780 , 0.786

[a] $R = \sum||F_0|-|F_c||)/\sum|F_0|$
[b] $wR = |\sum w(F_0-F_c)^2/\sum w(F_0^2)^2|^{1/2}$

D.7 References

(1) Chun, H.; Dybtsev, D. N.; Kim, H.; Kim, K., Synthesis, X-ray crystal structures, and gas sorption properties of pillared square grid nets based on paddle-wheel motifs: implications for hydrogen storage in porous materials. *Chemistry* **2005,** *11* (12), 3521-9.

(2) Karra, J. Development of porous metal organic frameworks for gas adsorption applications. Georgia Institute of Technology, Atlanta, 2011.

APPENDIX E

RATIONAL TUNING OF WATER VAPOR AND CO_2 ADSORPTION IN HIGHLY STABLE ZR-BASED MOFS

E.1 PXRD (Powder X-Ray Diffraction)

Powder X-ray diffraction patterns (PXRD) were collected using an X'Pert X-ray PANalytical diffractometer with an X'celerator module using Cu Kα (λ = 1.5418 Å) radiation at room temperature, with a step size of 0.02˚ in two theta (2θ). In order to use UiO-66-DM as support for a catalyst, or catalyst itself, its stability in the aqueous media needs to be verified. Since, some reactions run under acidic or basic conditions too, hence stability in the presence of a strong acid (1N HCl, pH = 0) and a strong base (1N NaOH, pH = 14) is also checked. Figures E.3-E.5 indicate that UiO-66-DM is well stable in neutral (water) and acidic (1N HCl solution) media. However, it loses its crystallinity in basic (1N NaOH) solution. Valenzano et al.[1] treated parent UiO-66 with H_2O, HCl and NaOH for 2 hrs. and reported that after NaOH treatment, UiO-66 started losing its crystallinity but there was no effect on crystallinity of UiO-66 due to H_2O, and HCl. Similarly, nitro and amino functionalized UiO-66 MOFs were also shown to be stable after H_2O, and HCl treatment but they lost crystallinity after NaOH treatment for 2 hrs.[2] However, there is no explanation available for loss of crystallinity after NaOH treatment.

Engineering MOFs for large scale applications e.g., use of MOFs as adsorbents for fixed bed adsorption systems will require their pelletization. Hence, we have examined the effect of pelletization on the crystallinity of UiO-66-DM. The UiO-66-DM material has been exposed to increasing pressure up to 6000 PSI. Figure E.6 shows that

PXRD pattern remains unaltered by the applied treatment similar to the observation of Cavka et al. for parent UiO-66.[3] Thus, UiO-66 and its functionalized analogues are amenable to pelletization without the loss of porous properties.

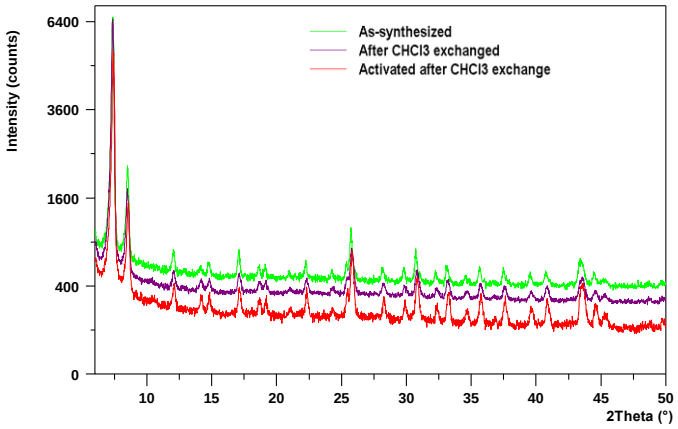

Figure E.1 Comparison of Powder XRD pattern for as-synthesized, solvent ($CHCl_3$) exchanged, and activated UiO-66-MM.

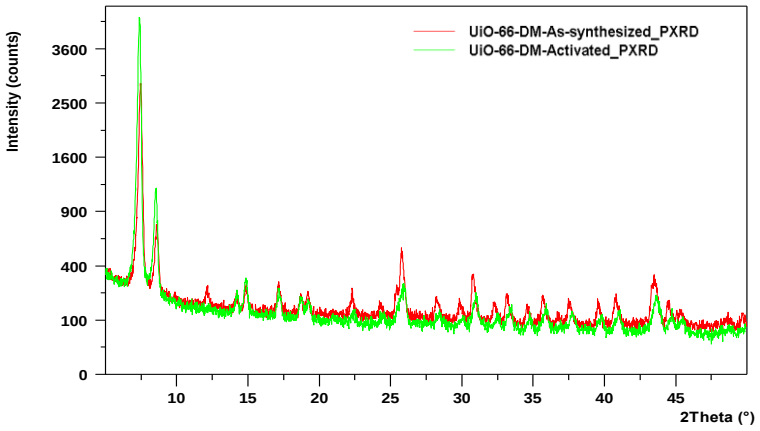

Figure E.2 Comparison of Powder XRD pattern for as-synthesized and activated UiO-66-DM.

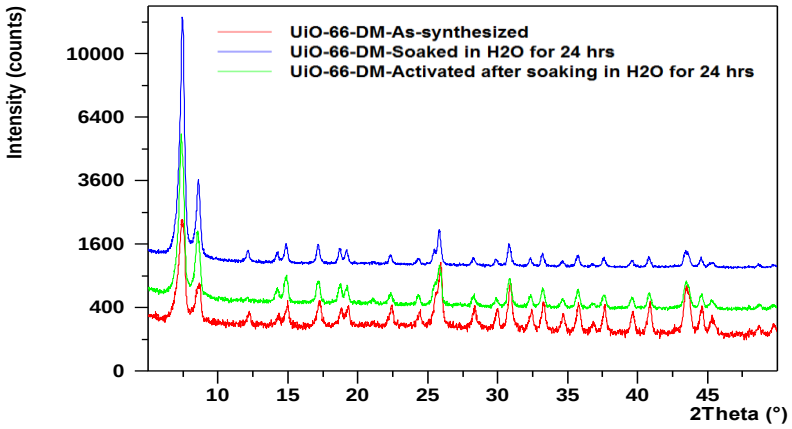

Figure E.3 Powder XRD patterns of UiO-66-DM showing the stability toward treatment with H_2O for 24 hrs.

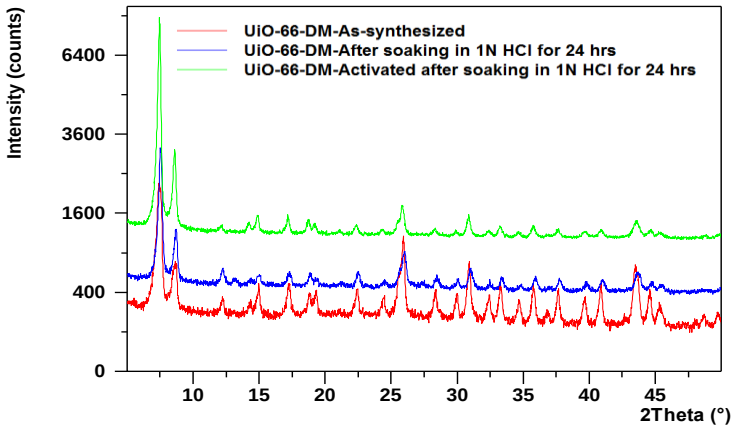

Figure E.4 Powder XRD patterns of UiO-66-DM showing the stability toward treatment with 1N HCl for 24 hrs.

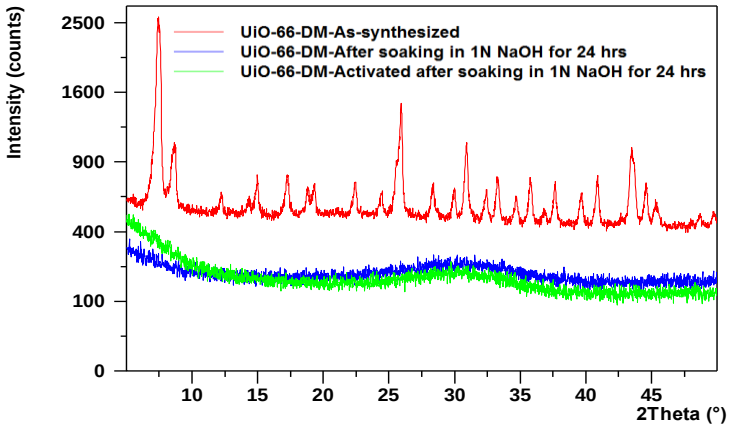

Figure E.5 Powder XRD patterns of UiO-66-DM showing the stability toward treatment with 1N NaOH for 24 hrs.

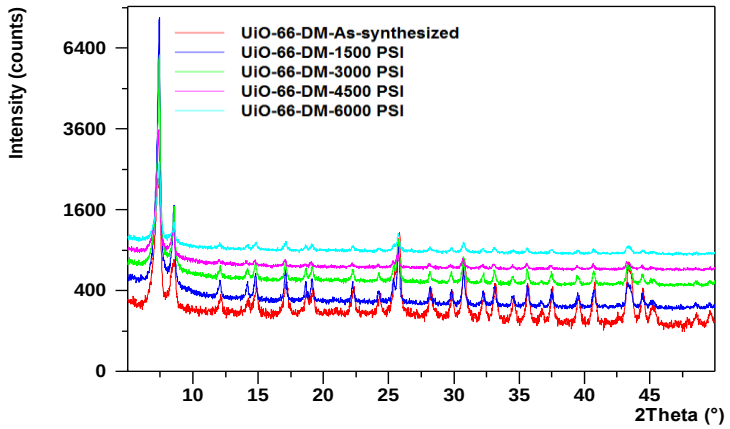

Figure E.6 Powder XRD pattern of as-synthesized UiO-66-DM and patterns of UiO-66-DM after exposure to increasing mechanical pressure.

E.2 Surface Area Analysis

Specific surface areas were determined by applying the BET model to nitrogen adsorption isotherms (Figures E.7-E.10) measured at 77 K for each activated MOF before and after water exposure using a Quadrasorb system from Quantachrome Instruments.

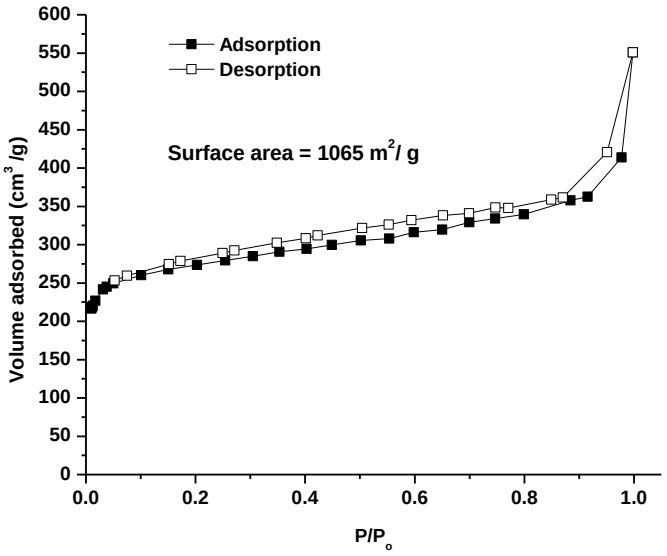

Figure E.7 Nitrogen isotherm of activated UiO-66-MM at 77 K (closed symbols – adsorption, open symbols – desorption).

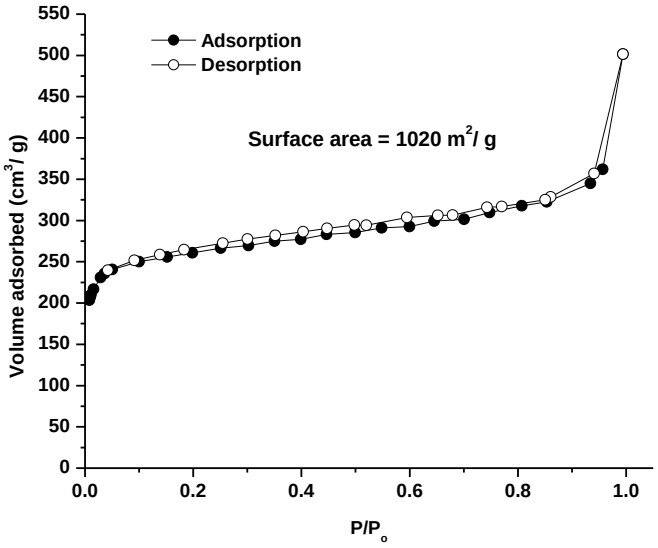

Figure E.8 Nitrogen isotherm of regenerated (after water vapor exposure) UiO-66-MM at 77 K (closed symbols – adsorption, open symbols – desorption).

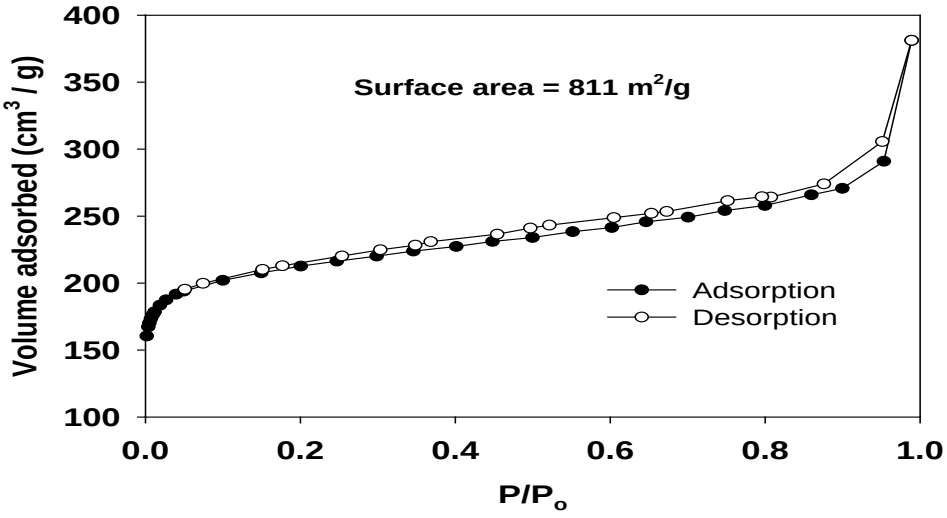

Figure E.9 Nitrogen isotherm of activated UiO-66-DM or Zr-DMBDC at 77 K (closed symbols – adsorption, open symbols – desorption).

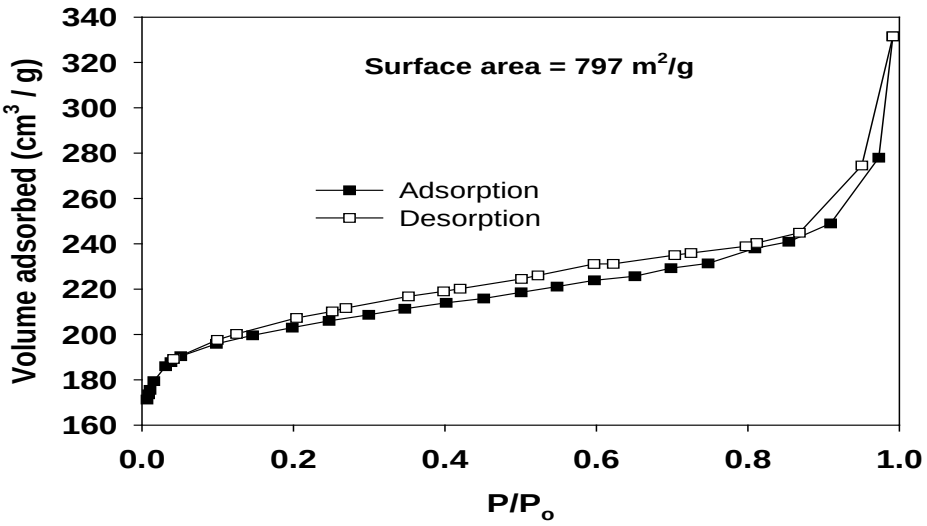

Figure E.10 Nitrogen isotherm of regenerated (after water vapor exposure) UiO-66-DM or Zr-DMBDC at 77 K (closed symbols – adsorption, open symbols – desorption).

E.3 Fit with Toth equation

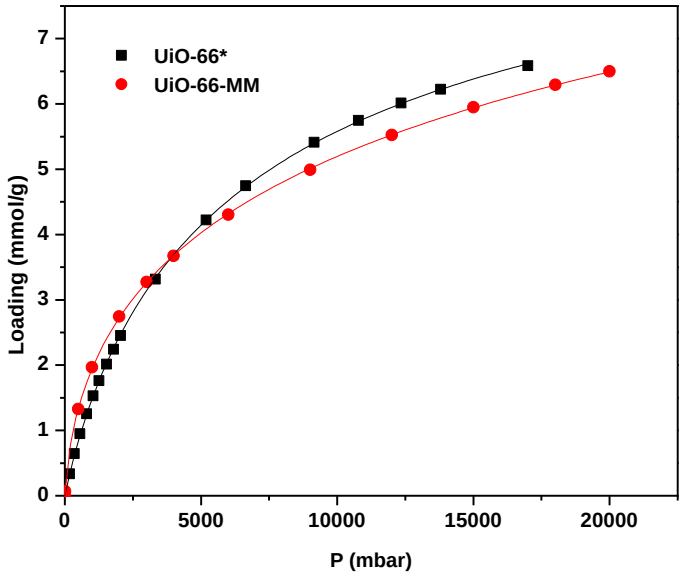

Figure E.11 CO_2 adsorption isotherms at 30 ^{o}C for activated UiO-66, and UiO-66-MM. (symbol- experimental data, solid curve- Fit from the Toth model).*Experimental data is taken from literature.[4]

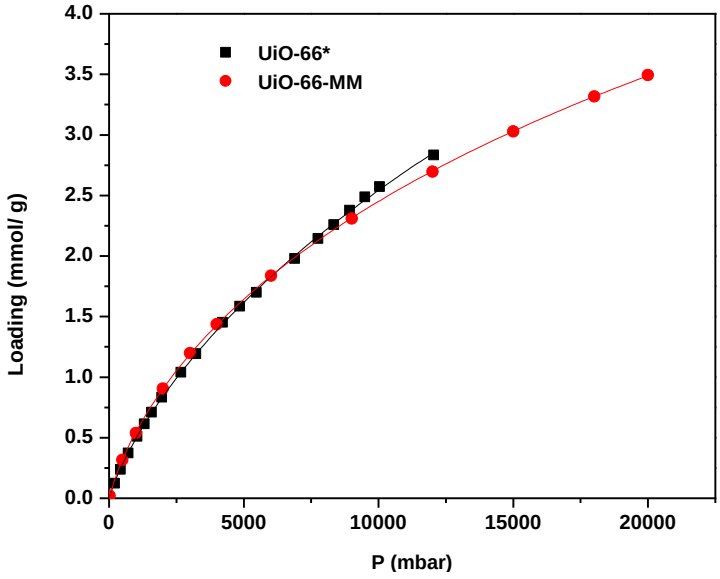

Figure E.12 CH_4 adsorption isotherms at 30 ^{o}C for activated UiO-66, and UiO-66-MM. (symbol- experimental data, solid curve - Fit from Toth model). *Experimental data is taken from literature.[4]

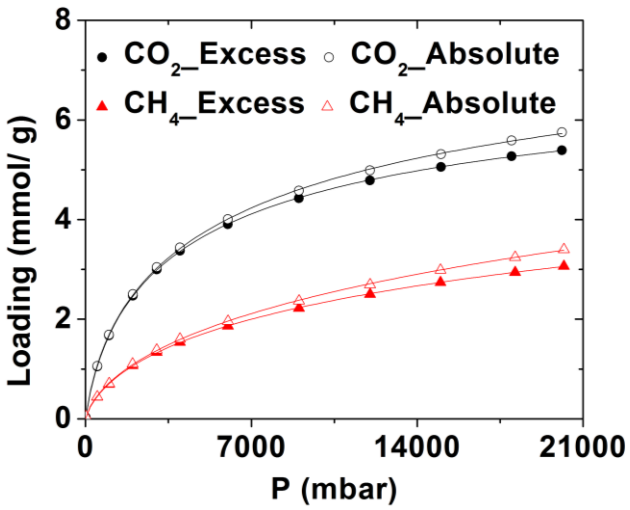

Figure E.13 Adsorption isotherms for CO_2 and CH_4 in UiO-66-DM at 30 ^oC (closed symbols- excess loading data; open symbols- absolute loading data, solid curve- Toth equation fit).

E.4 References

(1) Valenzano, L.; Civalleri, B.; Chavan, S.; Bordiga, S.; Nilsen, M. H.; Jakobsen, S.; Lillerud, K. P.; Lamberti, C.*Chemistry of Materials* **2011,** *23* (7), 1700-1718.

(2) Kandiah, M.; Nilsen, M. H.; Usseglio, S.; Jakobsen, S.; Olsbye, U.; Tilset, M.; Larabi, C.; Quadrelli, E. A.; Bonino, F.; Lillerud, K. P. *Chemistry of Materials* **2010,** *22* (24), 6632-6640.

(3) Cavka, J. H.; Jakobsen, S.; Olsbye, U.; Guillou, N.; Lamberti, C.; Bordiga, S.; Lillerud, K. P. *Journal of the American Chemical Society* **2008,** *130* (42), 13850-13851.

(4) Wiersum, A. D.; Soubeyrand-Lenoir, E.; Yang, Q. Y.; Moulin, B.; Guillerm, V.; Ben Yahia, M.; Bourrelly, S.; Vimont, A.; Miller, S.; Vagner, C.; Daturi, M.; Clet, G.; Serre, C.; Maurin, G.; Llewellyn, P. L. *Chem.- Asian J.* **2011,** *6* (12), 3270-3280.

APPENDIX F

STRUCTURAL STABILITY OF ZR-BASED MOFS WITH PORES LARGER THAN UIO-66

This work was conducted in collaboration with the Walton and Sholl group members- Nicholas C. Burtch and Dalar Nazari.

F.1 Introduction

Metal-organic frameworks (MOFs) are a fascinating new class of porous materials, synthesized by the self-assembly of metal-containing inorganic nodes and organic ligands.[1] Various different types of coordination chemistry is possible between the wide variety of metal groups and organic ligands available. Hence, more than 10,000 MOF structures[2] have already been synthesized experimentally since their discovery in 1990-2000 and more than 120,000 hypothetical MOF structures have been envisaged by Wilmer et al.[3] Counter to this, there are only 213 (natural + artificial) zeolites structures [4] available even though these materials have been used commercially as adsorbents, ion exchangers, and catalysts since 1960.[5,6] Moreover, MOFs possess tremendously high porosities and tunability compared to traditional porous materials such as zeolites, mesoporous silicas, and activated carbons.[7] Hence, MOFs have attracted significant amounts of interest from various disciplines and physicists, chemists, material scientists, and chemical engineers are trying to utilize their potential in applications such as nonlinear optics, magnetism, photoluminescence, air purification, gas storage, gas separation, gas sensing, catalysis, and drug delivery.[7-10]

However, commercial usage of MOFs in aforementioned applications has been plagued by their instability under humid or aqueous environments,[11-24] and there is a need to identify features, which can have a major impact on their water stability. Among the popular MOFs such as MOF-5/IRMOF-1, MOF-177, MOF-74/CPO-27, Cu-BTC/HKUST-1, MIL-53, MIL-100, MIL-101, UiO-66, and ZIF-8, only a few structures such as UiO-66, ZIF-8, and members of the MIL series of materials are reported to be water stable.[12,14,23-28] However, it has also been shown that the water stability of unstable MOFs such as Cu-BTC and MOF-5 can be improved by using techniques such as plasma-enhanced chemical vapor deposition,[29] carbon-coating,[30] ligand functionalization,[23,31-33] and post-synthetic cation exchange.[34] Recently, we have submitted the first review article summarizing water stability and adsorption in MOFs.[35] Based on an extensive review of previously existing MOF water stability studies,[11-34] we have shed light on factors such as acid-base effects of metal centers and organic ligands having a major impact on the thermodynamic stability of MOFs, and factors such as hydrophobicity and sterics around metal centers and organic ligands defining the kinetic stability of MOFs.[35]

In our previous work,[16] using a combination of water vapor and nitrogen adsorption isotherms, powder XRD, and FTIR spectroscopy we showed that the Zr-based MOFs such as UiO-67 and UiO-67-BIPY synthesized with double ring ligands (BPDC: biphenyl-4,4'-dicarboxylic acid and BIPY: 2,2'-bipyridine-5,5'-dicarboxylic acid respectively) are less stable than single ring ligand (BDC: benzene-1,4-dicarboxylic acid)-based Zr-MOFs such as UiO-66 and UiO-66-NH_2 under humid environments. It should be noted that all of these MOFs are isostructural and hence, they consist of a

$Zr_6O_4(OH)_4$ SBU (secondary building unit), which is twelve-coordinated to dicarboxylate ligands.[36] We proposed two hypotheses for this instability: (i) the larger pore space available in the UiO-67 MOF system compared to UiO-66 (Table F.1) increases the accessibility for water clustering near $Zr_6O_4(OH)_4$ SBU and thus, this leads to hydrolysis of metal-ligand bonds[25] (ii) rotational dynamics of the double ring ligands distorts the Zr-O bonds between $Zr_6O_4(OH)_4$ SBU and organic ligands rendering them more vulnerable to hydrolysis.[16] This is counter to the observation of Lillerud and coworkers[36-38] who report that all the UiO series of MOFs are stable under aqueous and acidic conditions. However, post-water exposure they characterized MOFs using only powder XRD, which is a qualitative technique and not a comprehensive way to characterize MOFs. Moreover, Schaate et al.[39] and Guillerm et al.[40] support our observation about the water instability of UiO-67.

Isolating the specific factors that have a major impact on the water stability of MOFs is a challenging task. Here, we have extended our previous work[16] and attempted to decouple the effect of porosity (window diameter and cage dimensions) and ligand dynamics on the water stability of the Zr-based UiO series of MOFs. Differences in the ligand dynamics should be mainly due to the rotation (flipping) of the benzene rings. The MOF system used in this work consists of three isostructural Zr-based MOFs: UiO-66, UiO-67, and UiO-66-N' (Figure F.1). UiO-67 and UiO-66-N' both have a similar pore space (window diameter and cage dimensions) but their pore space is larger than UiO-66 (Table F.1). Moreover, intuitively the 2,6-NDC ligand in UiO-66-N' should have lower ligand rotational dynamics due to the more non-linear axis of rotation than the BPDC ligand in UiO-67. Hence, if UiO-66-N' were to be stable upon exposure to humid

environments but UiO-67 degraded upon water exposure this would have to be mainly due to the higher rotational dynamics of the BPDC ligand since both of these MOFs have similar porosity (window diameter and cage dimensions). It should also be noted that by using an isostructural MOF system we have kept the effect of other factors such as metal type and coordination state, framework topology, catenation, and ligand character (pK_a, Table F.1) on the MOF water stability constant. ^{13}C cross-polarization magic-angle spinning (CPMAS) solid-state NMR experiments with a variation of contact times were performed on the activated MOF samples to compare the dynamics of a series of ligands (Figure F.1) relative to each other. Similar information could also be obtained through ^{13}C edited ^{1}H $T_{1\rho}$-relaxation experiments. As mentioned before, differences in the ligand dynamics should be mainly due to the rotation (flipping) of the benzene rings. Water vapor adsorption isotherms at 25 ^{o}C and 1 bar were measured up to 80% or 90% relative humidity (RH) to avoid water condensation in the equipment at higher humidities. Post-water exposure, MOFs were characterized comprehensively by performing porosity analysis via N_2 adsorption in addition to powder XRD. Analysis of the results obtained after this comprehensive characterization provides a conclusion with a high confidence level about the water stability or instability of the Zr-based UiO series of MOFs considered here.

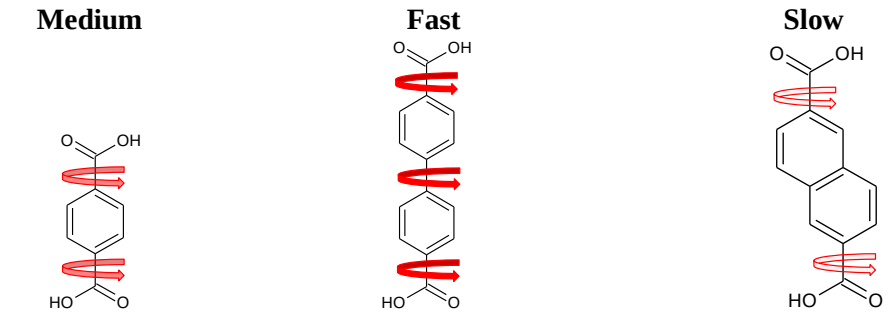

Figure F.1 Ligands utilized in synthesis of Zr-based UiO series of MOFs. Red arrows show speculated axis of rotation within the ligands. Decrease in the intensity of red color implies decrease (fast, medium, and slow) in ligand rotational dynamics, i.e., the rotation is hindered, which is associated with smaller rates of motion.

F.2 MOF Synthesis and Characterization

F.2.1 Synthesis and Activation

All the commercially available chemicals and solvents were used as received without further purification. Ligands used in the synthesis of Zr-based UiO series of MOFs are shown in Figure F.1. All the MOFs were synthesized solvothermally and their detailed synthesis procedures are as follows:

UiO-66. Synthesis of this MOF was performed as reported by Decoste et al.,[16] i.e., $ZrCl_4$ (0.641 mmol), BDC (0.641 mmol) were mixed in 10 mL of N,N′-dimethylformamide (DMF). This resulting mixture was sealed in a 20 mL glass vial and heated at 120 °C for 1 day. The solution was then cooled to room temperature in air, and the resulting solid was filtered and repeatedly washed with DMF. The activated sample of

UiO-66 was prepared by heating the as-synthesized sample at 150 °C overnight under vacuum.

UiO-67. Synthesis of this MOF was performed as reported by Decoste et al.,[16] i.e., $ZrCl_4$ (0.641 mmol), BPDC (0.641 mmol) were mixed in 10 mL of N,N′-dimethylformamide (DMF). This resulting mixture was sealed in a 20 mL glass vial and heated at 120 °C for 1 day. The solution was then cooled to room temperature in air, and the resulting solid was filtered and repeatedly washed with DMF. The activated sample of UiO-67 was prepared by heating the as-synthesized sample at 150 °C overnight under vacuum. Recently, Farha and coworkers[41] reported that addition of HCl to the reaction mixture accelerates the synthesis of UiO-66, UiO-67 and their derivatives. We observed that synthesis of UiO-67 via the recipe of Farha et al.[41] provides more reproducible results than Decoste et al.[16]

UiO-66-N'. UiO-66-N' was synthesized as reported by Zhong et al.,[42] i.e., equal molar amounts (1.75 mmol) of $ZrCl_4$ and 2,6-NDC are combined in 20 mL of N,N′-dimethylformamide (DMF) and 0.5 mL of 12 M HCl. This resulting mixture was sealed in a 60 mL glass vial and heated in a programmable oven to 120 °C at a rate of 1 °C min^{-1}, held at this temperature for 24 h, then cooled to room temperature at a rate of 1 °C min^{-1}. The resulting solid was filtered and repeatedly washed with DMF and acetone. The dried as-synthesized sample was then soaked in methanol for three days at room temperature to remove DMF and the unreacted 2,6-NDC ligand. The activated sample of UiO-66-N' was prepared by heating the methanol exchanged sample at 150 °C overnight under vacuum.

F.2.2 PXRD

Powder X-ray diffraction (PXRD) patterns were recorded on a X'Pert X-ray PANalytical diffractometer with an X'celerator module using Cu Kα (λ = 1.5418 Å) radiation at room temperature, with a step size of 0.02˚ in two theta (2θ) over a range of 5-50 degrees.

F.2.3 N_2 Adsorption

Nitrogen adsorption isotherms were measured at 77 K using a Quadrasorb system from Quantachrome instruments. The BET model was fitted to nitrogen adsorption isotherms in the low pressure range ($P/P_o < 0.05$) as suggested by Walton et. al[43] for MOFs to calculate their specific surface areas (Table F.1).

F.2.4 C^{13} CPMAS NMR- Contact Time Variation

A Bruker AV3−400 spectrometer was used in conjunction with a dual channel magic-angle spinning (MAS) probe to measure variable contact-time CPMAS spectra. Using a glove box, activated MOF samples were loaded directly into the ZrO_2 4 mm MAS rotor, which were then sealed using Kel-F caps and kept in well-sealed, air-tight containers when not measured. R_f frequencies of 100 and 400 MHz were used for ^{13}C and ^{1}H, respectively. All cross-polarization (CP) variable contact-time measurements were performed at room temperature using a radio frequency field of 50 kHz for contact-times varying from 0.01−10 ms. A slightly lower rf-field was used for ^{1}H decoupling. A total of 512 scans were accumulated for each individual contact time and a recycle delay of 4 s between scans was used. These experiments worked best under conditions of slow MAS

spinning speeds. A spinning speed of 5 kHz was chosen, where no significant overlap between spinning-sidebands and peaks corresponding to isotropic chemical shifts were observed. Peak intensities measured for various contact times are usually associated with a curve consisting of an increase in peak-intensity due to the transfer of magnetization from ^{1}H to ^{13}C nuclei. This increase is followed by a decay caused by the relaxation of ^{1}H and ^{13}C spins in the rotating frame caused by the oscillating field of the radio-frequency excitation (relaxation constants $T_{1\rho}$). This relaxation reflects the molecular dynamics with frequencies covering the range of the rf-field (50 kHz in our case). It can be more effectively measured through a ^{13}C detected ^{1}H $T_{1\rho}$-relaxation experiment. This experiment starts with a time period, where the relaxation of ^{1}H magnetization is observed in the presence of a radio-frequency lock-field. Immediately after this time period, magnetization is transferred to the ^{13}C nucleus using cross-polarization. Detection is achieved using the ^{13}C-channel such that the relaxation of the ^{1}H nuclei is probed via their adjacent ^{13}C sites and the corresponding peaks in the ^{13}C NMR spectrum. ^{13}C detected ^{1}H $T_{1\rho}$-relaxation experiments were recorded under conditions comparable to those of the CP-MAS experiments. The relaxation was observed in 32 time intervals ranging from 0.05 ms to 20 ms. The contact time for the cross polarization was set to 1 ms. This ensures the good signal to noise needed for the recording of the data, however spin diffusion during the contact time may lead to an averaging such that the measured $T_{1\rho}$-values rather correspond to mobilities associated with an individual molecule and not to mobilities associated with individual sites in the molecule.

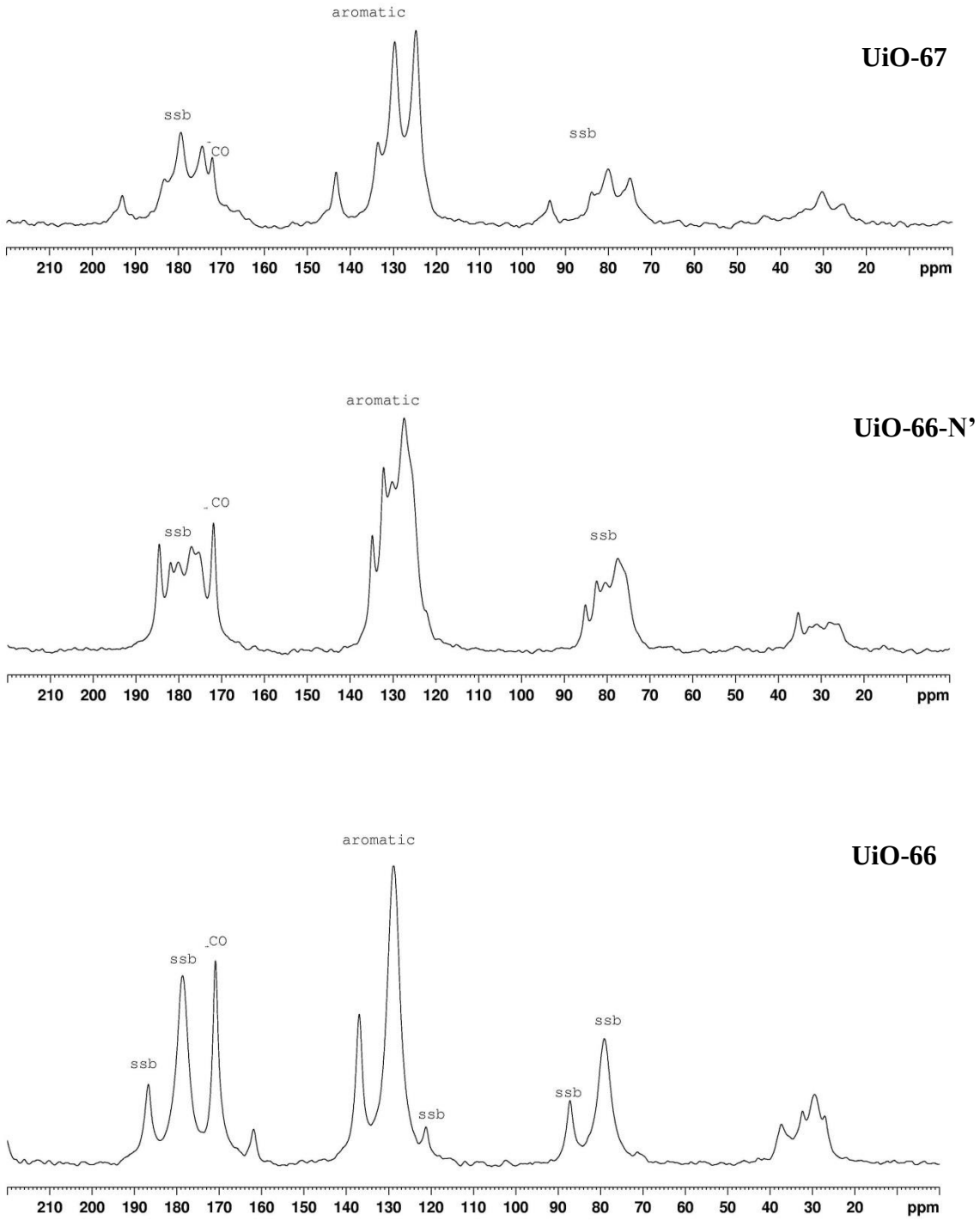

Figure F.2 ^{13}C CPMAS solid-state NMR spectra for UiO-67, UiO-66-N', and UiO-66 (top to bottom) at room temperature. CO, aromatic, and ssb indicate carbonyl peaks, aromatic peaks, and spinning sidebands respectively.

F.2.5 Water Vapor Adsorption

Water vapor adsorption isotherms were measured gravimetrically at 25 ^{o}C and 1 bar using the IGA-3 analyzer from Hiden Isochema. Samples (~ 30-40 mg) were activated *in situ* until no further weight loss was observed prior to the water adsorption measurements. Relative humidity (RH) was controlled by varying the ratio of saturated air and dry air with the help of two mass flow controllers. To avoid water condensation in the equipment at higher humidities, experiments were conducted up to 80% or 90% RH. All the water adsorption experiments were conducted with a total gas flow rate of 200 cm^3/min and each adsorption/desorption step was given sufficient time (from 15 minutes to 20 hrs) to approach equilibrium.

F.3 Results and Discussion

Figure F.2 shows ^{13}C CPMAS solid-state NMR spectra for UiO-67, UiO-66-N', and UiO-66 measured at room temperature. The variable contact-time solid state NMR data measured for the aromatic peak for the activated UiO MOF samples is shown in Figure F.3. Peak intensities measured for various contact times are usually associated with a curve consisting of an increase in peak-intensity due to the transfer of magnetization from ^{1}H to ^{13}C nuclei. This increase is followed by a decay caused by the relaxation of ^{1}H and ^{13}C spins in the rotating frame caused by the oscillating field of the radio-frequency excitation (relaxation constants $T_{1\rho}$). This relaxation constant $T_{1\rho}$ reflects molecular mobility[45] and hence, it is likely to provide a means to compare the dynamics of ligands relative to each other. As mentioned before, differences in the ligand dynamics should be mainly due to the rotation (flipping) of the benzene rings. However, for contact-times varying from 0.01−10 ms, we are unable to observe appreciable amount of

decay for UiO-66 and UiO-66-N' (Figure F.3). Measuring longer contact times is not recommendable due to the high amount of rf-power, which is applied simultaneously in both the ^{1}H and the ^{13}C channel. Hence, $T_{1\rho}$ is more accurately and effectively measured through a ^{13}C detected ^{1}H $T_{1\rho}$-relaxation experiment (Figure F.4) for times varying from 0.01−20 ms. The ^{13}C detected ^{1}H $T_{1\rho}$-relaxation experiment data may reasonably well described by a mono-exponential decay (fit equation: I = Io exp(-time/$T_{1\rho}^{H}$)). For our data $T_{1\rho}^{H}$ appears to correlate positively with increasing rigidity (decreasing mobility), i.e., lower $T_{1\rho}^{H}$ means higher ligand mobility (ring flipping). Hence, it can be seen that the BPDC ligand has the highest mobility whereas 2,6-NDC has the lowest mobility due to the non-linear axis of rotation (Table F.2). $T_{1\rho}^{H}$ for UiO-66 is higher than UiO-67. This could be due to hindered rotation in UiO-66 compared to UiO-67 (sterics for ring flipping is higher in the Zr-BDC framework than Zr-BPDC framework due to smaller size of the ligand).

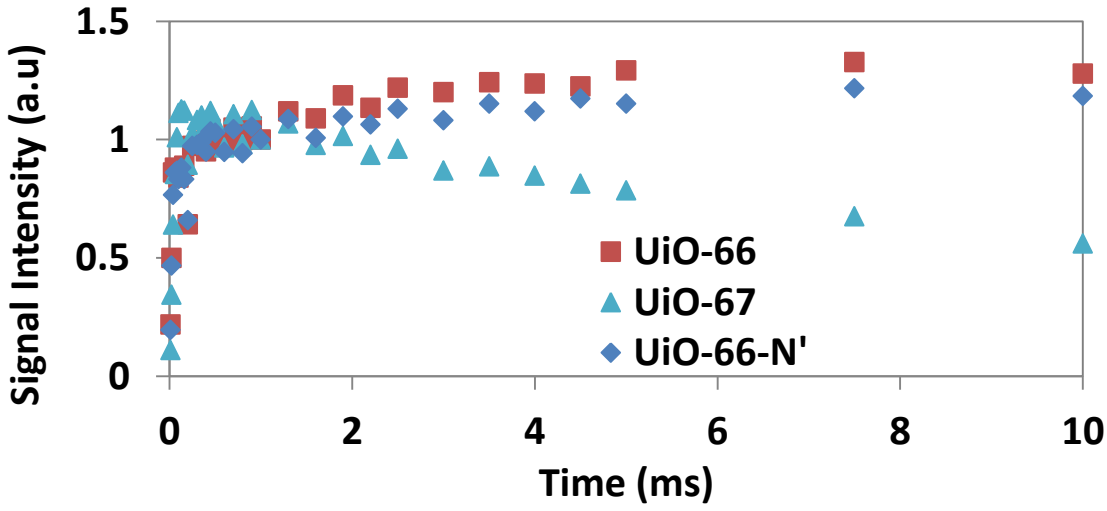

Figure F.3 Variable contact-time curves for the aromatic carbons in the Zr-based UiO series of MOFs.

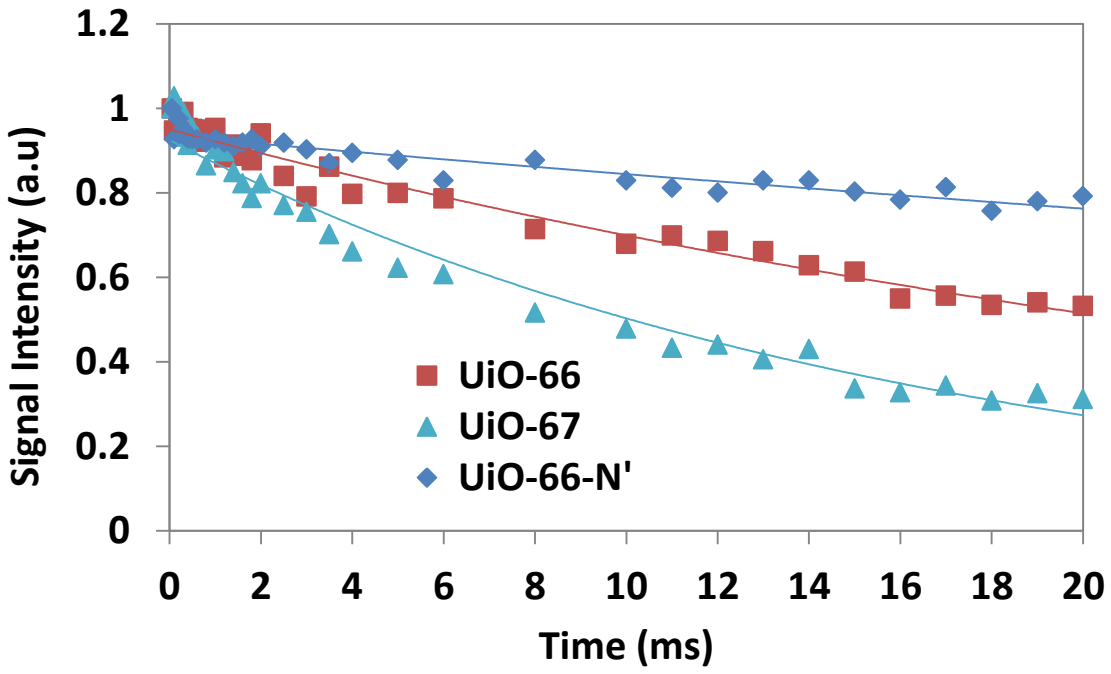

Figure F.4 ^{13}C detected ^{1}H $T_{1\rho}$-relaxation experiments evaluated for the aromatic peak for the Zr-based UiO series of MOFs. Lines connecting the experimental data points represent model fits from equation $I = Io \exp(-time/T_{1\rho}^{H})$.

Figure F.5 compares water vapor adsorption at 25 ^{o}C and 1 bar for the Zr-based UiO series of MOFs. It is interesting to note that the water vapor adsorption loading for UiO-66-N' is lower compared to UiO-66[16] and is quite similar to the loading for UiO-67[16] even when both of these MOFs have higher surface areas and pore volumes than UiO-66. This confirms that similar to UiO-67,[16] UiO-66-N' is also decomposing along the isotherm upon water exposure even when the 2,6-NDC ligand in UiO-66-N' has much lower ligand rotational dynamics than the BPDC ligand in UiO-67 (Table F.2). Hence, it seems the rotational dynamics of ligand does not have a major effect on the water stability of these Zr-based MOFs. The decomposition of UiO-66-N' was further confirmed by comparing its PXRD pattern and BET surface area before and after water

exposure (Table F.1, Figure F.6). It should be noted that the PXRD pattern of the regenerated (reactivated after water exposure) UiO-66-N' sample matches closely with its water-exposed sample. Hence, the decomposition of the UiO-66-N' MOF is taking place during water adsorption itself and not during the regeneration similar to UiO-67.[16]

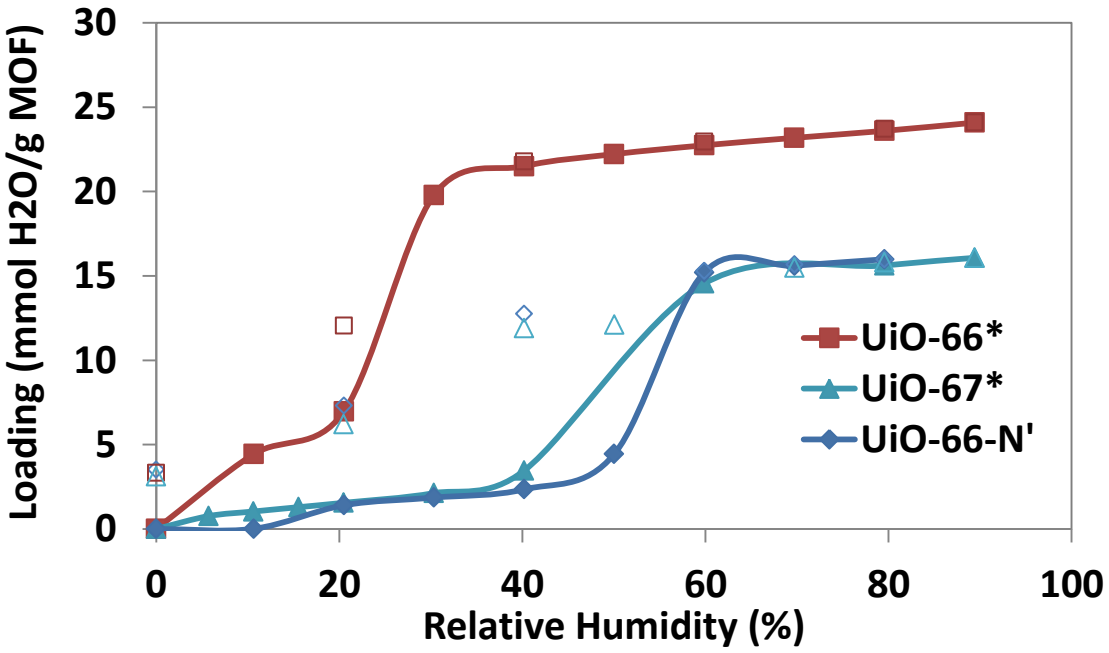

Figure F.5 Water vapor adsorption isotherms for activated samples of Zr-based UiO series of MOFs (closed symbols – adsorption, open symbols – desorption). Lines connecting the adsorption points are to faciliate viewing. *Reported from our previous work.[16]

Table F.1 Comparison of Properties of Isostructural UiO series of MOFs.

MOF	Ligand	pK_a[#]	Window Diameter[‡] (Å)	Cage Dimensions[‡] (Å)	Pore Volume[†] (cm^3/g)	BET Surface Area* (m^2/g)	
						Before	After
[16]UiO-66	BDC	3.73	6	7.5, 12	0.51	1080	1080
[16]UiO-67	BPDC	3.98	8	12, 16	0.89	2145	10
UiO-66-N'	2,6-NDC	3.91	8	11, 14	0.74	1635	9

[†]Obtained from the Dubinin-Astakov model of N_2 adsorption at 77K
Data for UiO-66 and UiO-67 are taken from our previous work[16]
[‡]Obtained from literature[36,37,42]
[#]Calculated using the approach of Hilal et al.[44]
*BET Analysis[43]

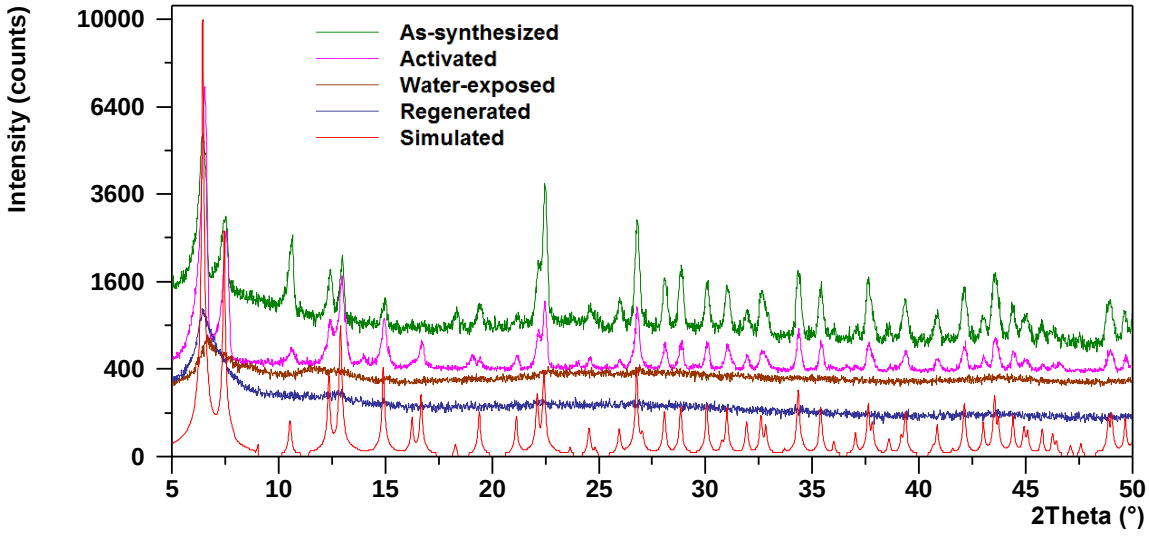

Figure F.6 Comparison between PXRD patterns of as-synthesized, activated, water-exposed (after 80% RH), regenerated (reactivated after water exposure) UiO-66-N', and its theoretical pattern simulated from single crystal data.

Table F.2 Comparison Between $T_{1\rho}^{H}$ Values for Isostructural UiO Series of MOFs as Measured by ^{13}C detected ^{1}H $T_{1\rho}$-Relaxation Experiments. The Aromatic Peak of the Ligand was Used to Evaluate These Values.

MOF	Ligand	$T_{1\rho}^{H}$ (ms)
^{16}UiO-66	BDC	32.1
^{16}UiO-67	BPDC	15.1
UiO-66-N'	2,6-NDC	96.7

Upon combining the contrasting rotational dynamics (ligand mobility or ring flipping, Table F.2) of double ring ligands BPDC and 2,6-NDC and similar instability of UiO-67 and UiO-66-N' upon water exposure (up to 80 % or 90% RH), it seems that the collapse of these double ring ligand-based MOFs is mainly driven by the increased accessibility for water clustering near $Zr_6O_4(OH)_4$ SBU. Hence, upon exposing UiO-66-N' to lower humidities (up to ~ 40 % RH) present in lab air for 10 months there is a slight decrease (~10 % drop, Table F.1) in its BET surface area and no change in its PXRD pattern (Figure F.7a) since water clustering will now be lower. It has already been shown that the breakdown of MOF-5 starts at water adsorption loadings higher than 6 wt. % since at lower loadings water is randomly distributed and not clustered.[46] Upon clustering, the reactivity or basicity for water increases and these clustered water molecules can now break the metal-ligand bond.[46,47] Kusgens and coworkers[25] have also suggested that the water molecules can cluster around the SBU via hydrogen bonding in the pore space of MOFs. Moreover, previous quantum chemical studies[48,49] performed to understand the mechanism of hydrolysis of molecules such as $SiCl_4$ and N_2O_5 have also shown that the activation

energy barrier for hydrolysis reaction reduces with the increasing size of water clusters. UiO-67 has slightly higher porosity (window diameter and cage dimensions) than UiO-66-N' and more pore space (less sterics) is now available for water molecules to cluster and coordinate with metal centers. Hence, stability of UiO-67 upon exposure to lower humidities (up to ~ 40 % RH) present in lab air is lower compared to UiO-66-N'. Upon exposure to lab air for 2 months, its PXRD pattern (Figure F.8) shows some signs of peak broadening and its BET surface area reduces to 955 m^2/g (~ 55 % drop, Table F.1). However, when soaked in liquid water even UiO-66-N' (Figure F.7b) collapses completely similar to UiO-67[16] due to higher clustering of water molecules.

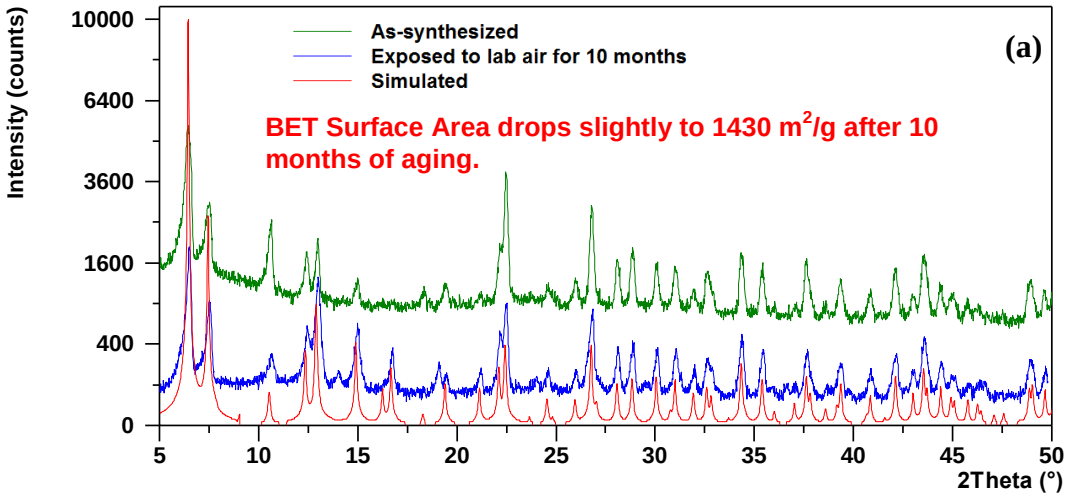

Figure F.7 Comparison between PXRD patterns of (a) as-synthesized, lab air-exposed (for 10 months under ~ 40 % RH) UiO-66-N', and its theoretical pattern simulated from single crystal data (b) as-synthesized, soaked in liquid water (for 24 hrs at room temperature) UiO-66-N', and its theoretical pattern simulated from single crystal data.

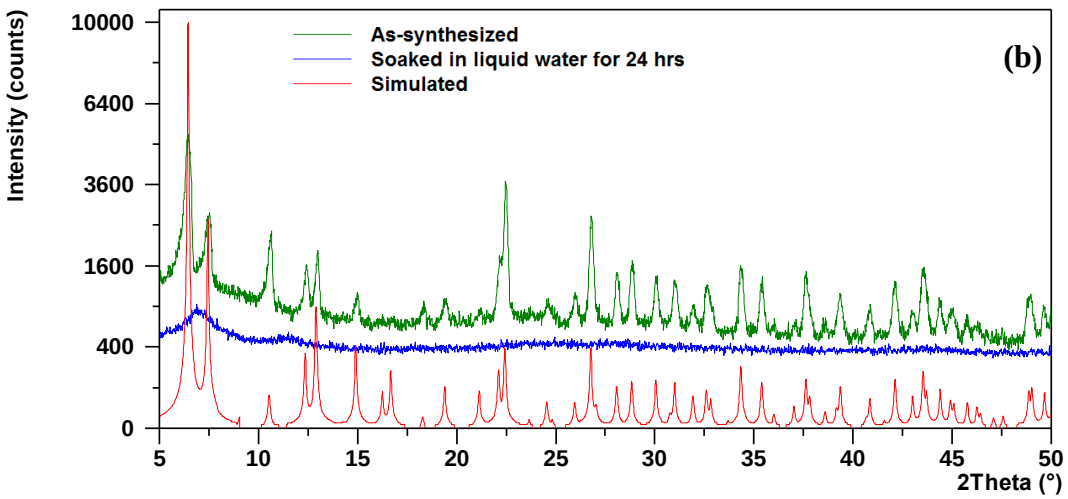

Figure F.7 Continued.

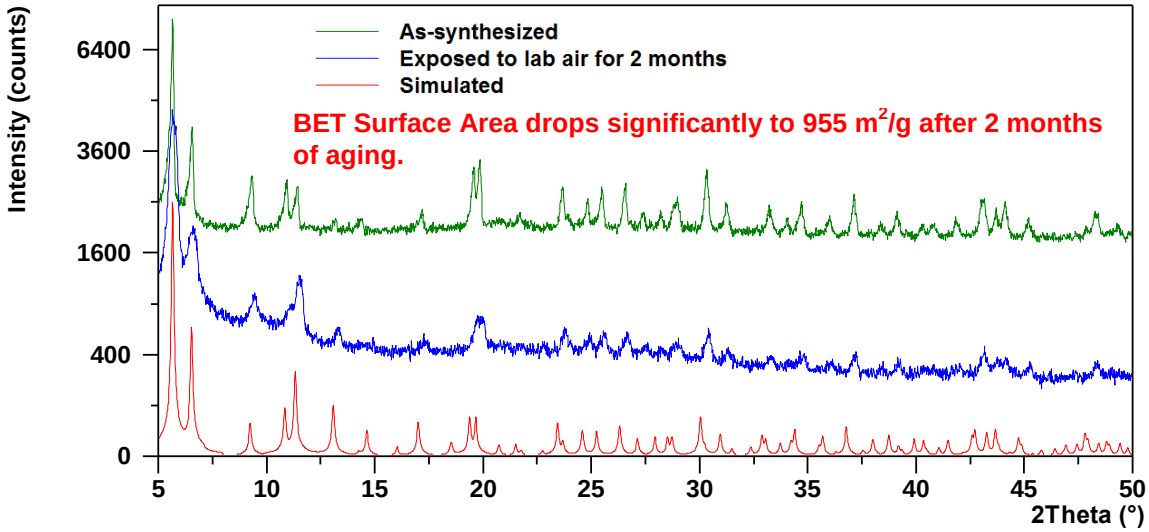

Figure F.8 Comparison between PXRD patterns of as-synthesized, lab air-exposed (for 2 months under ~ 40 % RH) UiO-67, and its theoretical pattern simulated from single crystal data.

Recently, Yaghi and coworkers[50] synthesized various new Zr-based MOFs such as MOF-805 and MOF-806, which are dihydroxy-functionalized variations of UiO-66-N' and UiO-67 respectively (Figure F.9). It was found that water adsorption loadings of these MOFs decreased constantly in every cycle during the cyclic water adsorption experiments. Moreover, there was significant decrease in their surface areas after the cyclic experiments. Similarly, sulfone-functionalized variation of UiO-67 or UiO-67-SO_2[51] and azo-functionalized variation of UiO-67 or UiO-67-Azo[52] were also found to be water sensitive similar to the parent UiO-67. In the future, water stability tests for other Zr-based MOFs such as PCN-56, PCN-57,[53] and UiO-68-NH_2[39] should be performed as these MOFs have pore space larger than UiO-67. We believe that clustering of water molecules is the main driving force behind the collapse of UiO-67 and UiO-66-N', hence, PCN-56, PCN-57, and UiO-68-NH_2 MOFs should also be moisture sensitive. This is counter to the observation of Lillerud and coworkers[36-38] who report that all the Zr-based UiO series of MOFs are water stable. It should also be noted that in this work, we did not consider effect of the presence of defects due to missing ligands ($Zr_6O_4(OH)_4$ SBU is not twelve-coordinated to dicarboxylate ligands anymore)[54] from the framework on the water stability of these Zr-based MOFs, and it is an ongoing research in our group. However, UiO-66-N' synthesized in this work does not seem to have defects due to missing ligands since its PXRD pattern matches nicely with the perfect UiO-66-N' or DUT-52 ($Zr_6O_4(OH)_4$ SBU is twelve-coordinated) and differs significantly from imperfect UiO-66-N' or DUT-53 ($Zr_6O_4(OH)_4$ SBU is eight-coordinated) synthesized by Kaskel and coworkers.[55] Hence, the main reason for the collapse of UiO-66-N' is due to the increased accessibility for water clustering near $Zr_6O_4(OH)_4$ SBU.

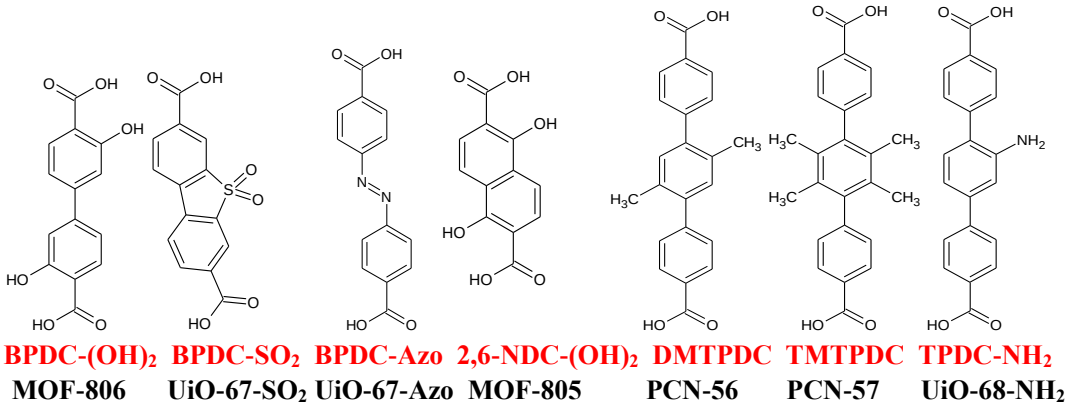

Figure F.9 Ligands utilized in the synthesis of Zr-based MOFs with pores larger than UiO-66 and same topology as the UiO series of MOFs.

F.4 Conclusions

Previously, we have shown that Zr-based MOFs consisting of double ring ligands have lower water stability than MOFs consisting of single ring ligands.[16] In this work, we extended our previous work[16] by using three isostructural Zr-based MOFs: UiO-66, UiO-67, and UiO-66-N' so that the effect of porosity (window diameter and cage dimensions) and ligand rotational dynamics on the water stability of Zr-based MOFs could be decoupled. ^{13}C detected ^{1}H $T_{1\rho}$-relaxation experiments measured for the activated UiO MOF samples show that the BPDC ligand in UiO-67 has the highest mobility whereas 2,6-NDC in UiO-66-N' has the lowest mobility due to the non-linear axis of rotation. Through an analysis of water adsorption isotherms, PXRD patterns, and N_2 adsorption before and after water exposure, it was observed that UiO-66-N' also decomposed upon water exposure similar to UiO-67.[16] Upon combining the results from NMR and water exposure studies, it seems that the increased accessibility for water clustering near

$Zr_6O_4(OH)_4$ SBU is mainly responsible for the collapse of these double ring ligand-based Zr-MOFs (UiO-66-N' and UiO-67). Hence, a similar explanation could be applied to other double ring ligand-based Zr-MOFs such as MOF-805, MOF-806, UiO-67-SO_2, and UiO-67-Azo, which have also been found to decompose upon exposure to humid environments.

F.5 References

(1) Garibay, S. J.; Cohen, S. M. Isoreticular Synthesis and Modification of Frameworks with the UiO-66 Topology. *Chem. Commun.* **2010**, *46*, 7700-7702.

(2) Cambridge Crystallographic Data Center. http://www.ccdc.cam.ac.uk/.

(3) Christopher, E. W.; Michael, L.; Chang Yeon, L.; Omar, K. F.; Brad, G. H.; Joseph, T. H.; Randall, Q. S., Large-scale screening of hypothetical metal–organic frameworks. *Nature Chemistry* **2011,** *4* (2), 83-89.

(4) Database of Zeolite Structures. http://www.iza-structure.org/databases/.

(5) Davis, M. E. Ordered Porous Materials for Emerging Applications. *Nature* **2002**, *417*, 813-821.

(6) Ferey, G. Hybrid Porous Solids: Past, Present, Future. *Chem. Soc. Rev.* **2008**, *37*, 191-214.

(7) Kitagawa, S.; Kitaura, R.; Noro, S. Functional Porous Coordination Polymers. *Angew. Chem.-Int. Edit.* **2004**, *43*, 2334-2375.

(8) Keskin, S.; Van Heest, T. M.; Sholl, D. S. Can Metal-Organic Framework Materials Play a Useful Role in Large-Scale Carbon Dioxide Separations? *ChemSusChem* **2010**, *3*, 879-891.

(9) Keskin, S.; Kizilel, S. Biomedical Applications of Metal Organic Frameworks. *Ind. Eng. Chem. Res.* **2011**, *50*, 1799-1812.

(10) Sumida, K.; Rogow, D. L.; Mason, J. A.; McDonald, T. M.; Bloch, E. D.; Herm, Z. R.; Bae, T. H.; Long, J. R., Carbon dioxide capture in metal-organic frameworks. Chem Rev **2012**, *112 (2)*, 724-81.

(11) Low, J. J.; Benin, A. I.; Jakubczak, P.; Abrahamian, J. F.; Faheem, S. A.; Willis, R. R., Virtual high throughput screening confirmed experimentally: porous coordination polymer hydration. J Am Chem Soc **2009**, *131 (43)*, 15834-42.

(12) Soubeyrand-Lenoir, E.; Vagner, C.; Yoon, J. W.; Bazin, P.; Ragon, F.; Hwang, Y. K.; Serre, C.; Chang, J. S.; Llewellyn, P. L., How water fosters a remarkable 5-fold increase in low-pressure CO_2 uptake within mesoporous MIL-100(Fe). *J Am Chem Soc* **2012,** *134* (24), 10174-81.

(13) Liang, Z. J.; Marshall, M.; Chaffee, A. L., CO_2 adsorption, selectivity and water tolerance of pillared-layer metal organic frameworks. *Microporous and Mesoporous Materials* **2010,** *132* (3), 305-310.

(14) Schoenecker, P. M.; Carson, C. G.; Jasuja, H.; Flemming, C. J. J.; Walton, K. S., Effect of Water Adsorption on Retention of Structure and Surface Area of Metal–Organic Frameworks. *Industrial & Engineering Chemistry Research* **2012,** *51* (18), 6513-6519.

(15) Ma, D.; Li, Y.; Li, Z., Tuning the moisture stability of metal-organic frameworks by incorporating hydrophobic functional groups at different positions of ligands. *Chem Commun (Camb)* **2011,** *47* (26), 7377-9.

(16) DeCoste, J. B.; Peterson, G. W.; Jasuja, H.; Glover, T. G.; Huang, Y. G.; Walton, K. S., Stability and degradation mechanisms of metal-organic frameworks containing the Zr6O4(OH)(4) secondary building unit. *Journal of Materials Chemistry A* **2013,** *1* (18), 5642-5650.

(17) DeCoste, J. B.; Peterson, G. W.; Schindler, B. J.; Killops, K. L.; Browe, M. A.; Mahle, J. J., The effect of water adsorption on the structure of the carboxylate containing metal-organic frameworks Cu-BTC, Mg-MOF-74, and UiO-66. *Journal of Materials Chemistry A* **2013,** *1* (38), 11922-11932.

(18) Tan, K.; Nijem, N.; Canepa, P.; Gong, Q.; Li, J.; Thonhauser, T.; Chabal, Y. J., Stability and Hydrolyzation of Metal Organic Frameworks with Paddle-Wheel SBUs upon Hydration. *Chemistry of Materials* **2012,** *24* (16), 3153-3167.

(19) Jasuja, H.; Huang, Y. G.; Walton, K. S., Adjusting the stability of metal-organic frameworks under humid conditions by ligand functionalization. *Langmuir* **2012,** *28* (49), 16874-80.

(20) Jasuja, H.; Burtch, N. C.; Huang, Y. G.; Cai, Y.; Walton, K. S., Kinetic water stability of an isostructural family of zinc-based pillared metal-organic frameworks. *Langmuir* **2013,** *29* (2), 633-42.

(21) Li, Y.; Yang, R. T., Gas adsorption and storage in metal-organic framework MOF-177. *Langmuir* **2007,** *23* (26), 12937-44.

(22) Jasuja, H.; Walton, K. S., Effect of catenation and basicity of pillared ligands on the water stability of MOFs. *Dalton Trans* **2013,** *42* (43), 15421-6.

(23) Yang, J.; Grzech, A.; Mulder, F. M.; Dingemans, T. J., Methyl modified MOF-5: a water stable hydrogen storage material. *Chem Commun (Camb)* **2011,** *47* (18), 5244-6.

(24) Kaye, S. S.; Dailly, A.; Yaghi, O. M.; Long, J. R., Impact of preparation and handling on the hydrogen storage properties of Zn4O(1,4-benzenedicarboxylate)3 (MOF-5). *J Am Chem Soc* **2007,** *129* (46), 14176-7.

(25) Kusgens, P.; Rose, M.; Senkovska, I.; Frode, H.; Henschel, A.; Siegle, S.; Kaskel, S., Characterization of metal-organic frameworks by water adsorption. *Microporous and Mesoporous Materials* **2009,** *120* (3), 325-330.

(26) Wiersum, A. D.; Soubeyrand-Lenoir, E.; Yang, Q.; Moulin, B.; Guillerm, V.; Yahia, M. B.; Bourrelly, S.; Vimont, A.; Miller, S.; Vagner, C.; Daturi, M.; Clet, G.; Serre, C.; Maurin, G.; Llewellyn, P. L., An evaluation of UiO-66 for gas-based applications. *Chem Asian J* **2011,** *6* (12), 3270-80.

(27) Jasuja, H.; Zang, J.; Sholl, D. S.; Walton, K. S., Rational Tuning of Water Vapor and CO_2 Adsorption in Highly Stable Zr-Based MOFs. *J. Phys. Chem. C* **2012,** *116* (44), 23526-23532.

(28) Jasuja, H.; Walton, K. S., Experimental Study of CO_2, CH_4, and Water Vapor Adsorption on a Dimethyl-Functionalized UiO-66 Framework. *J. Phys. Chem. C* **2013,** *117* (14), 7062-7068.

(29) Decoste, J. B.; Peterson, G. W.; Smith, M. W.; Stone, C. A.; Willis, C. R., Enhanced Stability of Cu-BTC MOF via Perfluorohexane Plasma-Enhanced Chemical Vapor Deposition. *Journal of the American Chemical Society* **2012,** *134* (3), 1486-1489.

(30) Yang, S. J.; Park, C. R., Preparation of Highly Moisture-Resistant Black-Colored Metal Organic Frameworks. *Advanced Materials* **2012,** *24* (29), 4010-4013.

(31) Wu, T.; Shen, L.; Luebbers, M.; Hu, C.; Chen, Q.; Ni, Z.; Masel, R. I., Enhancing the stability of metal-organic frameworks in humid air by incorporating water repellent functional groups. *Chem Commun (Camb)* **2010,** *46* (33), 6120-2.

(32) Nguyen, J. G.; Cohen, S. M., Moisture-resistant and superhydrophobic metal-organic frameworks obtained via postsynthetic modification. *J Am Chem Soc* **2010,** *132* (13), 4560-1.

(33) Cai, Y.; Zhang, Y. D.; Huang, Y. G.; Marder, S. R.; Walton, K. S., Impact of Alkyl-Functionalized BTC on Properties of Copper-Based Metal-Organic Frameworks. *Crystal Growth & Design* **2012,** *12* (7), 3709-3713.

(34) Li, H.; Shi, W.; Zhao, K.; Li, H.; Bing, Y.; Cheng, P., Enhanced Hydrostability in Ni-Doped MOF-5. *Inorganic Chemistry* **2012,** *51* (17), 9200-9207.

(35) Burtch, N. C.; Jasuja, H.; Walton, K. S., Water Stability and Adsorption in Metal-Organic Frameworks. *Chem Rev* **2014,** *Submitted*.

(36) Cavka, J. H.; Jakobsen, S.; Olsbye, U.; Guillou, N.; Lamberti, C.; Bordiga, S.; Lillerud, K. P., A new zirconium inorganic building brick forming metal organic frameworks with exceptional stability. *J Am Chem Soc* **2008,** *130* (42), 13850-1.

(37) Chavan, S.; Vitillo, J. G.; Gianolio, D.; Zavorotynska, O.; Civalleri, B.; Jakobsen, S.; Nilsen, M. H.; Valenzano, L.; Lamberti, C.; Lillerud, K. P.; Bordiga, S., H2storage in isostructural UiO-67 and UiO-66 MOFs. *Physical Chemistry Chemical Physics* **2012,** *14* (5), 1614-1626.

(38) Kandiah, M.; Nilsen, M. H.; Usseglio, S.; Jakobsen, S.; Olsbye, U.; Tilset, M.; Larabi, C.; Quadrelli, E. A.; Bonino, F.; Lillerud, K. P., Synthesis and Stability of Tagged UiO-66 Zr-MOFs. *Chemistry of Materials* **2010,** *22* (24), 6632-6640.

(39) Schaate, A.; Roy, P.; Godt, A.; Lippke, J.; Waltz, F.; Wiebcke, M.; Behrens, P., Modulated synthesis of Zr-based metal-organic frameworks: from nano to single crystals. *Chemistry* **2011,** *17* (24), 6643-51.

(40) Guillerm, V.; Ragon, F.; Dan-Hardi, M.; Devic, T.; Vishnuvarthan, M.; Campo, B.; Vimont, A.; Clet, G.; Yang, Q.; Maurin, G.; Ferey, G.; Vittadini, A.; Gross, S.; Serre, C., A series of isoreticular, highly stable, porous zirconium oxide based metal-organic frameworks. *Angewandte Chemie* **2012,** *51* (37), 9267-71.

(41) Katz, M. J.; Brown, Z. J.; Colon, Y. J.; Siu, P. W.; Scheidt, K. A.; Snurr, R. Q.; Hupp, J. T.; Farha, O. K., A facile synthesis of UiO-66, UiO-67 and their derivatives. *Chemical Communications* **2013,** *49* (82), 9449-9451.

(42) Zhang, W.; Huang, H.; Liu, D.; Yang, Q.; Xiao, Y.; Ma, Q.; Zhong, C., A new metal–organic framework with high stability based on zirconium for sensing small molecules. *Microporous and Mesoporous Materials* **2013,** *171* (0), 118-124.

(43) Walton, K. S.; Snurr, R. Q., Applicability of the BET method for determining surface areas of microporous metal-organic frameworks. *J Am Chem Soc* **2007,** *129* (27), 8552-6.

(44) Hilal, S., Karickhoff, S. W., Carreira, L. A. , A Rigorous Test for SPARC's Chemical Reactivity Models: Estimation of More Than 4300 Ionization pKa's. *Quant. Struc. Act. Rel.* **1995,** *14*, 348.

(45) Burgess, S. K.; Leisen, J. E.; Kraftschik, B. E.; Mubarak, C. R.; Kriegel, R. M.; Koros, W. J., Chain Mobility, Thermal, and Mechanical Properties of Poly(ethylene furanoate) Compared to Poly(ethylene terephthalate). *Macromolecules* **2014,** *47* (4), 1383-1391.

(46) Bellarosa, L.; Castillo, J. M.; Vlugt, T.; Calero, S.; López, N., On the Mechanism Behind the Instability of Isoreticular Metal–Organic Frameworks (IRMOFs) in Humid Environments. *Chemistry – A European Journal* **2012,** *18* (39), 12260-12266.

(47) De Toni, M.; Jonchiere, R.; Pullumbi, P.; Coudert, F.-X.; Fuchs, A. H., How Can a Hydrophobic MOF be Water-Unstable? Insight into the Hydration Mechanism of IRMOFs. *ChemPhysChem* **2012,** *13* (15), 3497-3503.

(48) Ignatov, S. K.; Sennikov, P. G.; Razuvaev, A. G.; Chuprov, L. A.; Schrems, O.; Ault, B. S., Theoretical Study of the Reaction Mechanism and Role of Water Clusters in the Gas-Phase Hydrolysis of SiCl4. *The Journal of Physical Chemistry A* **2003,** *107* (41), 8705-8713.

(49) McNamara, J. P.; Hillier, I. H., Structure and Reactivity of Dinitrogen Pentoxide in Small Water Clusters Studied by Electronic Structure Calculations. *The Journal of Physical Chemistry A* **2000,** *104* (22), 5307-5319.

(50) Furukawa, H.; Gándara, F.; Zhang, Y.-B.; Jiang, J.; Queen, W. L.; Hudson, M. R.; Yaghi, O. M., Water Adsorption in Porous Metal–Organic Frameworks and Related Materials. *Journal of the American Chemical Society* **2014,** *136* (11), 4369-4381.

(51) Xydias, P.; Spanopoulos, I.; Klontzas, E.; Froudakis, G. E.; Trikalitis, P. N., Drastic Enhancement of the CO_2 Adsorption Properties in Sulfone-Functionalized Zr- and Hf-UiO-67 MOFs with Hierarchical Mesopores. *Inorganic Chemistry* **2013,** *53* (2), 679-681.

(52) Schaate, A.; Dühnen, S.; Platz, G.; Lilienthal, S.; Schneider, A. M.; Behrens, P., A Novel Zr-Based Porous Coordination Polymer Containing Azobenzenedicarboxylate as a Linker. *European Journal of Inorganic Chemistry* **2012,** *2012* (5), 790-796.

(53) Jiang, H.-L.; Feng, D.; Liu, T.-F.; Li, J.-R.; Zhou, H.-C., Pore Surface Engineering with Controlled Loadings of Functional Groups via Click Chemistry in Highly Stable Metal–Organic Frameworks. *Journal of the American Chemical Society* **2012,** *134* (36), 14690-14693.

(54) Wu, H.; Chua, Y. S.; Krungleviciute, V.; Tyagi, M.; Chen, P.; Yildirim, T.; Zhou, W., Unusual and Highly Tunable Missing-Linker Defects in Zirconium Metal–Organic Framework UiO-66 and Their Important Effects on Gas Adsorption. *Journal of the American Chemical Society* **2013,** *135* (28), 10525-10532.

(55) Bon, V.; Senkovska, I.; Weiss, M. S.; Kaskel, S., Tailoring of network dimensionality and porosity adjustment in Zr- and Hf-based MOFs. *CrystEngComm* **2013,** *15* (45), 9572-9577.

APPENDIX G

RAW DATA

1. All the reported powder X-ray diffraction (PXRD) data are available as .xrdml files on the Walton Group shared folder under the following extension: S:\Research\Walton group\Himanshu\PXRD-HJ-2014.
2. All the reported N_2 adsorption data for BET analysis are available as .qps files on the Walton Group shared folder under the following extension: S:\Research\Walton group\Himanshu\Nitrogen-BET-HJ-2014.

G.1 Water Stability of MOFs (Chapters 3-6)

G.1.1 Chapter 3

Table G.1.1.1 Water Vapor Adsorption Isotherm Data for DMOF-X at 298 K

DMOF		DMOF-N		DMOF-A	
RH (%)	Loading (mmol/g)	RH (%)	Loading (mmol/g)	RH (%)	Loading (mmol/g)
		0.0000	0.0433		
		10.6250	0.3445		
0.0000	0.0000	20.4860	0.5824		
10.6250	0.1081	30.3300	0.7424	0.0000	0.0000
20.4910	0.2084	40.1710	0.8735	10.6170	0.1137
30.3350	3.4295	50.0240	0.9675	20.4890	0.3902
40.1820	4.7058	59.8790	1.0418	40.1840	14.9263
59.8610	2.4052	69.7080	1.1044	59.8720	15.5062
79.5420	2.4835	79.5450	1.1629	79.5480	16.2407
89.3810	2.5929	89.4010	1.2172	89.4080	16.3668
89.3810	4.6673	89.4010	1.2172		
79.5330	4.4951	79.5530	1.1948		
59.8660	4.3460	59.8740	1.1090	89.4080	16.3668
40.1830	4.2456	40.1850	0.9954	59.8770	15.8577
20.5120	4.1024	20.4930	0.8043	20.4770	0.0451
0.0000	3.8000	0.0000	0.2044	0.0000	0.0340

Table G.1.1.2 Water Vapor Adsorption Isotherm Data for DMOF-X at 298 K

DMOF-TM1		DMOF-TM2		DMOF-NO_2	
RH (%)	Loading (mmol/g)	RH (%)	Loading (mmol/g)	RH (%)	Loading (mmol/g)
0.0000	0.0000	0.0000	0.0000	0.0000	0.0000
10.6360	0.4155	10.6410	0.1316	10.6250	1.9641
20.4910	0.9607	20.4930	0.7102	20.4810	2.0592
30.3400	2.3307	30.3280	14.1069	30.3380	2.1334
40.1700	5.1685	40.1800	17.3649	40.1740	2.3285
50.0290	14.5105	50.0330	17.9218	50.0290	6.3902
59.8730	14.8394	59.8720	18.3921	59.8670	6.6947
69.7200	15.0552	69.7060	18.7851	69.7190	7.1938
79.5520	15.2009	79.5490	19.1452	79.5650	7.2495
89.4090	15.3146	89.3990	19.4593	89.4040	7.3906
89.4090	15.3146	89.3990	19.4593	89.4040	7.3906
79.5660	15.2171	79.5410	19.2003	79.5560	7.3547
59.8800	14.8484	59.8740	18.5440	59.8770	7.2723
40.1740	4.0431	40.1850	17.3139	40.1760	7.1564
20.4830	1.2586	20.4900	0.6163	20.4850	6.9611
0.0000	0.2649	0.0000	0.0000	0.0000	0.7757

Table G.1.1.3 Water Vapor Adsorption Isotherm Data for DMOF-X at 298 K

DMOF-Br		DMOF-Cl_2		DMOF-OH	
RH (%)	Loading (mmol/g)	RH (%)	Loading (mmol/g)	RH (%)	Loading (mmol/g)
0.0000	0.0000	0.0000	0.0373		
10.6300	0.6415	10.6180	0.1904		
20.4870	1.2212	20.4920	0.4237		
30.3300	1.7137	30.3250	0.5885	0.0000	0.0000
40.1750	2.1645	40.1790	3.1687	10.6260	1.1711
50.0260	2.5232	50.0170	3.7197	20.4900	2.5419
59.8770	2.6680	59.8620	3.7943	40.1790	3.1562
69.7100	2.9757	69.7100	3.9482	59.8780	3.6898
79.5600	3.0317	79.5500	4.0520	79.5550	5.1351
89.4080	3.3673	89.3970	4.3054	89.4020	5.7899
89.4080	3.3673	89.3970	4.3054		
79.5580	3.3082	79.5480	4.2595		
59.8680	3.1918	59.8820	4.1002	89.4020	5.7899
40.1840	2.9868	40.1770	3.6817	59.8730	5.0649
20.4810	2.5597	20.4860	2.6309	20.4850	4.6168
0.0000	0.5254	0.0000	1.6425	0.0000	2.4126

G.1.2 Chapter 4

Table G.1.2.1 Water Vapor Adsorption Isotherm Data for DMOF-X at 298 K

DMOF-MM1		DMOF-MM2		DMOF-DM1	
RH (%)	Loading (mmol/g)	RH (%)	Loading (mmol/g)	RH (%)	Loading (mmol/g)
0	0	0	0	0	0
10.645	0.20365	10.645	0.13092	10.63	0.21659
20.499	0.38408	20.499	0.24691	20.484	0.38877
30.348	3.17832	30.348	1.92585	30.342	0.63235
40.189	5.78751	40.189	3.60319	40.18	7.48502
59.869	6.37163	59.869	3.97869	59.869	7.81597
79.539	7.1962	79.539	4.50878	79.545	8.45906
89.379	7.3433	89.379	4.60334	89.391	8.79549
89.379	7.3433	89.379	4.60334	89.391	8.79549
79.543	7.05357	79.543	4.53444	79.557	8.37915
69.709	6.89414	69.709	4.43194	59.87	7.92638
50.025	6.53804	50.025	4.20302	50.025	7.64284
40.18	6.25215	40.18	4.01924	40.178	7.27377
20.503	5.27612	20.503	3.39179	20.496	5.14854
0	2.37328	0	1.52568	0	1.77305

Table G.1.2.2 Water Vapor Adsorption Isotherm Data for DMOF-X at 298 K

DMOF-DM2		DMOF-TF	
RH (%)	Loading (mmol/g)	RH (%)	Loading (mmol/g)
		0	0
0	0	10.632	0.33087
10.622	0.21241	20.494	0.51544
20.486	0.28046	30.345	1.04526
30.336	0.3698	40.187	3.33104
40.181	4.91129	50.033	3.62336
59.864	3.29767	59.871	4.56232
79.554	3.26405	69.715	5.51745
89.4	3.34596	79.543	8.35016
89.4	3.34596		
79.545	3.25845	79.543	8.35016
59.869	3.15621	69.711	4.49598
50.013	3.103	59.875	3.62858
40.18	3.04909	40.186	1.92352
20.499	2.91161	20.493	1.58365
0	2.61096	0	1.11974

Table G.1.2.3 Cyclic Water Vapor Adsorption Isotherm Data for DMOF-TM2 at 298 K

DMOF-TM2- 1st Cycle		DMOF-TM2- 2nd Cycle		DMOF-TM2- 3rd Cycle	
RH (%)	Loading (mmol/g)	RH (%)	Loading (mmol/g)	RH (%)	Loading (mmol/g)
0	0	0	0	0	0
10.637	0.08046	10.627	0.20825	10.639	0.15886
20.496	0.51937	20.499	0.69824	20.502	0.78836
30.342	19.3571	30.346	19.84856	30.338	19.02461
40.197	21.47377	40.19	21.35538	40.185	21.00703
50.033	21.9021	50.034	21.84247	50.034	21.46571
59.875	22.26066	59.876	22.23141	59.866	21.84062
69.721	22.57593	69.712	22.52303	69.72	22.15052
79.542	22.87306	79.551	22.78187	79.562	22.39916
89.396	23.21544	89.409	23.05376	89.393	22.64605
89.396	23.21544	89.409	23.05376	89.393	22.64605
79.536	22.92159	79.542	22.82504	79.559	22.44183
59.873	22.41671	59.883	22.31642	59.874	21.94758
40.185	21.53298	40.188	21.44214	40.198	21.0359
20.491	0.59941	20.494	0.75443	20.494	0.59234
10.642	0.16346	10.633	0.25589	10.635	0.17347
0	0	0	0.02587	0	0

G.1.3 Chapter 5

Table G.1.3.1 Water Vapor Adsorption Isotherm Data for MOF-508-X at 298 K

MOF-508		MOF-508-TM	
RH (%)	Loading (mmol/g)	RH (%)	Loading (mmol/g)
0.0000	3.7519e-3		
10.6190	0.0264		
20.4860	0.0443		
30.3280	0.0579	0.0000	0.0000
40.1820	0.0710	10.6320	1.5540
50.0250	0.0837	20.4890	2.9609
59.8820	0.0953	40.1750	4.6100
69.7130	0.1067	59.8690	6.6244
79.5530	0.1193	79.5470	7.3856
89.3870	0.1326	89.4020	7.5955
89.3870	0.1326		
79.5560	0.1222	89.4020	7.5955
59.8720	0.1007	89.3930	7.5951
40.1780	0.0764	59.8690	7.1688
20.4820	0.0471	20.4840	6.6468
0.0000	8.1054e-3	0.0000	2.6396

G.1.4 Chapter 6

Table G.1.4.1 Water Vapor Adsorption Isotherm Data for M-DMOF-TM at 298 K

Co-DMOF-TM		Ni-DMOF-TM		Cu-DMOF-TM	
RH (%)	Loading (mmol/g)	RH (%)	Loading (mmol/g)	RH (%)	Loading (mmol/g)
0.0000	0.0000	0.0000	0.0000	0.0000	0.0000
10.2620	0.4132	10.6360	0.4731	10.6350	0.4179
20.2140	1.0028	20.5000	0.9939	20.4980	0.9016
30.1510	2.2971	30.3350	1.8434	30.3350	1.1842
40.0870	17.9777	40.1880	4.3987	40.1880	1.9102
50.0230	20.1284	50.0280	16.4595	50.0280	5.6129
59.9620	20.2844	59.8700	19.3083	59.8760	19.9384
69.8910	20.4862	69.7170	19.7470	69.7150	20.5287
79.8200	20.6901	79.5580	20.4926	79.5470	21.5453
		79.5470	20.5959		
		69.7140	20.4863		
		59.8770	20.5826		
79.8200	20.6901	50.0350	19.3188	79.5470	21.5453
69.8930	20.2989	40.1840	18.6904	69.7230	21.4408
59.9640	19.8939	30.3380	9.8272	59.8740	21.5047
40.0860	17.9878	20.4990	4.6696	40.1860	5.8595
20.2120	2.3182	10.6320	4.0004	20.5000	1.2130
0.0000	0.7892	0.0000	1.6227	0.0000	0.1873

Table G.1.4.2 Water Vapor Adsorption Isotherm Data for M-BTTB-DMBPY at 298 K

Co-BTTB-DMBPY		Zn-BTTB-DMBPY	
RH (%)	Loading (mmol/g)	RH (%)	Loading (mmol/g)
0.0000	0.0000	0.0000	0.0000
10.6310	0.1237	10.6430	0.0856
20.4980	0.3603	20.5020	0.1702
30.3450	0.4138	30.3500	0.2604
40.1950	0.5005	40.1850	0.3526
50.0350	0.6057	50.0310	0.4363
59.8720	0.7505	59.8750	0.5263
69.7110	0.9656	69.7080	0.6581
79.5470	1.4733	79.5460	0.9587
89.3970	10.9432	89.3930	11.7179
89.3970	10.9432	89.3930	11.7179
79.5390	6.0584	79.5410	9.4387
59.8820	2.2681	59.8770	0.6926
40.1890	1.8795	40.1870	0.5645
20.4950	1.1789	20.5030	0.3079
0.0000	0.5642	0.0000	0.1262

G.2 Ammonia Adsorption in MOFs (Chapter 7)

All the reported ammonia breakthrough data are available in the excel spreadsheet on the Walton Group shared folder under the following extension: S:\Research\Walton group\Himanshu\Break Thru raw data-all samples.

G.3 Rational Tuning of Water Vapor and CO_2 (Chapter 8)

Table G.3.1 Water Vapor Adsorption Isotherm Data for UiO-66-X at 298 K

UiO-66		UiO-66-MM		UiO-66-DM	
RH (%)	Loading (mmol/g)	RH (%)	Loading (mmol/g)	RH (%)	Loading (mmol/g)
0	0				
11.239	1.6719				
20.939	3.234	0	0	0	0
30.631	7.0056	10.637	1.49789	10.634	1.02285
40.352	14.7357	20.489	2.73082	20.502	2.12314
50.01	20.4498	30.343	9.49289	30.338	4.43883
59.721	20.9815	40.178	12.91653	40.183	5.86016
69.403	21.4392	59.861	15.85348	59.864	9.45798
79.111	21.8702	79.539	17.09718	79.549	11.86008
88.803	22.4186	89.403	17.64282	89.401	12.72864
		89.403	17.64282	89.401	12.72864
88.803	22.4186	79.535	17.11923	79.537	12.12539
79.091	22.1657	69.702	16.62866	69.707	11.49626
59.71	21.3969	50.025	14.99329	50.03	7.60379
40.335	20.1303	40.192	13.18837	40.194	6.60708
20.937	14.3876	20.501	3.37576	20.504	4.0775
0	2.422	0	1.53838	0	1.75317

Table G.3.2 CO_2 Adsorption Isotherm Data for UiO-66-X at 303 K

UiO-66		UiO-66-MM		UiO-66-DM	
Pressure (mbar)	Loading (mmol/g)	Pressure (mbar)	Loading (mmol/g)	Pressure (mbar)	Loading (mmol/g)
0	0				
170	0.3349				
350	0.6464				
560	0.9477				
800	1.2533				
1040	1.529	0.722	0	1.39	0
1260	1.7609	15.288	0.06713	12.616	0.02954
1530	2.014	497.715	1.32586	498.784	1.05139
1790	2.2427	996.847	1.96792	995.11	1.67394
2050	2.451	1998.451	2.74295	2000.723	2.47013
3330	3.3169	3007.405	3.27251	3006.069	2.99766
5190	4.2228	4000.055	3.67453	3994.042	3.37223
6640	4.7462	6006.204	4.30397	6008.876	3.90785
9150	5.4136	9007.675	4.99305	9007.809	4.42749
10780	5.7489	12005.4	5.52428	12009.01	4.78376
12350	6.0145	15004.6	5.94928	15006.21	5.05492
13800	6.2253	18009.68	6.29355	17986.03	5.27263
17000	6.5845	19994.31	6.49732	20110.71	5.39321
		19994.31	6.49732	20110.71	5.39321
		18997.39	6.38801	19179.94	5.35779
		15498.52	6.01275	15645.39	5.11532
		11998.59	5.52331	11992.44	4.80042
		8487.695	4.89973	8499.055	4.38645
17000	6.5845	5000.991	4.02721	4993.106	3.72198
13920	6.2881	1487.159	2.42606	1495.845	2.22139
11390	5.9374	5.399	0.02768	4.197	0.06289

Table G.3.3 CH_4 Adsorption Isotherm Data for UiO-66-X at 303 K

UiO-66		UiO-66-MM		UiO-66-DM	
Pressure (mbar)	Loading (mmol/g)	Pressure (mbar)	Loading (mmol/g)	Pressure (mbar)	Loading (mmol/g)
0	0				
210	0.1228				
420	0.238				
710	0.3725				
1040	0.5105				
1310	0.6133				
1580	0.7103				
1960	0.833	0	0	0	0
2670	1.041	15.823	0.02139	18.228	0.04465
3220	1.1935	499.185	0.31678	496.646	0.43782
4210	1.452	996.045	0.53841	994.441	0.69573
4850	1.5842	1998.852	0.90604	1987.225	1.07198
5470	1.6995	3011.414	1.19897	3003.797	1.33581
6890	1.9784	3999.521	1.43551	3987.761	1.54003
7750	2.1433	6010.212	1.83844	6009.411	1.86295
8340	2.26	9008.343	2.30941	9008.209	2.22271
8930	2.3773	12004.87	2.69575	12006.87	2.50062
9490	2.4886	15004.87	3.0286	14982.69	2.74078
10040	2.5722	18009.82	3.31645	18130.62	2.94287
12050	2.8348	19993.91	3.49483	20188.22	3.06665
12050	2.8348				
10690	2.7136				
9500	2.5519				
8460	2.3677				
6870	2.0977	19993.91	3.49483	20188.22	3.06665
5580	1.8466	18998.32	3.41403	19017.3	2.99685
4550	1.6013	15498.79	3.08382	15498.66	2.76416
3470	1.3202	11998.72	2.69636	11998.32	2.50377
2520	1.0465	8500.124	2.22335	8497.317	2.15255
1640	0.7549	5002.061	1.61258	4996.715	1.66596
1070	0.5074	1492.771	0.67049	1497.181	0.83729
0	0	2.727	0	4.865	0.05369

G.4 Appendix F

Table G.4.1 Water Vapor Adsorption Isotherm Data for Zr-based UiO series of MOFs at 298 K

UiO-66		UiO-67		UiO-66-N’	
RH (%)	Loading (mmol/g)	RH (%)	Loading (mmol/g)	RH (%)	Loading (mmol/g)
0	0	0	0		
10.645	4.433485245	5.708	0.761294441	0	0
20.502	6.965850686	10.623	1.035037379	10.636	0.00725182
30.337	19.78689952	15.56	1.292960166	20.498	1.404715337
40.18	21.50041089	20.487	1.550830393	30.342	1.858355656
50.021	22.21645195	30.336	2.125331413	40.19	2.347073997
59.874	22.73989076	40.181	3.452577334	50.034	4.434062767
69.717	23.18191866	59.884	14.55028249	59.871	15.20633436
79.561	23.59756724	79.548	15.61715288	69.719	15.60447581
89.401	24.0842409	89.412	16.07211803	79.56	15.98453496
		89.412	16.07211803		
89.401	24.0842409	79.565	15.80741518	79.56	15.98453496
79.565	23.70927289	69.727	15.48200709	69.722	15.67947428
59.872	22.96393253	50.036	12.10996712	59.867	15.28737994
40.185	21.77701221	40.181	11.90237799	40.185	12.74594772
20.499	12.04589485	20.488	6.215742933	20.502	7.305003992
0	3.330414685	0	3.111681968	0	3.514912293

Table G.4.2 Variable Contact-Time Curve Data for the Aromatic Carbons in the Zr-based UiO Series of MOFs

UiO-66		UiO-67		UiO-66-N'	
Time (ms)	Intensity (arb. units)	Time (ms)	Intensity (arb. units)	Time (ms)	Intensity (arb. units)
0.01	0.218889	0.01	0.110014	0.01	0.19544
0.02	0.5	0.02	0.344308	0.02	0.466884
0.04	0.861111	0.04	0.640605	0.04	0.765472
0.06	0.880555	0.06	0.853225	0.06	0.86102
0.08	0.863888	0.08	1.0096	0.08	0.867535
0.1	0.838888	0.1	1.11248	0.1	0.83279
0.13	0.874999	0.13	1.12757	0.13	0.880564
0.16	0.888888	0.16	1.12209	0.16	0.831704
0.2	0.641666	0.2	0.893006	0.2	0.659066
0.25	0.972222	0.25	1.02058	0.25	0.972855
0.3	0.977777	0.3	1.08231	0.3	0.977198
0.35	0.994444	0.35	1.10151	0.35	0.990228
0.4	0.949999	0.4	1.06585	0.4	0.947882
0.45	1.04444	0.45	1.12072	0.45	1.03366
0.5	0.999999	0.5	1.07133	0.5	1.02823
0.6	0.991666	0.6	0.965708	0.6	0.946797
0.7	1.05	0.7	1.107	0.7	1.04343
0.8	0.997222	0.8	0.979426	0.8	0.941368
0.9	1.05555	0.9	1.12483	0.9	1.05429
1	0.999999	1	1	1	1
1.3	1.11944	1.3	1.06722	1.3	1.08578
1.6	1.08889	1.6	0.976682	1.6	1.00651
1.9	1.18611	1.9	1.01509	1.9	1.09663
2.2	1.13333	2.2	0.93553	2.2	1.06297
2.5	1.21944	2.5	0.960221	2.5	1.12921
3	1.2	3	0.868314	3	1.08035
3.5	1.24167	3.5	0.886147	3.5	1.15092
4	1.23611	4	0.847738	4	1.11835
4.5	1.225	4.5	0.813445	4.5	1.17264
5	1.29167	5	0.784638	5	1.15092
7.5	1.32778	7.5	0.674898	7.5	1.21607
10	1.27778	10	0.561044	10	1.1835

Table G.4.3 ^{13}C Detected ^{1}H $T_{1\rho}$-Relaxation Experiment Data for the Aromatic Peak for the Zr-based UiO Series of MOFs

UiO-66		UiO-67		UiO-66-N'	
Time (ms)	Intensity (arb. units)	Time (ms)	Intensity (arb. units)	Time (ms)	Intensity (arb. units)
0.05	1	0.05	1	0.05	1
0.1	0.947253	0.1	1.0283	0.1	0.926829
0.2	0.964835	0.2	0.933019	0.2	0.97561
0.3	0.991209	0.3	0.990566	0.3	0.95122
0.4	0.953846	0.4	0.913208	0.4	0.926829
0.5	0.951648	0.5	0.95283	0.5	0.926829
0.6	0.920879	0.6	0.933962	0.6	0.926829
0.8	0.949451	0.8	0.865094	0.8	0.918699
1	0.953846	1	0.90283	1	0.926829
1.2	0.883516	1.2	0.898113	1.2	0.918699
1.4	0.914286	1.4	0.849057	1.4	0.910569
1.6	0.887912	1.6	0.822642	1.6	0.918699
1.8	0.876923	1.8	0.787736	1.8	0.926829
2	0.940659	2	0.822642	2	0.910569
2.5	0.83956	2.5	0.770755	2.5	0.918699
3	0.791209	3	0.754717	3	0.902439
3.5	0.861538	3.5	0.701887	3.5	0.869919
4	0.797802	4	0.661321	4	0.894309
5	0.8	5	0.622642	5	0.878049
6	0.786813	6	0.607547	6	0.829268
8	0.714286	8	0.516038	8	0.878049
10	0.679121	10	0.478302	10	0.829268
11	0.698901	11	0.433019	11	0.812195
12	0.685714	12	0.440566	12	0.800813
13	0.661538	13	0.40566	13	0.829268
14	0.628571	14	0.430189	14	0.829268
15	0.613187	15	0.336792	15	0.802439
16	0.549451	16	0.327358	16	0.78374
17	0.556044	17	0.343396	17	0.813008
18	0.534066	18	0.307547	18	0.756911
19	0.540659	19	0.325472	19	0.779675
20	0.531868	20	0.311321	20	0.79187